

Case Studies for

Fatigue Education

Ralph I. Stephens, editor

STP 1250



STP 1250

Case Studies for Fatigue Education

Ralph I. Stephens, Editor

ASTM Publication Code Number (PCN):
04-012500-30



ASTM
1916 Race Street
Philadelphia, PA 19103
Printed in the U.S.A.

Library of Congress Cataloging-in-Publication Data

Case studies for fatigue education / Ralph I. Stephens, editor.

(STP ; 1250)

"ASTM publication code number (PCN) 04-012500-30."

Includes bibliographical references.

ISBN 0-8031-1997-6

1. Materials—Fatigue—Case studies. I. Stephens, R. I. (Ralph Ivan) II. Series.

III. Series: ASTM special technical publication ; 1250.

TA418.38.C37 1994

620.1'126—dc20

94-41520

CIP

Copyright ©1994 AMERICAN SOCIETY FOR TESTING AND MATERIALS, Philadelphia, PA. All rights reserved. This material may not be reproduced or copied, in whole or in part, in any printed, mechanical, electronic, film, or other distribution and storage media, without the written consent of the publisher.

Photocopy Rights

Authorization to photocopy items for internal or personal use, or the internal or personal use of specific clients, is granted by the AMERICAN SOCIETY FOR TESTING AND MATERIALS for users registered with the Copyright Clearance Center (CCC) Transactional Reporting Service, provided that the base fee of \$2.50 per copy, plus \$0.50 per page is paid directly to CCC, 222 Rosewood Dr., Danvers, MA 01923; Phone: (508) 750-8400; Fax: (508) 750-4744. For those organizations that have been granted a photocopy license by CCC, a separate system of payment has been arranged. The fee code for users of the Transactional Reporting Service is 0-8031-1997-6/94 \$2.50 + .50.

Peer Review Policy

Each paper published in this volume was evaluated by three peer reviewers. The authors addressed all of the reviewers' comments to the satisfaction of both the technical editor and the ASTM Committee on Publications.

The quality of the papers in this publication reflects not only the obvious efforts of the authors and the technical editor, but also the work of these peer reviewers. The ASTM Committee on Publications acknowledges with appreciation their dedication and contribution to time and effort on behalf of ASTM.

Foreword

This publication, *Case Studies for Fatigue Education*, contains papers presented at the symposium of the same name, held in Atlanta, GA, 18 May 1993. The symposium was sponsored by ASTM Committee E-8 on Fatigue and Fracture and its Subcommittee E-08.01 on Research and Education. Symposium session chairpersons were: R. I. Stephens, The University of Iowa; R. C. Rice, Battelle Memorial Institute; and N. C. Dowling, Virginia Polytechnic Institute and State University. R. I. Stephens presided as symposium chairperson and editor of this publication.

Contents

| | |
|--|-----|
| Overview —R. I. STEPHENS | 1 |
| 1. Automotive Wheel Assembly: A Case Study in Durability Design — R. W. LANDGRAF, S. THANGJITHAM, AND R. L. RIDDER | 5 |
| 2. The Use of Failure Analysis and Materials Testing in the Redesign of a Boat Trailer Roller Arm —G. C. SALIVAR | 23 |
| 3. Design of a Composite Hip Prosthesis for Long-Term Performance —K. LIAO AND K. L. REIFSNIDER | 32 |
| 4. Fatigue of a Landing Gear Actuator Beam in a Fighter Aircraft — S. KANTIMATHI AND T. N. WHITE | 53 |
| 5. Fatigue Evaluation of Agitator Paddle Shafts —H. R. JHANSALE | 67 |
| 6. Fatigue Cracking of a Welded Roll Used in a Paper-Mill Roll Press — J. E. ZAPATA AND S. C. ANDERSON | 77 |
| 7. Welded Pipeline Fatigue Analysis —D. SOCIE AND E. SEGAN | 86 |
| 8. Thermal Fatigue Analysis: A Case Study of Recuperators —S. P. BHAT | 101 |
| 9. Shell and Detail Fracture Formation in Railroad Rails —R. C. RICE | 109 |
| 10. Equating Damped Vibration to Constant Amplitude Fatigue Loading for a Thick-Walled Pressure Vessel —R. I. STEPHENS, T. B. ADAMS, AND S. L. CARLSON | 139 |
| 11. Development of a Numerical Model for Predicting Fatigue Lives of Tubular Threaded Connections —T. D. LIEBSTER AND G. GLINKA | 156 |
| 12. Fatigue Life Prediction for Wind Turbines: A Case Study on Loading Spectra and Parameter Sensitivity —H. J. SUTHERLAND, P. S. VEERS, AND T. D. ASHWILL | 174 |
| 13. Fatigue Cases Involving the Use of Wood and a Wood Composite — G. H. KYANKA | 208 |

Overview

The *Case Studies for Fatigue Education* special technical publication (STP) was planned to provide engineering educators and students with a broad range of non-trivial, real-world fatigue problems/situations and solutions for use in the classroom. Hopefully, these cases will provide stimulation for a better understanding of the major causes of mechanical failure. The 13 cases included in this publication involve new designs, rework designs, failure analysis, prototype decisions, environmental aspects, metals, non-metals, components, structures, and fasteners. As Rice points out in his case involving railroad rails, the cases bring out the need for students to integrate elements of engineering that commonly enter into a fatigue design or failure analysis. These elements include mechanics of deformable bodies, materials science and characterization, fractography, nondestructive inspection, design of experiments, performing and evaluating experiments, data acquisition and reduction, damage modeling, life prediction, and reliability. Rice also points out that most fatigue problems do not have one unique solution, and in fact, the “best” solution can often be dictated by financial constraints, time limitations, availability of pertinent material and processing information, liability concerns, and public perception. Based upon the above, the solutions for these cases range from complex to simple.

In order to provide real-life cases rather than technical research papers, authors were requested to use a format suitable for educational case studies. A variety of different formats could be successful in achieving this end. Authors were given excerpts from an American Society for Engineering Education (ASEE) paper, on writing engineering cases. It was suggested that each case should have specific comments, questions, instructions, and so forth for student/faculty readers to consider. The three referees of each paper were also given these instructions concerning format to aid them in their review decisions. Thus, the authors and referees worked very hard to hopefully bring together quality case studies on fatigue that will be beneficial in an educational environment. This educational environment includes undergraduate and graduate level courses and continuing education such as short courses and telecommunication media courses. The cases are also applicable to practicing engineers involved with fatigue problems either on a single involvement basis or as a group learning situation. Thus, the market or interest for these cases has actually expanded from the original goals of principally university/college usage to include the practicing engineer.

Faculty, students, and practicing engineers may have a difficult time in choosing cases for specific goals. In order to simplify this choosing and to provide a better understanding and content of each case, the following table is provided in this overview. The table includes headings that emphasize the principal aspects of each case. The paper number agrees with the number in the table of contents. The second column, entitled Major Topic, includes one to six words that best describe the product involved. It is quickly seen that a variety of different products are involved in the thirteen cases. The Author column includes the names of all authors for each case. In the Material column, it is seen that a variety of carbon steels (1010, 1018, 1040, 1080), alloy steels (HSLA, 4340, D6AC), stainless steels (A312, 304), aluminum alloys (5454, 6063), wood and wood composite, and a polymer composite are involved with these cases. Both low- and high-strength materials are involved. The next three columns provide information as to the type of fatigue model involved. An X in the ϵ - N column means that case involves the local notch strain methodology involving strain-life data. An X in the S - N column means the case involves the nominal stress methodology involving stress-life data. An X in the LEFM column means that the case involves linear elastic fracture mechanics using fatigue crack growth rate, da/dN , which is a function of the

stress intensity factor range, ΔK . Seven cases involve ϵ - N , three cases involve S - N , and five cases involve $da/dN - \Delta K$. Two cases have more than one fatigue methodology. The next two columns, FEA and Experimental Stress Analysis, provide whether stresses/strains were determined through finite element analysis and/or through experimental means. In other cases, stress calculations using a strength of materials approach were used if needed. Three cases include FEA and four cases include experimental stress analysis. The next two columns, Fatigue Life Predictions and Fatigue Tests are involved in every case; that is, every case involved fatigue life predictions and/or fatigue tests, which is probably expected. The last column indicates six cases that involved some form of fractographic analysis. This included both macro and micro analysis using optical and/or scanning electron fractography. Hopefully, this table will aid in making appropriate case selections for a given objective. It is suggested that potential case users review this table before considering a specific case.

Case reproduction as class handouts will be a very important consideration for users. ASTM offers quantity discounts for this STP, as well as for reprints of individual cases. Please call ASTM customer service for more information at (215) 299-5585. As for photocopying, this authorization is addressed in a paragraph that appears in the front matter of this, and all ASTM STPs. Please refer to this paragraph for photocopying requirements.

The thirteen cases in this publication involve authors representing six universities, six private companies, and two government agencies. The cases come from ten different states within the United States and one province in Canada. They represent a broad spectrum of engineering fatigue problems. Not the least of these problems is product liability litigation. Two additional papers had to be withdrawn by the authors during the refereeing stage due to lawyer requests, based upon active products liability litigation. This just points out additional difficulties in fatigue education and that hopefully this publication will contribute to quality engineering education involving fatigue.

The editor would like to thank the authors, referees, symposium session chairpersons, the organizing committee, and the ASTM staff for making this publication possible. The organizing committee included R. I. Stephens, The University of Iowa, Chairperson; R. C. Rice, Battelle Memorial Institute; N. C. Dowling, Virginia Polytechnic Institute and State University; B. I. Sandor, The University of Wisconsin; and H. Sehitoglu, The University of Illinois.

Ralph I. Stephens

Mechanical Engineering Department
The University of Iowa,
Iowa City, IA 52242;
symposium chairperson and STP editor.

Automotive Wheel Assembly: A Case Study in Durability Design

REFERENCE: Landgraf, R. W., Thangjitham, S., and Ridder, R. L., “**Automotive Wheel Assembly: A Case Study in Durability Design,**” *Case Studies for Fatigue Education, ASTM STP 1250*, Ralph I. Stephens, Ed., American Society for Testing and Materials, Philadelphia, 1994, pp. 5–22.

ABSTRACT: A project to decrease the weight of a stamped metal automotive wheel assembly, through material substitution and downgaging, is presented as a case study in durability design. A coordinated analytical/experimental approach is used to assess wheel fatigue performance under laboratory and simulated service conditions. Finite element modeling is employed to develop relations between bending moments applied to the wheel during cornering maneuvers and peak stress excursions in the wheel spider. Cyclic material properties for candidate materials (high-strength steel and aluminum), that include the effects of cold work resulting from the wheel-forming operation, are used with strain-based fatigue methods to obtain estimates of wheel performance under various cyclic loading situations, including a standard Society of Automotive Engineers (SAE) laboratory fatigue test and service histories representative of different drivers and customer routes. Finally, reliability design methods are employed to evaluate the effects of variations in wheel geometry, materials properties, and service loading on the expected fatigue performance of a fleet of vehicles in service situations. This approach provides failure probability information based on measured or estimated variations in design parameters and is particularly relevant to quality and warranty issues.

KEY WORDS: fatigue analysis, wheel design, materials substitution, finite elements, service histories, reliability, fatigue education

Automotive wheels have evolved over the decades from early spoke designs of wood and steel, carry overs from wagon and bicycle technology, to flat steel discs and, finally, to the stamped metal configurations of modern vehicles. Historically, successful designs were arrived at through experience and extensive field testing. In recent times, these procedures have been supplanted by a variety of experimental and analytical techniques for structural analysis (strain gages and finite element methods), durability analysis (fatigue life prediction), and reliability methods for dealing with the variations inherent in engineering structures. This newer technology provides unique opportunities to improve the product development process through the application of more rational and time saving procedures.

Wheels are clearly safety related components and, hence, fatigue performance has always been a prime concern. Further, wheels continue to receive considerable attention as part of industry efforts to reduce weight, in this case unsprung weight, through material substitution and down-gaging. The disc, or spider, portion of the wheel assembly is particularly vulnerable to the high bending moments generated during cornering maneuvers. This situation is

¹ Professor and associate professor, respectively, Virginia Polytechnic Institute, Blacksburg, VA 24061-0219.

² Design engineer, B&W Fuel Company, Lynchburg, VA 24506-0935.

portrayed in Fig. 1 where the applied loading is seen to be a function of vehicle geometry and weight and the lateral acceleration achieved in cornering. Shown in Fig. 2 is the configuration of a standard Society of Automotive Engineers (SAE) laboratory test (SAE J328a, Wheel-Passenger Cars: Performance Requirements and Test Procedures), designed to simulate cornering loads and which, in the United States, is used as an acceptance test by wheel designers.

The case study presented here is based on a comprehensive project to reduce the weight of a 14 by 5 in. stamped automotive wheel spider through material substitution. The student is exposed to modern approaches for selecting materials and sizing components based on specified performance objectives based either on a standard accelerated laboratory test or on expected service history spectra. In a more general vein, the study provides a platform for introducing students to modern design tools for structural and durability analysis and for critically assessing their applicability in product development and evaluation.

After a statement of project objectives, the study is presented in three parts, each representing an increasing level of sophistication. The first part focuses on initial component sizing, that is, selection of appropriate thicknesses for each candidate material, to successfully meet the standard laboratory fatigue test requirement. Finite element analysis (FEA) is employed to determine stress distributions in the rather complex wheel spider; these results are compared with experimental strain measurements on production wheels as a validation check. Tests results on prototype wheel assemblies are provided to assess predictive accuracy.

In the second part, estimates of the performance of prototype wheels under simulated service conditions are developed using field measurements representative of various percentile drivers and various customer routes. Here attention is focused on the influence of variations in service usage and material properties on wheel life. Finally, a combined durability and reliability analysis is presented to project the probability of wheel failure under service conditions when expected variations in material properties and component geometry are simultaneously considered.

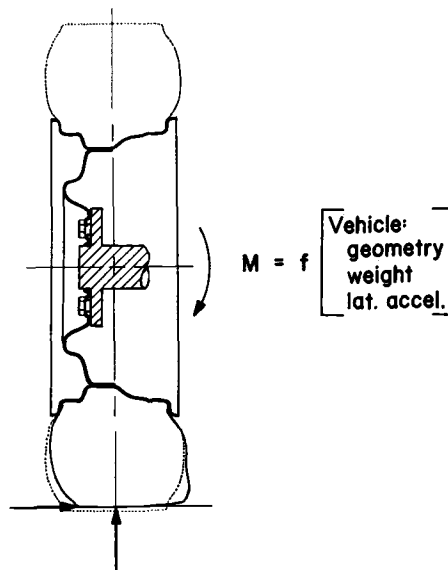


FIG. 1—Wheel loading during cornering maneuver.

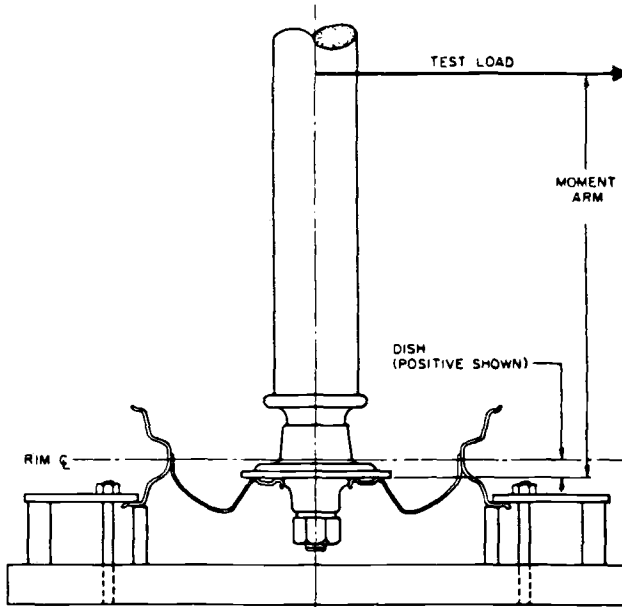


FIG. 2—SAE rotary fatigue test for evaluating wheel performance.

Project Objective

Determine, through the use of computer simulation and analysis tools, the extent of weight reduction possible by the substitution of high-strength, low-alloy (HSLA) steel or aluminum for conventional hot-rolled, low-carbon steel in an automotive wheel spider.

Stage One: Initial Component Sizing

Performance Requirements

- SAE standard rotary fatigue test (SAE J328a),
- applied moment = 1 528 ft-lbs (2 072 N · m),
- required fatigue life = 50 000 cycles (Weibull B_{10} , 90% confidence level), and
- for initial sizing, use 100 000 cycles.

Technical Issues

- fatigue testing to established standard procedures,
- stress analysis using finite element methods,
- incorporating plasticity considerations in elastic stress analysis,
- correlating calculated stresses with experimental (strain gage) measurements,
- fatigue analysis using strain-based methods, including material processing effects,
- establishing component dimensions for least-weight design, and
- material selection for fatigue resistance.

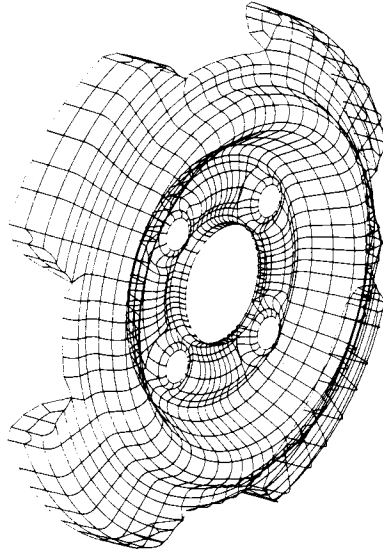


FIG. 3—Finite element model of wheel spider.

Technical Approach

The first step in arriving at an estimate of fatigue performance for the wheel spider is to locate the highly stressed areas under the prescribed test loading. Because of the complex geometry of the wheel spider, finite element modeling is employed for this purpose. Local stresses and strains at potential failure-sites are then determined as a function of load level and thickness. These in turn are used in conjunction with material fatigue properties to calculate allowable thicknesses for candidate materials.

Stress Analysis

Figure 3 shows a finite element model of the wheel spider; isostress contours (von Mises stress), resulting from the application of a bending moment through the wheel hub, are displayed in Fig. 4. Because it is the range of stress, and not the maximum value, that is of significance for fatigue calculations, the stress excursions during one wheel revolution must be determined. This can be accomplished by incrementally altering the orientation of the applied moment. The results of such an analysis are shown for three critical locations in Fig. 5. By performing additional analyses at different applied moments and material thicknesses, a general stress relationship can be developed

$$S_a = 0.153 \cdot M \cdot (t^{-1.4}) \quad (1)$$

where

- S_a = stress amplitude (ksi),
- M = moment (in.-kips), and
- t = thickness (in.).³

³ For stress in MPa, moment in N · m, and thickness in mm, the constant in Eq 1 is 0.0344.

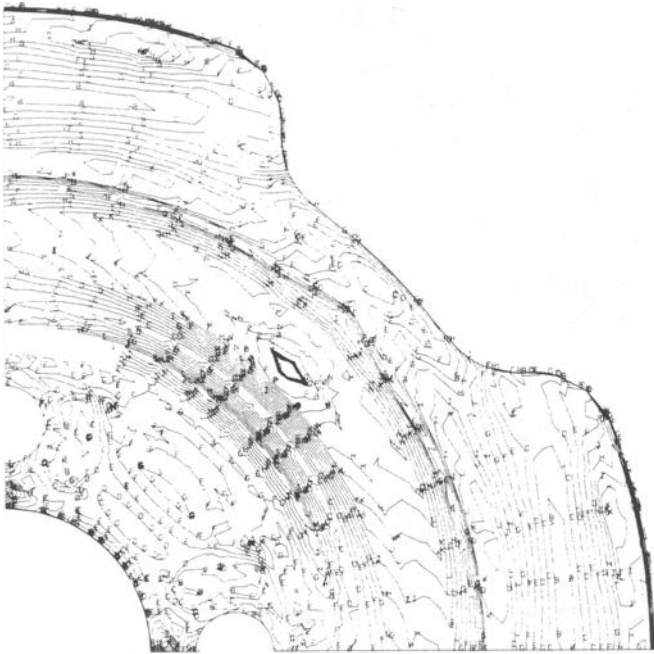


FIG. 4—Stress contour plot for applied bending moment.

When using computer simulation tools in engineering design, it is important to establish the validity of design calculations by experimental confirmation. Only in this way can the necessary confidence in computational methods be established. In the current study, production wheels had been instrumented with single-leg strain gages at observed failure locations, thus providing the necessary experimental check on finite element results. The location of fatigue cracks and strain gages are shown in Fig. 6. These locations are seen to be consistent with the finite element results in Fig. 5.

A problem arises, however, when, with reference to the material stress-strain curves in Fig. 7, it is noted that the stresses achieved during the finite element simulation of the SAE laboratory test exceed the yield strength of the production steel, thus violating the elastic assumptions of the finite element model. An approach for resolving this dilemma entails using a plasticity correction proposed by Neuber [1] for notched members. This method is illustrated in Fig. 8 where the elastic finite element solution, when plotted on the elastic line, allows determination of a rectangular hyperbola which, at the point of intersection with the material stress-strain curve (cyclic), provides an estimate of the actual local stress and strain. A check of the validity of this approximate, but easily applied, method is provided by strain gage measurements on the production wheel. These results for the two highest stress points, presented with the corrected finite element strains in Fig. 9, indicate that the method gives quite reasonable results.

Thickness Determination

With an adequate stress-strain analysis in hand, appropriate material thicknesses, and hence weight reductions, can be determined based on the relative fatigue resistances of candidate

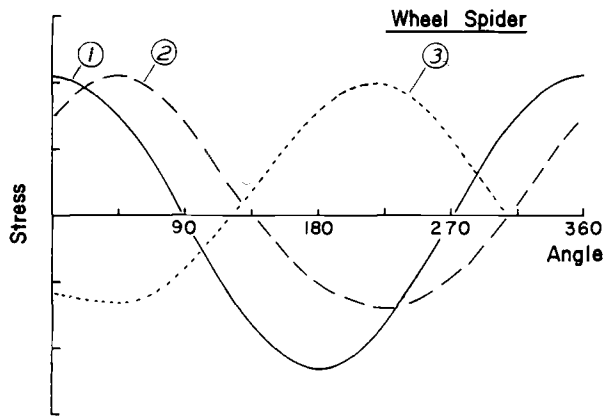
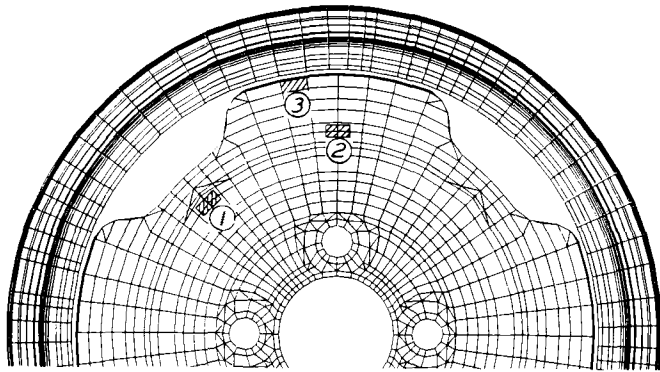


FIG. 5—Stress excursions at critical locations during one-wheel revolution.

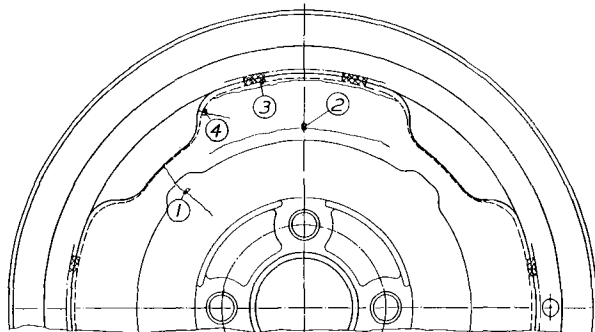


FIG. 6—Fatigue cracks in tested wheel and strain gage locations.

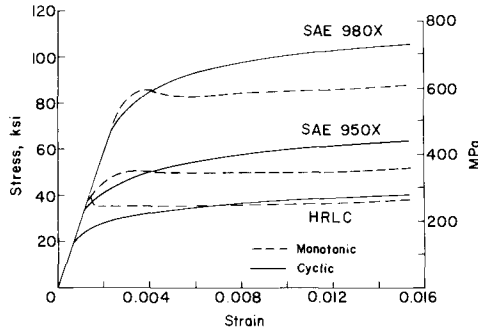


FIG. 7—Stress-strain curves for three-wheel steels.

materials. Strain-life curves for three steels are displayed in Fig. 10. The strain-life relation is of the form

$$\epsilon_a = \frac{\sigma'_f}{E} (2N_f)^b + \epsilon'_f (2N_f)^c \tag{2}$$

where the relevant cyclic properties, along with density and cost information, for candidate wheel materials are presented in Table 1. Properties are reported both for the as received and a 20% cold worked condition for each material to account for metal forming effects on wheel performance. Cold working of this magnitude, which is typical of wheel forming processes, can measurably improve material fatigue performance.

An additional computational aid is provided when the strain-life curve for the candidate materials are presented in the parametric form shown in Fig. 11. By entering this curve at the elastic stress solution, the Neuber correction is automatically applied and the estimated life can be directly determined. This relation is a function of the cyclic material properties and is of the following form

$$S_a = [(\sigma'_f)^2 (2N_f)^{2b} + \sigma'_f \epsilon'_f E (2N_f)^{b+c}]^{1/2} \tag{3}$$

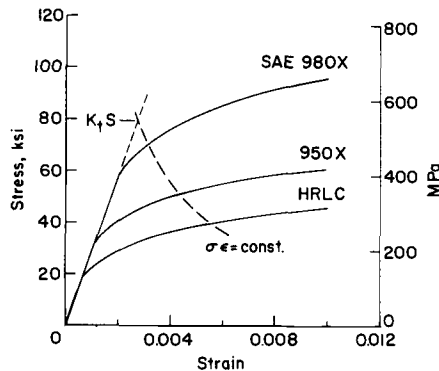


FIG. 8—Neuber procedure for applying plasticity correction to elastic analysis.

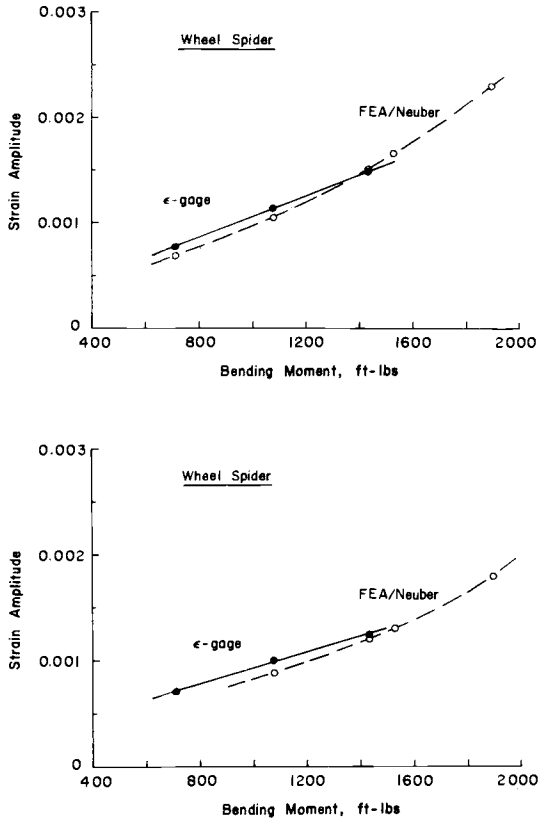


FIG. 9—Comparison of corrected FEA results with strain-gage measurements for Locations 1 and 2 in Figs. 5 and 6.

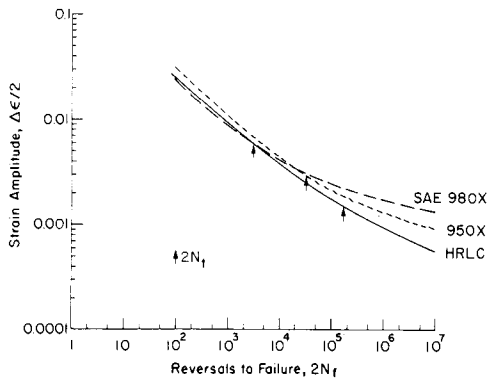


FIG. 10—Strain-life curves for candidate steels.

TABLE 1—Wheel material data.

| Material | E , ksi(MPa) | σ'_f , ksi(MPa) | b | ϵ'_f | c | ρ , lbs/in. ³ (g/cm ³) | \$/lb |
|---------------|----------------|------------------------|-------|---------------|-------|--|-------|
| SAE 1015 | 29 500 (203) | 90 (621) | -0.10 | 0.16 | -0.44 | 0.284 (7.87) | 0.20 |
| 20% CW | | 80 (552) | -0.07 | 0.17 | -0.45 | | |
| SAE 980X | 29 500 (203) | 190 (1310) | -0.10 | 0.25 | -0.56 | 0.284 (7.87) | 0.26 |
| 20% CW | | 190 (1310) | -0.07 | 0.25 | -0.56 | | |
| 5454 Aluminum | 10 000 (69) | 80 (552) | -0.12 | 1.80 | -0.85 | 0.096 (2.66) | 1.00 |
| 20% CW | | 80 (552) | -0.10 | 1.75 | -0.80 | | |

Material thicknesses required to satisfy the SAE laboratory test (100 000 cycles) can be determined using Eqs 1 and 3. Results of these calculations are summarized in Table 2 where it is seen that the SAE 980X steel provides a 21% weight savings with no cost penalty, while the 5454 aluminum alloy provides a substantial 47% weight savings but at a large cost penalty. Finally, evidence of the legitimacy of the described method is provided in Fig. 12 where predicted fatigue lives are compared with experimental results from rotary wheel tests. The agreement is found to be quite reasonable, particularly in light of the rather large scatter evident in the test results; the symbols represent average lives, while the bands indicate the range of the test data.

Summarizing Stage 1 Tasks, finite element results, corrected for plasticity effects and validated by experimental measurements, are used to accomplish initial component sizing based on the standard SAE rotary fatigue test. Material processing effects (cold working) are included through alterations in cyclic material properties. An initial evaluation of weight saving potential and relative material costs is thus accomplished. In the next part, these results will be extended to predictions of service performance.

Stage 2: Prediction of Service Performance

Objective

Using measured wheel service loading spectra, estimate the expected service life, in miles, of the wheel spiders.

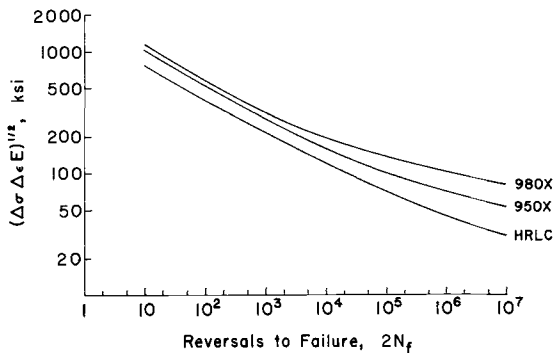


FIG. 11—Parametric fatigue curves for finite element life predictions.

TABLE 2—Weight reduction results.

| Weight | Thickness, mm (in.) | Relative Weight | Relative Cost (material) |
|---------------|---------------------|-----------------|--------------------------|
| SAE 1010 | 3.56 (1.14) | 1.0 | 1.0 |
| SAE 980X | 2.79 (0.11) | 0.79 | 1.0 |
| 5454 Aluminum | 5.72 (0.22) | 0.53 | 2.6 |

Additional Technical Issues

- service loads measurement,
- determination of driver variability,
- accounting for material variability in fatigue calculations,
- estimating service performance, and
- use of damage distribution histograms.

Technical Approach

With high volume products such as automotive wheels, it is important to anticipate, as accurately as possible, the extremes of field usage. Audi engineers [2] have reported wheel service spectra developed using an instrumented vehicle that was driven over a standard route by a cross-section of customers. Results of this sampling are tabulated in Table 3 and displayed in Fig. 13 as a series of bending moment-frequency spectra for various percentile drivers. Wheel bending moments are normalized to the levels obtained by a professional test driver (100%). These usage profiles, when combined with the previous finite element results and material property information, provide predictions of expected lifetimes for the various percentile drivers. The procedure involves performing a linear cumulative damage analysis

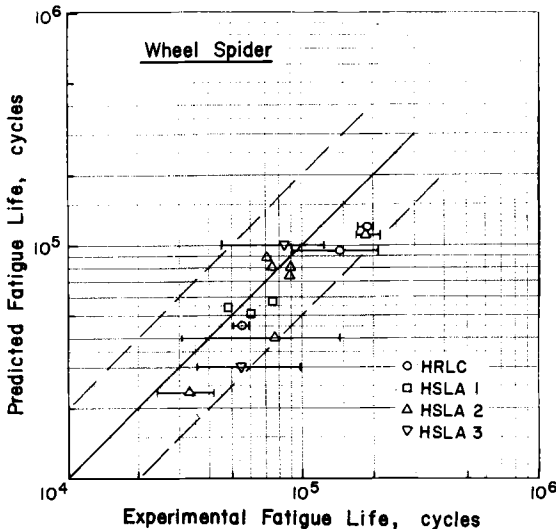


FIG. 12—Comparison of predicted fatigue lives with wheel test results.

TABLE 3—Audi wheel spectra.

| Moment, % FS | Cycle Count per Driver | | | | |
|--------------|------------------------|--------|--------|--------|--------|
| | Test | 1% | 3% | 50% | 97% |
| 100 | 3 | | | | |
| 95 | 17 | | | | |
| 90 | 35 | | | | |
| 85 | 55 | 2 | | | |
| 80 | 60 | 5 | 2 | | |
| 75 | 50 | 13 | 4 | | |
| 70 | 100 | 15 | 9 | | |
| 65 | 50 | 35 | 20 | | |
| 60 | 100 | 50 | 35 | 3 | |
| 55 | 100 | 80 | 80 | 12 | |
| 50 | 200 | 100 | 150 | 35 | 2 |
| 45 | 150 | 200 | 200 | 70 | 6 |
| 40 | 300 | 300 | 300 | 180 | 22 |
| 35 | 800 | 400 | 400 | 400 | 120 |
| 30 | 2 000 | 800 | 800 | 1 300 | 450 |
| 25 | 6 000 | 4 000 | 4 000 | 2 000 | 1 400 |
| 20 | 10 000 | 9 000 | 9 000 | 11 000 | 6 000 |
| 15 | 15 000 | 15 000 | 15 000 | 15 000 | 17 000 |
| 10 | 20 000 | 25 000 | 25 000 | 25 000 | 30 000 |
| Total | 55 020 | 55 000 | 55 000 | 55 000 | 55 000 |
| Miles | | | 64.6 | | |

NOTE—100% = 1900 ft-lbs (2576 N · m) for calculations.

using appropriately scaled bending moment distributions for various drivers from Table 3. Damage at each level is obtained by iteratively solving Eq 3. The total damage for one sequence is then determined and a lifetime, in miles, projected.

Results

Such results, shown in the form of probability plots in Fig. 14, compare two candidate steels on the basis of average- and lower-bound properties. Lower-bound estimates were

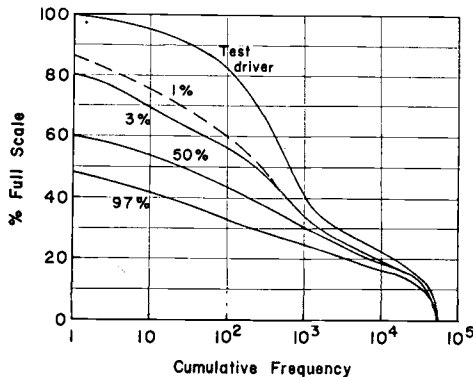


FIG. 13—Audi service loading spectra for various percentile drivers [2].

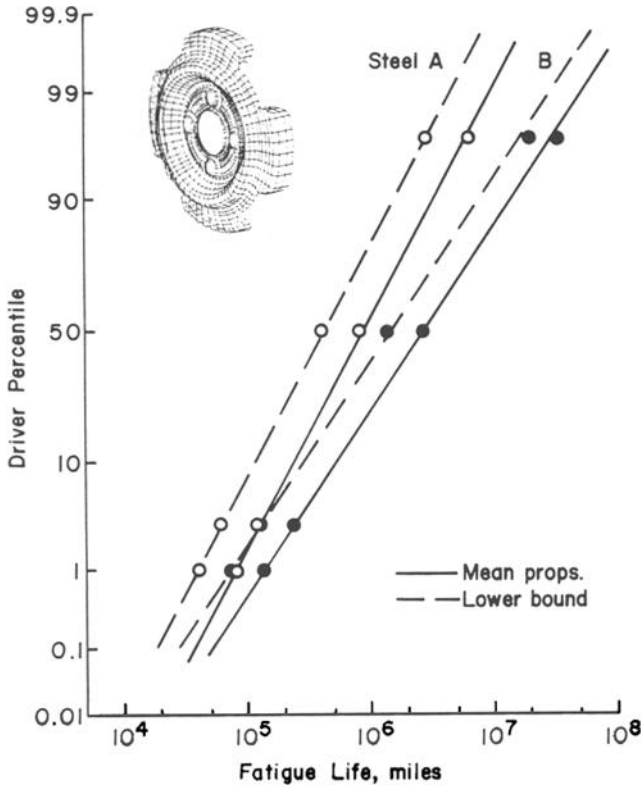


FIG. 14—Service life estimates for two steels.

obtained using the lower 95% confidence interval from a statistical analysis of strain-life material data sets to adjust the material constants in Eq 2. In this way, both material and usage variability can be conveniently incorporated in design analysis. Note the significant difference in expected lifetime between an average (50 percentile) and severe (1 percentile) driver. Also, the performance improvement achieved by material selection becomes less at the shorter lives. Another useful output from such an analysis is shown in Fig. 15 in the form of damage distribution histograms for the various drivers. These profiles are seen to be quite driver dependent and can provide valuable insights concerning which events are most important in a spectrum. This information is particularly relevant to the establishment of more realistic laboratory simulation tests. It can be argued that this approach gives a more reliable indication of wheel performance than the constant amplitude rotary test used for initial component sizing; it is used routinely by European manufacturers.

In the next section, a more rigorous treatment of the various sources of variability is presented using combined durability and reliability concepts.

Stage 3: Combined Durability/Reliability Analysis

Objective

Through the use of combined durability and reliability methods, quantify variations in component geometry, material properties, and loading, in order to project wheel lifetimes in terms of failure probabilities.

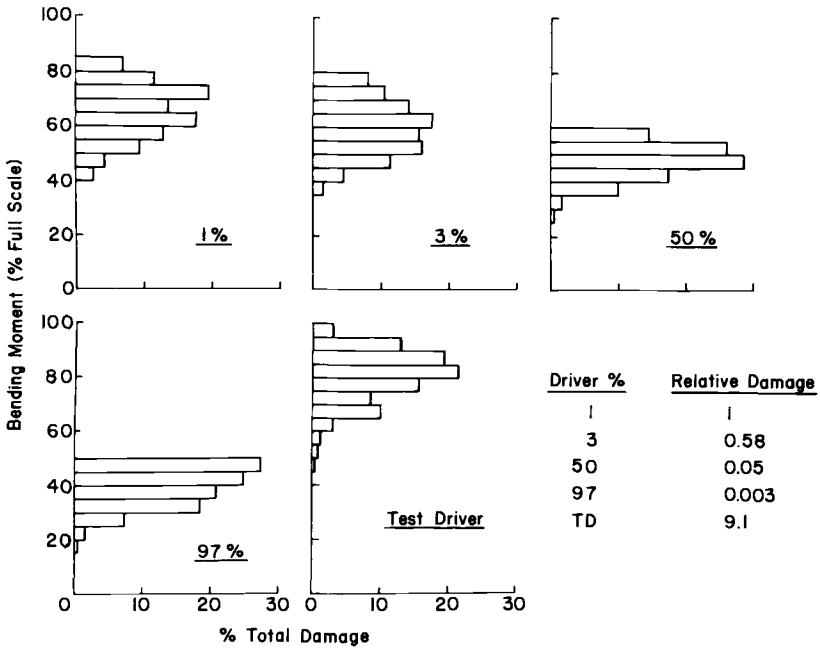


FIG. 15—Damage distribution profiles for different percentile drivers.

Additional Technical Issues

- dealing with variability and uncertainty using reliability methods,
- integrated application of reliability and durability methods,
- fatigue life in terms of probability of failure,
- modeling driver usage by route synthesis, and
- sensitivity analysis in fatigue design.

Background

An additional issue involved with high volume manufacture is the necessity to consider in a quantitative way how the myriad of often subtle component-to-component variations can influence the service performance of large fleets of vehicles. Reliability methods [3] provide a rigorous approach for combining the specified or expected uncertainties in design and performance parameters into probabilistic design methods that can provide estimates of the likelihood of fatigue failure at prescribed lifetimes. This information provides the designer with valuable guidance for optimizing designs and for selecting and controlling material and processing parameters to assure a given safe level of performance.

Technical Approach

The basic steps involved in combined durability and reliability design are outlined in Fig. 16 [4]. Here, material properties, geometry, and loads data, along with their distributions, are accessed and divided into stress and strength elements. These stress and strength func-

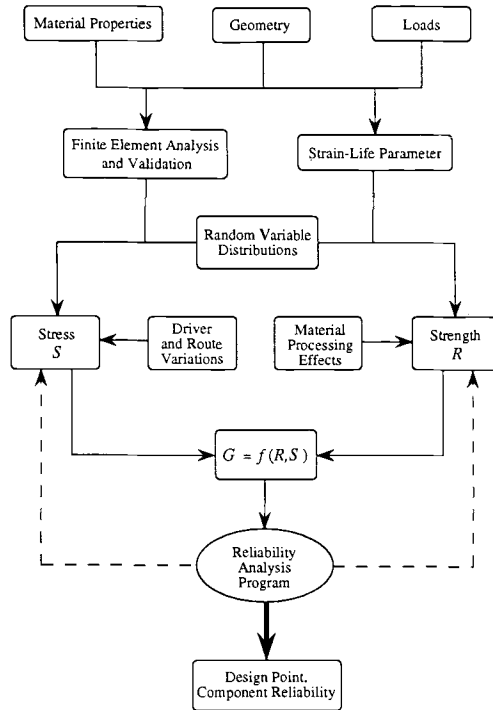


FIG. 16—Flow chart for combined durability/reliability analysis.

tions are then combined into the performance function, $G(R,S)$, developed from Eqs 1 and 3, which is called repeatedly by the reliability analysis program in order to arrive at a design point (most probable failure point) by an iterative scheme [3]. Details of the development and application of this procedure are presented in Ref 4. The results and implications of the approach will be emphasized here. For the wheel study, variations in geometry (thickness) and material fatigue properties are combined and a probabilistic analysis carried out for various service spectra. Included are the Audi percentile driver data and additional data generated by MIRA in England for a variety of continental and British routes [5]. These routes are tabulated in Table 4 in the form of relative bending moment-cycle count distributions.

Results

Probability of failure-fatigue life plots for various percentile drivers are shown in Fig. 17. The steel and aluminum display quite similar trends, with the 1% driver producing a failure probability of about one in 100 at 200 000 miles for steel wheels and 7 in 1 000 for aluminum. An average driver produces failure probabilities of 3 in 100 and 2 in 1 000, respectively, for the steel and aluminum at similar mileage.

Using the data in Table 4, it is possible to synthesize the various route segments into a realistic service history for different types of driver usage. Three such combined routes were developed: an "average" route, composed of 40% freeway, 30% highway, 15% city, 10% rural, and 5% mountainous routes; a "traveler" route, with a respective breakdown of 60,

TABLE 4—MIRA wheel spectra.

| Moment, % FS | Continental | | | | | | British | | | |
|--------------|-------------|-------------|--------------|---------------|--------|----------------|-----------|--------|--|--|
| | Turini Fast | Turini Slow | Col de Braus | Col de Bleine | London | Derby, Part II | Leicester | A5 | | |
| 100 | 146 | ... | 21 | ... | 8 | 5 | ... | ... | | |
| 85 | 54 | ... | 305 | ... | 17 | 80 | 62 | 9 | | |
| 69 | 1 172 | 51 | 633 | 225 | 46 | 299 | 46 | 66 | | |
| 54 | 3 534 | 368 | 1 054 | 784 | 54 | 912 | 196 | 180 | | |
| 38 | 3 005 | 1 540 | 935 | 1 861 | 152 | 2 414 | 899 | 180 | | |
| 23 | 3 790 | 3 292 | 2 416 | 3 921 | 281 | 4 524 | 2 789 | 657 | | |
| 8 | 4 933 | 4 690 | 3 465 | 6 713 | 5 482 | 16 888 | 23 014 | 10 345 | | |
| Total Miles | 31 665 | 31 687 | 26 035 | 37 524 | 15 351 | 46 780 | 41 624 | 49 420 | | |
| | 38 | 38 | 32 | 44 | 18 | 54 | 49 | 59 | | |

Note.—100% = 1210 ft-lbs (1640 N · m) for calculations.

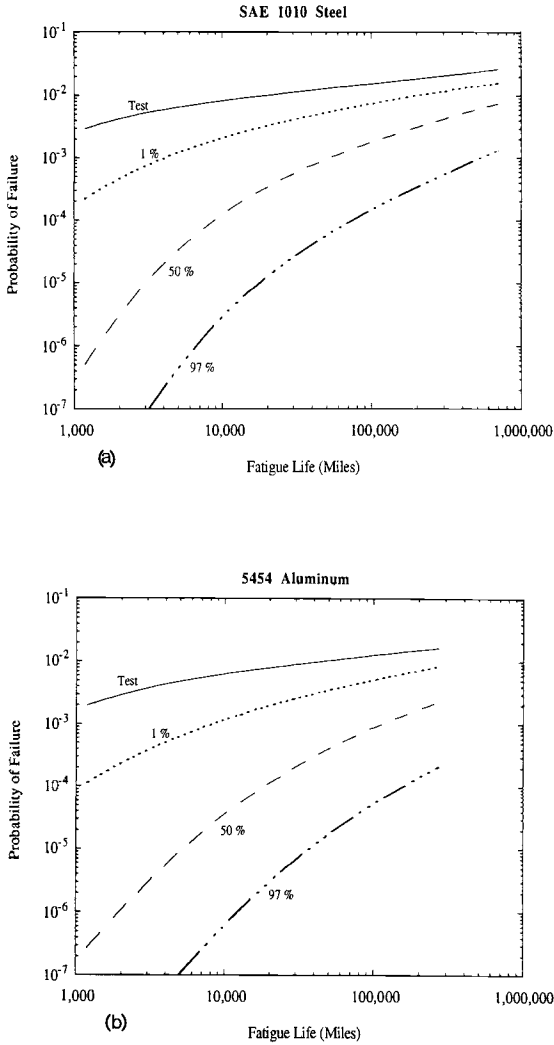


FIG. 17—Failure probability estimates for different drivers.

20, 15, 5, and 0%; and a “local” route entailing a 10, 20, 35, 20, and 15% relative route distribution. Results for the steel and aluminum are shown in Fig. 18. Again, similar trends are noted between the materials with about a factor-of-five difference in failure probability noted between the traveler and local driver at 100 000 miles.

Exercises of this type can provide valuable guidance to designers in component optimization by relating probable service performance to variations in design, material, and manufacturing parameters. Any number of “what if . . . ?” scenarios can be readily performed and sensitivity analyses carried out to generate quantitative relationships between component design, production parameters, and structural durability. These considerations hold special relevance to product quality and warranty issues.

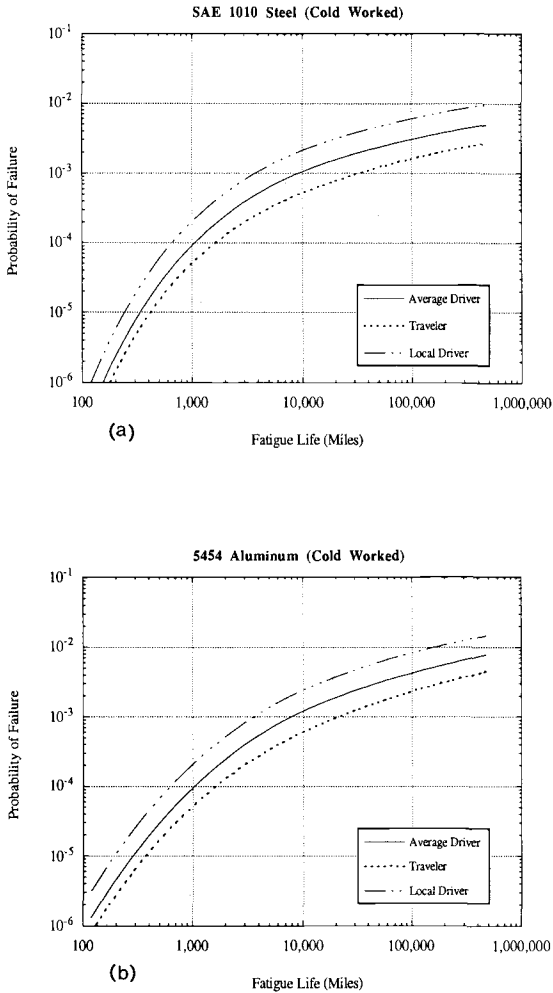


FIG. 18—Failure probability estimates for synthesized service routes.

Conclusions

Taken together, the three phases of wheel development presented provide a range of educational opportunities for engineering students. In addition to gaining a rather broad view of product development and evaluation methods currently applied in industry, the study provides a framework for presenting and developing treatments of several technical areas of importance in engineering practice. Examples include:

- materials selection in design,
- material processing effects,
- strain-based fatigue methods,
- finite element methods (plasticity corrections),

- correlation of analysis with experimental (strain gage) measurements,
- laboratory testing,
- service loads measurement and usage,
- estimating service performance (cumulative damage), and
- deterministic versus probabilistic design methods (dealing with variability).

In a capstone design course, the study can be used to demonstrate open-ended problem solving in a mode that emphasizes the importance of integrating and synthesizing the knowledge base and skills acquired throughout a student's undergraduate educational experience. Opportunities for computer-based exercises are many. Here students can gain experience in developing and manipulating data bases for material properties, service histories, and so forth, performing damage analyses using standard spreadsheets, and presenting technical information in clear and concise ways using computer graphics. With regard to computer usage, it is vitally important that students gain an appreciation of both the power and limitations of computational methods and the numerical "accuracies" (real or believed) obtainable from them.

Finally, the wheel study can be extended to incorporate broader design issues such as the need to control the unsprung mass in ground vehicles in order to meet ride and handling objectives. Simple dynamics models of a vehicle system can be used to demonstrate how vehicle sprung and unsprung weights and suspension characteristics interact in influencing overall system performance. In this way, another impetus for weight reduction, in addition to fuel economy, can be introduced.

References

- [1] Neuber, H., "Theory of Stress Concentration for Shear Strained Prismatical Bodies with Arbitrary Non-Linear Stress-Strain Law," *Journal of Applied Mechanics*, Vol. 28, 1961, p. 544.
- [2] Wimmer, A. and Peterson, J., "Road Stress Resistance and Lightweight Construction of Automobile Road Wheels," SAE Paper 790713, Society of Automotive Engineers, Warrendale, PA, 1979.
- [3] Ang, A. H-S. and Tang, W. H., *Probability Concepts in Engineering Planning and Design, Vol. I: Basic Principles and Vol. II: Decision, Risk, and Reliability*, John Wiley & Sons, New York, 1975 and 1984, respectively.
- [4] Ridder, R. L., Landgraf, R. W., and Thangjitham, S., "Reliability Analysis of an Automotive Wheel Assembly," SAE Paper 930406, Society of Automotive Engineers, Warrendale, PA, 1993.
- [5] Bingham, D. C. H. and Crane, C., "Road Wheel Stresses," MIRA Research Report 1977/1, The Motor Industry Research Association, Warwickshire, United Kingdom, 1977.

Gary C. Salivar¹

The Use of Failure Analysis and Materials Testing in the Redesign of a Boat Trailer Roller Arm

REFERENCE: Salivar, G. C., "The Use of Failure Analysis and Materials Testing in the Redesign of a Boat Trailer Roller Arm," *Case Studies for Fatigue Education, ASTM STP 1250*, Ralph I. Stephens, Ed., American Society for Testing and Materials, Philadelphia, 1994, pp. 23–31.

ABSTRACT: A successful design for a small-capacity boat trailer roller arm was extended to a new larger-capacity boat trailer and placed into service. After operation of the trailers for a period of time, several failures of the roller arms were reported. The failures occurred while the trailers were loaded in service with resulting damage to the boat hulls. There was no prior warning of the failures.

This paper discusses the background of the components and the methods used for manufacturing the roller arms. It will discuss the analysis procedures used to determine the cause of the failures. Alternatives for design changes to the roller arms will be presented, along with the results of a test program that confirms the improvement in component life, based on the recommended change.

KEYWORDS: benchmark; failure analysis, fatigue, fracture surface, hardness, plasticity, stress concentration

Historical Information

A boat trailer manufacturer had successfully been using a particular hull support design for a number of years. An example of this type of trailer and the support structure is shown in Fig. 1. The design uses rollers to support the hull and allows the boat to be moved easily on and off the trailer. The rollers minimize the sliding damage to the hull that may occur with trailers that use padded fixed-beam supports.

The trailer in Fig. 1 has four roller assemblies attached to the frame. Each assembly consists of a pivot beam that is attached to the frame cross-member: two roller arms (affectionately called "birds" due to their V-shape (see Fig. 2)), one attached to each end of the pivot beam, and two rubber rollers, one attached to each end of the roller arm. These assemblies provide two axis movement to accommodate the hull as it passes over the trailer. The critical piece in this design is the roller arm, as shown in Fig. 2. The central hole provides for attachment to the pivot beam and allows for movement of the arm.

The manufacturer offered trailers with weight capacities of 2000 to 28 910 N. Initially, the roller support design was limited to the lower capacity trailers, with the large capacity trailers using padded fixed-beam supports. A decision was made to extend this successful

¹ Professor, Florida Atlantic University, Department of Mechanical Engineering, Boca Raton, FL 33431-0991.

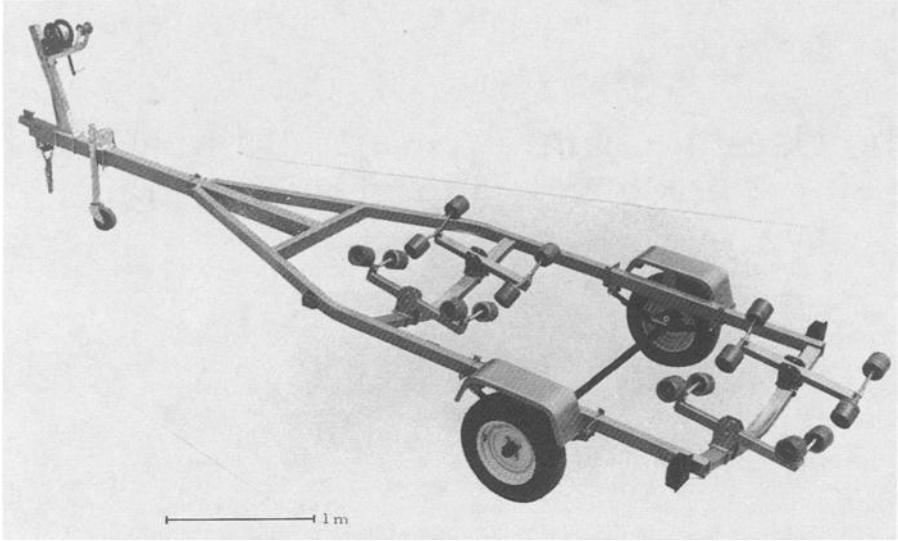


FIG. 1—Boat trailer with roller supports.

roller-support design to the larger-capacity trailers, with no change in the geometry or size of the roller arms and the parts of the roller assemblies. After introduction of the large capacity trailers with these roller assemblies, a number of failures of roller arms occurred in relatively short order, resulting in damage to the hulls of several boats and subsequent litigation. At this point, the manufacturer contacted a private consultant to review the design of the roller arms and determine the cause of the failures.

Student Questions

1. What information would you request from the trailer manufacturer in order to be able to analyze the failures?

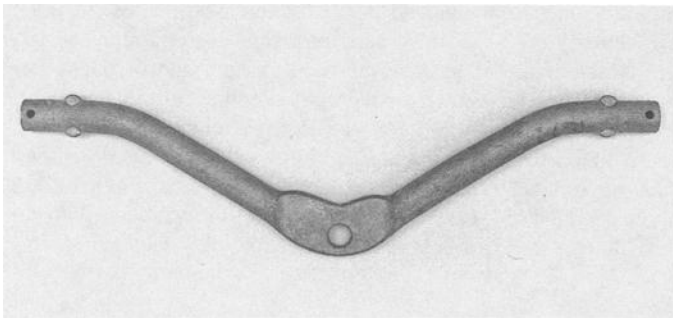


FIG. 2—Boat trailer roller arm (original design).

2. What procedures would you use to initially observe and handle any failed parts that you receive?

While it is always desirable to do a complete analysis of the failure, in terms of materials characterization and fracture analysis, often it is not possible due to financial or informational constraints placed on the consultant by the customer. In this case, the manufacturer specified their interest in determining the cause of the failures, if possible, but within a very limited budget. Also, the manufacturer did not have good knowledge of the loads experienced by the roller arms in service. This many times is the "typical" failure analysis scenario presented to the consultant. At no time does the consultant have an unlimited budget; however, the budget is often such that complete chemical analyses, moderate testing programs, or fracture surface analysis procedures (that is, scanning electron microscope (SEM)) are not possible. In addition, the consultant almost never has all of the necessary information, and many times important information about the service loads is unavailable. The problem becomes one of determining as much information about the failure as possible within the cost and informational constraints. In these cases, hopefully, the limited analysis will be sufficient to determine the cause of the failure and recommend design and material changes, or both to alleviate the problem. The consultant needs to inform the client that the financial and informational constraints, or both may not allow a complete determination of the cause of failure. This case study is submitted for discussion as an example of a failure analysis that has severe financial restrictions and is lacking basic information on the service loads experienced by the components.

Material Information and Manufacturing of the Roller Arm

Several new and failed roller arms were forwarded by the manufacturer for investigation. A plan drawing of the roller arm was supplied, a schematic of which is shown in Fig. 3. An estimate of the operational loads experienced by the roller arms in service was not provided, due to the manufacturer's lack of this information, as mentioned previously.

The material was hot rolled 1040 steel bar stock with a 1.91-cm diameter. The center section of the roller arm was flattened in a press to the final 0.95-cm thickness to fit in the pivot beam clevis. The bar was then hot-formed into the V configuration by bending around a square-corner die in a press to the desired angle and dimensions. This operation was performed at the center of the roller arm and 5.72 cm in from each end of the arm (Fig. 3). The roller retention ears were also pressed into the ends of the arm. A 0.48-cm diameter hole was drilled in each end of the bar for a cotter key to secure the roller. The center attachment hole was punched into the flattened center section of the arm and the surface was left in the as-punched condition. Finally, the entire roller arm was galvanized for corrosion resistance.

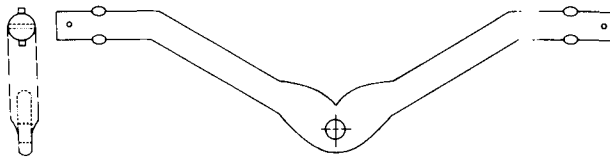


FIG. 3—Schematic of a boat trailer roller arm.

Student Questions

1. Are you comfortable with the material and manufacturing information that has been supplied, or would you ask for more specific information in certain areas? If so, where? What if this information is not available?
2. Which tests might you suggest to verify the materials composition and properties?
3. Which tests would you specify if the manufacturer has placed you on a very limited budget? Are tests always necessary?

Investigation and Failure Analysis

Initially in the investigation, the fracture surfaces of the failed roller arms were observed visually with a 10X eyepiece. A typical surface (Fig. 4) will exhibit the classic fatigue-fracture surface appearance [1,2]. Upon further investigation with a low-power stereomicroscope, the crack origin was located at the upper surface of the roller arm in the plane of the center of the clevis attachment hole. Beachmarks were evident on the fracture surface that were indicative of fatigue. The arrows in Fig. 4 showed the beachmark that represented the final profile of the fatigue crack at the point of instability (final failure). The fracture region between the upper surface of the roller arm and the final beachmark exhibited very little macroscopic plasticity, which is characteristic of fatigue. The remaining fracture surface above and below the attachment hole exhibited ductile overload failure as was evidenced by the significant macroscopic plasticity and shear-lip formation.

Further examination under the stereomicroscope revealed that the origin of the cracking was coincident with a notch on the upper surface of the roller arm (Fig. 5). This notch provided a stress concentration at the upper surface in the vicinity of the attachment hole, which under the applied service loads resulted in fatigue cracking and failure of the component. This behavior was consistent for all of the roller arms. Again it should be noted that the manufacturer did not have knowledge of the magnitude of the loads experienced by the roller arms, nor did he have a cycle count for the failed parts.

Observing the schematic of the design drawing of the roller arm (Fig. 3), it is evident that a sharp notch was designed into the component. In production, the notch was much less severe; however, it was still significant (Fig. 5). As mentioned earlier, the V configuration

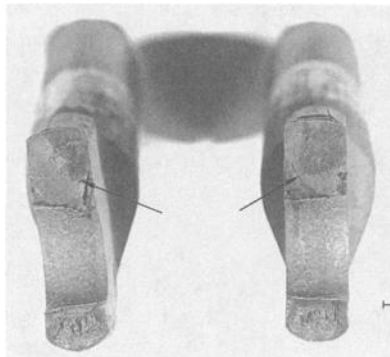


FIG. 4—Fracture surface of a roller arm.

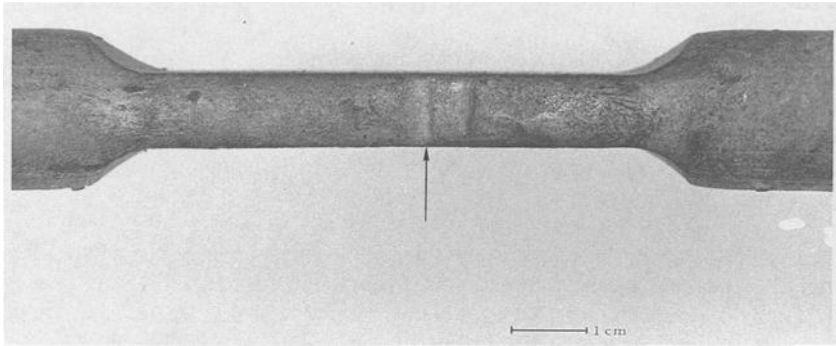


FIG. 5—Notch on upper surface of roller arm.

was obtained by hot-forming the bar stock around a square-cornered die which resulted in the notch in the upper surface of the roller arm.

Hardness measurements were taken on the flattened center section of the roller arms in the vicinity of the notches and resulted in Rockwell B scale readings of 78 to 80. This was consistent with the strength levels of hot rolled 1040 steel [3]. Since the problem was not believed to be material related, and to minimize expenses, chemical analysis was not performed on the material. Due to the convincing evidence of a fatigue failure under microscopic evaluation, the fracture surfaces were not observed under an SEM. Whereas many times SEM analysis is necessary to determine the mode of fracture, and striation counting is performed to determine a cycle count for the failure, they were not required in this case and represented unnecessary expense.

Student Question

1. Given the new information in this section, are there further comments that you can make in regard to the necessity of the tests that you discussed previously for determining the material composition and properties?

Cause of the Failure

The cause of the failure is fatigue cracking originating in a notch in the upper surface of the roller arm that is the result of the manufacturing operation used to deform the bar stock.

When this design was originally used for low capacity trailers, there were no failures of the roller arms. The lack of failures suggests that the combination of the service loads and the stress concentration due to the notch was not severe enough to cause fatigue cracking within the current lives of the low-capacity trailers. Only when the design was extended to the large-capacity trailers with higher loads did failures begin to occur. It would be desirable to perform simple stress calculations for this geometry and compare them to stress versus cycles-to-failure data for the material to estimate the life of the roller arms. However, in this case, no load or accumulated cycles information was available for the parts. The question then arises as to how to resolve the problem in the large-capacity trailers?

Student Questions

1. How would you estimate the stresses in the roller arms at the critical location? Discuss the procedures that could be used to estimate the stress concentration factor for the notch.
2. What possibilities for changes to the roller arms can you suggest to eliminate the failure problem?

The local stress at the failure location in the roller arm in the large-capacity trailers needs to be reduced in order to prevent the failures. This can be accomplished in two ways. First, the bar diameter can be increased to lower the service stress. Changing the bar diameter would require a significant amount of change in the design because it would affect the size of the roller arm, the attachment clevis, and the rollers themselves. The second alternative is to eliminate the stress concentration in the roller arm that would lower the local stress and possibly eliminate the failures. This change is the easiest to investigate with minimum reconfiguration of the roller assembly.

Recommendation

The recommendation was made to the manufacturer to eliminate the notch on the upper surface of the roller arms by deforming the arms to shape around a die with a large radius instead of a square-corner. The reduction of the stress concentration was believed to be significant enough to lower the stress and eliminate the early failures. This belief is based on the notches being inadvertent and not part of the design, in addition to the fact that all of the cracks originated at these notches.

The manufacturer agreed to the production change to the roller arms, as shown in Fig. 6. This new procedure resulted in the complete elimination of the V configuration above the attachment hole in the roller arm (Fig. 6). The manufacturer requested that some limited fatigue testing be done to quantify the difference in life as a result of the change.

Student Questions

1. What type of testing would you suggest to investigate the difference in life, if any, between the new and the old design?

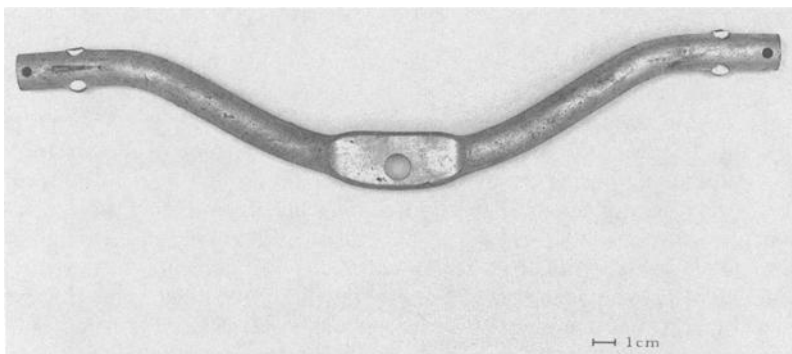


FIG. 6—Boat trailer roller arm (new design).

2. What test conditions would you specify based on the information you have from the manufacturer?
3. What statistical procedures are available to you to determine the number of tests that need to be performed to statistically conclude that any differences in life between the new and old designs is significant? Is it necessary or cost effective to go this far in every failure case?

A three-point bend apparatus was constructed to load the roller arms in the manner in which they were loaded in service (Fig. 7). Rollers were not attached to the arm during testing. As stated before, the manufacturer did not know the magnitude of the in-service loads, and therefore, specified what he thought would be a reasonable maximum test load (6670 N) for comparison purposes between the old and new designs. Constant amplitude fatigue tests were performed with a stress ratio of +0.1 (667 N minimum load) at a frequency of 10 Hz.

Four roller arms of the original configuration (Fig. 2) were tested to failure, with the results shown in Table 1. The lives ranged from approximately 63 000 to 223 000 cycles. All of the cracks in these tests originated from the notch in the upper surface of the roller arms, identical to the in-service components. As is seen in the results, there is significant variability in the lives of these parts, showing the lack of uniformity in the manufacturing process, in terms of the bar size and the notch configuration.

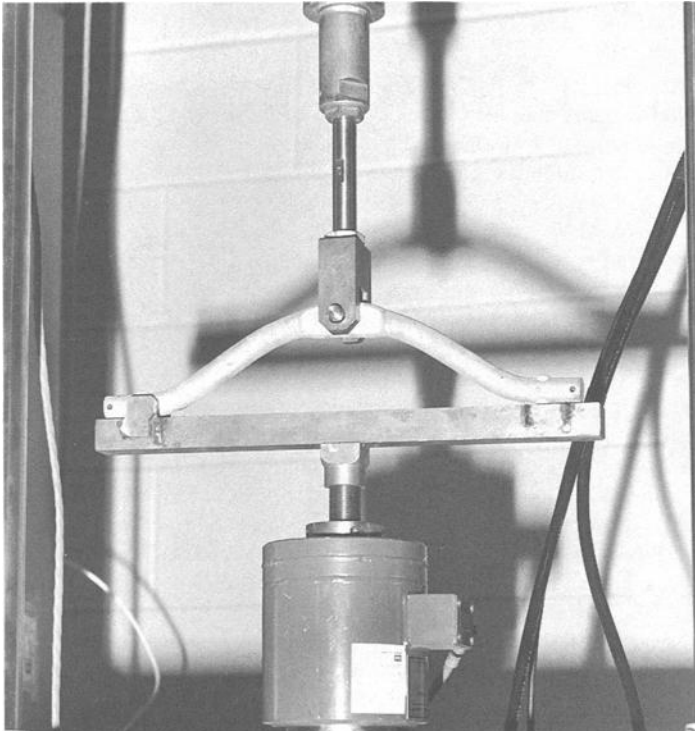


FIG. 7—Three-point bend test apparatus.

TABLE 1—*Fatigue tests of roller arms (old design).*

| Specimen Number | Cycles to Failure |
|-----------------|-------------------|
| 2 ^a | 118 890 |
| 4 | 223 420 |
| 1 | 62 820 |
| 3 | 92 710 |

NOTE— $P_{\max} = 6670$ N; $P_{\min} = 667$ N; frequency = 10 Hz, square wave-form, three-point bending.

^aSpecimens were tested in random order mean life = 111 525 cycles.

Four roller arms of the new configuration (Fig. 6) were also tested. It was decided to consider the test a run-out when the life reached one million cycles (four times the life of the longest lasting old design roller arm). Each of the four new configuration specimens reached this run-out life without failure and were overloaded at the completion of the tests to check for crack initiation. The four specimens yielded between 14 720 and 17 125 N, without any cracks found in the upper surface of the arm. As a comparison, a new configuration roller arm that was not fatigue cycled, yielded at 14 767 N when it was overloaded. These tests confirm that the manufacturing change to remove the notch and the resulting stress concentration in the roller arm significantly improves the fatigue life of the component. A reduction in stress concentration will lower the local stress and extend the life. The new design was placed into service without any further failures being reported to date.

Summary and Discussion

Analysis of the boat trailer roller arms indicated that the failures were the result of fatigue cracking, and subsequent fracture. The origin of the failures was determined to be an inadvertent notch in the roller arm that was the result of the deformation process used during manufacture. Constant amplitude fatigue testing under three-point bending in the laboratory showed that this notch was responsible for the initiation of fatigue cracks and the very early failure of the arms within a range of 63 000 to 223 000 cycles. A design change in the manufacturing operation was suggested, which eliminated the notch and the V configuration of the roller arm. Fatigue tests of the new design showed no failures of the roller arms within a runout period of one million cycles. The roller arms were subsequently overloaded with no evidence of cracking found. The new design was placed into service with no failures reported.

This case study presents the important example that design and manufacturing planning need to be performed together, with an appropriate understanding of the influence of stress concentration. All too often, stress concentrations are overlooked in the design, even by experienced engineers, which subsequently provide the source for the origin of the failures. Care must also be exercised that inadvertent stress concentrations are not built into the components during manufacturing operations, as was the case in this example. These simple considerations need to be addressed to prevent what all too often results in early catastrophic failures.

This case study also presents an example of a situation where there is little money for analysis and important service-load information is unavailable. At this point, the experience of the failure analyst must come into play. Basic solutions can be presented that will help the situation, but may not eliminate the failures. A small test program can help to confirm an improvement in part life but the actual change will only be known by the accumulation

of in-service history. Many times, this is all that the failure analyst can do under the various constraints that he is placed.

Student Questions

1. The failure analyst is often constrained by budget, in terms of the analysis procedures that are available for a particular project. Discuss the limitations this places on the analysis and the ability to determine the cause of failure conclusively.
2. What are your views as to how the failure analyst should deal with budget situations with the client?

References

- [1] Wulpi, D. J., *Understanding How Components Fail*, American Society for Metals, Metals Park, OH, 1985, p. 124.
- [2] American Society for Metals, "Failure Analysis and Prevention," *Metals Handbook, Ninth Edition*, Vol. 11, Metals Park, OH, 1986, p. 104.
- [3] American Society for Metals, "Properties and Selection of Irons and Steels," *Metals Handbook, Ninth Edition*, Vol. 1, Metals Park, OH, 1978, p. 204.

Design of a Composite Hip Prosthesis for Long-Term Performance

REFERENCE: Liao, K. and Reifsnider, K. L., “**Design of a Composite Hip Prosthesis for Long-Term Performance,**” *Case Studies for Fatigue Education, ASTM STP 1250*, Ralph I. Stephens, Ed., American Society for Testing and Materials, Philadelphia, 1994, pp. 32–52.

ABSTRACT: In this paper, a performance simulation model is described for the design and simulation of the long-term behavior of a composite hip prosthesis (an engineering device for implant in the human body), that is subjected to repeated mechanical and environmental loads during service. The life prediction method for the composite hip prosthesis is developed from a critical element concept, a cumulative, mechanistic approach for predicting the residual strength and life of composite material systems subjected to cyclic loads. Results from the experimental characterization of prototype specimens are also presented, and how that information can be used for the life-prediction scheme is discussed.

KEYWORDS: polymeric composite materials, hip prosthesis, compression-compression fatigue, fatigue damage, life prediction

Osteoporosis and osteomalacia found in the elderly population are two major causes of intracapsular fracture of the neck of the femur. The porotic and softer bone structure resulting from these diseases suggest a decrease in load-carrying and energy-absorbing capacities; therefore, the bone is more susceptible to fracture. A number of surgical treatments can be employed to repair such a fracture. However, it is generally believed that elderly patients are more likely to benefit from total hip arthroplasty [1]. Such treatment is also employed for patients with osteoarthritis. This is illustrated schematically in Fig. 1. There are over 200 000 such operations a year in the United States alone, and that number is expected to increase with rapid aging of the population structure [2,3]. For this reason, improved and more durable hip prostheses are in demand for patients who need such treatment.

Metallic hip prostheses now used in hip arthroplasty have a number of disadvantages. The stiffness of the implant material is relatively high compared to the cortical bone, the load-carrying tissue of the human femur. As a result of this mismatch in mechanical properties, the implant carries most of the applied loads and the supporting bone is not properly stressed. This so-called stress-shielding effect is believed to be the reason for bone resorption, which may lead to a higher incidence of implant loosening and fracture of the prosthesis. In addition, patients may experience hypersensitivity as a result of release of metallic ions from the prosthesis, caused by wear [4,5].

With advances in materials science, fiber-reinforced polymeric composite materials are being considered as candidate materials for making hip prostheses. The structure of a laminated composite material is illustrated in Fig. 2. The structure of a single layer, a *lamina*, is

¹ Research associate and Alexander Giacco professor, respectively, Virginia Polytechnic Institute and State University, Engineering Science and Mechanics Department, Materials Response Group, Blacksburg, VA 24061-0219.

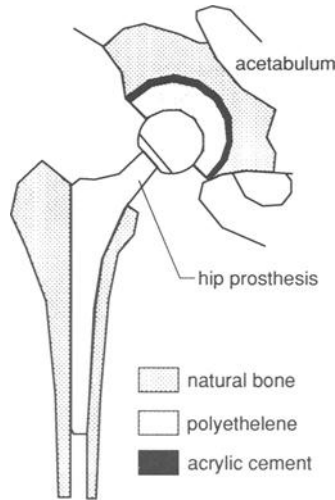


FIG. 1—Schematic representation of total hip arthroplasty.

composed of continuous fibers embedded in a polymeric matrix. Typical values of the diameter of an AS graphite fiber and lamina thickness are $7\ \mu\text{m}$ and $0.13\ \text{mm}$, respectively. These single layers (laminae) can be put together in different ways (that is, with fibers in different directions) and cured under heat and pressure to form a laminate. The mechanical properties (such as stiffness and Poisson's ratio) and strength of a laminate with a specific arrangement of laminae differs from one another. For instance, the stiffness of a unidirectional (all the laminae are in the same direction) and quasi-isotropic (laminae arranged in the -45 , 45 , 0 , and 90 degrees directions such that its in-plane extensional stiffness are the same in all directions) composite laminate made from T300/5028 graphite (fiber)/epoxy (matrix) are about 180 and 70 GPa, respectively [6].

Prostheses made from fiber-reinforced composite materials possess some advantageous characteristics that their metallic counterparts do not: the stiffness of a polymeric composite material can be tailored to provide a state of stress in the proximal femur closer to physiologic level, compared to materials such as alloys (for example, cobalt/chrome/molybdenum

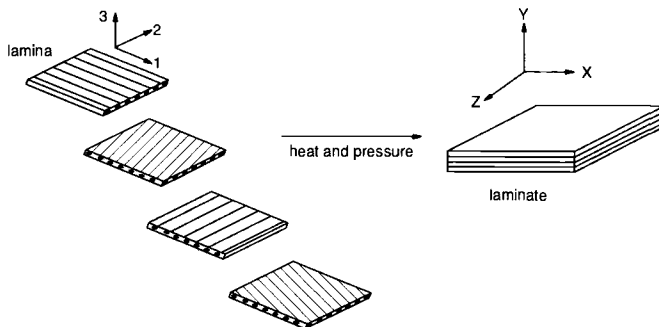


FIG. 2—Structure of a composite laminate.

alloys) and stainless steel, which are widely used for making hip prostheses; the strength a composite prosthesis can also be tailored according to service loads, and many polymeric composites are resistant to harsh human body environments. In addition, they are superior in damage tolerance and fatigue performance, as well as being more biocompatible [4,5].

When designing an engineering structure, three basic sequential questions are frequently asked by engineers: (1) How should the structure be made? (2) How strong is it (and/or, for structures where stiffness is a basic concern, how stiff is it?)? and, (3) How long can it last? If these three inter-related questions are properly addressed, a structure will serve its purpose properly, at least in theory, if not in practice. The last question is of particular importance for structures subjected to long-term repeated loads (which may be a combination of mechanical, thermal, or chemical loads during service). If one can tell in advance when the structure should be retired from service, undesired events associated with structural failure can be prevented. Moreover, if a comprehensive engineering scheme can be established to address these questions, more product competitiveness can be achieved in terms of cost and performance. In this paper, we attempt to construct such an engineering scheme for designing and simulating the performance of a composite hip prosthesis under repeated mechanical and environmental loads in the human-body environment.

How Should it be Made?

Before answering the first question, the loading environment for a hip prosthesis must be well understood. The biomechanics of hip prosthesis has been studied in detail by many investigators [7]. A comprehensive review on the subject can also be found in Ref 8. Briefly, under static conditions, (for instance, in one-legged stance), the prosthesis is subjected to a resultant mechanical force (of body and muscle forces) acting at an angle to the anterior and medial plane of the prosthesis, on the head of the prosthesis. This is illustrated in Fig. 3. The loading angle may vary with activities. The resultant force on the head of the prosthesis can be resolved into a force acting normal to (hereafter referred to as the out-of-plane force) and one parallel to the anterior plane (hereafter referred to as the in-plane force). The angles between the resultant joint force and the in- and out-of-plane forces are in- and out-of-plane

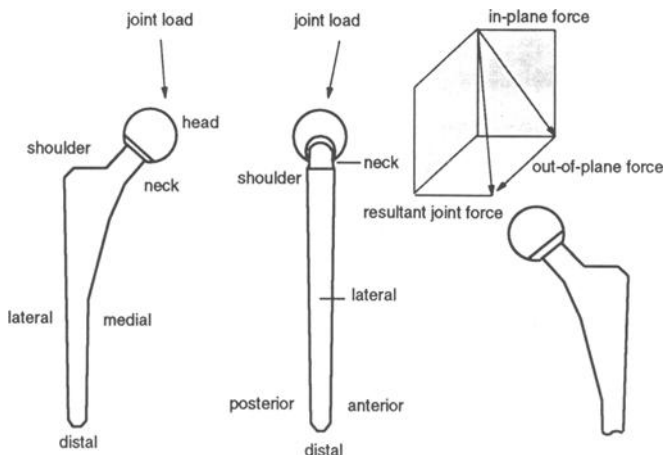


FIG. 3—Nomenclatures and joint forces for a hip prosthesis.

load angles, respectively. The in- and out-of-plane forces acting on the head of the prosthesis result in in- and out-of-plane bending moments, torsional, shear, and compressive forces. These moments and forces vary from point to point along the prosthesis, resulting in varying stress states in the structure. In addition to the mechanical loads, boundary conditions for the prosthesis must also be considered, as the prosthesis is either cemented or press-fitted in the femoral canal. During its service, a prosthesis is subjected to long-term repeated mechanical loading, moisture, and temperature. The influence of these factors on the mechanical behavior of the composite hip prosthesis will be discussed in a later section.

Several preliminary design considerations for composite hip prosthesis are shown in Fig. 4. Configuration A is a "flat-plate" design, Configuration B is a "curved-plate" design, and Configuration C is somewhat in between, a "rotated-plate" design. Each of these three configurations may have its own advantages and disadvantages. For instance, the flat-plate design is more resistant to in-plane bending, but is stiffer; the curved-plate design may be less stiff in response to in-plane bending moment, but at the same time is weaker; and the rotated-plate design may possess additional freedom in balancing stiffness and strength, but this may also imply additional complexity, from the standpoint of manufacturing.

We choose the flat-plate configuration for our investigation. A prototype specimen is obtained by cutting from a cured laminate, and its contour is machined, according to the design, based on the geometry of the femoral canal. The basic design approach is to first determine the stress distributions in prostheses made from laminates of various stacking sequence and the associated stiffness and strength. Stiffness and strength of various laminate configurations are compared and an optimum design is selected. Such a design is one with a balanced stiffness and strength such that it is more compatible to the stiffness of the femoral bone structure and possesses the required strength to sustain service loads. Specifically, the laminates picked for consideration in this study were selected from a study of dozens of possibilities, with the criteria that the fatigue life at four times average body weight should be more than one hundred million cycles and that the stiffness should be as low as possible, given that constraint.

In order to design a composite hip prosthesis *effectively*, a stress-analysis model was developed using a strength-of-materials approach. The structure of the composite prosthesis, which consists of more than 100 individual plies with different ply orientations, is highly

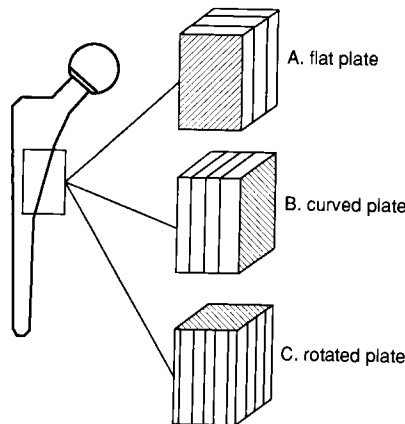


FIG. 4—Three basic design considerations: (a) flat plate, (b) curved plate, and (c) rotated plate.

anisotropic. Considerable computation time would be required if a finite element method (FEM) was used to evaluate the stress state of each individual ply along the prosthesis. This is a major obstacle with the use of the FEM as an effective design tool. For this reason, a strength-of-materials approach was chosen.

The general approach for the stress-analysis model is shown schematically in Fig. 5. The prosthesis is assumed to be embedded in a layer of elastic foundation. The geometry of the structure is first defined. This includes description of the longitudinal profile of the prosthesis by polynomial equations and calculation of cross-sectional geometric properties, such as the area moment of inertia. In- and out-of-plane applied loads are defined next. Under the three-dimensional applied load, global stress and moment distributions on each arbitrary chosen section along the prosthesis are determined. Curved-beam theory is used in this model to account for curved geometry of the prosthesis. Beam on elastic foundation approach is used to simulate the supporting bone structure for the prosthesis. Global stress and moment components determined are then transformed into the laminate coordinate system at three locations of a section, namely, an element on the lateral, center, and medial curve. Laminate analysis is performed at each of these three locations to determine stress and strain components of each individual ply. A number of phenomenological strength theories (such as Tsai-Hill, maximum stress, and maximum strain) are computed in association with the stress state of each individual ply to predict the strength of the structure.

How Strong and How Stiff is it?

Typical strain distributions along the medial and lateral surfaces of a prototype hip prosthesis, as determined from the stress-analysis model, are shown in Fig. 6. Note that the decreasing trend in both distributions beyond 3.8 cm, as the prosthesis is supported by the elastic foundation from that location to its distal end. It is obvious from Fig. 6 that a local high-stressed area (represented by the local high strain) is found at the mid-neck region (at about 2.6 cm from the head). The results were verified experimentally by scanning the surface of a cyclically stressed hip prosthesis using a thermographic stress imaging system

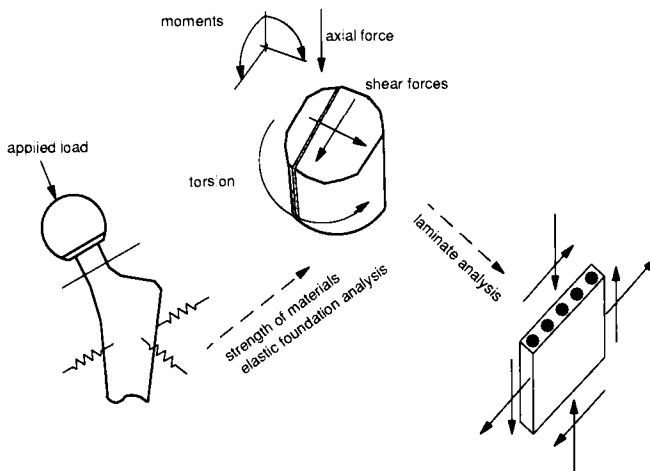


FIG. 5—Schematic representation of the stress-analysis model.

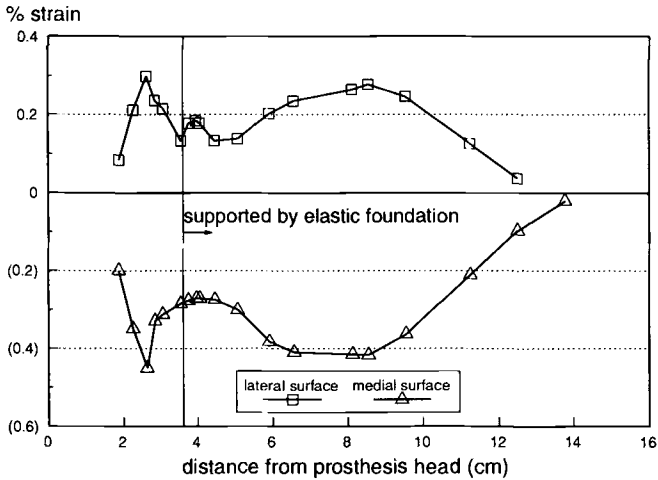


FIG. 6—Strain distributions along a composite hip prosthesis.

known as stress pattern analysis by thermal emission (SPATE). The SPATE system is developed based on a thermoelastic theory by Thomson [9], which states that when a homogeneous, isotropic, linear-elastic material is cyclically loaded under adiabatic conditions within its elastic range, the reversible change in the temperature of the material is proportional to the sum of its principal stresses. The SPATE system uses a highly sensitive, infrared photon detector to sense the infrared emission from the specimen surface, and those signals can be converted to stress values by a conversion factor [10,11]. A result of the SPATE image is shown in Fig. 7, which represents the *qualitative* change in sum of principal stresses in the material surface, as indicated by the scale on the right. Note that the local stress peak is at mid neck (indicated by the arrow), which is in agreement with the result of stress analysis.

To choose an optimum design with balanced strength and stiffness, one may compare, using the stress-analysis model, the strength of the critical region (that is, the neck region) and the associated laminate stiffness for various laminates. A strength versus stiffness plot for a number of laminates at the neck region is shown in Fig. 8. The stiffness and strength (determined using the maximum strain criterion, which states that the material is said to have failed if the applied strain exceeds its failure strain) for all data points that appear on the plot are normalized to the stiffness and strength of a quasi-isotropic laminate. The stacking sequence for these laminates are as follows (the ply angle is defined with respect to the prosthesis axis, see Fig. 9):

- Design 1—optimum design
- Design 2— $[-45/0/45/90]_s$
- Design 3— $[80/65/45/25/10/-25]_s$
- Design 4— $[80/45/10/-25]_s$
- Design 5— $[65/45/25/-25]_s$
- Design 6— $[45/60/-30/90]_s$
- Design 7— $[-45/0/45/90]_{2s}[80/60/10/-25]_1[65/45/25/-25]_1$

The subscript *s* denotes “symmetric.” For example, the actual laminae arrangement for Design 2 is $[-45/0/45/90/90/45/0/-45]$. As can be seen from Fig. 9, a design with

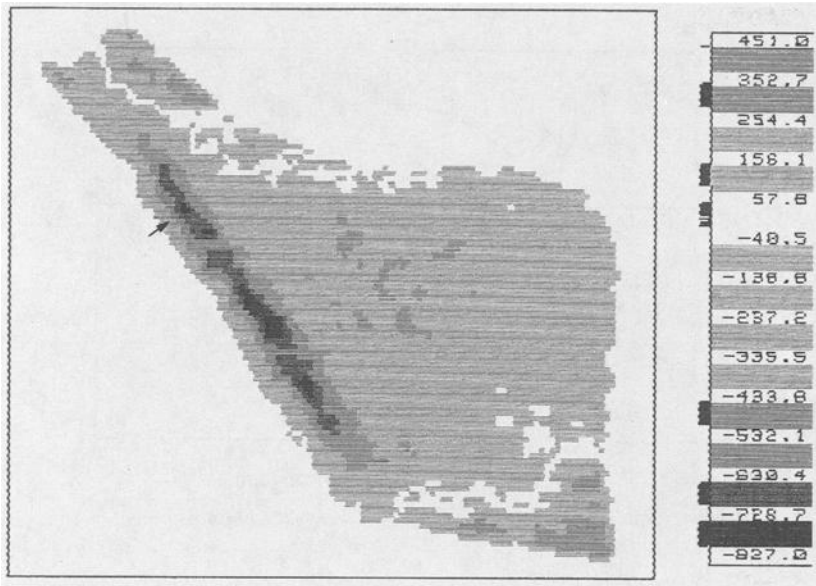


FIG. 7—Stress distribution pattern in the neck region from the SPATE system.

relatively high strength is also one with high stiffness (such as Design 5), and vice versa. However, an ideal design would be one with high strength and low stiffness, a data point at the upper left hand corner of Fig. 8. From the Fig. 8, Designs 1, 6, and 7, which are closer to the upper left-hand corner of the plot, may be more desirable than those of Designs 2, 3, 4, and 5. Note that Design 7 is an unsymmetric laminate, where the stronger [65/45/25/-25]_s sublaminates is designedly chosen to support higher compressive stress in the medial-

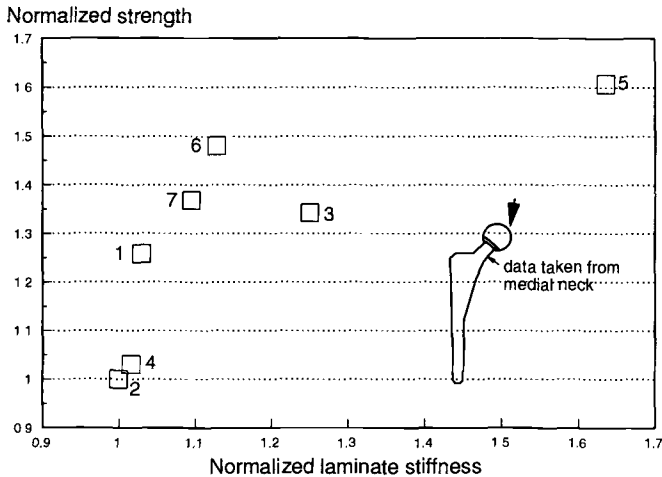


FIG. 8—Strength versus stiffness plot for several laminate designs.

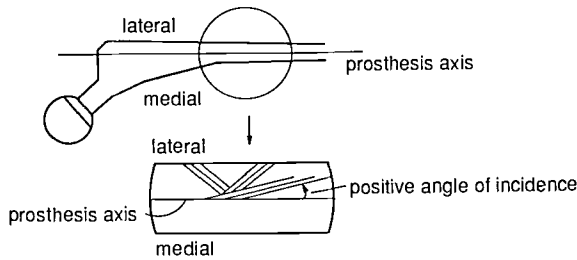


FIG. 9—Ply identification scheme.

posterior corner of the prosthesis, which arises as a result of out-of-plane moment. The less stiff quasi-isotropic sublaminar $[-45/0/45/90]_{2s}$ has the effect of lowering the structural stiffness as a whole.

We chose Design 1, the “optimum design,” for further investigation. Due to the proprietary nature of the stacking sequence, it will not be discussed in this paper. However, to facilitate further discussion, plies in this design are identified as follows (Fig. 9):

- Ply X—plies with the lowest positive angle of incident (PAI) to the prosthesis axis (first quadrant of the angular coordinate plane).
- Ply Y—plies with the second lowest PAI to the prosthesis axis (first quadrant).
- Ply Z—plies with the highest PAI to the prosthesis axis (second quadrant).

The prototype specimens were manufactured from C/PEEK (carbon fiber-reinforced poly(ether ether ketone)). The laminate consisted of approximately 100 individual plies at its thickest section (shoulder).

How Long Can it Last?

Once a specific design has been chosen, one would like to know what factors and to what extent these factors may influence its long-term behavior in the human-body environment. If one can anticipate the long-term behavior of the implant device under complex loading conditions (mechanical and environmental), in terms of its damage mode, remaining stiffness and strength, and failure mode, not only unwanted events associated with structural failure can be prevented, but further improvement for the structure may also arise. To this end, laboratory test procedures to obtain necessary information, as well as life prediction methodologies to use and interpret that information, should be established [72]. Conventional life-prediction schemes (such as equivalent damage concept) is denied in this case due to the fact that it is almost impossible to produce a complete phenomenological data base of stress and life associated with such factors as complex loading conditions, required testing time, as well as cost. Instead, the life-prediction scheme should represent, mechanistically and physically, the property change in a composite hip prosthesis and be able to predict its long-term behavior under cyclic loading.

A life-prediction model is developed based on the concept of a critical-element model [13], a mechanistic, cumulative damage model for predicting the residual strength and life of composite laminates subjected to arbitrary cyclic loading. A conceptual chart of the model is shown in Fig. 10. The failure mode of a component or structure is first established. Generally, there are only a fairly small number that apply to specific engineering situations.

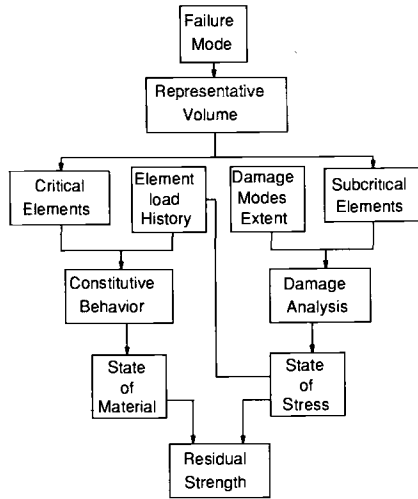


FIG. 10—Schematic representation of the critical-element concept.

Based on the failure mode and the damage mechanism, a “representative volume” in the laminated component is identified. It is the process of continuous property degradation in this representative volume (as a function of applied cycles) that causes reduction of strength, and eventually, failure of the structure, that is to be described in the model. For instance, in our case, the composite prosthesis, that is a representative volume, is identified experimentally to be within either the medial neck or the medial mid-stem region where structural failure usually occurred [14,15]. Analytically, the location of the representative volume, a locally high-stressed point, can be determined from the stress analysis model.

Once the representative volume is established, it is subdivided into two types of elements, “critical” and “subcritical.” Critical elements are defined as those parts of the representative volume whose failure causes failure of the component. Since critical elements are the last part of a component to fail (after the failure of subcritical elements), the strength of a component is dominated by the response of the critical element to applied load. For tensile loading of a quasi-isotropic laminate, for example, the critical element may be the zero-degree plies. Subcritical elements are defined as those parts of a component or laminate that sustain damage during the fatigue loading process, but cause redistribution of internal stress because of fatigue damage, such as matrix cracking. For the example just mentioned, the subcritical elements may be the off-axis plies where matrix cracking usually occurs. The response of the subcritical elements is determined by mechanics analysis, while the response of the critical elements is represented by phenomenological information and constitutive equations. Once the subcritical elements are defined, and information regarding the damage modes and the extent of damage is obtained, then a damage analysis can be conducted to establish the state of stress in the interior of the component, that is, the stress state in both the critical and the subcritical elements, as functions of the number of applied load cycles. Damage modes and damage mechanisms can be assessed using some nondestructive (NDE) and destructive techniques. The local state of stress in the critical element, the “element load history,” obtained at a given number of applied cycles, may be used to determine the instantaneous element response, that is, the “state of the material.” For instance, such a re-

sponse may be represented by an $S-N$ curve, from which the remaining life (cycles) of the critical element at the current stress level is determined. If the state of stress and the state of the material have been determined for the critical elements, then one should be able to use some strength philosophy to determine the residual strength of the critical elements and, therefore, of the component.

To illustrate how one can actually apply the model concept, we begin with Fig. 11, a schematic representation of the basic relationships for laminate fatigue behavior. Figure 11 can be considered as a one-dimensional case where the residual strength curve of the critical element (and, therefore, the laminate) and the $S-N$ curve of the laminate are determined from unidirectional loading. Under an applied load, S_a , the reduction in strength, ΔS_r , of the critical element at any point p on the residual strength curve can be written as

$$\Delta S_r = \left(1 - \frac{S_a}{S_u}\right) \left(\frac{n}{N}\right)^i \quad (1)$$

where

- S_u = strength of the unidirectional coupon,
- n = applied cycles,
- N = critical element response (remaining life) at current stress, S_a , and
- i = nonlinear parameter.

The value of i is generally about 1.2 for polymeric composites. N is determined from phenomenological data ($S-N$ curve) of the critical element. Since the stress state of the critical element is constantly changing as a result of stress redistribution caused by damage development in the critical and subcritical elements, the applied stress, S_a , in the critical element is a function of the number of applied cycles, n . The critical element response, N , therefore, is also a function of n because of the changing S_a . The strength of the critical element, S_u , may also be cycle dependent, due, for instance, to environmental loadings.

To determine the accumulative reduction in residual strength over a normalized period, τ , Eq 1 is first expressed in differential form and integrated over τ

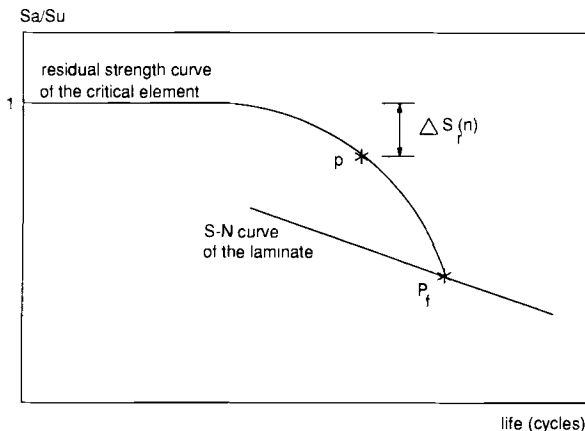


FIG. 11—Schematic diagram of critical-element strength-life relationship.

$$\Delta S_r(n) = \int_0^\tau \left[1 - \frac{S_a(n)}{S_u(n)} \right] i \left(\frac{n}{N(n)} \right)^{i-1} d \left(\frac{n}{N(n)} \right) \quad (2)$$

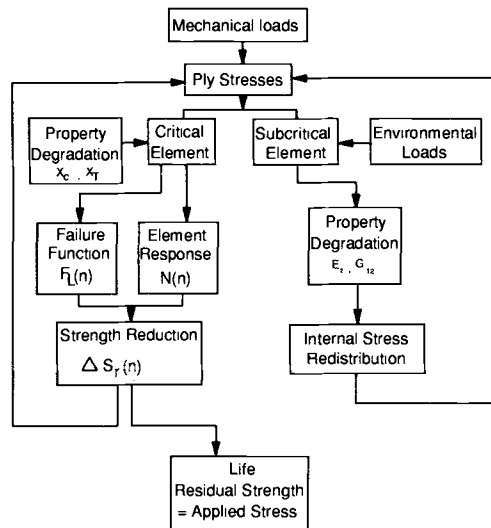
Up to this point, Eq 2 represents a one-dimensional residual strength reduction as a function of applied cycles. A local failure function, $F_L(n)$, that represents the three-dimensional stress state (such as the Tsai-Hill criterion) in the critical element may be introduced to replace the local applied stress-to-strength ratio, $S_a(n)/S_u(n)$

$$\Delta S_r(n) = \int_0^\tau [1 - F_L(n)] i \left(\frac{n}{N(n)} \right)^{i-1} d \left(\frac{n}{N(n)} \right) \quad (3)$$

The residual strength, $S_r(n)$, can be evaluated at any applied cycle by numerically integrating Eq 3.

To apply the critical element model concept to the composite hip prosthesis, we use the scheme shown in Fig. 12. We begin the calculation by computing the global and local stress state in the prosthesis as described in the stress-analysis model. After the stress state in each individual ply at each chosen computational point along the prosthesis has been determined, they are compared, so that the location of the critical element and the subcritical elements can be identified: a ply with the highest compressive stress in the fiber direction, σ_{11} , is identified as the critical element; all other plies are identified as subcritical elements.

As the number of applied cycles increases, damage development in the subcritical elements will cause degradation of material properties as a result of mechanical and environmental loadings. For instance, matrix cracking due to mechanical loading will cause reduction in the ply transverse and shear modulus [16–20]. Creep and moisture effects will produce the same consequences [21–31]. Evolution of material properties is represented as a function of



Life Prediction Model for Composite Prosthesis

FIG. 12—Schematic representation of the life-prediction model for composite hip.

applied cycles. The effect of mechanical loading, creep, and moisture on property degradation will be briefly discussed as follows.

Mechanical Loading

Characterization of damage in laminated fibrous composite materials due to mechanical fatigue has been the subject of numerous investigations [16–20]. In general, fatigue damage in composite materials consists of various combinations of matrix cracking, fiber-matrix debonding, delamination, void growth, and local fiber breakage. These damage mechanisms are complex and very difficult to describe in a general way. From previous studies, it has been found that matrix cracking due to compressive load is a dominant damage mode in the medial neck area of a composite prosthesis subjected to compression-compression fatigue loading [14,15].

These studies were carried out in a specially designed device to simulate *in vivo* loading conditions for the hip prosthesis, as shown in Fig. 13. 0-degrees in-plane and 10-degrees out-of-plane load angles were used for all the cyclic tests, according to a previous study by Gavens and Locke [7]. The applied (compression-compression) cyclic load level ranged from 47 to 84% of the quasi-static strength of the prototype specimens at $R = 10$, where R is the ratio of the minimum applied load to the maximum applied load. Penetrant enhanced X-ray radiography and a surface replication technique were used to monitor damage development in the hip prosthesis at selected intervals.

The medial-posterior corner of the mid-neck region is under highest local compressive stress, as a result of a combination of in- and out-of-plane bending moment and axial compressive force normal to the neck axis. Consequently, neck damage initiated from that location. Damage occurred mainly in the form of matrix cracking along fiber directions. This type of damage first occurred in X plies, plies with the closest orientation to the neck axis. Matrix cracking also occurred in Y and Z plies, but usually after mid-life or in late-life.

Selected results of X-ray radiography for a specimen tested under a maximum cyclic load of 75% static strength are shown schematically in Fig. 14. These drawings represent damage development in a portion of the medial neck region, and they are typical of the prototype specimens under investigation. Thin penetrant lines in fiber directions were observed in the neck region and were the consequence of matrix cracking along fiber directions. A micrograph of a sectioned neck near the medial surface is shown in Fig. 15, where a through-the-

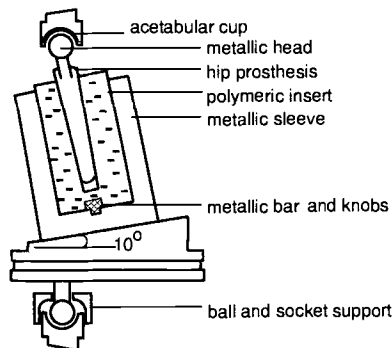


FIG. 13—Schematic diagram of the test fixture.

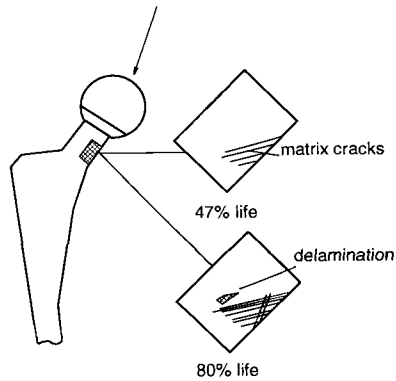


FIG. 14—Schematic representation of X-ray radiographs.

ply matrix crack is evident. The penetrant lines all initiated from the medial surface and extended to the lateral side. From X-ray radiographs, the density and area covered by these thin penetrant lines both increased with an increase in applied cycles (that is, more and longer penetrant lines were seen), indicating damage progression. Most of the neck damage occurred in *X* plies, some in *Y* plies. Only a few penetrant lines were seen in *Z* plies. A few tiny delaminations were also observed from the radiographs.

From surface replication images, damaged plies protruded from the specimen surface as a result of compression and shear, as shown in Fig. 16. Aided by X-ray radiographs, these

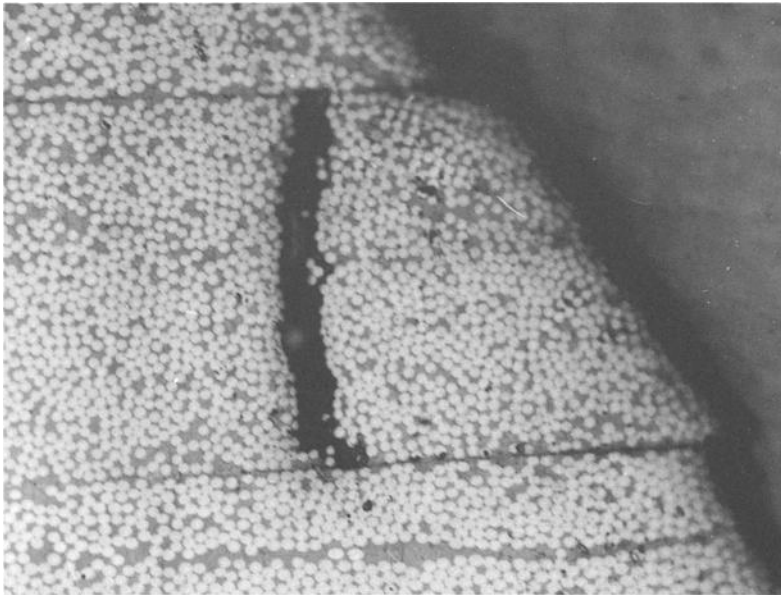


FIG. 15—Micrograph showing a matrix crack in the medial neck region.

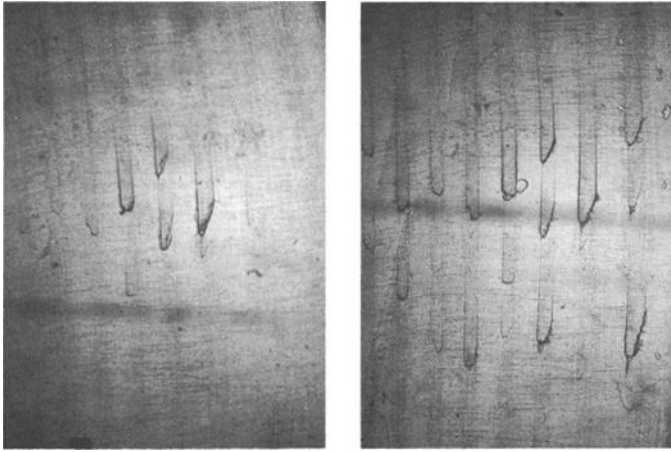


FIG. 16—Surface replications images showing damage development in the neck region: (a) 53% life and (b) 88% life.

damaged plies were identified to be the X plies. They first appeared in the medial-posterior corner, extending their distribution toward the anterior side and along the medial surface, with an increase of applied cycles. In general, results obtained from X-ray radiography and surface replication suggested the overall damage development pattern, shown in Fig. 17.

Although the results from the nondestructive and destructive tests were qualitative, they provided useful information for subsequent modeling. To represent transverse cracking in the matrix material during fatigue, it is required that the transverse ply modulus, E_2 , and shear modulus, G_{12} , both decrease as transverse crack density increases. Such a stiffness reduction relation also depends on stress and stacking sequence

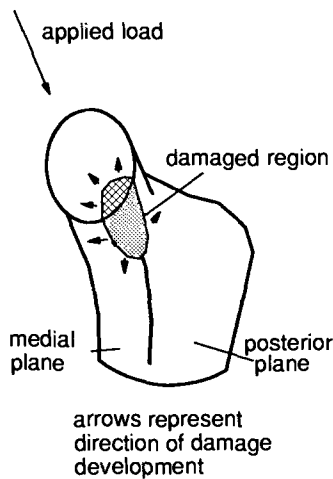


FIG. 17—Schematic representation of the damage development pattern in the neck region.

$$\frac{E_2}{E_2^0} = F \left(\frac{n}{N}, \sigma_{ij} \right) \quad (4)$$

where

E_2^0 = initial transverse ply modulus,
 E_2 = transverse ply modulus at n cycles, and
 σ_{ij} = stress components of an individual ply.

The same kind of equation also applies for the ply shear modulus, G_{12} . Equation 4 applies to all plies at all times.

Creep Effect

The effect of creep on stiffness change of the composite hip prosthesis has been studied in some detail [2]. To model the time-dependent effect, analysis similar to Yeow et al. [21] was followed. The relationship for the stiffness ratios (the ratio of the ply transverse and ply shear modulus to their initial values) is expressed by a master curve

$$\text{stiffness ratio} = \sum_{m=0}^4 a_m \hat{t}^m \quad (5)$$

where \hat{t} is creep time, defined by

$$\hat{t} = \log(t) + \log(a_T) \quad (6)$$

and

$$\log(a_T) = \sum_{m=0}^4 b_m T^m \quad (7)$$

where

a_m, b_m = coefficients,
 t = time in minutes,
 a_T = shift factor, and
 T = temperature.

In the life prediction model, creep time is converted into the number of applied cycles by multiplying by the loading frequency. The stiffness ratio is multiplied by the initial values of the ply transverse modulus, E_2^0 , and the ply shear modulus, G_{12}^0 , for each increment of life fraction, n/N , to obtain the instantaneous stiffness values.

Moisture Effect

It has been known that the presence of moisture in composite materials causes degradation of mechanical properties [21-31]. For example, the transverse ply modulus, E_2 , of a unidirectional ply is estimated by the relationship [25]

$$\frac{1}{E_2} = \frac{v_f}{E_{2f}} + \frac{v_m}{\overline{E}_m(m_r, T)} \quad (8)$$

where

$$\begin{aligned} v_m &= \text{matrix volume fraction,} \\ v_f &= \text{fiber volume fraction,} \\ E_{2f} &= \text{transverse modulus of the fiber,} \\ \overline{E}_m(m_r, T) &= \text{modulus of the matrix at certain moisture content, } m_r, \text{ and} \\ \overline{T} &= \frac{T_g - \Delta T}{T_g^0}, \end{aligned}$$

where

$$\begin{aligned} T_g &= \text{glass transition temperature of the matrix at } m_r, \\ T_g^0 &= \text{glass transition temperature of the matrix at dry air condition, and} \\ \Delta T &= \text{temperature above normal temperature.} \end{aligned}$$

The shear modulus of a unidirectional ply, G_{12} , can be found by a similar approach

$$\frac{1}{G_{12}} = \frac{v_f}{G_f} + \frac{v_m}{\overline{G}_m(m_r, T)} \quad (9)$$

where

$$\begin{aligned} G_f &= \text{shear modulus of the fiber at dry air and} \\ \overline{G}_m(m_r, T) &= \text{shear modulus of matrix at } m_r, \text{ and } T. \end{aligned}$$

In order to apply the aforementioned analysis to the life prediction model, moisture content, m_r , must be represented as a function of applied cycles, so that changes in E_2 and G_{12} due to moisture can be evaluated at any applied cycles. At sufficiently large time, t , the solution for a one-dimensional moisture diffusion problem is [6]

$$\frac{m_r}{m_x} = 1 - \frac{8}{\pi^2} e^{-\pi^2 K^H t / h^2} \quad (10)$$

where

$$\begin{aligned} m_x &= \text{saturated moisture content,} \\ K^H &= \text{moisture diffusion coefficient, and} \\ h &= \text{thickness of the specimen.} \end{aligned}$$

It is realized that the diffusion problem for the composite prosthesis is a two-dimensional one rather than one-dimensional. The solution for a two-dimensional moisture diffusion problem in a composite laminate was given by Farley and Herakovich using a finite difference method [28]. For simplicity, however, the aforementioned one-dimensional solution is used. Upon establishing the moisture-time relationship, moisture content at any applied cycle can be evaluated, and the degradation of mechanical properties can also be evaluated. This degradation of properties will also contribute to internal stress redistribution. Although the aforementioned analyses are established on a physical basis, it is by no means a complete rep-

resentation of the real situation. For instance, Gillat and Broutman [23] have shown that moisture gain in graphite/epoxy laminates was increased with an increase in the presence of external stress. In their analysis, the moisture diffusivities at different load levels were determined experimentally from initial slopes of the curve of the moisture gain as a function of square root of exposure time and the percent equilibrium weight gains; no explicit relation was given relating the applied load level and diffusivity. Moreover, all the aforementioned analyses are based on static conditions. The interaction of moisture diffusion and fatigue is not taken into consideration. Investigations of the effects of environment on fatigue of composite materials has indicated that the presence of moisture will accelerate matrix cracking, thus affecting the stiffness and strength of the material [30,31].

Having discussed property degradation due to mechanical and environmental loadings, we now return to Fig. 12. As discussed earlier, damage development in the subcritical elements will cause internal stress redistribution. Analytically, from laminate theory, this reduction in transverse stiffness will cause change in the stress state of all the plies, that is, in the critical and subcritical elements.

We now shift our attention to the critical element. At 0 applied cycles, no property degradation in the critical element has taken place. At this moment, the failure function $F_L(n) = F_L(0)$. The critical element response is determined by phenomenological data

$$\frac{\sigma_{11}}{X_c} = a + b \log(N) \quad (11)$$

or

$$N = \log^{-1} \left[\frac{(\sigma_{11}/X_c - a)}{b} \right] \quad (12)$$

where

σ_{11} = compressive stress in the fiber direction and
 a, b = constants.

Note that σ_{11} and X_c are both functions of the number of applied cycles, n , so that the element response, N , is also a function of applied cycles. Equation 12 is only used to determine $N(n)$.

Having calculated the failure function $F_L(0)$, and element response $N(0)$, we now skip the "strength reduction" step in Fig. 12 and go back to "ply stress," as it is assumed that no damage is introduced to the elements initially. Now, assume that the number of applied cycles is increased to n . In this instance, stress redistribution occurs in the interior of the laminate, due to damage development and accumulation. Usually this would mean that the critical elements are under higher stress than before. Moreover, environmental effects may cause a reduction of the compressive strength, X_c , of the critical element. An increase in the applied stress, σ_{11} , and reduction in strength X_c , of the critical element will cause an increase in the value of the failure function, so that $F_L(n) > F_L(0)$. The element response (remaining life), $N(n)$, is also changed by the stress redistribution. Since the ratio σ_{11}/X_c is no longer the same at n cycles when compared to 0 cycle, $N(n)$ is different from $N(0)$. Usually $N(n) < N(0)$. Now we have determined $F_L(0)$, $F_L(n)$, $N(0)$, $N(n)$, and n . These quantities will enter the strength reduction equation (Eq 3) and the change in residual strength is evaluated by integrating that equation numerically.

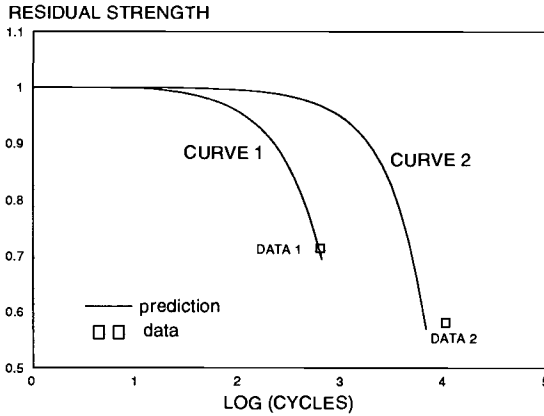


FIG. 18—Residual strength predictions for prototype specimens.

Examples

Results of two sample calculations from the life prediction model are shown in Figs. 18 and 19, where the residual strength of a kind of composite prosthesis (flat-plate design) under normalized load is plotted against applied cycles. The input parameters for the calculations are summarized in Table 1. The critical element, identified as a point under highest local compressive stress in the fiber direction, is found to be located on the medial-neck region, in the ply with the lowest angle of incidence to the neck axis. The unidirectional $S-N$ curve used is

$$\frac{\sigma_{11}}{X_c} = 1.0 - 0.12 \log N \quad (13)$$

The coefficient 0.12 is obtained by adjusting Curve 1 to Data 1 (Fig. 18). Damage due to

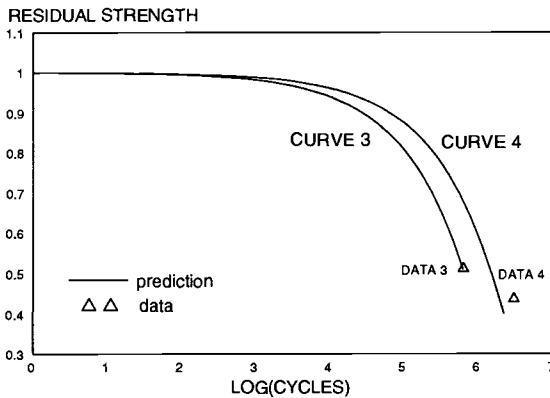


FIG. 19—Residual strength predictions for prototype specimens.

TABLE 1—Input parameters for examples.

| | Curve 1 | Curve 2 | Curve 3 | Curve 4 |
|-------------------------|---------|---------|---------|---------|
| % Ultimate load | 84 | 63 | 52 | 47 |
| Load angle ^a | 0, 10 | 0, 10 | 0, 10 | 0, 10 |
| Number of plies | 32 | 32 | 32 | 32 |
| Stiffness degradation | Eq 14 | Eq 14 | Eq 14 | Eq 14 |
| Strength degradation | ... | ... | Eq 15 | Eq 15 |

^a In-plane, out-of-plane.

mechanical loading is represented by linear degradation functions in the ply transverse and shear modulus

$$\frac{E_2}{E_2^0} = 1 - \left(\frac{n}{N}\right) \quad (14a)$$

$$\frac{G_{12}}{G_{12}^0} = 1 - \left(\frac{n}{N}\right) \quad (14b)$$

where

G_{12}^0 = initial shear modulus and

G_{12} = shear modulus at n .

For simplicity, effect of applied load level is not considered here. The ordinates of the experimental data points shown in Figs. 18 and 19 are taken to be the maximum strain ratio of the critical element at their respective applied load level as determined by the stress-analysis model. It should be mentioned that the linear degradation functions for the ply transverse and shear modulus were chosen for their simplicity. Here the residual strength is calculated based on the maximum strain ratios, since the local failure function, F_L , of the critical element is represented by that ratio. Hence, failure of the prosthesis occurs when the (instantaneous) maximum strain ratio exceeds the residual strength of the critical element, expressed in terms of such a ratio.

The second example is to illustrate the fatigue behavior of the same kind of composite prosthesis in the presence of moisture. The critical element was found to be at the same location as in the last example. In addition to the linear stiffness degradation equation, a strength degradation equation is also used

$$\frac{X_c}{X_c^0} = 1 - \sqrt{\frac{n}{N}} \quad (15)$$

The results are shown in Fig. 19. Note that Eq 15 is chosen so that Curve 3 can be adjusted to Data 3.

Conclusions

A performance simulation model for designing and predicting the remaining strength and life of a composite hip prosthesis subjected to cyclic mechanical and environmental loads is described. Laboratory tests necessary to characterize fatigue damage in the composite prosthesis are also highlighted. It is realized that some of the analyses presented here are still in

incomplete form. For future development, it is suggested that more refined treatments, such as micromechanics, be used to represent property and strength change in the composite system. Nevertheless, it is demonstrated that the critical element concept is a reasonable approach, both physically and mechanistically, for predicting the long-term behavior of engineering structures made of composite material systems.

Acknowledgment

The authors gratefully acknowledge the support of this work by Smith & Nephew Richards, Inc.

References

- [1] Marvin H. Meyers, Ed., *Fractures of the Hip*, Year Book Medical Publishers, Inc., Chicago, 1985.
- [2] Maharaj, G. R. and Jamison, R. D., "Creep Testing of a Composite Material Human Hip Prosthesis," *Composite Materials for Implant Applications in the Human Body: Characterization and Testing*, ASTM STP 1178, Russell D. Jamison and Leslie N. Gilbertson, Eds., American Society for Testing and Materials, Philadelphia, 1993, pp. 86–97.
- [3] Olshansky, S. J., Carnes, B. A., and Cassel, C. K., "The Aging of the Human Species," *Scientific American*, April 1993, pp. 46–52.
- [4] Davidson, J. A., "The Challenge and Opportunity for Composites in Structural Orthopedic Applications," *Journal of Composites Technology & Research*, Vol. 9, No. 4, 1987, pp. 151–161.
- [5] Reifsnider, K. L., Jamison, R. D., Gavens, A. J., and Maharaj, G. R., "Long Term Behavior of Biomedical Composites," *Proceedings*, American Society for Composites Fourth Technical Conference, Technomic Publishing Co., Inc., Lancaster, PA, 1989, pp. 886–895.
- [6] Tsai, S. W. and Hahn, H. T., *Introduction to Composite Materials*, Technomic Publishing Company, Inc., Lancaster, PA, 1980.
- [7] Gavens, A. J. and Locke, L. L., "Influence of the Abductor Muscle Force on Femoral Prosthesis Strain," *Proceedings*, American Society of Biomechanics 13th Annual Meeting, Burlington, VT, 23–25 Aug. 1989.
- [8] Callaghan, J. J., "The Clinical Results and Basic Science of Total Hip Arthroplasty with Porous-Coated Prostheses," *The Journal of Bone and Joint Surgery*, Vol. 75-A, No. 2, Feb. 1993, pp. 299–310.
- [9] Thomson, W., "On the Dynamic Theory of Heat," *Transactions of the Royal Society of Edinburgh*, Vol. 20, Royal Society of Edinburgh, Edinburgh, 1853, pp. 261–283.
- [10] Bakis, C. E. and Reifsnider, K. L., "Nondestructive Evaluation of Fiber Composite Laminates by Thermoelastic Emission," *Review of Progress in Quantitative Nondestructive Evaluation*, Vol. 7B, D. O. Thompson and D. E. Chimenti, Eds., Plenum Publishing Corp., NY, 1988, pp. 1109–1116.
- [11] Zhang, D., Enke, N. F., and Sandor, B. I., "Thermographic Stress Analysis of Composite Materials," *Experimental Mechanics*, Vol. 30, March 1990, pp. 68–73.
- [12] Reifsnider, K. L., "Interpretation of Laboratory Test Information for Residual Strength and Life Prediction of Composite Systems," *Cyclic Deformation, Fracture, and Nondestructive Evaluation of Advanced Materials*, ASTM STP 1157, M. R. Mitchell and O. Buck, Eds., American Society for Testing and Materials, Philadelphia, 1992, pp. 205–223.
- [13] Reifsnider, K. L. and Stinchcomb, W. W., "A Critical-Element Model of the Residual Strength and Life of Fatigue Loaded Composite Coupons," *Composite Materials: Fatigue and Fracture*, ASTM STP 907, H. T. Hahn, Ed., American Society for Testing and Materials, Philadelphia, 1986, pp. 298–313.
- [14] Liao, K. and Reifsnider, K. L., "Multi-axial Fatigue and Life Prediction of a Composite Hip Prosthesis," *Advances in Multiaxial Fatigue*, ASTM STP 1191, D. L. McDowell and R. Ellis, Eds., American Society for Testing and Materials, Philadelphia, 1993, pp. 429–449.
- [15] Liao, K. and Reifsnider, K. L., "Compression Response of a Fatigue-Loaded Composite Hip Prosthesis," *Compression Response of Composite Structures*, ASTM STP 1185, S. E. Groves and A. L. Highsmith, Eds., American Society for Testing and Materials, Philadelphia, 1994.
- [16] Stinchcomb, W. W. and Reifsnider, K. L., "Fatigue Damage Mechanisms in Composite Materials: A Review," *Fatigue Mechanisms*, ASTM STP 675, J. T. Fong, Ed., American Society for Testing and Materials, Philadelphia, 1979, pp. 762–787.

- [17] Charewicz, A. and Daniel, I. M., "Damage Mechanisms and Accumulation in Graphite/Epoxy Laminates," *Composite Materials: Fatigue and Fracture, ASTM STP 907*, H. T. Hahn, Ed., American Society for Testing and Materials, Philadelphia, 1986, pp. 274-297.
- [18] Reifsnider, K. L., Schulte, K., and Duke, J. C., "Long-Term Fatigue Behavior of Composite Materials," *Long-Term Behavior of Composites, ASTM STP 813*, T. K. O'Brien, Ed., American Society for Testing and Materials, Philadelphia, 1983, pp. 136-159.
- [19] Highsmith, A. L. and Reifsnider, K. L., "Internal Load Distribution Effects During Fatigue Loading of Composite Laminates," *Composite Materials: Fatigue and Fracture, ASTM STP 907*, H. T. Hahn, Ed., American Society for Testing and Materials, Philadelphia, 1986, pp. 233-251.
- [20] Bakis, C. E. and Stinchcomb, W. W., "Response of Thick-Notched Laminates Subjected to Tension-Compression Cyclic Loads," *Composite Materials: Fatigue and Fracture, ASTM STP 907*, H. T. Hahn, Ed., American Society for Testing and Materials, Philadelphia, 1986, pp. 314-334.
- [21] Yeow, Y. T., Morris, D. H., and Brinson, H. F., "Time-Temperature Behavior of a Unidirectional Graphite/Epoxy Composite," *Composite Materials: Testing and Design (Fifth Conference), ASTM STP 674*, S. W. Tsai, Ed., American Society for Testing and Materials, Philadelphia, 1979, pp. 263-281.
- [22] Shen, C. H. and Springer, G. S., "Moisture Absorption and Desorption of Composite Materials," *Journal of Composite Materials*, Vol. 10, Jan. 1976, p. 2.
- [23] Gillat, O. and Broutman, L. J., "Effect of an External Stress on Moisture Diffusion and Degradation in a Graphite-Reinforced Epoxy Laminate," *Advanced Composite Materials—Environmental Effects, ASTM STP 658*, J. R. Vinson, Ed., American Society for Testing and Materials, Philadelphia, 1978, pp. 61-83.
- [24] Whitney, J. M. and Browning, C. E., "Some Anomalies Associated with Moisture Diffusion in Epoxy Matrix Composite Materials," *Advanced Composite Materials—Environmental Effects, ASTM STP 658*, J. R. Vinson, Ed., American Society for Testing and Materials, Philadelphia, 1978, pp. 43-60.
- [25] Chang, F., Shahid, I., and Engdahl, R. A., "Predicting Moduli and Strengths Reduction of Unidirectional Graphite/Epoxy Composites Due to Hygrothermal Effects," *Journal of Reinforced Plastics and Composites*, Vol. 8, March 1989, pp. 106-132.
- [26] Chamis, C. C., Lark, R. F., and Sinclair, J. H., "Integrated Theory for Predicting the Hygrothermomechanical Response of Advanced Composite Structural Components," *Advanced Composite Materials—Environmental Effects, ASTM STP 658*, J. R. Vinson, Ed., American Society for Testing and Materials, Philadelphia, 1978, pp. 160-192.
- [27] Loos, A. C. and Springer, G. S., "Moisture Absorption of Graphite-Epoxy Composites Immersed in Liquids and in Humid Air," *Journal of Composite Materials*, Vol. 13, April 1979, p. 131.
- [28] Farley, G. L. and Herakovich, C. T., "Two-Dimensional Hygrothermal Diffusions Into a Finite Width Composite Laminate," VPI-E-77-20, Virginia Technical Institute, College of Engineering, Blacksburg, 1977.
- [29] Shirrell, C. D., "Diffusion of Water Vapor in Graphite/Epoxy Composites," *Advanced Composite Materials—Environmental Effects, ASTM STP 658*, J. R. Vinson, Ed., American Society for Testing and Materials, Philadelphia, 1978, pp. 21-42.
- [30] Hofer, K. E., Skaper, G. N., Bennet, L. C., and Rao, N., "Effect of Moisture on Fatigue and Residual Strength Losses for Various Composites," *Journal of Reinforced Plastics and Composites*, Vol. 6, Jan. 1987, pp. 53-65.
- [31] Sumsion, H. T. and Williams, D. P., "Effects of Environment on the Fatigue of Graphite-Epoxy Composites," *Fatigue of Composite Materials, ASTM STP 569*, J. R. Hancock, Ed., American Society for Testing and Materials, Philadelphia, 1975, pp. 226-247.

Fatigue of a Landing Gear Actuator Beam in a Fighter Aircraft

REFERENCE: Kantimathi, S. and White, T. N., “**Fatigue of a Landing Gear Actuator Beam in a Fighter Aircraft,**” *Case Studies for Fatigue Education, ASTM STP 1250*, Ralph I. Stephens, Ed., American Society for Testing and Materials, Philadelphia, 1994, pp. 53–66.

ABSTRACT: In 1988, inspectors discovered widespread cracking in the main landing gear actuator support beam in a U.S. Navy fighter aircraft. Fractography confirmed metal fatigue as the cause. The beam was made of D6AC steel, a high-strength material.

A flange with a small radius behind the attachment lug was the location of crack origination. A second radius had introduced a multiplication of stress concentrations. Some fixes were evaluated and ruled infeasible due to structural constraints or economic considerations.

The solution was to “beef up” (reinforce) the backup structure with a 17-7 stainless-steel plate. Interference fit fasteners were used to stiffen the surrounding structure. A finite element analysis was performed to analyze the rework design of the support structure. This helped in fracture mechanics calculations, which are included. Critical crack size and crack growth life determinations were made. This paper describes the investigations, analyses, and development of the solution to the cracking. Discussion of the causes of the cracking was given an emphasis. Questions for the students have been added.

KEYWORDS: fatigue, crack initiation or nucleation, crack propagation, fracture mechanics, repairs, stress concentration, aircraft

History

In 1988, an inspector performing a routine visual inspection of a U.S. Navy fighter jet discovered a crack in the shoulder of the main landing gear nacelle ring frame (Figs. 1 and 2) located within the left-hand sponson. The crack location was in the lower flange between the main landing gear trunnion lugs, adjacent to the retract cylinder attachment lug (Fig. 3). The beam is a forging whose material is D6AC steel with cadmium plating. The main landing gear support beam in this model aircraft is a crucial structural element in that many flight and landing critical functions are assigned to it. It is also an expensive item. Consequently, exhaustive investigations were made to many fleet aircraft belonging to this model. These investigations revealed widespread cracking in many fleet aircraft in the same region of the structure (Fig. 4).

The magnitude of the problem and its widespread nature, affecting combat readiness, necessitated immediate attention. The removal of this primary structure from the aircraft would involve “fixturing” the aircraft (supporting it on stands and locking it in position). After this task is accomplished, it would take several days to remove the primary structure by drilling out several hundred fasteners. Given the sense of urgency dictated by the then volatile geopolitical situation, this approach was deemed too slow. This forced the devel-

¹ President, Fatigue Concepts, El Dorado Hills, CA 95762-9734.

² Senior structures engineer, U.S. Navy, Norfolk, VA 23611-5899.

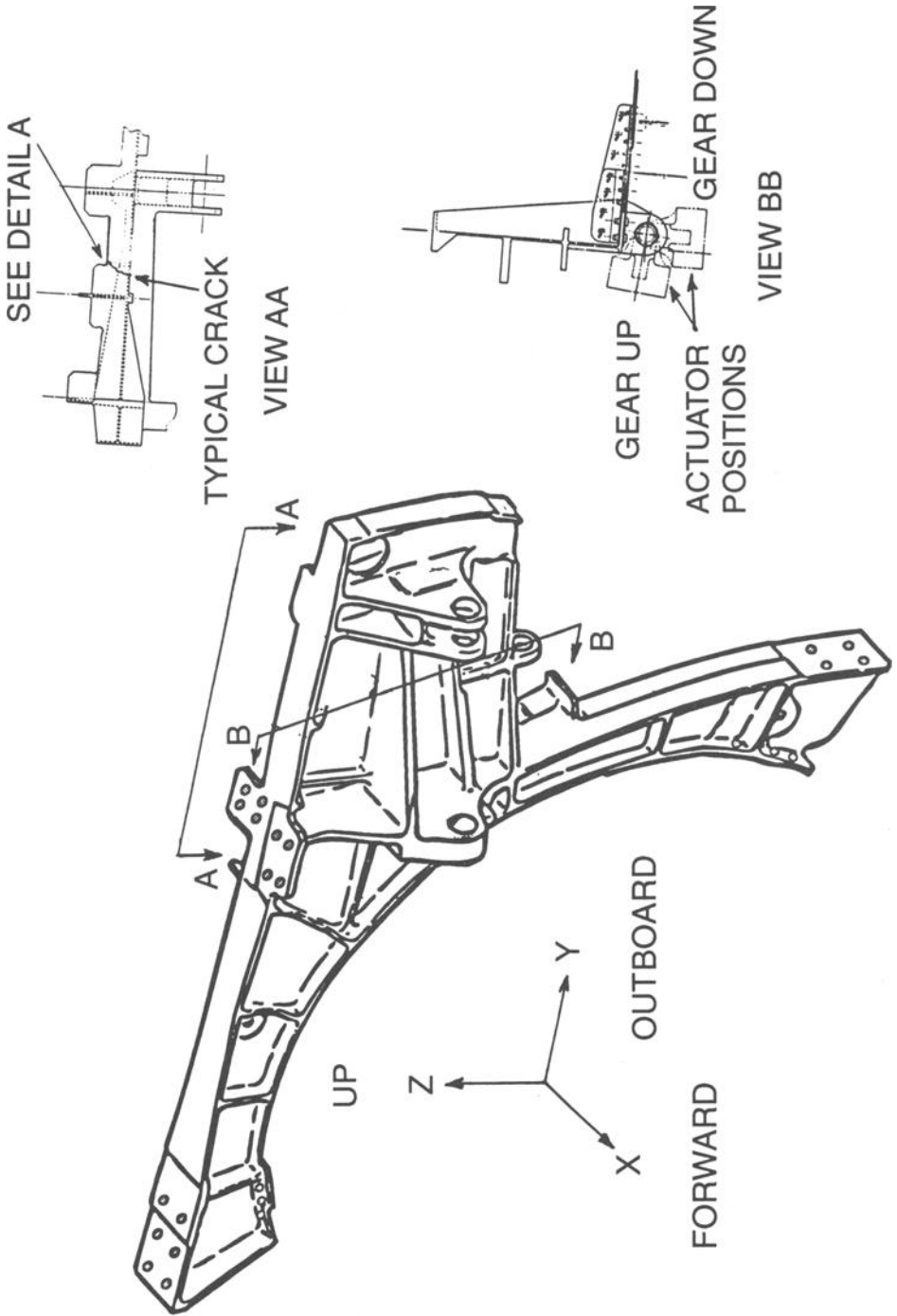


FIG. 1—Fighter aircraft main landing gear actuator support structure Nacelle ring frame.

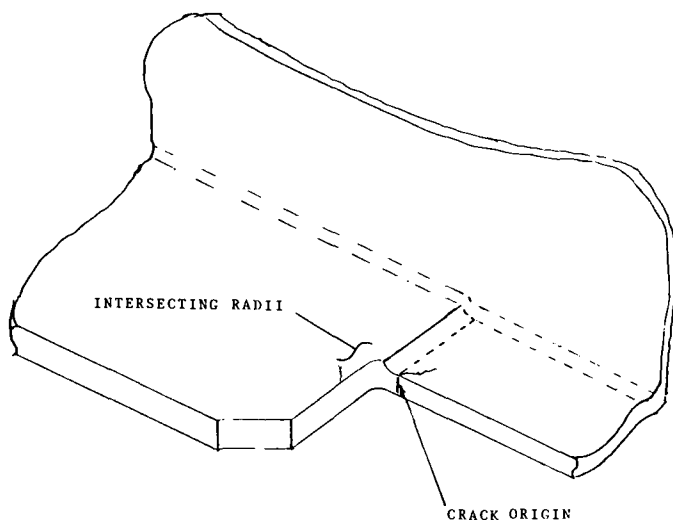


FIG. 2—Multiple stress concentrations and crack origin (Detail A of Fig. 1).

opment of structural modifications and reinforcements to remove existing damage and lower the high stresses without dismantling the primary structure. Several parts were sectioned and subjected to fractographic examination. Later, fractography of cracked parts pointed to metal fatigue as the cause of failure (Fig. 5).

The interim repair involved shaving off material at the flange radii to remove small cracks that had initiated and grown in that region. Such a crack is highlighted by fluorescent dye penetrants (Fig. 4). Additionally, overall magnetic particle inspection (Fig. 3) was carried out to quantify crack lengths. This was followed by later partial disassembly and in-depth inspection using a technique called "magnetic rubber." This fix would have been sufficient if it was an isolated problem resulting from *quality control* at the manufacturer's site, and if the cracking was restricted to only one airplane in the fleet. But, since the cracking was discovered in numerous aircraft, the problem pointed to one of a structural *design* in nature, and hence, it was necessary to find a more elaborate "fix" and apply it to all aircraft operational in the fleet, as well as to aircraft on the production line.

Small intersecting radii (Fig. 2) inadvertently introduced by weight reduction efforts in a flange adjacent to the main landing gear actuator attachment lug were the location of crack origination. Although statically the structure was still adequate, these intersecting radii provided a multiplication of stress concentrations, producing the magnitude of stresses sufficient for fatigue cracking to develop substantially sooner than the "design life" of the aircraft.

An instrumented flight test revealed that landing gear actuator loading was the only service condition that subjected the structure to subsequent fatigue damage. Due to an inadequate backup structure, these actuator loads were inducing beam bending into an adjacent flange containing the intersecting radii. Finite element analysis (Fig. 6) was performed to analyze the structure. The stresses from the analysis were confirmed by the instrumented flight test results (Fig. 7), both of which substantiated prior analysis findings. These stresses were then used to establish critical crack size and remaining life expectancy of in-service cracks and the residual strength of the part in the presence of these cracks. These were useful pieces of information in defining the subsequent usage of fleet aircraft.

Since flight loads, as determined by strain-gaged flight, did not play a significant role in the cracking of the structure, further flight testing was deemed unnecessary. The prototype



FIG. 3—*Photograph showing main landing gear trunnion lug and retract cylinder attachment lug.*

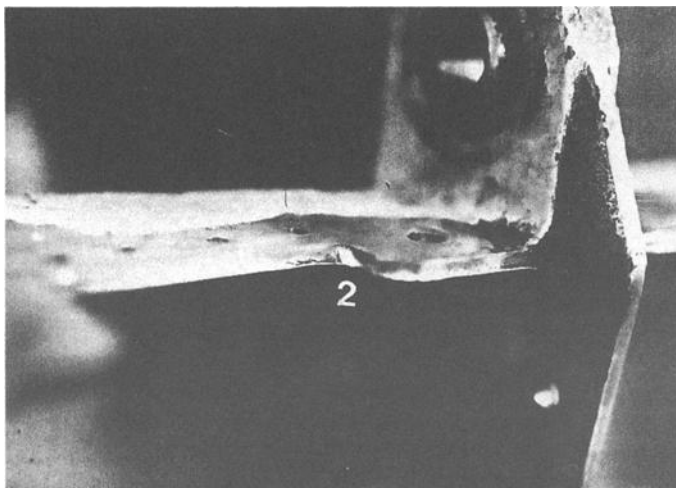


FIG. 4—*Typical crack locations.*

design was thus installed and tested on an aircraft supported with jacks to permit gear cycling. The appropriate gear actuator fatigue load spectrum was applied for an equivalent of one service tour (approximately $\frac{1}{4}$ of the service life, or approximately 2000 landing gear cycles). Strain gages were again used to monitor the stress profile in the reworked radii. Later fatigue analysis using the same stresses for crack initiation life and crack growth life were performed using strain-life curves and linear-elastic fracture mechanics, respectively; This indicated that adequate fatigue life and strength conditions were met for the aircraft's intended usage.

The discovery of this cracking problem was quite timely since the critical flaw size for the flange was just slightly larger than the size of most of the flaws detected in the fleet aircraft. Although this critical flaw size was for the flange alone and not for the entire structure, continued growth of the crack would have threatened the entire main landing gear support structure. Early detection of the cracks in the flange enabled salvage of the structure before irreversible damage occurred.

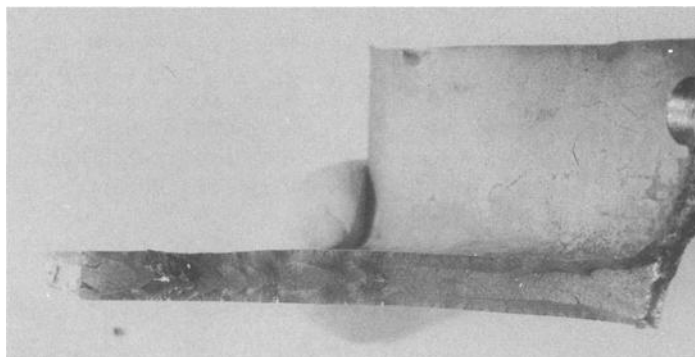


FIG. 5—*Fractography of cracked part exhibiting features of metal fatigue.*

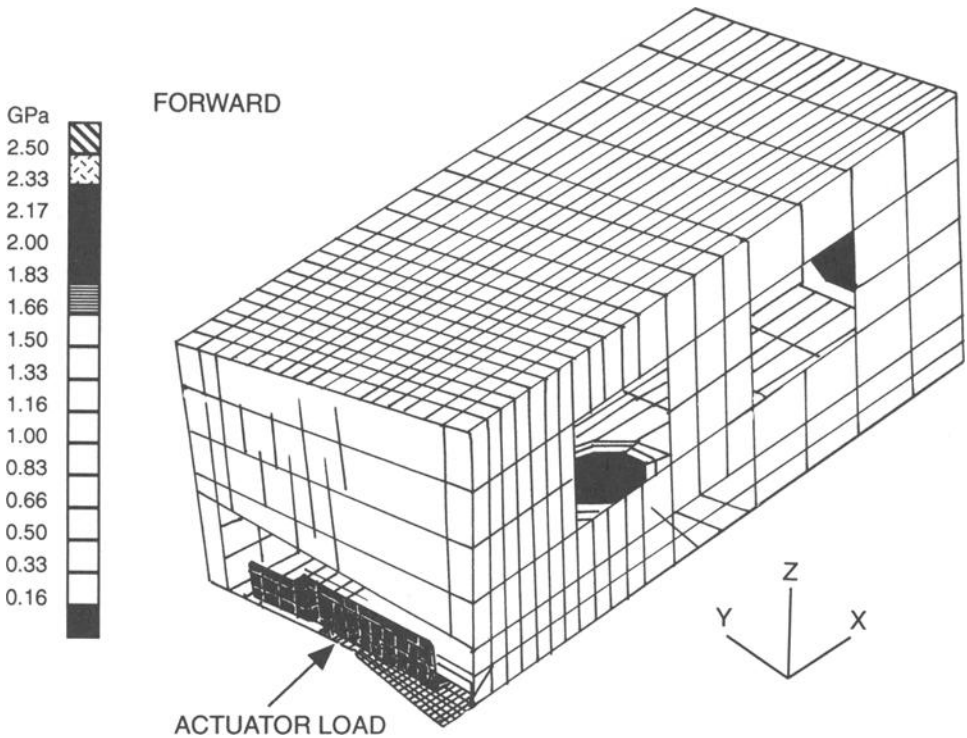


FIG. 6—An example of finite element analysis.

Investigations and Discussion

Cracking was found to originate at a compounded stress-raiser (radius) in the integral flange. It is well known that a structural discontinuity often called a stress concentration or stress-raiser results in elevation of local stresses in the immediate vicinity of the discontinuity. Multiple stress concentrations make the situation even worse. For example, for a central hole in a wide plate loaded in uniform remote tensile stress, the stress concentration factor is three at two diametrically opposite points at the edge of the hole along the minimum section. If another hole is drilled with axis normal to that of the first hole *and* normal to the load axis, then the extent of local maximum stresses at a point of intersection of the two holes could be three times three or nine times the original stress! Such a design has occurred in real life [7] where a small access hole for lubrication was thoughtlessly drilled almost perpendicular to the load axis, intersecting a pre-existing hole (Fig. 8).

Similarly, while a radius is unavoidable in stepped sections, existence of *compound radii* spells doom for most structures, especially highly stressed aircraft structures where stresses can be high in order to avoid weight penalties. That was precisely what happened in the landing gear support structure beam under discussion (Fig. 2). These high stresses at the notch can result in local plastic deformation that hastens the formation of cracks that can then grow due to time-variant in-service loadings (fatigue) or stress corrosion. The flange with multiple stress-raisers was also normal to the load path provided by the main landing gear actuator attachment lug. Also, the backup structure was found to be weak with low stiffness so the flange acted as a beam with fixed ends carrying a concentrated load from

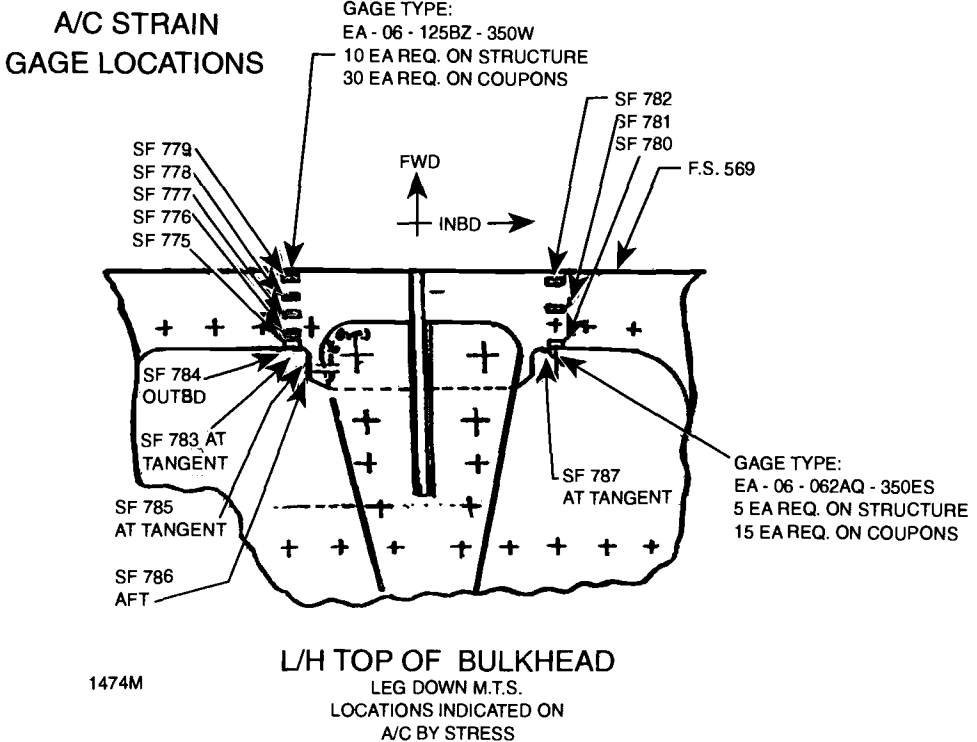


FIG. 7—Strain gage locations in instrumented flight test. FWD = forward of the aircraft and INBD = inboard of the aircraft.

the actuator. Moreover, the maximum bending moment happened to occur close to the location of the flange with a compound radii. In addition, out-of-plane deflections due to secondary bending aggravated flexural stresses, hastening crack initiation along with the other factors outlined in this paragraph.

Metallurgical examinations ruled out material and processing defects to be contributors of the cracking. Improper heat treating was eliminated as a causal factor. The percentage content of each constituent alloy was well within its specified range as verified by X-ray spectrography. Tensile strength, modulus of elasticity, and surface hardness were tested to be normal. The grain size and structure was also verified. Since the aircraft operated extensively in sea atmosphere, environmentally assisted cracking becomes a major concern. Stress corrosion cracking is a leading cause of structural failures in naval aircraft of this type [2]. Careful examination of the fracture regions showed no evidence of stress corrosion damage at this location. In addition, other environmental degradation, such as hydrogen embrittlement, can damage plated structural components. Electrolytic cadmium plating makes the forging more susceptible to hydrogen embrittlement. Vacuum deposited cadmium plating is a preferred process, due to the absence of hydrogen-inducing influences [3]. Examination of this forging revealed that it was indeed plated with cadmium using the vacuum-deposited process. Subsequently, hydrogen embrittlement from the plating process was ruled out to be a cause for the initiation of the cracks.

Examination of the fracture surface also revealed beach marks indicative of fatigue crack growth over a period of time. Micro-fissures were observed on closer examination. Striations

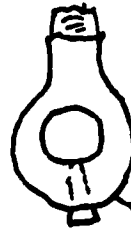
TIPS ON FATIGUE

5.52 INTERSECTING HOLES--Here is a case where a hole was tapped into the highly stressed region of another hole in the tension flange of a wing beam. This is similar to the case of a grease fitting hole for a bearing.

If you must have a hole, the idea is to move it to the least damaging position. A little local reinforcing (beef up) is also helpful.



POOR



BETTER

beef up



ALSO ACCEPTABLE

FIG. 8—The dangers of intersecting holes. (This rough sketch is a true reproduction from Ref 1.)

were observed, but not in such a way that quantitative information could be gleaned from them. Typically, in steel surfaces, it is more difficult to find quantitatively useful striations [4]. This is in contrast with the more prevalent structural materials in aircraft, namely, aluminum alloys, which usually exhibit nice striations. The main reason is that steels lack the protective nature of the oxide film that forms quickly in the fracture surface in aluminum alloys. It is virtually impossible to identify clearly defined areas of striations in steels, thereby making fractographic examination most difficult [4]. The situation is even more difficult for high-strength steels, and the beam was made of a high-strength steel (Rc 46-49).

The final solution became a combination of several modifications intended to improve the fatigue life of the cracking structure. These included:

- (1) reductions in stress concentrations through modified geometry,

- (2) reinforcement of adequate backup structure, and
- (3) use of interference fit fasteners to increase joint stiffness.

Analysis

Fractography of the available crack surfaces revealed typical beach marks found in fatigue fracture surfaces (Fig. 5). The origin for this fracture was located near two intersecting radii, originally described using Fig. 2. The initial slow crack growth region near the origin was approximately 1.5-mm in length. Under microscopic examination, this region revealed micro-fissure formations of fatigue crack growth. The adjacent section of fracture surface was an area about 25-mm long with eight or nine thumbnail-shaped areas exhibiting over-stress dimpling and shear lips, with subsequent crack arrest (Fig. 5). The crack arrest areas also had micro-fissure formations typical of fatigue. Each thumbnail-shaped area, which was approximately 2.5-mm long, characterized a crack "jump," due initially to the overstress, with crack arrest occurring upon dissipation of the energy applied. Fast crack growth (overstress) was observed beyond this region.

Initially, the frame flange containing the intersecting radii was modeled as a beam with fixed ends, including an elastic spring aft of the actuator lug representing the backup structure and a concentrated load applied at the actuator lug. The maximum bending stress was derived from beam analysis to be 1079 MPa. This value compared favorably with the stresses measured during instrumented flight test in locations outlined in Fig 7. Then a Neuber corrected notch factor, $K = 2.35$, was obtained from the theoretical stress concentration factor, $K = 2.4$, by using the relation

$$K_n = 1 + \frac{K_t - 1}{1 + P/r} \quad (1)$$

from Peterson's *Stress Concentration Factors* [5]. This compounded with the maximum bending stress produced a stress value of 2535 MPa at the intersecting radii.

Subsequently, an elementary finite element load analysis was employed to study the loads in the region of failure. A two-dimensional coarse grid mesh was prepared of this "beam" structure. Load values resulting from this analysis were indicative of an ineffective backup structure. The backup structure lacked sufficient stiffness to carry the actuator loads away from the frame flange, which in turn was left to deflect the load into adjacent, integral parts of the frame.

Later, a more developed finite element stress analysis was employed to better understand the stresses in the critical structural location. A two-dimensional fine-grid mesh was prepared with a particularly close mesh in and around the site of crack initiation (the intersecting radii). This provided stress values at the intersecting radii that were comparable to those measured by instrumented flight test and conventional notch stress calculations from Neuber corrected theoretical stress concentration factors for applied bending.

Since the notch-corrected stress calculation exceeded the yield strength of the material, and is not representative of the true stress state, a notch strain analysis was performed. In lieu of notch stress, the notch strain, ϵ_n , is used as a function of nominal strain, e , namely $\epsilon_n = Ke$. This notch strain then relates to the correct notch stress using the cyclic stress strain curve for the material. First, a notch strain was calculated by graphically solving the cyclic stress-strain curves simultaneously with Neuber's rule [6]. Neuber's rule applies to thin structures and was used since the part being analyzed is thin, approximately 6 mm, and the linear

rule that applies to thicker structures is too liberal in this case. The cyclic stress-strain curve is given by the relation

$$\delta\epsilon = \delta\epsilon_e + \delta\epsilon_p$$

where

$$\delta E_e = \frac{\delta\sigma}{E} \text{ and}$$

$$\delta E_p = 2 \left(\frac{\delta\sigma}{2K'} \right)^{1/n'}$$

The Neuber's rule is given by the relation $E\sigma = K_t^2 e S$. Stress values calculated compare closely to those observed earlier from instrumented flight tests as well as those derived from finite element considerations. An initiation fatigue life, approximately 2000 cycles, was then obtained from contractor stress-life curves specifically generated for this material. It was interesting to note that the crack initiation life corresponded roughly to the number of in-service landing gear cycles, including flight and maintenance cycles, accumulated for those aircraft that exhibited the smaller cracks.

A residual strength diagram and a critical crack size, a , were then developed from linear elastic fracture mechanics in the following manner. First a reference stress, σ , was chosen to be the flange bending stress previously arrived at by conventional analysis for the affected geometry. As mentioned earlier, an instrumented flight test had revealed that landing gear actuator loading was the only service condition that subjected the structure to subsequent fatigue damage. Therefore, a simple constant amplitude loading spectrum was adequate in this case, with the stress fluctuating between a maximum of 1079 MPa and a minimum of 0 MPa ($R = 0$). Next, the appropriate stress intensity factor, β , of approximately 0.9 for this geometry and loading condition was obtained from a compendium of such factors [7]. Now, the material's plane-strain fracture toughness was taken to be 105 MPa \sqrt{m} [8]. By using the above information and solving for stress levels for incrementally increasing crack sizes, starting at an initial flaw size a_r of 0.125 mm, a residual strength diagram (Fig. 9) was generated from $[\sigma_c = (K_{Ic}/\beta\sqrt{\pi a})]$ by plotting σ_c versus a . From the residual strength diagram, the critical crack size can be determined by finding the applied reference stress on the ordinate and then locating the critical flaw size, which was found to be 3.7 mm on the abscissa.

Next, the Paris crack growth rate equation

$$\frac{da}{dN} = C(\Delta K)^m \quad (3)$$

where Δ stands for an increment, was integrated to produce a crack growth diagram (Fig. 10) and to calculate the crack growth life to failure. Using the relationship [5,6] for $\Delta K = \Delta\sigma\beta\sqrt{\pi a}$ we get

$$\frac{da}{dn} = C(\Delta\sigma\beta\sqrt{\pi a})^m$$

in the above expression for the Paris equation, we find that for D6AC steel, $C = 1.75 \text{ E-}07$, and $m = 2.5$ [6]. However, the constant C applies only to English units specifically, when the crack growth rate is measured in inches per cycle and ΔK is in ksi $\sqrt{\text{in}}$. An overwhelm-

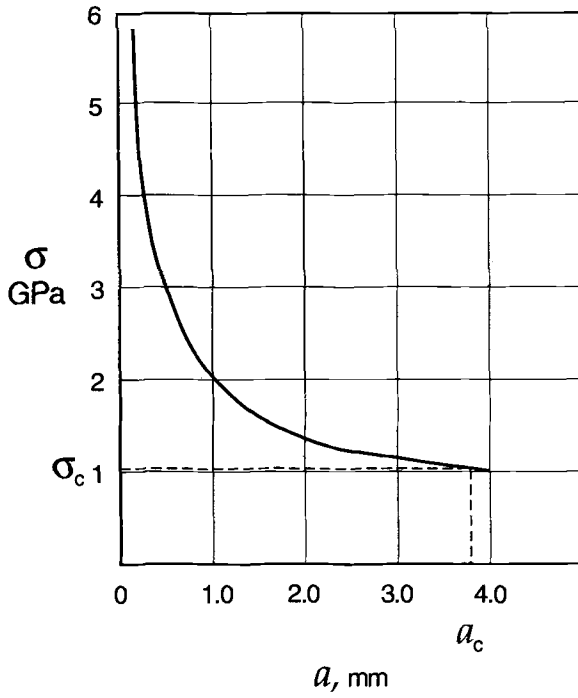


FIG. 9—Residual strength diagram.

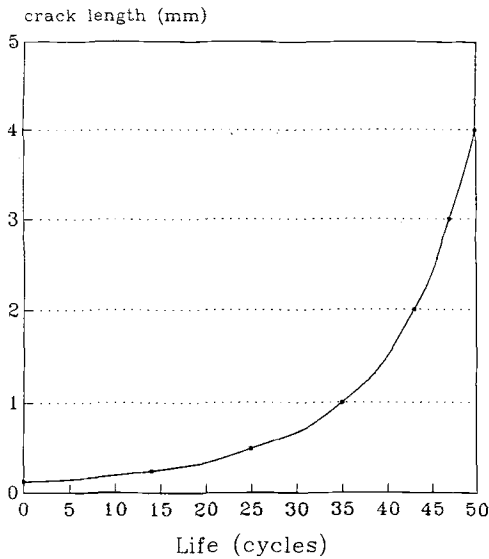


FIG. 10—Crack growth diagram for constant amplitude loading.

ing majority of the crack growth data available in the literature is still in English units. The useful conversion factor given below [6] is left to the student as an exercise.

$$C[m/\text{cyc}; \text{MPa}\sqrt{m}] = \frac{C[\text{in.}/\text{cyc}; \text{ksi} \sqrt{\text{in.}}]}{39.37 (1.1)^m} \quad (6)$$

to be used in the relation

$$\frac{da}{dN} [m/\text{cyc}] = C (\Delta K [\text{MPa} \sqrt{m}])^m$$

Using the conversion factor (m remains the same), in metric units, the Paris parameters are: $C = 3.51 \text{ E-}09$, and $m = 2.5$. Using the crack growth rates for a water environment is appropriate, since the structure is periodically exposed to moisture intrusion from field environments.

Integrating this, and assuming that σ , β , C , and m are all constants with respect to crack size, we find that [5,6]

$$N = \frac{1}{C\sigma^m\beta^m\pi^{m/2}} \left[\frac{a_f^{(1-m/2)} - a_i^{(1-m/2)}}{1 - m/2} \right] \quad (6)$$

where

$$\begin{aligned} a_i &= \text{initial crack length and} \\ a_f &= \text{final crack length.} \end{aligned}$$

Now plotting $a_i - a_f$ versus N produces a crack growth diagram for the constant amplitude loading (Fig. 10). The crack growth life to failure can now be determined by finding the critical crack size on the ordinate, then finding the corresponding crack growth life, which was found to be fifty landing cycles on the abscissa. This very low number of cycles for crack growth was also apparent in the fracture surfaces exhibited using metallurgical examinations (Fig. 5).

Conclusions

Numerous examples of fatigue failures brought about by carelessly or inadvertently induced high-stress concentrations are given in Ref 8. The author of that reference, Dr. Friedrich Karl Naumann, remarks in Chapter 3 entitled, "Failures Caused by Planning Errors:"

It has been known for a long time that during construction of machine parts and tools, sharp edges and cross-sectional changes should be avoided because stress concentrations form in such places. These can result in stresses substantially above the nominal stress. It is surprising how often this well-known design axiom is violated even today.

Let us examine some of the possible reasons for such a violation of a fundamental principle. One reason could be a lack of communication among various engineers and other professionals involved in the design and processing stages of the landing gear actuator support beam. It appears that a good design had fallen victim to the well-intentioned trimming at the hands of a weight engineer. A double radius resulted, and while the static strength of

the part remained acceptable, the fatigue performance clearly suffered. Another example of an inadvertent introduction of a stress concentration came about in another fighter aircraft due to accumulation of positive tolerances in one direction that left a tighter radius at one end. Finally, in another manufacturing situation, a generous fillet radius stipulated by the design engineer was destroyed by a machinist who decided to reduce the number of passes using the numerical control machine, thereby saving the manufacturer some money! Though he achieved his goal in the short run, the part did fail in fatigue later due to the higher stress concentration he introduced.

In the current case, failure to follow through in original design of the actuator support backup structure had resulted in an unintended and unwanted load path. Equally important, a double-stress concentration was introduced in the actuator support beam during structural optimization efforts for the least weight design. This necessitated an expensive and time-consuming fix in hundreds of cracked fleet aircraft. However, this fix has proved successful and has developed into a permanent design change. No additional cracking at the actuator beam has been reported to date.

Student Questions

1. Why were striations not quantitatively useful in the failure analysis in this case?
2. If the backup structure resulted in reducing the stress level by 25% in the actuator beam, from 1079 to 810 MPa, calculate the increase in its crack growth life.
3. If the backup structure resulted in halving the stress level in the actuator beam, from 1079 to 540 MPa, calculate the increase in its crack growth life.
4. Can you infer a rough idea about the relationship between the stress level in a part and its crack growth life, using the result of the calculation done in the text of this case study, as well as your answers to questions 2 and 3?
5. You have found a material with the same fracture toughness, but roughly half the Paris constant C . Estimate the improvement in crack growth life, if you use this new material.
6. Your partner in this project suggests that choosing a material with twice the fracture toughness and roughly the same C and m will result in a much better life for the part than switching to a material where C is cut in half. Do you agree? Prove it!
7. What steps would you undertake to ensure that the doubled stress concentration does not occur during weight optimization or other steps?
8. If the aircraft is continuously operated in a non-water environment, by how many cycles will the crack growth life improve? Use $C = 9.1 E-10$, and $m = 2.5$. Repeat for 3.5% sodium chloride environment (use $C = 7.9, E-09, m = 2.5$). Comment on the results.

References

- [1] Smith, C. R., "Tips on Fatigue," NAYWEPS 00-25-559, U.S. Government Printing Office, Washington, D.C., 1966.
- [2] White, T. N. and Kantimathi, S., "Stress Corrosion Cracking of a High-Strength Steel in a Landing Gear Support Frame in a Fighter Aircraft," in *Handbook of Case Histories in Failure Analysis*, ASM International, Materials Park, OH, 1992.
- [3] Kamdar, M. H., "Embrittlement by Solid-Metal Environments," in *Failure Analysis and Prevention, Metals Handbook, Ninth Edition*, Vol. 11, American Society for Metals, Materials Park, OH, 1986.
- [4] Hertzberg, R. W., *Deformation and Fracture Mechanics of Engineering Materials, Third Edition*, John Wiley & Sons, New York, 1989.
- [5] Peterson, R. E., in *Stress Concentration Factors*, John Wiley & Sons, New York, 1974.
- [6] Fuchs, H. O. and Stephens, R. I., in "Metal Fatigue in Engineering," John Wiley and Sons, New York, 1980.

- [7] Kantimathi, S., in *Fracture Mechanics—Aerospace Applications*, American Institute of Aeronautics and Astronautics, Washington, D.C., 1995.
- [8] *Damage Tolerant Design Handbook, A Compilation of Fracture and Crack Growth Data for High-Strength Alloys*, MCIC-HB-01, Metals and Ceramics Information Center, Battelle, Columbus, OH.
- [9] Naumann, F. K., *Failure Analysis Case Histories and Methodology* Dr. Riederer-Verlag GmbH, Stuttgart, Germany, English Translation by American Society for Metals (ASM), 1983.

Fatigue Evaluation of Agitator Paddle Shafts

REFERENCE: Jhansale, H. R., “**Fatigue Evaluation of Agitator Paddle Shafts,**” *Case Studies for Fatigue Education, ASTM STP 1250*, Ralph I. Stephens, Ed., American Society for Testing and Materials, Philadelphia, 1994, pp. 67–76.

ABSTRACT: Existing agitator paddles in material feeders were failing in fatigue. An experimental evaluation was undertaken to assess the fatigue strengths of the existing agitator paddles and the newly designed replacement paddles. As in most typical industrial situations, the study was constrained by budget and time limitations. After considering several options, it was decided to strain gage and test the paddles in their own feeder frame and drive motor with minimum mock-up fixturing to achieve several load levels. While using real-time test speeds, the test durations were accelerated by using higher than normal operating loads. Results were analyzed using strain-based cumulative fatigue damage-analysis techniques and component fatigue-life curves were developed to project the long life fatigue strengths. The investigation showed that while the newly designed replacement paddles would have significantly improved fatigue strengths, the actual improvements may be limited by other built-in weld discontinuities in the paddle stiffeners.

KEYWORDS: steel, torsional fatigue, cumulative damage analysis, fatigue test, rainflow histogram data analysis

Nomenclature

| | |
|--------------------|----------------------------------|
| $\Delta\epsilon/2$ | Local strain amplitude |
| $\Delta\sigma/2$ | Local stress amplitude |
| $\Delta s/2$ | Nominal stress amplitude |
| K_f | Fatigue notch factor |
| K' | Cyclic strength coefficient |
| n' | Cyclic strain hardening exponent |
| σ_f | True tensile factor strength |
| σ'_f | Fatigue strength coefficient |
| ϵ'_f | Fatigue ductility coefficient |
| b | Fatigue strength exponent |
| c | Fatigue ductility exponent |
| E | Elastic modulus |
| D | Damage |
| n | Applied cycles |
| N_f | Cycles to failure |

¹ Principal engineer, Fatigue and Fracture Mechanics, Siemens Power Corporation, 1040 S. 70th Street, Milwaukee, WI 53214.

The Problem

Figure 1 shows a view of a material feeder with two agitator paddles as part of the test setup used in the study. The flexible hopper bag has been removed and replaced by a central frame in which are mounted shoe pads to provide the load resistance to the paddles. In service, these paddles oscillate and agitate the hopper bag from outside to keep the material flowing freely down the hopper. These material feeders are made in several sizes and are used in various industries including chemical, plastics, pharmaceutical, and food processing. The materials are usually in dry powder or granular form and require constant agitation to keep them flowing.

Each of the two existing paddles included a 1-in. diameter shaft made from a 1018 cold-rolled steel with a reduced diameter splined section at one end to transmit the torque from a driving motor arrangement. The shaft was welded to the backside of the paddle, along with stiffener webs by using circumferential and longitudinal fillet and spot welds (Fig. 2). These shafts were prematurely failing in the field at the splined section due to torsional fatigue. Information was not available regarding either the load levels or life durations.

The manufacturer had developed a newly designed paddle with a 1.25-in. diameter shaft that used friction coupling instead of a reduced spline section to replace the failed paddles.

Basically, the manufacturer wanted to evaluate the long-life fatigue strengths of both the existing (old) and replacement (new) paddles and determine the degree of improvement in fatigue strength, if any. As in most typical industrial situations, the scope of the investigation was constrained by budget and time limitations.

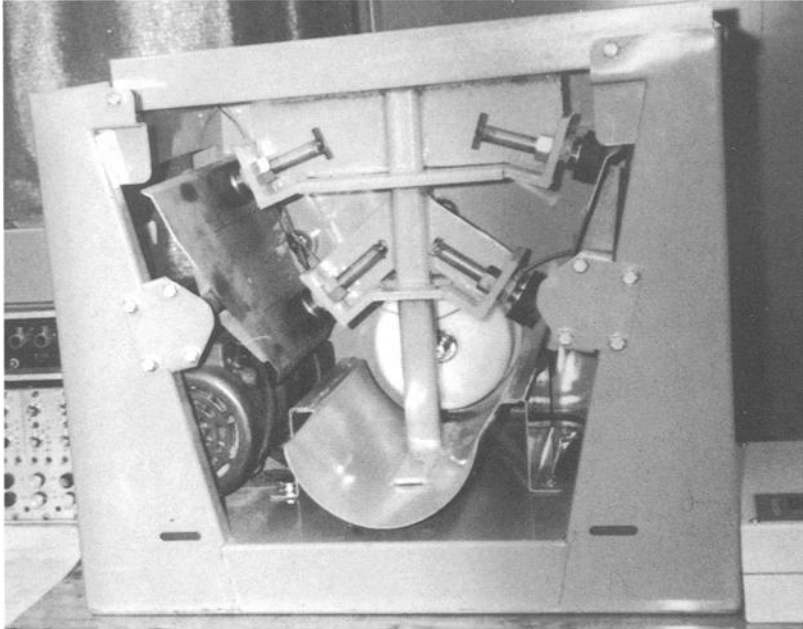


FIG. 1—Test setup showing material feeder box with a central frame and adjustable shoe pads for resisting the two paddles. Approximate scale = $1/8$.

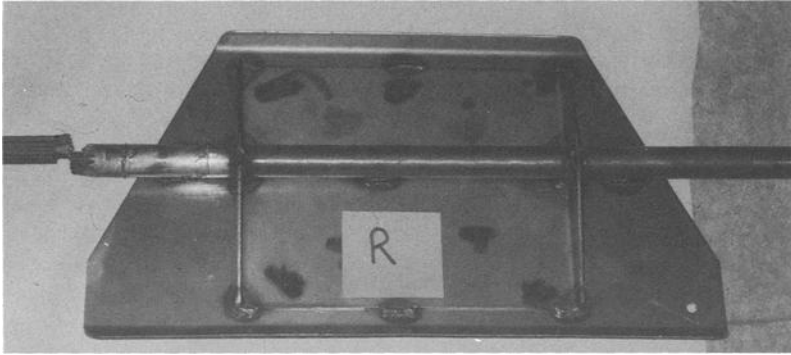


FIG. 2—Back side of a failed paddle showing welds and failure through spline section. Approximate scale = $\frac{1}{6}$.

The Approach

Student Question

- What type of study should be considered?

Answer

- Since there were several unknown factors such as material properties, stress concentration factor, notch sensitivity, and so forth, it was decided that a testing program was needed in addition to analytical estimations to develop the required answers. This paper describes the test method used and the subsequent analyses required to interpret the less-than-adequate results.

Student Question

- What testing and analytical approaches should be used?

Answer

- The plan was to perform constant amplitude fully reversed torsional cycling tests at several load levels on both the old and new design paddle shafts. The load levels were to be selected to obtain finite lives in the range of about 10^3 to 10^6 cycles. Using estimated strain-life and cyclic stress-strain properties of the material, a Neuber rule-based notch-fatigue analysis [1,2] was performed. By matching the results of this analysis with the test data, appropriate “component factors,” which are essentially “fatigue notch factors,” would be determined. By extrapolating this fatigue curve, the expected fatigue strengths, corresponding to the desired service-life durations, would be determined.

The Test Method

The first choice was to use the existing axial closed-loop test system to perform the tests. However, the cost and time required for making appropriate fixturing to develop torsional loading from linear actuator motion were not acceptable. Therefore, it was decided to use the existing feeder arrangement as it was, and measure the torques and bending moments by way of strain gages.

Each paddle was instrumented with two-arm rosette strain gages to measure torque. These gages were mounted slightly inward from the spline section on the 1-in. diameter section. Linear strain gages were mounted near the weld to measure bending strain. The actual locations of these strain gages were selected based on the results of a separate stress-analysis test using brittle coating. Scale factors for converting the strain-gage output to appropriate nominal stresses and torque were derived using both analytical calculations and static dead-weight calibrations.

Instead of using the hopper and the material for load resistance, a central frame was fabricated with adjustable shoe pads to allow for the change in load levels (Fig. 1). Portable "rain flow" histogram recorders were used to collect the load history data, which included strain range, mean strain, and cycle counts. Test durations in minutes were also monitored and recorded. Under-peak detection and tripping switches were provided to sense cracking and stop the tests.

Test Experience

Each test consisted of one pair of paddles, designated as left and right paddles. A total of four pairs of old paddles and one pair of new paddles were tested. The tests were performed at about 100 cycles per min, which was within the range of operating frequency in the field (60 to 100 cpm).

Typically, each test was set up to apply constant fully reversed torque on the shaft. In reality, due to lack of precise closed-loop control and system dynamics, a spectrum of amplitudes were encountered in each test, as measured by the histogram recorders.

In the case of the first pair of old paddles and the only pair of new paddles tested, the initially selected load level was not sufficient to produce failure in a reasonable number of cycles. Load levels were increased several times to induce failure. While cracking was eventually achieved in the first set of old paddles, the new paddles tested did not experience any cracking in the shaft or weld locations, even after several increases in load level. However, these tests had to be interrupted to repair weld cracks that formed in the paddle blade edges and outer frame. Since the new paddle shafts were stronger than the blade and the frame, and since the allotted time and budget was exhausted, the test program was terminated at this point.

Torsional Fatigue Results Analysis

Student Question

- How should the multiple amplitude test data and the new paddles data, which did not fail, be analyzed and interpreted to arrive at the required simple answers?

TABLE 1—Torsional fatigue test results.

| Specimen Number | Equivalent Torque Amplitude, N·m | Equivalent Cycles | Failed |
|-----------------|----------------------------------|-------------------|--------|
| OLT1 | 289.5 | 47 039 | Yes |
| ORT1 | 289.5 | 47 130 | Yes |
| OLT2 | 315.7 | 23 395 | Yes |
| ORT2 | 315.7 | 28 187 | Yes |
| OLT3 | 252.6 | 110 186 | Yes |
| ORT3 | 252.6 | 155 286 | Yes |
| OLT4 | 315.7 | 26 840 | Yes |
| ORT4 | 336.8 | 18 215 | Yes |
| NLT1 | 369.9 | 422 027 | No |
| NRT1 | 369.9 | 338 693 | No |

NOTE—All failures represent cracks initiated in the spline section.

Answer

- The multiple amplitude data required a cumulative fatigue-damage analysis procedure and a conversion to an equivalent constant-load amplitude for interpretation. The unfailed new paddle data were used as conservative failure data. The details of the procedure used are described in Appendix A and summarized in the following section.

The equivalent torque versus the equivalent cycles data derived in Table 1 are plotted as torque amplitude versus cycles to cracking for both old and new paddle shafts (Fig. 3). Estimated torque amplitude versus cycles-to-failure curves, derived from the cumulative damage analysis (Appendix A) are also plotted. The component calibration factors (or fatigue notch factors) for each paddle, which was required for deriving the component fatigue curve, was developed by trial and error, as described in Appendix A. These values ranged from 1.43 to 1.49 for the old paddles. They reflect not only the effective stress concentration due to spline geometry, but also errors in the assumed material properties and specimen-to-specimen variations. An average value of 1.46 was used for predicting the component fatigue

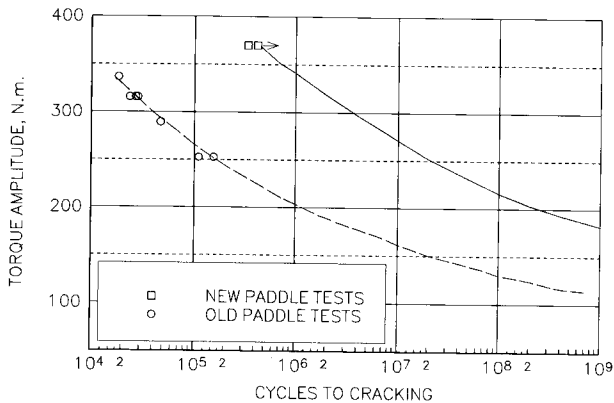


FIG. 3—Torsional fatigue life curves for old and new paddles.

life curve. In the case of the new paddles, the required factor was 2.76 to 2.81. Although the stress concentration factor is virtually eliminated in the new paddle shafts, the calculated high factor is due to the fact that these paddles did not fail but were assumed to be failures for conservative analysis.

In the field, the paddles are reported to experience about $3 \cdot 10^7$ to 6×10^7 cycles per year. Therefore, the torsional fatigue strength of the old paddles, corresponding to about 10 or more years of service (about 10^9 cycles), is estimated from the projected curve to be about 113 N·m. In the case of the new paddles, the data points do not represent failure. However, the projected curve extrapolated from the data points is assumed to conservatively represent the torsional fatigue strengths of the new paddles. From this curve, the estimated torsional fatigue strength of the new paddle shafts is about 186 N·m.

Fatigue Analysis of Welded Locations

Although the manufacturer did not specifically express a concern for the weld locations, it was thought appropriate to evaluate the on-going fatigue damage at these locations.

Student Question

- What procedure should be used to evaluate the fatigue damage at the weld locations?

Answer

- Raw histogram data from bending strain gages were analyzed, similar to the torsional data, to calculate equivalent load levels for each of the paddles. The cumulative damage analysis was performed using the fatigue curves and procedure as per British Standard BS5400 (Steel, Concrete and Composite Bridges, Part 10, Code of Practice for Fatigue). This standard, although somewhat conservative, is believed to be the most comprehensive and up-to-date procedure for weld joints. A brief outline of the procedure is included in Appendix B.

Table 2 summarizes the bending and torsion levels experienced by each paddle in the vicinity of welds. The last column shows the calculated maximum principal stress. Ideally, the loading was supposed to be proportional; however, the independently collected data from the several histograms showed some discrepancy in the number of cycle counts recorded

TABLE 2—Summary of weld location history.

| Specimen Number | Torsional Stress, MPa | Torsional Cycles | Bending Stress, MPa | Bending Cycles |
|-----------------|-----------------------|------------------|---------------------|----------------|
| OLT2 | 98.1 | 23 395 | 41.4 | 29 372 |
| ORT2 | 98.1 | 28 187 | 41.4 | 23 818 |
| OLT3 | 78.5 | 110 186 | 41.4 | 134 300 |
| ORT3 | 78.5 | 155 286 | 35.5 | 252 700 |
| OLT4 | 98.1 | 26 840 | 41.4 | 26 946 |
| ORT4 | 104.7 | 18 215 | 35.5 | 33 223 |
| NLT1 | 58.9 | 422 027 | 53.3 | 857 600 |
| NRT1 | 58.9 | 338 697 | 82.9 | 317 700 |

between bending and torsional loadings. Therefore, for the purpose of the analysis, the load history was assumed to consist of a combined torsional and bending history and a pure bending history for cases where the bending cycles were higher in number compared to the torsion cycles (Tables 2 and 3).

None of the weld locations on any of the paddles showed any cracking as tested by dye penetrant and magnetic particle examinations. However, as shown in Column 6 of Table 3, the cumulative damage analysis showed accumulation of significant damage in the old paddles. The third set of old paddles (OLT3 and ORT3) and the only set of new paddles (NLT1 and NRT1) were predicted to have cracked (predicted blocks is less than 1.0). Since none of the paddles showed any cracking, the fatigue analysis performed is considered to be too conservative.

Therefore, it appears that although the torsional fatigue strength of the new paddles has been increased, as discussed earlier, the fatigue strengths in the weld and other locations such as blade edges and outer frame may be the limiting factors in the fatigue performance of the material feeder as a whole. Since the degree of conservatism in the analysis is unknown, the only way to assess this situation is to gain some field experience with the new paddles. If weld location cracking is experienced in the new paddles, within the design lifetimes, then fatigue strength improvements, such as post weld grinding and shot peening, or both, can be considered.

Conclusions

It was concluded that the long life fatigue strength of the old paddle shafts was about 113 N·m of alternating torsion with the spline section being the critical location. The long life torsional fatigue strength of the new paddle shafts was estimated to be at least 186 N·m. However, the weld regions may be relatively weaker in the new paddles. Since the degree of conservatism in the weld fatigue analysis procedure is not known, it was suggested that the new paddles be field tested, before any fatigue improvement techniques are considered for weld regions.

This case study illustrates the following from an educational point of view. As found in this study, most real-life industrial problems require "solutions" with less than ideal or no input information available, in addition to constrained budget and time limits. Experimental investigations may or may not yield ideally expected results. This forces the engineering analyst to make "reasonable" assumptions, prioritize needs, improvise techniques, and creatively solve the problem.

TABLE 3—Summary of weld location fatigue analysis.

| Specimen Number | Stress, MPa, Combined/Bending | Cycles, Combined/Bending | Predicted Blocks to Failure ^a | Cracked |
|-----------------|-------------------------------|--------------------------|--|---------|
| OLT2 | 121/41 | 23 395/5977 | 1.28–3.65 | No |
| ORT2 | 121/... | 28 187/... | 1.08–2.98 | No |
| OLT3 | 102/41 | 110 186/24 000 | 0.37–1.06 | No |
| ORT3 | 96/36 | 155 286/97 400 | 0.45–1.29 | No |
| OLT4 | 121/41 | 26 840/106 | 1.1–3.2 | No |
| ORT4 | 124/36 | 18 215/15 008 | 1.5–4.3 | No |
| NLT1 | 91/53 | 422 027/415 500 | 0.14–1.07 | No |
| NRT1 | 113/... | 338 693/... | 0.10–0.83 | No |

^aLower bound and mean predictions.

Acknowledgments

This investigation was performed for ACCURATE, INC., in Whitewater, WI, with Mr. Jayant Sharma as the key project engineer. The experimental part of this investigation was performed by DATASYST, INC., in Delafield, WI, with Messrs. Dave Hoisington and Tom Kinzel were the key staff.

APPENDIX A

Torsional Data Analysis

Rosette stain gages mounted on the 1-in. diameter section of the shaft just outside of the splined section were used to monitor strains and evaluate the applied nominal torques. Portable histogram recorders [3] were used to collect the strain histories and process the data using the "rain flow" counting technique. Strain-based cumulative fatigue damage analysis techniques [1,2] were used to evaluate the data.

The four basic equations used for performing the strain based cumulative fatigue damage analysis are as follows

- (1) The Cyclic Stress-Strain Curve

$$\Delta\epsilon/2 = (\Delta\sigma/2)/E + [(\Delta\sigma/2)/K']^{1/n'}$$

- (2) The strain versus Life Curve

$$\Delta\epsilon/2 = (\sigma'_f/E) (2N_f)^b + \epsilon'_f (2N_f)^c$$

- (3) The nominal versus Notch Root Stress-Strain Relationship (Neuber Rule)

$$K_f(\Delta s/2) = [(\Delta\sigma/2)(\Delta\epsilon/2)E]^{1/2}$$

- (4) The Linear Damage Summation Rule

$$D_i = N_i/N_f$$

$$D_{\text{total}} = \sum_{i=1}^n D_i$$

In the above equations, the elastic modulus, E ; the cyclic strength coefficient, K_f ; the cyclic strain hardening exponent, n ; the fatigue strength coefficient, σ'_f ; the fatigue strength exponent, b ; the fatigue ductility coefficient, ϵ'_f ; and the fatigue ductility exponent, c , are the material fatigue properties. These properties were estimated from the known tensile properties of the material using established empirical equations available in the literature [1]. The actual values used in the present analysis are listed in Table 4.

For a given nominal stress, $\Delta s/2$, and a selected value of the fatigue notch factor, K_f , the damage, D_i , corresponding the number of applied cycles, N_i , is calculated by simultaneous solution of the equations shown previously. Typically, these calculations are accomplished through a computer program [2]. Table 5 illustrates a typical cumulative damage calculation for the tested paddle OLT2. The nine levels of torsional amplitudes and corresponding cycles experienced by this paddle are listed in columns 2 and 3, respectively. The absolute and

TABLE 4—*Estimated fatigue properties for shaft material (1018 cold rolled steel).*

| |
|--|
| • Tensile Strength = 627 MPa, measured |
| • Percent reduction of area = 56, measured |
| • Elastic modulus = 206 000 MPa |
| • Fatigue strength coefficient, $\sigma' = 965$ MPa |
| • Fatigue strength exponent, $b = -0.08$ |
| • Fatigue ductility coefficient, $\epsilon'_f = 0.425$ |
| • Fatigue ductility exponent, $c = -0.60$ |
| • Cyclic strength coefficient, $K' = 1083$ MPa |
| • Cyclic strength exponent, $n' = 0.137$ |

percent values of the damages calculated for each of the load levels are also shown. These calculations were repeated for various selected values of K_f until the total damage of unity was obtained. As shown in Table 5, the K_f value for the paddle OLT2 is 1.45. The amplitude that has the maximum percent contribution is chosen as the equivalent single amplitude. In the example shown it is the eighth level with a 69.02% contribution to damage. The corresponding equivalent cycles are obtained by dividing the actual cycles experienced at this amplitude by the contribution fraction. In the present case, it is $16\ 147/0.6902 = 23\ 395$. Table 1 summarizes these results for all the tests.

APPENDIX B

General Outline of BS5400, Part 10

The fatigue life of a welded component is governed by several factors including the material properties, the residual stresses, the inherent flaws, such as undercuts and overlaps, and other stress raisers due to geometrical discontinuities of the weld. Taking all of these factors into consideration, the British Standard BS5400, Part 10 (1980), Code of Practice for

TABLE 5—*Typical torsional fatigue data analysis for specimen OLT2.*

| Component Factor, $K_f = 1.45$ | | | | |
|--------------------------------|--|------------------|---------------------|---------------------------------|
| Event | Equivalent Uniaxial Nominal Stress, MPa, $s/2$ | Cycles, N_i | Damage N_i/N_f | Contribution to Damage, % |
| 1 | 170.4 | 46 | 5.2E-6 | 0.00 |
| 2 | 191.7 | 879 | 3.8E-4 | 0.04 |
| 3 | 213.0 | 176 | 2.3E-4 | 0.02 |
| 4 | 234.3 | 2 216 | 7.7E-3 | 0.77 |
| 5 | 255.6 | 407 | 3.1E-3 | 0.31 |
| 6 | 276.9 | 11 551 | 1.7E-1 | 17.23 |
| 7 | 298.3 | 4 697 | 1.2E-1 | 12.47 |
| 8 | 319.5 | 16 147 | 6.9E-1 | 69.02 |
| 9 | 340.9 | 22 | 1.4E-1 | 0.14 |
| Totals | | | 1.0 | 100.00 |

NOTE—equivalent nominal stress = 319.5 MPa (Event 8); equivalent torque amplitude = 315.7 N·m and equivalent cycles = $16\ 147/0.69 = 23\ 395$.

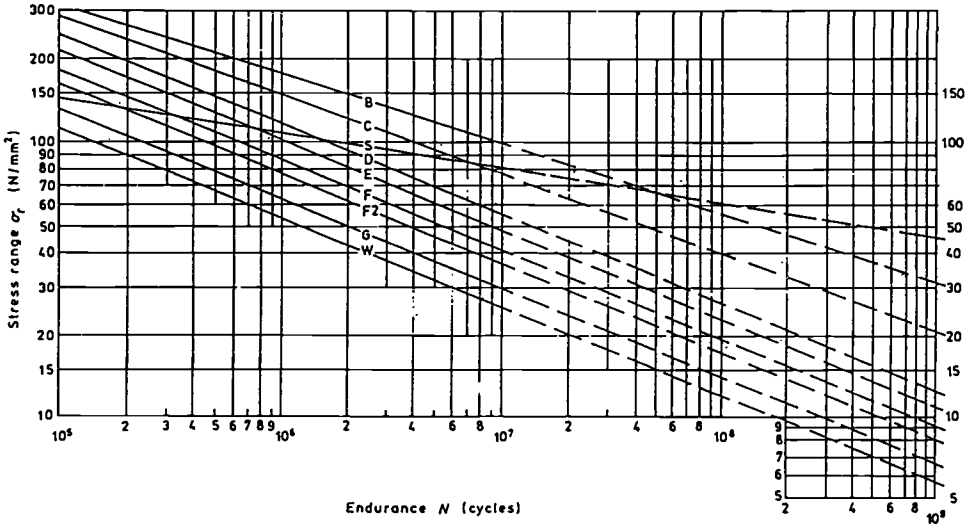


FIG. 4—Fatigue design curves, as per British Standard BS5400.

Fatigue: Steel Concrete and Concrete and Composite Bridges,” has developed a family of fatigue design curves (Fig. 4) for various weld configurations classified with letter codes. These curves are plots of applied stress range versus cycles-to-failure at selected levels of probability. The stresses to be used for the type of welds considered in this study are maximum principal stresses. For histories comprised of multiple amplitudes, a linear damage summation procedure is used.

The welds in old paddles were classified as F2 welds and those in the new paddles as Class E to account for reportedly better welding practice in the new paddles. For each paddle, two sets of fatigue curves representing mean and mean minus two standard deviations (essentially a lower bound curve) were used to predict lower bound and average blocks to failure, as shown in Table 3.

References

[1] Society of Automotive Engineers, *Fatigue Design Handbook*, AE-10, Society of Automotive Engineers, Warrendale, PA, 1988.

[2] Jhansale, H. R. and McCann, D. R. “Fatigue Analysis Techniques for Vintage Steam Turbine/Generator Components,” *Advances in Fatigue Lifetime Predictive Techniques*, ASTM STP 1122, M. R. Mitchell and R. W. Landgraf, Eds., American Society for Testing and Materials, Philadelphia, 1992, pp. 474-489.

[3] Socie, D., “A Field Recording System with Applications to Fatigue Analysis,” Technical Report 132, Electrogenal Corporation, Minneapolis, MN, 1977.

Fatigue Cracking of a Welded Roll Used in a Paper-Mill Roll Press

REFERENCE: Zapata, J. E. and Anderson, S. C., “**Fatigue Cracking of a Welded Roll Used in a Paper-Mill Roll Press,**” *Case Studies for Fatigue Education, ASTM STP 1250*, Ralph I. Stephens, Ed., American Society for Testing and Materials, Philadelphia, 1994, pp. 77–85.

ABSTRACT: A 1-m fatigue crack was found after approximately four months of service in a welded steel roll that had an intended life of 20 years. The roll was part of a roll press used in a paper mill. The fatigue crack originated in a surface discontinuity and propagated parallel to the girth weld. Metallographic examination revealed the discontinuity to have been produced by entrapped welding slag. The discontinuity was 5.5-mm deep by 41-mm long and was small with respect to the overall size of the roll (8.6-m long, 1.5-m in diameter, with a 110-mm wall thickness). Furthermore, the nominal bending stresses in the part were found to be far below the endurance limit of the material. A fatigue crack propagation study, based on Paris law fatigue crack growth, was performed to determine if the stress level in the roll was sufficient to propagate the fatigue crack from the initial flaw size in the transpired time. Further studies were performed to investigate the effect of different flaw sizes and loading conditions on the life of the roll.

KEYWORDS fatigue, weld, defect, slag, paper mill, roll

A paper mill roll, which was expected to function for at least 20 years, developed a large crack after only four months of service. This fracture caused some concern as other rolls were operating in similar circumstances. Of significant importance was that the operational loads produced stresses that were substantially below the endurance limit of the material.

Background

Operation

The paper mill roll in question was the bottom roll of a two-roll press used in the production of paper. The function of the roll press was to reduce the water content of pulp as an initial step in transforming pulp to paper. The pulp was carried on a conveyor between the two rolls of the roll press. Linear actuators were in place above the top roll that served to produce a distributed load on the rolls. The top roll produced a distributed load on the pulp of 350 N/mm. This load was supported entirely by the bottom roll, as illustrated in Fig. 1.

The bottom roll, in turn, was supported by two journal bearings with the center-to-center distance being 9 800 mm. It rotated at 150 rpm and had been in continuous operation for about four months from the time it was installed until, the 1-m crack was detected.

¹ Senior mechanical engineer and company president, respectively, Anderson & Associates, Inc., 919 FM 1959, Houston, TX 77034-5425.

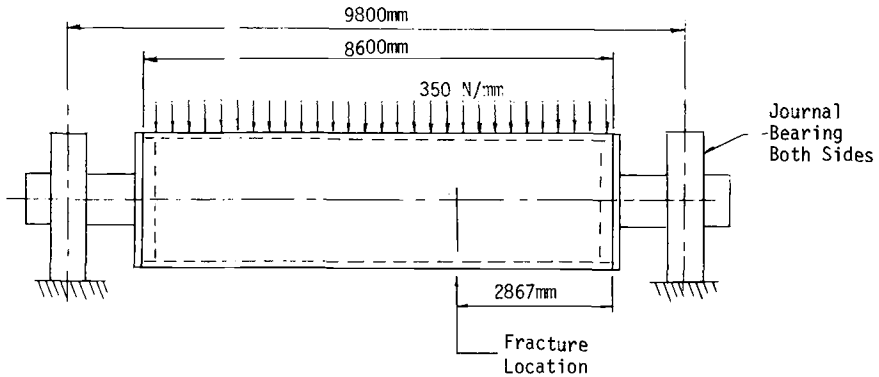


FIG. 1—Schematic of the bottom roll in the papermill roll press. The distributed load of 350 N/mm is shown to be acting over 8600 mm. The entire assembly is supported by journal bearings.

Fabrication

The roll was fabricated by taking three mild steel plates, rolling them to round, and seam welding them to produce three cylinders of equal size. The three cylindrical sections were then joined by two girth welds to form the roll. After welding, the entire roll was stress-relieved by heating to 580°C. The roll was then inspected and the surface machined. A rubber coating was applied to the outside diameter surface to provide a larger contact area with the pulp. The final length of the cylinder was 8600 mm, the diameter 1500 mm, and the wall thickness 110 mm. The roll mass, not including heads and journals, was 32 200 kg.

Examination

The roll was taken out of service and the rubber coating removed for examination of the fracture. The crack was circumferential and was in the approximate location of one of the girth welds. The fracture was removed by torch cutting about 200 mm away from the crack surfaces. A uniform layer of rust was visible on the entire fracture surface, which was smooth. The fracture origin area was on the outside diameter surface and was surrounded by faint radial markings. The fracture origin area and areas close to the final stages of the fracture were removed and cleaned electrolytically in a sodium-cyanide solution [1]. The rust came off easily and in a uniform fashion. No excessive corrosion or mechanical damage was found in the origin area. The origin site appeared to have occurred at the surface where a peculiar mark was present, shown in Fig. 2. This mark was approximately 41-mm long in the circumferential direction, 5.5-mm wide in the radial direction, and 1-mm deep in the longitudinal direction. The mark was restricted to one of the fracture surfaces; the mating fracture surface was smooth.

The origin area, crack-termination area, as well as intermediate areas were examined in the scanning electron microscope (SEM). Although macroscopically the fracture faces were free from mechanical damage, at the microscopic level no fracture mode was discernible. Evidence of mechanical damage was visible and corrosion pits covered the surface. A difference, however, was discernible between the surface of the fracture and the topography at the origin site. As shown in Fig. 3, the origin site has a smoother surface than the fracture. A clear delineation of the boundary between the two is also visible.

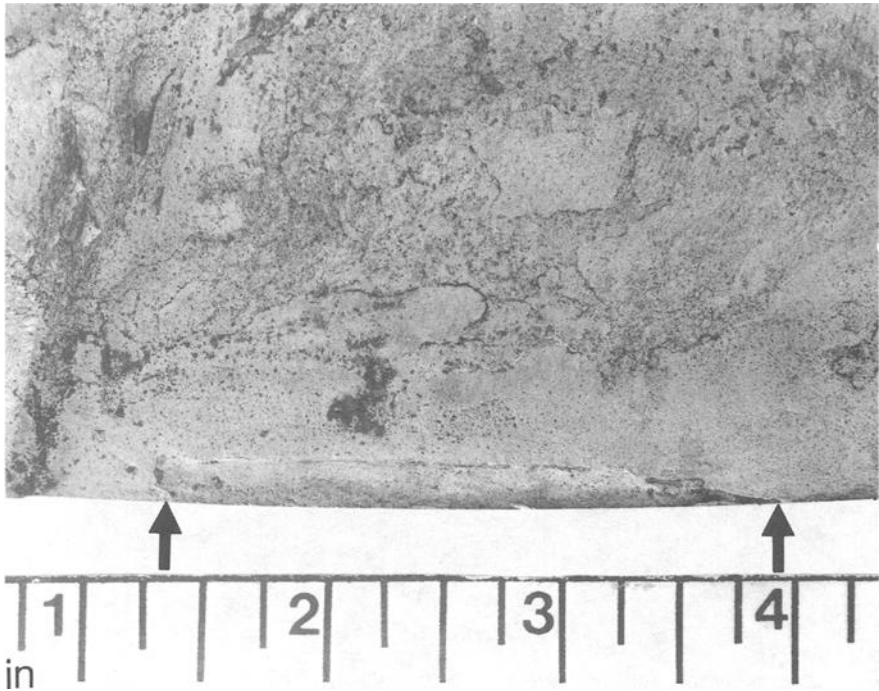


FIG. 2—The pre-existing flaw at the fracture origin is bounded by the arrows. Faint radial lines can be seen surrounding the flaw. The scale is in inches (1 in. = 2.54 cm).

A cross-section was taken through both fracture faces at the origin site showing the entire wall thickness. The cross section was surface ground and etched in 10% Nital. The fracture could be seen to have originated at a discontinuity on the outside diameter surface. This discontinuity was at the edge of the girth weld. The crack extended from this discontinuity across the wall thickness perpendicular to the inside and outside diameter surfaces (Fig. 4).

A smaller cross-section containing the discontinuity was removed from the through-wall cross section previously discussed. The sample was mounted, ground, polished, and etched in 3% Nital. On one side of the discontinuity the girth weld acicular microstructure was readily observed. On the other side of the weld the microstructure was consistent with a hot rolled low-carbon steel. No coarse grain heat affected zone was evident on either side of the discontinuity. Elsewhere, surrounding the weld, heat-affected zones were clearly discernible (Figs. 5 and 6).

Hardness tests showed that the weld and the heat-affected zone were harder than the base metal. The base metal hardness was approximately 66 HRB, the weld metal ranged from 85 to 90 HRB, and the heat-affected zone ranged from 83 to 87 HRB.

Student Questions

- What is a possible explanation for the presence of the discontinuity at the fracture origin?

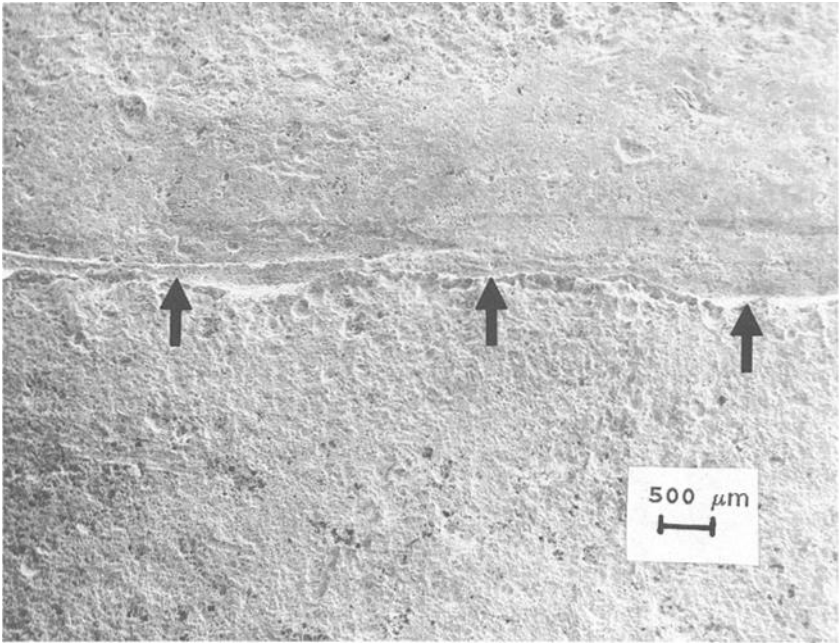


FIG. 3—Fractograph showing the boundary between the preexisting flaw, top, and the fatigue crack, bottom. The boundary is indicated by the arrows.

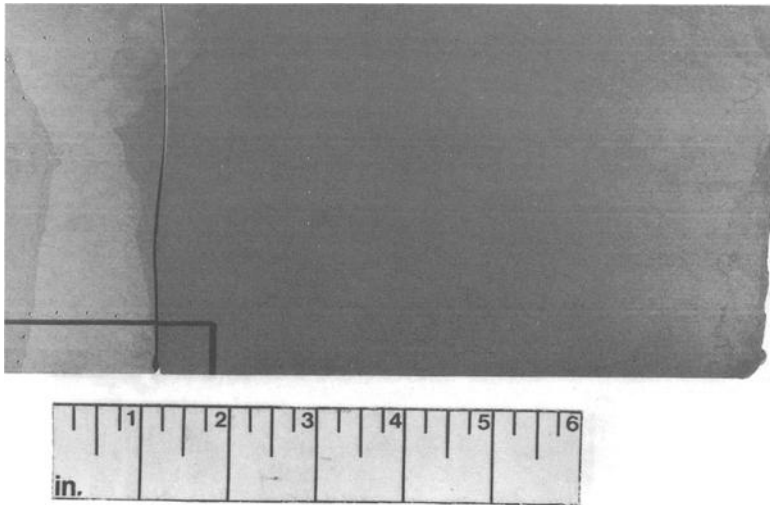


FIG. 4—Photomacrograph of a cross-section taken through the fatigue fracture and the initial flaw. The area to be mounted is marked in black. The scale is in inches (1 in. = 2.54 cm).

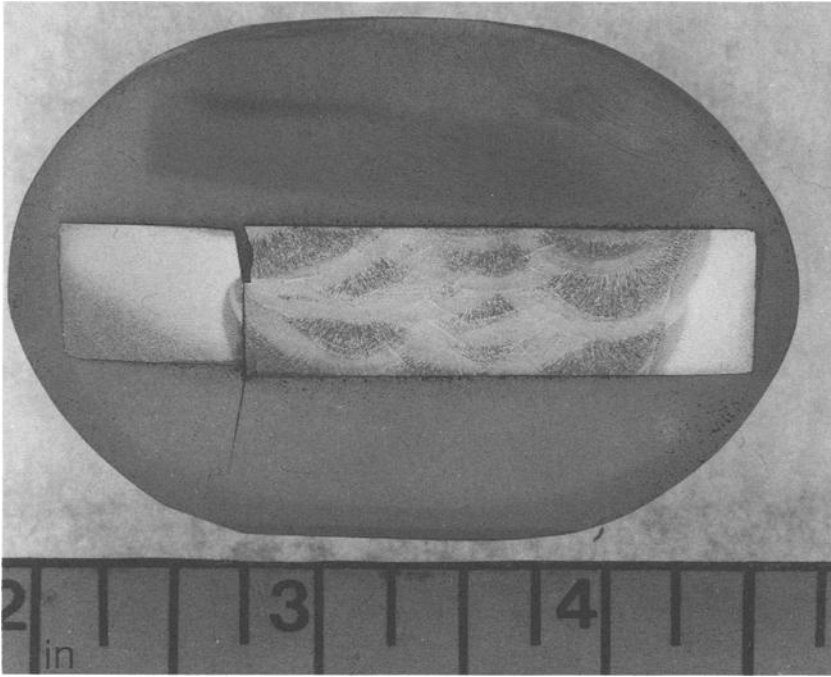


FIG. 5—Photomicrograph of the initial flaw and the fatigue crack. The scale is in inches (1 in. = 2.54 cm).

- What is the fracture mechanism? How can this be substantiated?
- What was the nominal stress at the origin site before the crack initiated?
- How does the amplitude of the reverse bending stress in the roll compare to published endurance limits for low-carbon steel?
- How can a fatigue crack start and grow under such a low amplitude of cyclic stress? How can this be substantiated?
- What are possible remedies to the cracking situation? What are their limitations?

Analysis

Examination of Fig. 6, the photomicrograph taken through the fracture origin, gives some insight into the presence of the discontinuity. The columnar weld microstructure is clearly seen on one side of the discontinuity whereas the other side shows an unaffected base metal. Furthermore, the base metal side tapers slightly with respect to the normal to the outer diameter surface of the roll. This taper is probably the original bevel in the plate present to facilitate welding. A foreign object must have been present to prevent the weld metal from contacting the base metal in that area. Additionally, this object must have been an insulator so as to shield the base metal from heat of welding, thereby preventing a heat-affected zone adjacent to the discontinuity.

Macroscopically, the fracture had all the characteristic fatigue features. The crack was flat and perpendicular to the principal stress direction and radial features surrounded the initiation area in a semicircular fashion. The smoothness and lack of excessive corrosion pointed to

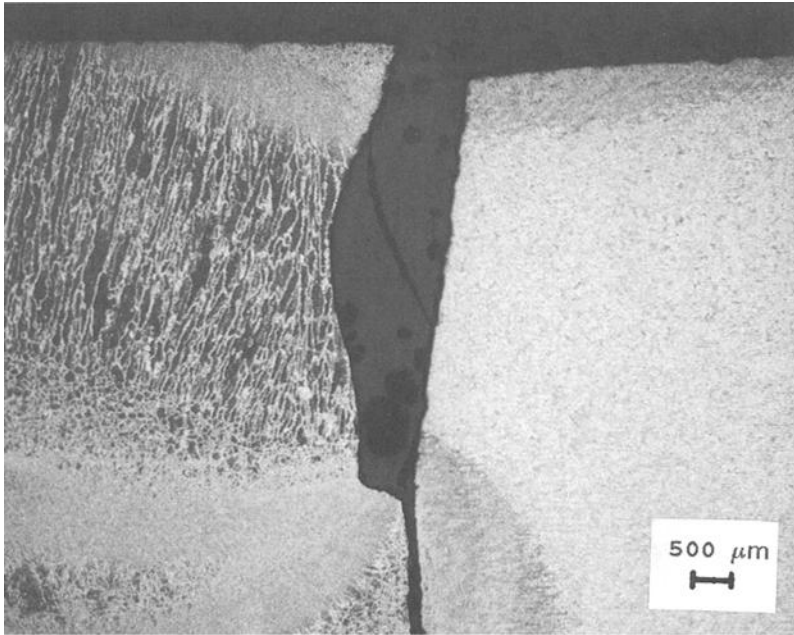


FIG. 6—Photomicrograph of the initial flaw. The columnar microstructure of the weld is at the left. The base metal, right, was not affected by the heat of welding, indicating that an insulator was present.

purely mechanical fatigue. The relative ease with which the rust was removed suggested that the corrosion had not significantly attacked the surface. Furthermore, since the corrosion product came off in a uniform fashion, the entire crack was probably exposed to the corrosive environment for roughly the same amount of time. It was concluded that, at least for the initial stages of the fatigue fracture, the environment did not contribute to the fracture because it was isolated by the rubber coating.

Examination of the pre-existing flaw showed that it was long, slender, and parallel to the welding direction. The flaw was not planar but exhibited some thickness. It was confined to the weld metal and, as shown in the metallographic examination, it was an insulator. Entrapped welding would clearly fit the description of such a defect.

At the microscopic level, no fracture features, like striations, were observable under SEM examination. It is not uncommon for these to be erased in parts undergoing reverse bending. Additionally, the crack faces were exposed to a slightly corrosive environment that would serve to erase the microscopic fracture features.

The nominal stress in the roll was calculated by assuming the roll to be a simply supported beam under a distributed load. The journal bearings were assumed to be incapable of supporting a bending load, thus the justification for simple supports. The distributed load was taken from the operational parameters as 350 N/mm that acted over the roll length of 8600 mm. The section modulus was easily found from the dimensions to be 0.156 m^3 . The bending moment was primarily due to two factors, the distributed press load and the weight of the bottom roll. The total weight of the roll, including the heads and journals was unknown, but it was assumed that the same distributed load produced by the cylindrical section was constant for the bearing-to-bearing distance. This was a reasonable assumption since the mass of the roll was greatest close to the bearing, and the distributed press load only acted on the

cylindrical section. The bending moment at the fracture was therefore calculated to be 4.18 MN m. The static tension stress was in turn found to be 26.8 MPa on the outside diameter surface at the fracture plane at the bottom of the roll.

A quick survey of the literature shows endurance limits for low-carbon steels to be much higher than the fluctuating stress in the roll. Endurance limit values were found to range from about 90 MPa up to 200 MPa for various conditions of welds and base metal [2-4].

The low nominal stress at the fracture compared to the reported endurance limits raised questions about the effect of the initial flaw size on the life of the roll. A fatigue crack propagation study was therefore undertaken to determine if such an initial flaw size could account for a large through-wall fatigue crack in the time the roll was in service. The analysis assumed the initial flaw was a sharp crack instead of a three dimensional discontinuity detected. The Paris equation for fatigue crack propagation [5] was employed.

$$da/dN = A (\Delta K)^m$$

where

- a = the crack length parameter, m;
- N = the number of cycles;
- K = the stress intensity range, MPa \sqrt{m} ;
- A = a material constant; and
- m = a material constant.

Rolfe and Barsom [6] report material constants of $A = 3.6(10^{-10})$ and $m = 3.0$ for K in ksi $\sqrt{in.}$ and a in inches for steels with a ferrite/pearlite microstructure. The material constants become $A = 6.9(10^{-12})$ and $m = 3.0$ for K in Mpa \sqrt{m} and the crack length a in meters. The equation for the stress intensity ΔK used was [7]

$$\Delta K = \frac{\Delta \sigma \sqrt{a}}{Q}$$

where

- σ = the tensile stress amplitude, MPa;
- Q = crack shape parameter; and
- a = the crack length parameter, m.

The tensile stress amplitude, $\Delta \sigma$, was assumed to act only due to the loading and did not consider any effects of residual stress.

The crack growth study using the operational loads found that the crack growth rate was insufficient to account for the fatigue crack encountered. It was judged, however, that since the failure occurred next to a weld, the effects of the residual stress could not be neglected. Although a stress relief had been performed on the part, it is generally assumed that some residual stresses remain. In the absence of actual data, it was assumed that the residual stresses served to raise the alternating stresses so that the entire range of stress fluctuation due to bending was tensile. The net effect was to double the amplitude of the stress from 26.8 to 53.6 MPa.

With the stress amplitude doubled by the presence of tensile residual stresses, the Paris equation adequately predicted the crack propagation. Figure 7 shows fatigue crack propagation curves considering both alternating stress situations and the approximate location of the actual fracture. It should be noted that the constants A and m used in the Paris equation

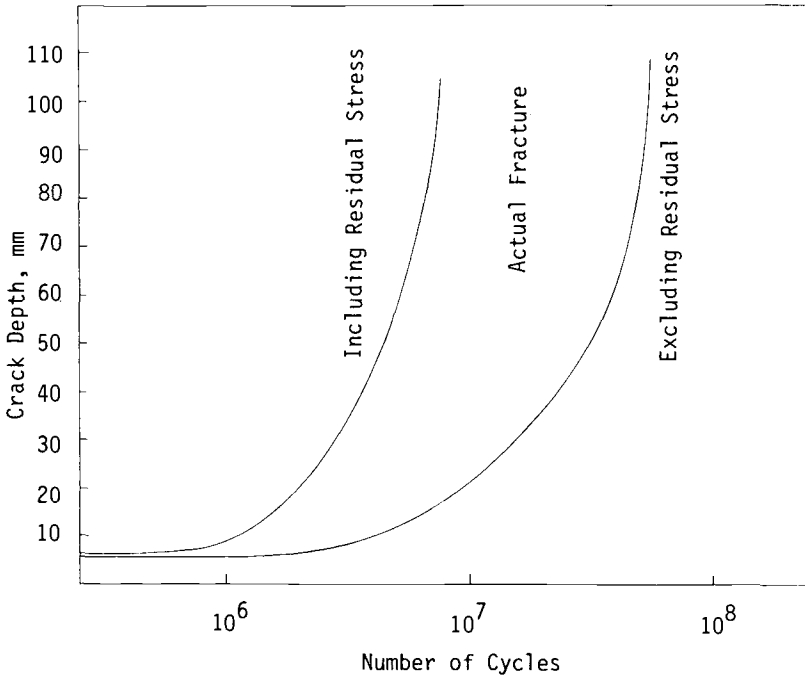


FIG. 7—Crack depth versus the number of cycles. The predictions were calculated with and without considering a tensile residual stress from welding. The initial flaw depth was taken as 5.5 mm.

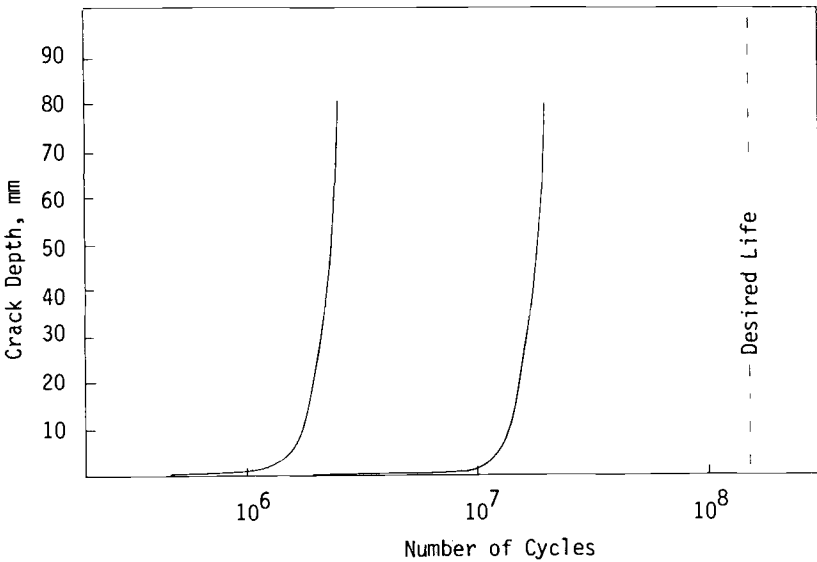


FIG. 8—Crack depth versus the number of cycles. The predictions were calculated with and without considering a tensile residual stress from welding. The initial flaw depth was taken as 0.25 mm. The desired life was $1.5(10^9)$ cycles.

predict conservative estimates fatigue crack propagation and actual fatigue cracking should lie to the right of the curves.

After ascertaining that the operational stresses were sufficient to cause the fatigue fracture in the time expended, the next logical step was to determine what size of a flaw could be tolerated for the roll to survive the desired life of 20 years. If a strict Paris crack growth model was employed, the initial flaw size would have to be intolerably small. Figure 8 shows two curves for an initial flaw size of 0.25 mm under the two stress situations as compared to the desired life of $1.5 (10^9)$ cycles. It can be seen that this poses an unrealistic situation as it is not possible to detect an initial flaw of that size. Using a strict Paris equation, the desired life could not be designed for practically.

A viable alternative would be to consider the threshold stress intensity factor for fatigue crack propagation. The flaw in this case, if assumed to be planar, would have given rise to a stress intensity of $6.59 \text{ MPa } \sqrt{\text{m}}$. A flaw of similar length but only 2.5-mm in depth would have produced a stress intensity of $4.67 \text{ MPa } \sqrt{\text{m}}$ that is below the reported threshold stress-intensity factor for fatigue crack propagation in a similar material [8]. Using threshold stress-intensity factors for fatigue can allow for larger flaws than would otherwise be ruled out when using a strict Paris equation.

References

- [1] Dahlberg, E. P. and Zipp, R. D., "Clean Breaks and SEM," Chemteck, Washington, DC, Feb. 1985, pp. 118-122.
- [2] Boyer, H. E., *Atlas of Fatigue Curves*, American Society for Metals, Metals Park, OH.
- [3] Bosch, R., *Automotive Handbook*, 2nd English Edition, Society of Automotive Engineers (SAE) Inc., Warrendale, PA, Delta Press Limited, 1986, p. 142.
- [4] Campbell, J. E., Gerberich, W. W., and Underwood, J. H., *Application of Fracture Mechanics for Selection of Metallic Structural Material*, American Society for Metals, Metals Park, OH.
- [5] Paris, P. C. and Erdogan, F., "A Critical Analysis of Crack Propagation Laws," *Journal of Basic Engineering*, Vol. 85, 1960, pp. 528-534.
- [6] Rolfe, S. T. and Barsom, J. M., *Fracture and Fatigue Control in Structures—Applications of Fracture Mechanics*, Prentice-Hall, Englewood Cliffs, NJ, 1977, p. 239.
- [7] British Standards Institution, "Guidance on Some Methods for the Derivation of Acceptance Levels for Defects in Fusion Welded Joints," PD6493:1980, British Standards Institution, March 1980.
- [8] Taira, S., Tanaka, K., and Hoshina, M., "Grain-Size Effect on Crack Nucleation and Growth in Long-Life Fatigue of Low Carbon Steel," *Fatigue Mechanisms, ASTM STP 675*, Jeffrey T. Fong, Ed., American Society for Testing and Materials, Philadelphia, 1979, pp. 135-162.

Welded Pipeline Fatigue Analysis

REFERENCE: Socie, D. and Segan, E., “**Welded Pipeline Fatigue Analysis,**” *Case Studies for Fatigue Education, ASTM STP 1250*, Ralph I. Stephens, Ed., American Society for Testing and Materials, Philadelphia, 1994, pp. 86–100.

ABSTRACT: This case study shows the importance of considering welding flaws in pipelines that may be subjected to cyclic pressures. The case study will demonstrate that the ASTM specifications currently used to purchase welded pipe do not ensure adequate safety for cyclic loading.

A piping system was installed using Specification for Seamless and Welded Austenitic Stainless Steel Pipe (ASTM A 312) welded pipe. Longitudinal welds are made without the addition of filler metal by resistance welding from both sides of the pipe wall. This process frequently results in lack of fusion (LOF) flaws in the pipe. Hydrostatic testing used to demonstrate conformance with ASTM standards does not detect flaws that will grow in service.

An example of a failed pipeline system is presented. Pressure loading histories were obtained during normal operation of the piping system. Crack growth materials data were available for a fracture mechanics analysis of the system. A discussion of the ASTM standards as they relate to this problem are included.

KEYWORDS: fatigue failures, design codes, lack of fusion (LOF) flaws

Background

There have been several premature failures of stainless steel fueling systems designed in accordance with the American Society for Mechanical Engineers/American National Standards Institute (ASME/ANSI) B31.3 Piping Code for Chemical Plant and Petroleum Refinery Piping. These failures pose significant safety and environmental risks. A fueling system is an underground piping system that is designed to pump fuel from above ground storage tanks to fueling trucks that control the flow of fuel to an aircraft. Failure consists of a ruptured pipe that allows fuel to leak into the surrounding soil. In addition to the environmental damage, fuel in some cases has reached the surface and could have resulted in a serious fire. Failures at the pump house have not yet occurred but could be catastrophic as the volatile fuel comes into contact with electric motors and switch gear. An analysis of the fuel system failures was made to identify the cause or causes of the failure and to make recommendations for new and existing systems. The following questions were addressed:

- Why did the fuel lines fail?
- Are more failures likely?
- Did the failed pipes meet specifications?
- Is the design adequate?
- What is the appropriate course of action for operation of existing systems and design of future systems?

¹ University of Illinois at Urbana-Champaign, Mechanical Engineering Department, Urbana, IL 61801.

² U.S. Army, Construction Engineering Research Laboratory, Champaign, IL 61826.

In any failure analysis of a mechanical system there is always a question as to whether the failure is due to a material or manufacturing flaw, overload in service, change in function or intended purpose, or a design oversight. All of these factors must be considered and the most likely cause determined. Frequently, failures are a result of a combination of causes. Inevitably, responsibility for causing and repairing the failure will be established. In addition to the technical questions listed above, the answer to "Who caused the problem?" is often determined from the technical evaluation through litigation. With this in mind, it is important to determine the chain of events that led to the failure.

Why Did the Fuel Lines Fail?

An 8-ft section of 16-in. diameter ASTM A 312 stainless steel schedule 10 pipe (from ASTM Specification for Seamless and Welded Austenitic Stainless Steel Pipe) that leaked in service was removed for testing and analysis. Before excavating the failed pipe section, the entire fueling system was drained and cleaned of residual fuel. A spark from the repair operation could have ignited residual fuel and extreme care was taken while working around the fueling systems. Fortunately, this particular failure occurred on the side of a taxiway. The piping system is buried 6 ft into the ground. Fuel leaked into the ground, rose to the surface, and was detected in the grass. Had the pipe rupture occurred underneath the reinforced concrete runway, it would have been difficult to accurately locate the even more expensive to repair. A schematic illustration of the pipe is given in Fig 1. The pipe was fabricated from a plate that was rolled into a cylinder and resistance welded along the seam. There was a visible longitudinal crack in the weld on the outside of the pipe approximately 6-in. long. The owner of the system claimed that the failure was a result of defective pipe installed by the contractor who installed the system. Not surprisingly, the contractor claimed that the failure was the result of an overload due to improper usage of the system by the owner. Each side can often find a consultant to support their point of view. In this case, an independent consultant was selected to determine the failure origin. It was essential to consider all possible causes and not act as a referee between opposing viewpoints.

The cross section of the pipe was measured to determine if the failure was the result of an overload. A transient pressure could have been produced by the sudden closure of a valve and the resulting pressure could have burst the pipe. Pressure in the system could also have exceeded the design pressure due to some mechanical malfunction in the pump house. Measurements of the pipe shape did not show any indication that the pipe was plastically deformed during failure. The ductile stainless steel pipe would have bulged outward if excessive pressure caused the failure. Radiography showed that a crack-like flaw extended well beyond the visible surface crack. These observations lead to the preliminary conclusion that an overload was not responsible for the failure. The pipe was cut into small sections to examine the crack-like flaw.

A section of pipe 32-in. long and 6-in. wide containing the weld was removed from the pipe for detailed metallurgical examination. The pipe was transversely sectioned at various locations along the length. Figure 2 shows the fracture surface that was revealed during sectioning. Three zones are shown in Fig. 2: lack of fusion, fatigue crack growth, and final fracture. Fatigue cracks that have not yet grown to the outside surface were also observed in many of the other transverse sections. They were etched to show the welds with a typical result, shown in Fig. 3. Arrows indicate the original position of the seam in the pipe. In a good weld, the welds are located on the centerline of the seam. Both inside and outside welds are located off center in this section. The outside weld (top of Fig. 3) shows evidence of a growing fatigue crack. The inside weld completely misses the weld seam and the outside weld does not penetrate to the center of the plate. Figure 4 shows a similar example. Here

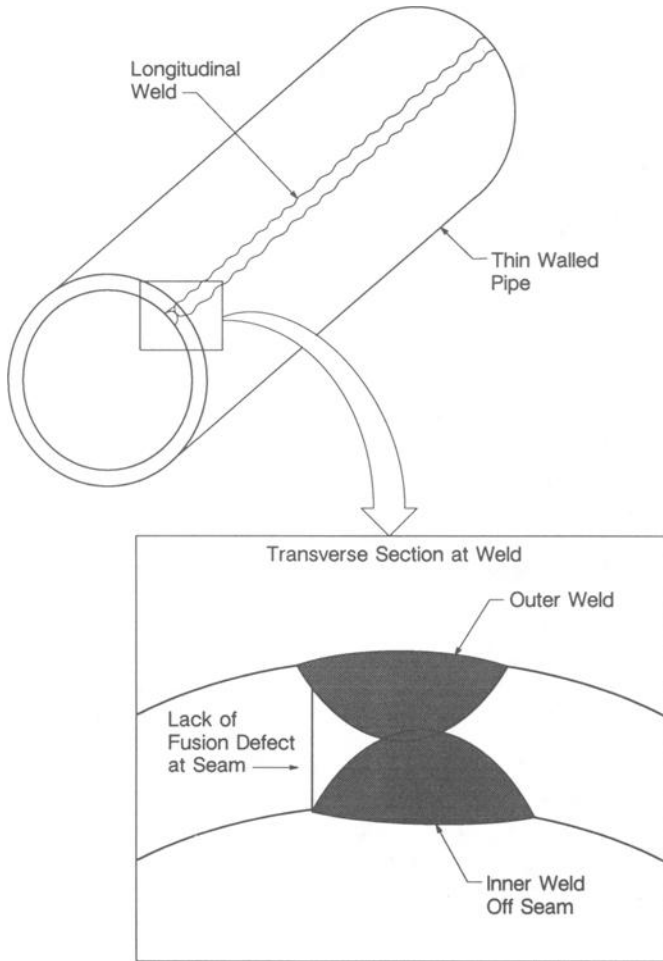


FIG. 1—Pipe illustration.

the inside weld is off center but the outside weld penetrates to the center of the plate. This results in a smaller initial flaw size than the one shown in Fig. 3. A fatigue crack has not yet formed. These types of flaws would not be found during a visual inspection of the outside of the pipe. Pipes are purchased in 40-ft lengths so that it would also be difficult to find them on the inside as well. These flaws could have been found during an ultrasonic or radiographic inspection of the pipe. Ironically, the field-butt welds where two pipes are joined were radiographed. There were no requirements for radiographing the factory welds that failed in service. Internal LOFs (lack of fusion) that were not visible from either surface were also found and are shown in Fig. 5. This type of flaw is very difficult to find with either radiography or ultrasonic inspection techniques. Both techniques require an air gap for good resolution. All of the transverse sections near the failure crack show LOFs that extend approximately one-half to two-thirds of the wall thickness.

Operating pressures of the system were monitored for five weeks to determine the distribution of operating pressures during normal operation of the fueling system. These pressures

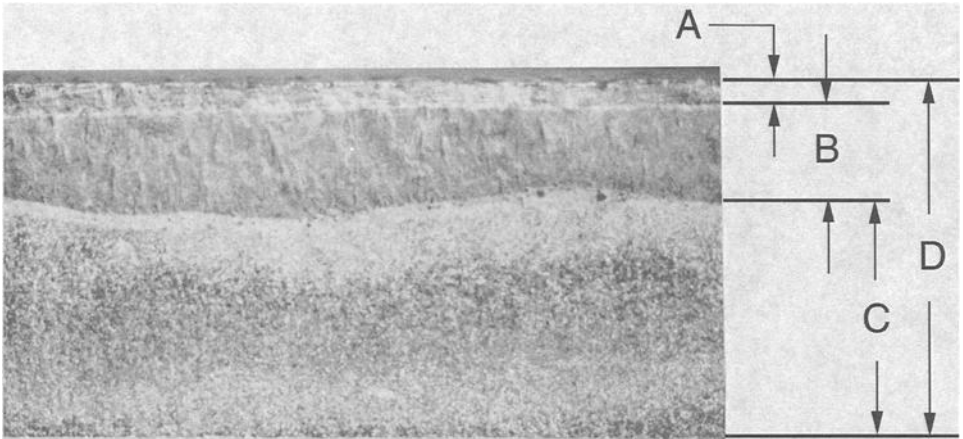


FIG. 2—Fracture surface showing: (a) fracture zone (0.011 in.; 0.028 cm), (b) fatigue zone (0.045 in.; 0.114 cm), (c) lack of fusion zone (0.110 in.; 0.280 cm), and (d) pipe thickness (0.165 in.; 0.420 cm).

were measured at the point of failure after the failed pipe was replaced. A histogram of the pressures is given in Table 1. Data have been normalized to occurrences per year. Rainflow cycle counting was used to determine the ranges. These measurements were used for a fatigue analysis of the piping system. Pressures were measured with a pressure transducer and recorded with appropriate battery-powered long-term data acquisition equipment. Figure 6 shows the pressure for a 2 h period when two aircraft were being fueled. Multiple pressure

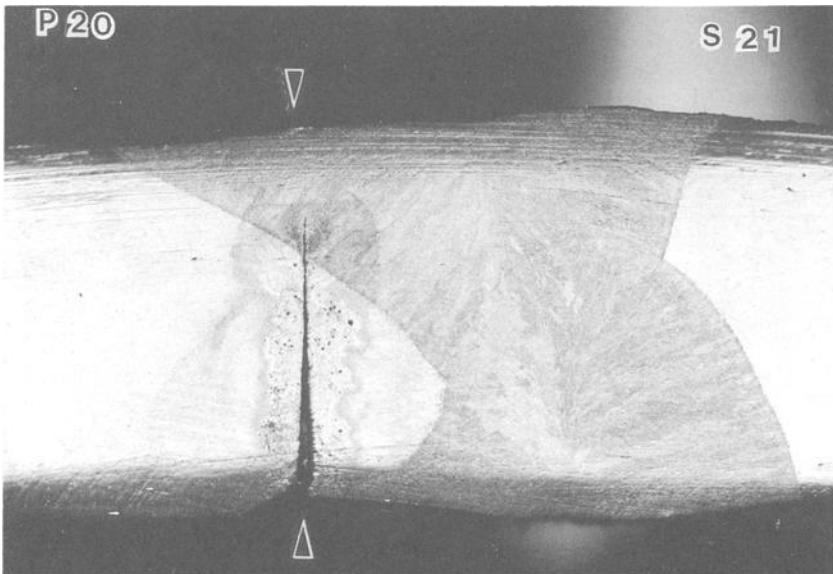


FIG. 3—Off center welds.

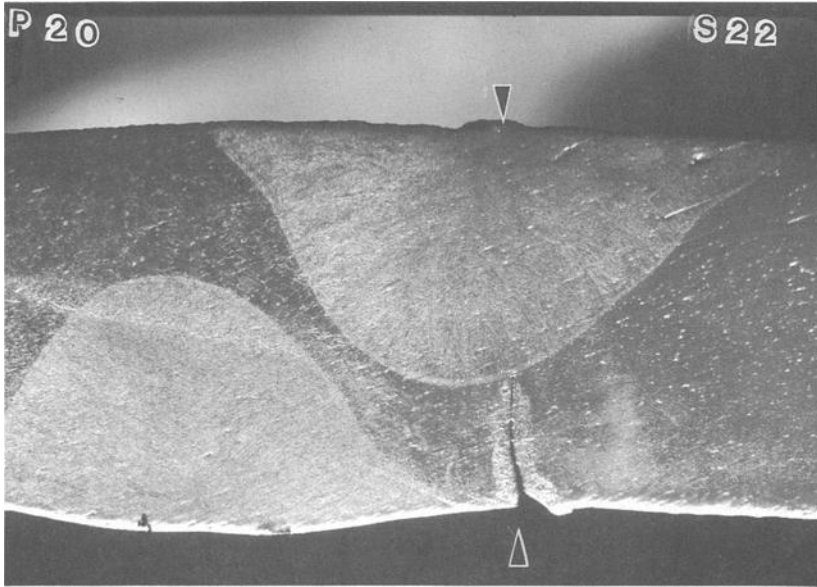


FIG. 4—Off center inside weld.

drops to near zero were observed as the valves were opened and pressure increases were observed when the valves were closed. Several pressure cycles were observed for each aircraft fueling. Test data showed that the maximum operating pressure never exceeded 250 psi (1724 kPa), which was within the design pressure of 275 psi (1896 kPa) for this system. Similar measurements made on another fueling system confirmed that the measured pressures were typical of normal service usage.

A simple limit load calculation was used to make an estimate of the final fracture zone, shown in Fig. 2. Readers unfamiliar with these calculations and assumptions will find an excellent review in Chapter 2 of Ref 1. Stainless steel has a high ductility and is plastically deformed in the net section before failure. As a result, plane strain fracture toughness calculations were not appropriate. Hoop stress, σ_{hoop} , in the uncracked ligament could have been estimated from the stress calculated with thin-walled tube assumptions.

$$\sigma_{\text{hoop}} = \frac{Pr}{t - a} \quad (1)$$

Operating pressure in the pipe was denoted P (250 psi; 1724 kPa), pipe wall thickness t (0.165 in.; 0.419 cm), pipe radius r (8 in.; 20.32 cm), and flaw size, a . The maximum flow size was estimated from a simple lower bound limit-load calculation by substituting the flow stress σ_{flow} , for the hoop stress and treating the pipe as a plate.

$$\sigma_{\text{flow}} = \frac{\sigma_{\text{yield}} + \sigma_{\text{ultimate}}}{2} \quad (2)$$

Test reports from the pipe manufacturer showed that the stainless steel piping had tensile strength varying from 81.2 to 94.2 ksi (559.85 to 649.49 MPa), yield strengths varying from

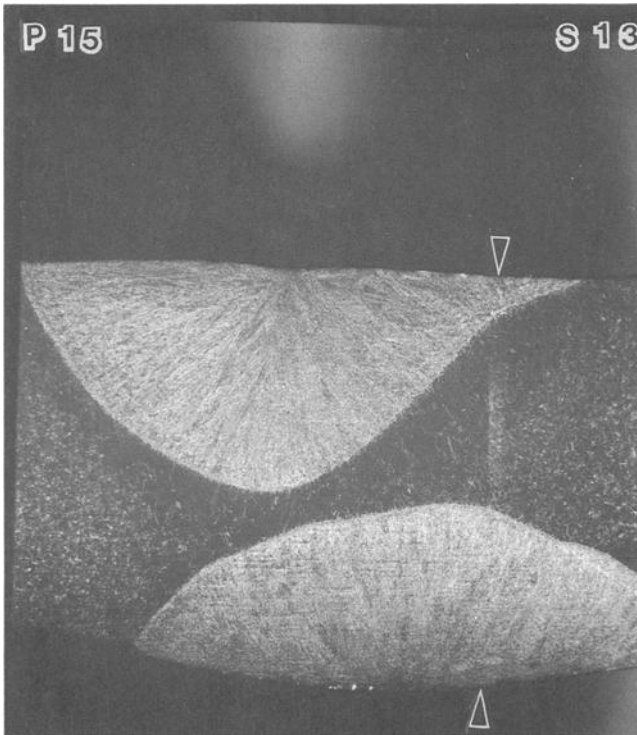


FIG. 5—Internal lack of fusion (LOF).

33.8 to 54.6 ksi (233.04 to 376.45 MPa), and elongation varying from 31.3 to 63%. The resulting average flow stress was 66 ksi (455.05 MPa). An estimated final crack size of 0.135 in. (0.34 cm) and uncracked ligament of 0.030 in. (0.008 cm) was calculated. This compares to the uncracked ligament of 0.011 in. (0.03 cm), shown in Fig. 2. As expected, a simple lower bound solution overestimates the actual uncracked ligament size. Bending stiffness in

TABLE 1—Measured pressure ranges.

| Pressure Range, psi ^a | Occurrences per year |
|----------------------------------|----------------------|
| 260 | 35 |
| 240 | 17 |
| 220 | 122 |
| 200 | 1502 |
| 180 | 716 |
| 160 | 506 |
| 140 | 506 |
| 120 | 646 |
| 100 | 1380 |
| 80 | 3807 |
| 60 | 5396 |

^a 1 psi = 6.8948 kPa.

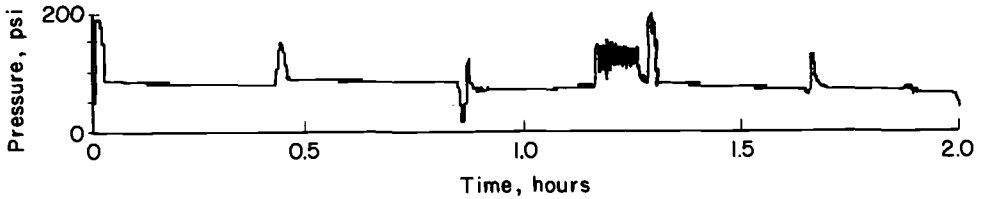


FIG. 6—Pressure in the pipe during an aircraft fueling operation.

the longitudinal direction was ignored in the simple calculation. This calculation clearly shows that only a small fraction of the pipe wall is needed to support the normal operating pressure in the fueling system. It also provides further verification of the conclusion that the pipe was not overloaded in service. An uncracked pipe would require more than six times the normal operating pressure to cause a burst or overload failure.

Fracture mechanics was used to make an estimate of the time required for the LOF to grow to a critical size for failure.

$$N_f = \int_{a_o}^{a_f} \frac{da}{C\Delta K^m} \quad (3)$$

The cyclic stress intensity factor, ΔK , for longitudinal cracks in a pipe subjected to internal pressure is available from the literature [2]. Materials data for crack growth (C and m) in stainless steel are also available [3]. Initial, a_o , and final, a_f , crack sizes can be selected from the preceding figures and calculations. Numerical integration using the techniques outlined in Ref 4 were used to obtain estimates of the fatigue lives given in Fig. 7 for various initial flaw sizes. These estimates were based on mean material data and should be interpreted as 50% probability of failure and not design lives. They compared well with the observed failure time of one year.

Metallographic analysis in Figs. 2 through 5 showed that LOFs were responsible for nucleating fatigue cracks. Normal operating pressures of the system were sufficient to cause the crack to grow to a critical size that allowed the pipe to rupture and leak during the last few cycles of loading. Estimated life from the fatigue analysis for the initial crack of 0.11 in. (0.28 cm) taken from Fig. 2 was well within the normal scatter in fatigue life when

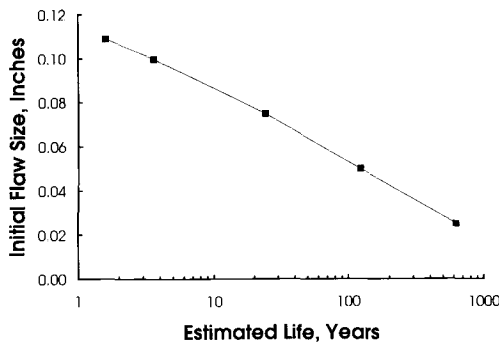


FIG. 7—Estimated fatigue life as a function of initial flaw size.

compared to the observed life of one year. This correlation provides additional verification of the measurements, observations, and calculations and allows us to conclude that the failure was a result of flaws in the pipe and not abnormal operation.

Are More Failures Likely?

Experience with the systems provides further substantiation of the fatigue calculations. Fatigue cracks have been discovered in other unfailed sections of pipe that have been excavated to look for LOF flaws. ASTM A 312 pipe has been extensively investigated for applications in the nuclear industry. A summary of the relevant work from Cipolla et al. [5,6] on lack of penetration defects in double seam welded A 312 stainless steel pipe is given below by reproducing appropriate conclusions from their work.

- Neither radiographic examination nor conventional ultrasonic examination techniques are able to detect the defect reliably.
- A log normal distribution of flaw size data indicated a mean flaw size of 12% of the wall thickness and the size of flaw for 95% occurrence level with 95% confidence is 36% of the pipe wall thickness.

Results of these studies and experience with fueling systems demonstrates that ASTM A 312 pipe will contain LOFs, many of which cannot be identified during the manufacturing process using conventional post weld inspection techniques. The piping system contains additional LOFs that will nucleate fatigue cracks and grow to failure under normal operation. There is no known way to determine the quality of the pipe (more than 10 000 feet) that is already installed in a single fueling system. Therefore, one must conclude that more failures are indeed likely unless the operating conditions are changed to eliminate the cyclic loading.

Did the Failed Pipes Meet Specifications?

Sixteen inch schedule 10 pipe was purchased, according to ASTM A 312. The major specifications relevant to this investigation are summarized below with the same numbering system used in the specification:

3.0 General Requirements

- (a) material conforming to ASTM A 530/A 530M³

5.0 Materials/Manufacture

- (a) no additional filler metal

6.0 Chemical Composition

10.0 Mechanical Tests

- (a) transverse or longitudinal tension tests
- (b) flattening test
- (c) hydrostatic test

12.0 Workmanship, Finish, and Appearance

- (a) reasonably straight/workmanlike finish
- (b) imperfections can be removed with grinding providing wall thickness requirements are maintained

S5 Supplementary Requirements

³ Specification for General Requirements for Specialized Carbon and Alloy Steel Pipe.

(a) radiographic examination

The major specifications included in specification ASTM A 530/A 530M are summarized as follows:

6.0 Hydrostatic Test

(a) not less than 50% of specified minimum yield strength for austenitic steel

11.0 Variation in Wall Thickness

(a) minimum wall thickness *at any point* shall not be more than 12.5% under the nominal wall thickness specified.

Chemical composition was measured and compared to the specification for 304L stainless steel. Particular attention is placed on distinguishing between 304 and 304L. Austenitic stainless steels with higher carbon contents are known to be sensitive to intergranular attack known as weld decay. Although there was no microscopic evidence that weld decay played any role in the failure, it was considered important to verify the chemical composition. If the pipe did not meet the composition requirements, further investigation to determine how the chemical composition may have affected the failure would be needed. In this case the pipe material was found to meet the nominal compositional requirements for 304L.

All of the mechanical specifications relate to performance under static loading. These tests will not determine the performance under cyclic loading. A static pressure test was used to test the integrity of the pipe to meet the A 312 specification. The tensile requirements for ASTM A 312 304L stainless steel require minimum tensile and yield strengths of 70 and 25 ksi (482.63 and 172.369 MPa), respectively. However, delivered pipe typically exceeds these minimum requirements as described above. Pipes containing the LOFs shown in Figs. 2 through 5 could easily pass the hydrostatic test specified in the Specification for General Requirements for Specialized Carbon and Alloy Steel Pipe (ASTM A 530). It is interesting to note that the design code ASME/ANSI B31.3 allows operating stresses as large as $\frac{2}{3}$ of the minimum yield strength while the ASTM standard only requires hydrostatic testing to $\frac{1}{2}$ of the minimum yield strength.

Lack of fusion in the pipe has clearly been demonstrated to be a contributing factor to the failures, yet there is no specific requirement for weld quality. It is common practice in the pressure vessel industry to have specific requirements for weld quality and to make the weld inspection requirements part of the purchase specification. No weld inspection requirements were specified when purchasing this pipe; therefore, it could incorrectly be assumed by the supplier that weld quality was not critical. It is interesting that the owner did not specify radiography for the factory longitudinal welds but did specify 100% radiography for the field installed butt welds that join sections of pipe together. No failures have yet been observed in any of the field welds. Stresses in these welds are only half the magnitude of the hoop stresses.

The specification clearly states that minimum wall thickness at any point shall not be more than 12.5% under the nominal wall thickness specified. Schedule 10 pipe calls for a nominal wall thickness of 0.188 in. (0.477 cm). The minimum allowable thickness is 0.164 in. (0.416 cm) compared to the measured value of 0.165 in. (0.420 cm) in the failed pipe. The question now becomes: Does an LOF constitute a lack of wall thickness? Common sense would dictate that the weld is part of the pipe wall and should be subjected to the wall thickness requirement. The counter argument is that LOFs are a known flaw that results from the welding process and are excluded from the wall thickness requirements, particularly if no radiography is specified. The pipe supplier may conclude (rightly or wrongly) that there is

no particular concern about LOFs since no radiography was requested. Does the presence of an LOF come under the good workmanship provision of the specification? The situation is further complicated by the statement in the specification that imperfections can be removed with grinding providing wall thickness requirements are maintained. There is no question that delivered products were able to meet the acceptance tests but there is question as to whether the pipe meets the minimum wall requirements in regions where there is lack of fusion.

Is the Design Adequate?

The piping system was designed with ASME/ANSI B31.3. As is the case for many systems, there is no specific design code for underground fueling systems. As a result, the designer must use some judgment in selecting the appropriate sections of the code. The code is used to determine the size and wall thickness (schedule) of the pipe required for a given pressure and number of operating cycles.

ASME/ANSI B31.3 Summary

A short summary of relevant sections of ASME/ANSI B31.3 are reproduced here using the numbering system from the code.⁴

The Code sets forth engineering requirements deemed necessary for safe design and construction of pressure piping. While safety is the basic consideration, this factor alone will not necessarily govern the final specifications for any piping system. The designer handbook does not do away with the need for the designer or for competent engineering judgment.

300.2 Definitions

Severe cyclic conditions—Those in which S_E , computed in accordance with para. 319.4.4 exceeds $0.8S_A$ (as defined in para. 302.3.5), and the equivalent number of cycles (N in para. 302.3.5) exceeds 7000; or other conditions that the designer determines will produce an equivalent effect.

NOTE—Both S_E and SE are used in the code and have different meanings.

301.2 Design Pressure

The design pressure of each component in a piping system shall be not less than the pressure at the most severe condition of coincident internal or external pressure and temperature.

301.10 Cyclic Effects

Fatigue due to pressure cycling, thermal cycling, and other cyclic loadings shall be considered in the design of piping.

⁴ Permission to reprint ASME B31.3, Chemical Plant and Petroleum Refinery Piping, granted from the American Society of Mechanical Engineers, New York, NY.

301.5 Dynamic Effects

See Appendix F, para. F301.5.

301.5.1 Impact—Impact forces caused by external or internal conditions (including changes in flow rate, hydraulic shock, liquid or solid slugging, flashing, and geysering) shall be taken into account in the design of piping systems.

302.2.4 Allowances for pressure and temperature variations, metallic piping—Occasional variations of pressure or temperature, or both, above operating levels are characteristic of certain services. The most severe conditions of coincident pressure and temperature during the variation shall be used. . .

302.3.5 Limits of calculated stresses due to sustained loads and displacement strains—(a) Internal Pressure Stresses. Stresses due to internal pressure shall be considered safe when the wall thickness of the piping component, and its means of stiffening, meet the requirements of para. 304. (b) External Pressure Stresses. Stresses due to external pressure shall be considered safe when the wall thickness of the piping component, and its means of stiffening, meet the requirements of para. 304. (c) Longitudinal Stresses S_L . The sum of longitudinal stresses due to pressure, weight, and other sustained loadings S_L shall not exceed S_H in (d) below. The thickness of pipe used in calculating S_L shall be the nominal thickness T minus mechanical, corrosion, and erosion allowance c . (d) Allowable displacement stress range S_A . The allowable displacement stress range (see para. 319.2.3) for the computed displacement stress range S_E (see para. 319.4.4) shall be

$$S_A = f(1.25 S_c + 0.25 S_H)$$

In the above equation

S_c = basic allowable stress at minimum metal temperature expected during the displacement cycle under analysis,

S_H = basic allowable stress at minimum metal temperature expected during the displacement cycle under analysis, and

f = stress range reduction factor for displacement cycle conditions for the total number of cycles over the expected life (Table 1).

302.3.6 Limits of calculated stresses due to occasional loads—(a) Operation. The sum of the longitudinal stresses due to pressure, weight, and other sustained loadings, S_L and of the stresses produced by occasional loads, such as wind or earthquakes, may be as much as 1.33 times the basic allowable stress given in Appendix A. For castings, the basic allowable stress shall be multiplied by the casting quality factor E_c . Where the allowable stress value exceeds two-thirds of yield strength at temperature, the allowable stress value must be reduced as specified in Note (3) in para. 302.3.2. Wind and earthquake forces need not be considered as acting concurrently. Table 2, which follows, shows the stress range reduction factors.⁵

304. Pressure Design of Metallic Components

304.1.2 Straight pipe under internal pressure—(a) For $t < D/6$, the internal pressure design thickness for straight pipe shall be not less than that calculated in accordance with

TABLE 2—*Stress range reduction factors.*⁵

| Cycles | Factor <i>f</i> |
|-------------------|-----------------|
| < 7000 | 1.0 |
| 7 000 to 14 000 | 0.9 |
| 14 000 to 22 000 | 0.8 |
| 22 000 to 45 000 | 0.7 |
| 45 000 to 100 000 | 0.6 |
| > 100 000 | 0.5 |

$$t = \frac{PD}{2SE}$$

The following nomenclature is used in this equation:

- t* = design thickness,
- P* = internal design gage pressure,
- D* = outside diameter of pipe,
- S* = allowable stress value from Table A-1, and
- E* = quality factor from Table A-1A or A-1B.

(b) For $t > D/6$ or for $P/SE > 0.385$, calculation of pressure design thickness for straight pipe requires special consideration of factors such as theory of failure, effects of fatigue, and thermal stress.

305.2.3 Pipe for severe cyclic conditions—Only the following pipe may be used under severe cyclic condition: (c) Stainless Steel Alloy Pipe (ASTM A 268,⁶ seamless; ASTM A 312, seamless; ASTM A 358,⁶ $E_c > 0.90$; ASTM A 376,⁶ ASTM A 430,⁶ and ASTM 451,⁶ $E_c > 0.90$).

319.2.3 Displacement stress range—As contrasted with stresses from sustained loads, such as internal pressure or weight, displacement stresses may be permitted to attain sufficient magnitude to cause limited overstrain in various portions of a piping system. When the system is initially operated at the condition of greatest displacement (highest or lowest temperature, or greatest imposed movement) from its installed condition, any yielding or creep brings about a reduction or relaxation of stress. When the system is later returned to its original condition (or a condition of greater displacement), a reversal and redistribution of stresses occurs which is referred to as selfspringing. It is similar to cold springing in its effects.

⁵ This table is reproduced here from the ASME Piping Code B31.3, with permission from ASME.

⁶ ASTM A 268—Specification for Seamless and Welded Ferritic Martensitic Stainless Steel Tubing General Service.

ASTM A 358—Specification for Electric-Fusion-Welded Austenitic Chromium-Nickel Alloy Steel Pipe for High Temperature Service.

ASTM A 376—Specification for Seamless Austenitic Steel Pipe for High-Temperature Central-Station Service.

ASTM A 430—Specification for Austenitic Steel Forged and Bored Pipe for High-Temperature Service.

ASTM A 451—Specification for Centrifugally Cast Austenitic Steel Pipe for High Temperature Service.

319.4.5 Required Weld Quality Assurance—Any weld at which SE exceeds $0.8SA$ (as defined in paragraph 302.3.5 for any portion of the piping system, and the number of cycles N exceeds 7000, shall be fully examined in accordance with paragraph 341.4.3.

341.4.3 Examination-severe cyclic conditions—Metallic piping to be used under severe cyclic conditions shall be examined to the extent specified herein or any greater extent specified in the engineering design. Acceptance criteria are as stated in paragraph 341.3.2 and in Table 341.2.3A, applicable to severe cyclic conditions, unless otherwise specified. (b) All circumferential butt and miter groove welds and all fabricated branch connection welds . . . shall be examined by 100% radiography.

Design Calculation Summary

Construction projects such as fueling systems usually have a formal design analysis. All calculations supporting the design are documented. The following calculations were used to select the size of the pipe used in the fueling system [7]. Some editing has been done to eliminate calculations not relevant to the pipe failure.

NOTE—Metric conversion for the data that follows is: 1 ksi = 6.8948 MPa.

Maximum pressure—1.5 times maximum system pressure equals 225 psi; maximum allowable pump pressure equals 250 psi. Check compliance with ANSI B31.3.

301.2 Design pressure—302.2.4, over 7000 cycles per lifetime, must use most severe conditions.

301.5.1—Impact by surge is considered since short duration stresses are allowably higher than static pressures.

302.2.3 Design temperature—Since temperature is below 100°F, use fluid temperature.

302.3—Allowable stress (SE) is the maximum allowable stress (S) multiplied by the quality factor (E). Quality factor, defined in 302.3.4, equals 0.85.

302.3.2 Basis for allowable stress—Minimum tensile stress = $(70 \text{ ksi})^{(1/3)} = 23.3$; $\frac{2}{3}$ minimum yield = $(25 \text{ ksi})^{(2/3)} = 16.7$; use 16.7.

302.3—Allowable stress $SE = (16.7 \text{ ksi})(0.85) = 14.2 \text{ ksi}$.

302.3.5—Allowable displacement stress range:

$$SA = f(1.25 S_C + 0.25 S_H),$$

$$S_C = S_H = 14.2,$$

$$f = 0.7 \text{ for up to } 45\,000 \text{ cycles (assumed),}$$

$$SA = 14.9, \text{ and}$$

$$SA > SE; \text{ therefore, displacement stress is not a factor.}$$

304.1 Internal Pressure

12.5% tolerance on thickness.

$$P = (0.188.0 \ 0.875) (14.2 \text{ ksi})/8 = 292 \text{ psi.}$$

The designer then concludes that all pipe sizes and schedules are acceptable per the code.

We now consider the design of the system. Selection of the appropriate wall thickness for the steady-state pressure in the piping system is straightforward. Consideration of the cyclic loading is somewhat problematic. Longitudinal welded ASTM A 312 pipe is not permitted if the designer determines that severe cyclic conditions exist (see Section 305.2.3 of the reprinted ANSI B31.3 Code). The critical issue is in determining the magnitude of the stress

cycles and the number of stress cycles that constitute severe cyclic loading conditions. The code contains several references to severe cyclic conditions. The only reference to allowable stresses for severe cyclic loading are given in Section 302.3.5 of ANSI B31.3 for displacement stresses. Paragraph 319.2.3 of B31.3 makes it quite clear that stresses due to internal pressure are not displacement stresses. It appears that the designer only considered fatigue by computing the displacement stress range. A designer more familiar with fatigue would have recognized a problem with Section 302.3.5 of the analysis. How can the computed maximum stress for fatigue loading (14.9 ksi; 102.73 MPa) exceed the allowable static stress (14.2 ksi; 97.90 MPa)?

The code requires that cyclic loading be considered but only provides guidance for the case of displacement stresses. Could the requirements of the code be met by applying a stress range reduction factor from Table 302.3.5 of ANSI B31.3 to the design allowable stress, SE ? There is nothing in the code that would prohibit this approach. The result would have been a larger pipe wall thickness as the allowable stress would be reduced to $(0.7)(14.2 \text{ ksi}) = 9.9 \text{ ksi}$ (97.90 and 68.26 MPa, respectively), resulting in schedule 20 pipe rather than schedule 10 pipe. The designer would have considered cyclic loading from internal pressure, made an allowance for it with a stress range reduction factor, selected the appropriate wall thickness and concluded that severe cyclic loading conditions did not exist. Since the designer concluded severe cyclic loading conditions do not exist, welded A 312 pipe is permitted and paragraph 341.4.3 of ANSI B31.3 is not applicable; therefore, radiography is not mandatory.

Designers refer to codes such as this one because they are not experts in all aspects of failure. Unfortunately, only an expert would have recognized the possibility of crack-like LOF flaws and concluded that severe cyclic loading conditions existed for the fueling system.

What is the Appropriate Course of Action for Operation of Existing Systems?

Results of these studies and experience with fueling systems demonstrate that ASTM A 312 pipe contains LOFs, many of which cannot be identified with conventional post-weld inspection techniques. The piping code recognizes this and does not permit ASTM A 312 welded pipe to be used under severe cyclic loading. This pipe should not be used in cyclic applications unless the influence of LOFs is specifically taken into consideration in the design. As a result, we believe that continued operation of the systems will result in more failures. Reducing the operating pressures in the system will prolong the life of the system but it is impossible to determine how long since the flaw size distribution is unknown.

Conclusions

The technical aspects of the failure are clearly established. LOF flaws initiated fatigue cracks that grew to failure under normal operations of the fueling system. Limitations in the design code and purchasing specifications of the pipe played a major role in the failure. Designers, through the various design codes, need to consider the possibility of flawed welds under cyclic loading. Design codes need to be improved in this area.

Discussion Questions

The following questions set forth by the author are listed here for further discussion.

- What is the role and responsibility of the designer, pipe supplier, contractor, and system operator in the failure?

- How can these small LOFs be found in a buried pipeline? What techniques are available to inspect the pipe before installation?
- Assuming the same size LOF, how would the burst pressure and fatigue lives be altered if 304 was used instead of 304L?
- If 100% radiography had been specified, what is the maximum LOF size that would be permitted in the pipe? How will it be measured?
- Do you think the pipe meets the specifications? How could the ASTM specification be improved? Remember that a good specification has a means to measure, quantify, and validate compliance. Construction projects are frequently awarded on the basis of the lowest bidder. Should the pipe supplier pay for 12.5% more material than needed to meet the minimum specification?
- Is considering displacement stress range as an indication of severe cyclic conditions a contributing factor to the failure? Could paragraph 304.1.2 (b) of ANSI B31.3 be interpreted by a non-expert that fatigue only needs to be considered if $t > D/6$?
- What types of loading constitute severe cyclic loading? If the cyclic stresses were low enough, the LOFs would not grow since they would be below the threshold stress intensity. Would this be severe cyclic loading? How could the design code be improved? Would schedule 20 pipe be better than schedule 10 pipe? Based on the work of Cipolla et al., schedule 20 pipe would be expected to have larger LOF flaws. Is it reasonable to assume that designers are experts on fracture mechanics?

References

- [1] Broek, D., *The Practical Use of Fracture Mechanics*, Kluwer Academic Publishers, The Netherlands, 1989.
- [2] Raju, I. S. and Newman, J. C., Jr., "Stress Intensity Factors for Internal and External Surface Cracks in Cylindrical Vessels" *Journal of Pressure Vessel Technology*, Vol. 104, 1982, pp. 293–298.
- [3] James, L. A., "Fatigue Crack Propagation in Austenitic Stainless Steels," *Atomic Energy Review*, Vol. 14, No. 1, 1976, pp. 37–85.
- [4] Brussat, T. R., "An Approach to Predicting the Growth to Failure of Fatigue Cracks Subjected to Arbitrary Uniaxial Cyclic Loading," *Damage Tolerance in Aircraft Structures, ASTM STP 486*, 1971, pp. 122–143.
- [5] McNaughton, W. P., Egan, G. R., and Cipolla, R. C., *Significance of Centerline Lack-of-Penetration in Double Welded Steel Pipe—Fracture Analysis*, Aptech Engineering Services, Inc, Palo Alto, CA, 1979.
- [6] Cipolla, R. C., Grover, J. L., Beaupre, G. S., and McNaughton, W. P., *Lack-of-Penetration Defects in Double-Seam-Welded SA-312 Stainless Steel Pipe*, Aptech Engineering Services, Inc, Palo Alto, CA, 1980.
- [7] "Supplement to Final Design Analysis," Ellsworth Air Force Base, South Dakota, U.S. Army Corps of Engineers, July 1984.

Thermal Fatigue Analysis: A Case Study of Recuperators

REFERENCE: Bhat, S. P., "Thermal Fatigue Analysis: A Case Study of Recuperators," *Case Studies for Fatigue Education, ASTM STP 1250*, Ralph I. Stephens, Ed., American Society for Testing and Materials, Philadelphia, 1994, pp. 101–108.

ABSTRACT: Continually increasing energy cost is an impetus to increasing the operating temperatures in industrial recuperators. However, higher service temperatures increase the risk of thermal fatigue failures. This paper presents a case study involving thermal fatigue analysis of a recuperator in an integrated steel plant.

The paper first describes the background and the rationale for a proposal to operate recuperators at the Inland 80" Hot Strip Mill at a higher than normal temperature for the purpose of fuel savings. A quick engineering analysis identified thermal fatigue as a high risk item that needed to be analyzed before deciding to operate the recuperators at a higher temperature. To quantify the resulting thermal effects, temperature profiles were recorded on an experimental basis for one furnace run at both the normal and higher operating temperatures. The paper describes the steps and assumptions involved in analyzing the data and estimating the thermal fatigue life. The calculations indicate that increasing the operating temperature from 1100° to 1250°F (593 to 677°C) may reduce the thermal fatigue life of the recuperator by as much as 63%. Based on these calculations and practical difficulties in achieving higher degree of skin temperature regulation, the option of operating recuperators at a higher temperature was considered unattractive.

KEYWORDS: thermal fatigue, recuperators, elastic strain, plastic strain, cumulative damage

In spite of major improvements, energy costs represent 28 to 30% of steel manufacturing cost in the United States [1]. Thus, the economic impetus for improving the efficiency of recuperators, a commonly used method for waste heat recovery, is quite clear. Conceptually, a recuperator recycles the heat from waste exhaust gases from a furnace to preheat the incoming combustion air or fuel. This results in lower waste gas temperature and reduced fuel and air input [1]. In the early 80s, the Energy Technology Team at Inland Steel began finding ways to recover more energy from waste gases as a means to reduce total energy costs at the 80" Hot Strip Mill. One means of increasing the efficiency of recuperators is to increase the operating temperatures. The proposal included raising the recuperator skin temperature so that the combustion air would be preheated to a higher temperature. However, in raising the operating temperatures, trade off between energy savings and the potential reduction in component life must be considered. Obviously, it is prudent to carry out a risk-benefit analysis before changing the operating temperature. The Energy Technology Team identified thermal expansion, creep, high-temperature gaseous corrosion, and thermal fatigue as the major risk factors for further analysis. Engineering estimates made, based on the physical dimensions and materials' data, provided by the manufacturers of the recuperator,

¹ Section manager, Inland Steel, Research and Development Department, 3001 East Columbus Drive, East Chicago, IN 46312.

convinced the team that thermal expansion, creep, and high-temperature gaseous corrosion would not deteriorate the recuperator life significantly as a result of increasing the operating temperature. (See the next section for the magnitude of temperature increase being considered.) To address the remaining critical issue of thermal fatigue, the involvement of the R&D Department and the present author was requested. The case study presented here is based on the thermal fatigue analysis conducted as part of an engineering analysis of the effects of increasing the operating temperature of the 80" Hot Strip Mill recuperator. The intent is to demonstrate how basic principles of fatigue analysis may be applied in determining whether or not raising the operating temperature will have detrimental effects on the service life of steel mill recuperators.

Topics for Further Study

What are the different materials used in the construction of an industrial recuperator and what factors go into deciding the optimum operating temperature?

Thermal History

In this section, attention is focused on identifying what data are pertinent to represent the anticipated thermal cycling history of the recuperator and how to incorporate the typical variations in mill operating conditions.

Based on experience and recommendations of the equipment supplier, the recuperators at the Inland 80" Hot Strip Mill were operated with a skin temperature set point of 1100°F (593°C). The proposal consisted of increasing the skin temperature to 1250°F (677°C) by controlling water sprays in the waste gas stream. This increase in skin temperature was estimated to increase the preheat air temperature by about 120F^o,² resulting in a final air temperature of 800°F (427°C). Since the thermal load on the recuperators depends on the mill working schedule, any realistic thermal fatigue analysis has to be based on the actual thermal profile rather than the set point. Therefore, to quantify the effects of increasing the recuperator skin temperature, one furnace was selected as the candidate to be run at the higher temperature on an experimental basis. A minimum of 48 h of temperature profile recordings were suggested to capture typical variations in mill operating conditions.

Figure 1 is a schematic of the recuperator.³ The skin temperature was monitored at a point where previous experience had shown to indicate the highest operating temperature (Fig. 1). This approximately represents the region where the temperature difference between the outgoing waste gas and the incoming air is maximum and is typically subject to maximum fluctuations in temperature. The skin temperature profiles were recorded on an expanded scale for the two recuperators in the furnace. For each recuperator, temperature profiles were recorded at two locations on the same elevation (identified as north and south thermocouples). In addition, to verify the impact of increasing the skin temperature, a six channel Beckman recorder was used to monitor and record combustion air and waste gas temperatures.

Temperature profiles were recorded as detailed above with skin temperature set points at 1100°F (593°C) for 64 h and at 1250°F (677°C) for 53 h. (The mill operations dictated the different lengths of the observation period). In the following, data from the run with set point at 1100°F (593°C) will be used to establish the base line for the analysis.

² The nomenclature of 120F^o, to denote a range (Δ) of temperature, and 120°F, to denote the actual temperature, will be used throughout this paper. The author gratefully acknowledges one of the reviewers for suggesting this unambiguous notation.

³ Buggy, E. J., unpublished reports, Inland Steel Company, 1982-83.

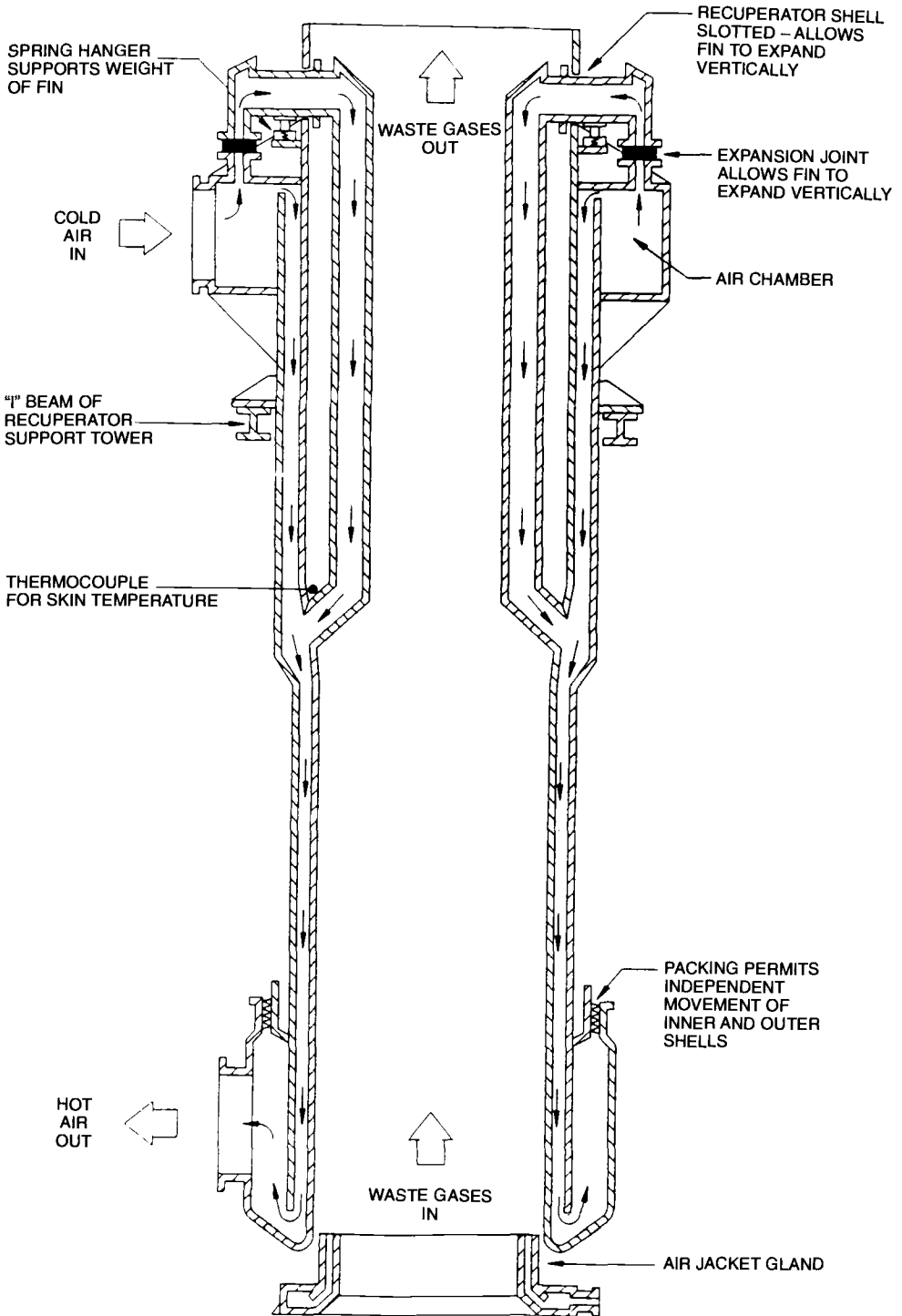


FIG. 1—Schematic drawing of the cross section of a recuperator at the Inland 80" Hot Strip Mill (not to scale).

Visual inspections of temperature recordings revealed very similar profiles on both recuperators at the two recording locations. Thus, only one location on one recuperator was chosen for detailed analysis.

Thermal Fatigue Analysis

When a component undergoes temperature fluctuations and the natural expansions/contractions are either wholly or partially inhibited, thermal stresses are produced that can lead to fatigue failures. This is called "thermal fatigue." It is emphasized that it is not thermal expansion that causes fatigue but rather the restraint of this expansion (or contraction) that leads to fatigue. The details of the nature and problems of thermal fatigue can be found in Ref 2.

For the purpose of the present analysis, the recuperator is considered essentially free-hanging, and, as seen in Fig. 1, a packing gland at the bottom of the recuperator allows the inner and outer shells to expand independently of one another. Further, it is assumed that over a period of time, the recuperator reaches the naturally expanded state corresponding to the operating temperature. This is especially true since the recuperator is slowly heated. (Typical firing time is approximately 5 h.) However, during its operation, due to variations in heat input demands at the furnace, fluctuations occur in the recuperator skin temperature lasting less than 30 min per cycle. In the present analysis, it is assumed that this short interval of time is not sufficient for "natural" (entire skin) expansion/contraction of the recuperator. Further, for ease in calculation, it is assumed that these local thermal expansions/contractions are fully constrained and are the cause of thermal fatigue. In other words, the damage accumulates due to temperature fluctuations rather than due to a specific operating temperature. The direct effects of changing the operating temperature (within the range considered here) are the minor changes in the material cyclic properties, which, as an engineering approximation, are ignored in the present study. However, inspection of the temperature recordings revealed that increasing the operating temperature results in a greater number of temperature fluctuations of larger magnitude. Steps involved in calculating the relative effects of these temperature fluctuations are explained below. Because the proposed change in set temperature is comparatively small (120F° or 67C°) and the primary interest is in the relative effects of such changes in the operating temperature, a simple uniaxial analysis can be made, although temperature fluctuations may lead to more complex multiaxial strain/stress situation.

Step 1—Temperature Fluctuations

From the expanded temperature profile recordings, fluctuations were categorized into four groups of magnitude: 99, 198, 297 and 396F° (55, 110, 165 and 220C°), respectively. In general, the cycle time was found to be independent of both the magnitude of temperature fluctuations and the operating set point. Typically, each fluctuation lasted about 15 to 20 min. The number of fluctuations in each group for the entire recording period were counted without regard to their sequence. The results are summarized in Table 1 for both 1100°F (593°C) and 1250°F (677°C) aim skin temperatures. It is significant to note that at the higher operating temperature, there were three temperature cycles of 396F° (220C°) magnitude; whereas, none was found of this magnitude at the lower operating temperature. In addition, the number of fluctuations increased as the amplitude of temperature cycles decreased for both operating temperatures.

TABLE 1—Thermal fatigue calculations for recuperator.

| Magnitude of Temperature Fluctuation, F° (C°) | Set Point 1100°F (593°C) ^a | | | Set Point 1250°F (677°C) ^b | | |
|--|---------------------------------------|------------|----------|---------------------------------------|-----------|----------|
| | 99(55) | 198(110) | 297(165) | 99(55) | 198(110) | 297(165) |
| No. of temperature cycles (Step 1) | 15 | 9 | 1 | 9 | 6 | 2 |
| Total strain range ($\epsilon \Delta T$) 10^{-3} (Step 2) | 1.03 | 2.059 | 3.088 | 1.03 | 2.059 | 3.088 |
| Plastic strain range ($\Delta \epsilon_{pl}$) 10^{-3} (Step 2) | 0.051 | 1.08 | 2.11 | 0.099 | 1.13 | 2.15 |
| No. of Cycles to Failure (Step 3) | $> 10^6$ | 30 000 | 10 000 | $> 10^6$ | 30 000 | 10 000 |
| Damage n_i/N_i (Step 4) | 0 | 0.0003 | 0.0001 | 0 | 0.0002 | 0.0002 |
| Total damage for the observation period, $\sum n_i/N_i$ (Step 4) | | 0.0004 | | | 0.0009 | |
| Predicted life | | 18.3 years | | | 6.7 years | |

^a Observation period, 64 h.^b Observation period, 53 h.

Step 2—Conversion of Thermal to Mechanical Strain

A temperature fluctuation of ΔT results in a total strain fluctuation of

$$\Delta \varepsilon_t = \alpha \Delta T \quad (1)$$

where α is the coefficient of thermal expansion. Obviously, this represents an upper-bound for $\Delta \varepsilon_t$, calculated as if the component was totally constrained from any thermal expansion. Thus, these calculations are conservative and provide some built-in engineering safety factors. Knowing the yield stress, σ_{ys} , and the modulus of elasticity, E , at the mean operating temperature, the elastic portion ($\Delta \varepsilon_{el}$) of this total strain and then the plastic strain ($\Delta \varepsilon_{pl}$) component can be calculated

$$\Delta \varepsilon_{el} = \frac{\sigma_{ys}}{E} \text{ at the operating temperature} \quad (2)$$

$$\Delta \varepsilon_{pl} = \Delta \varepsilon_t - \Delta \varepsilon_{el} \quad (3)$$

Note that it is the plastic strain that is most damaging for fatigue analysis. Combining Eqs 1 and 2, we get

$$\Delta \varepsilon_{pl} = \alpha \Delta T - \frac{\sigma_{ys}}{E} \quad (4)$$

The outer shell of the recuperator is made of the AISI 304 stainless steel and the relevant material properties are listed in Table 2 [3].

The calculated total and plastic strain ranges corresponding to the observed temperature fluctuations are listed in Table 1.

Topics for Further Study

Equations 2 through 4 make use of high temperature monotonic properties (yield strength and modulus of elasticity) to estimate the strain components. How significant are the changes in these properties due to cycling at high temperatures?

Step 3—Estimation of Fatigue Life

Specific thermal fatigue data for 304 stainless steel that fully encompass the operating conditions of a recuperator (that is, numerous time dependent processes) were not available

TABLE 2—High temperature properties of 304 stainless steel (extracted from Ref 3).

| | |
|--|---|
| Coefficient of thermal expansion, 32 to 1200°F (0 to 650°C) | 10.4×10^{-6} in./in./F° (18.72×10^{-6} cm/cm/C°) |
| Modulus of elasticity | |
| • 1100°F (593°C) | 23.5×10^6 psi (162 GPa) |
| • 1250°F (677°C) | 21.5×10^6 psi (148 GPa) |
| Yield strength | |
| • 1100°F (593°C) | 23 000 psi (159 MPa) |
| • 1250°F (677°C) | 10 000 psi (69 MPa) |

in the literature. In view of project time constraints and the need for making an engineering assessment rather than a rigorous analysis, approximate analysis using existing data was considered adequate. The approach taken consists of estimating thermal fatigue life from isothermal low cycle fatigue data for the material [2,4,5].

Topics for Further Study

For the purpose of correlating thermal cyclic life to isothermal fatigue life, should the isothermal tests be carried out at the average temperature of thermal excursions or at another effective temperature? Highlight the role of temperature regime and possible metallurgical changes in the material that can influence the choice of test temperature.

Fatigue lives corresponding to the plastic strain components calculated in Step 2 were estimated from the published strain-life data at high temperatures [6]. While frequency, hold time, wave shape, and environment all are known to have significant influence on fatigue life at high temperatures, in this case study, life was estimated based on the results published by Kuwabara and Nitta [6] at 600°C, 0.2 Hz frequency, and no hold periods. In other words, the thermal fatigue life over the temperature range T_1 and T_2 , corresponding to the upper and lower limits of temperature fluctuations, is estimated from the low cycle fatigue data at 600°C (1112°F) for the plastic strain range estimated from these temperature fluctuations. These results at various strain levels are listed as the number of cycles to failure in Table 1. In view of a number of approximations involved, these values are only trend indicators and caution should be exercised in using these numbers for any other purpose. It is clear that as the magnitude of temperature fluctuations increases, the fatigue life decreases rather rapidly. Thus, the recuperator can withstand temperature fluctuations of 99°F (55°C) almost forever, but for 396°F fluctuations life is only about 6000 cycles.

Step 4—Cumulative Damage

It is clear from the above discussion that the recuperator is subject to thermal cycles of different magnitudes and, therefore, one must consider the cumulative effects of these events in estimating the final failure life. In the present calculations, use is made of the linear damage equation due to Miner [7]. Thus, if N_i is the number of cycles to failure corresponding to a temperature fluctuation of magnitude ΔT_i , and if n_i is the actual number of cycles spent, then the damage due to these cycles is

$$D_1 = \frac{n_i}{N_i} \quad (5)$$

The failure is supposed to occur when the sum of all the damaging events equals 1.

$$\sum \frac{n_i}{N_i} = 1 \quad (6)$$

Table 1 lists the calculated damage during the observation period due to each group of temperature fluctuations and the total damage for the period. The results are presented for both the 1100°F (593°C) and 1250°F (677°C) operations. Converting these into time-scale results in an estimated life of approximately 18.3 years at 1100°F (593°C) and 6.7 years at 1250°F (677°C). While a number of factors contribute to the overall economics of operating the recuperators, long lives, in excess of 10 years, are favored in commercial usage. In fact,

typical life is about 15 years. In view of a number of simplifying assumptions made during the calculations, the predicted life of 18 years at 1100°F (593°C) operation agrees reasonably well with what is observed in commercial practice. Assuming that these assumptions are equally valid at the higher operating temperature (1250°F or 677°C), these calculations indicate that the life of the recuperator may be reduced by as much as 63%. In other words, thermal fatigue may shorten the recuperator life substantially if operated at 1250°F (677°C).

Conclusions

The above calculations indicate that increasing the operating skin temperature from 1100 to 1250°F (593 to 677°C) may reduce the recuperator life due to thermal fatigue by as much as 63%. This drop is directly attributable to the 396°F (220°C) fluctuations seen only at the higher operating temperature. Further, data in Table 1 indicate that if these large fluctuations in temperature can be avoided, then the higher operating temperature results in comparable life and, therefore, can profitably be used for fuel savings. As indicated earlier, the recuperator skin temperature is controlled by water sprays in the waste gas stream. Thus, the magnitude and frequency of skin temperature fluctuations are a function of how well the water sprays perform and can be controlled during the mill operation. Therefore, it was recommended to the Energy Technology Team to look into possible modifications to achieve a higher degree of temperature regulation. However, practical considerations such as the unpredictability of furnace cut-backs due to mill delays, and the transients imposed during light-ups and shutdowns, the option of operating recuperators at a higher temperature for the purpose of fuel savings was considered unattractive given the potential damage due to thermal fatigue.

Acknowledgments

The permission of the Inland Steel Company to publish this paper is appreciated. The cooperation of the Energy Technology Team during the course of this work and helpful comments of B. S. Levy during the preparation of the manuscript are gratefully acknowledged.

References

- [1] Bugyis, E. J. and Taylor, H. L., "Heat Exchange in Steel Industry," *Industrial Heat Exchangers*, A. J. Hays, W. W. Liang, S. L. Richlen, and E. S. Tabb, Eds., American Society for Metals, Metals Park, OH, 1986, pp. 3–12.
- [2] Manson, S. S., *Thermal Stress and Low Cycle Fatigue*, McGraw-Hill Book Company, New York, 1966.
- [3] American Society for Metals, *Source Book on Industrial Alloys and Engineering Data*, American Society for Metals, Metals Park, OH, 1978.
- [4] Bhat, S. P., *High Temperature Cyclic Deformation in Nickel, TD-Nickel and Al-4% Cu Alloy Aged to Contain θ' and θ''* , Ph.D. Thesis, University of Pennsylvania, Philadelphia, 1978.
- [5] Taira, S., "Relationship Between Thermal Fatigue and Low Cycle Fatigue at Elevated Temperatures," *Fatigue at Elevated Temperatures, ASTM STP 520*, A. E. Carden, A. J. McEvilly, and C. H. Wells, American Society for Testing and Materials, Philadelphia, 1973, pp. 80–99.
- [6] Kuwabara, K. and Nitta, A., "Thermal-Mechanical Low-Cycle Fatigue Under Creep-Fatigue Interaction on Type 304 Stainless Steels," *Fatigue of Engineering Materials and Structures*, Vol. 2, 1979, pp. 293–304.
- [7] Fuchs, H. O. and Stephens, R. I., *Metal Fatigue in Engineering*, John Wiley & Sons, New York, 1980.

Richard C. Rice¹

Shell and Detail Fracture Formation in Railroad Rails

REFERENCE: Rice, R. C., “Shell and Detail Fracture Formation in Railroad Rails,” *Case Studies for Fatigue Education, ASTM STP 1250*, Ralph I. Stephens, Ed., American Society for Testing and Materials, Philadelphia, 1994, pp. 109–138.

ABSTRACT: Detail fractures have been observed in railroad rails for many years and some serious railroad accidents have been attributed to these insidious rail defects [1]. In a study completed in the early 1980s for the Department of Transportation [2], it was found that nearly 10% of over 10 000 1.6-km segments of revenue-service railroad rail contained one or more detail fracture defects. Although in the aggregate, detail fractures are relatively uncommon. (They comprised only about 3½% of the 30 000 defects observed in the study cited in Ref 2.) These defects are of great concern in terms of rail reliability and safety since detail fractures typically initiate and grow within the head of the rail, and they may go unidentified until the strength of the rail is so deteriorated that a sudden failure occurs, which can lead to a train derailment.

Over the past decade, Battelle has worked closely with the Volpe National Transportation Systems Center (VNTSC) and the Federal Railroad Administration (FRA) on the problem of shell and detail fracture formation in railroad rails [3–7]. This problem remains a significant one for the rail transportation and freight industry, in spite of the fact that a considerable body of knowledge now exists regarding the cause of these defects.

This paper was prepared in the form of a case study for fatigue education to give students interested in the discipline an opportunity to test their growing expertise on this real-world, present-day engineering issue.

This paper is presented in three parts. The first part of the paper is informational. It provides a brief description of shell and detail fractures in railroad rails, and offers a variety of examples of both types of defects. Other potentially important information for the case study is also provided, including:

- (1) typical three-dimensional residual stress data on used rails,
- (2) wheel/rail loading spectra,
- (3) thermal stresses in rail,
- (4) approximate “live” stresses induced in rails by passage of railroad wheels, and
- (5) crack initiation and fatigue crack growth properties of rail steel.

The second part of the paper reviews some of the fundamental questions that the railroad community has faced regarding shell and detail fractures in rails. The student is asked to take the role of an independent researcher, perhaps working for the railroad community. The task is to assess the available information and provide informed responses to each of these questions (and perhaps others that arise in class discussions).

The third part of the paper provides a discussion on each of the questions posed in Part 2. An overall interpretation of shell and detail fracture formation processes is also offered, along with some comments on steps taken by the railroad industry to minimize their occurrence and reduce the risk that those that do occur will lead to rail failures.

For use as a case study for fatigue education, it is recommended that the three parts of this paper be given to students sequentially over a period of time sufficient to allow an independent

¹ Manager, Battelle, Structural Integrity Projects Office, 505 King Avenue, Columbus, OH 43201.

evaluation of related literature. In this way each response in Part 3 can be used more as an example of one plausible solution to the problem, rather than the only solution.

KEYWORDS: railroad rails, fatigue analysis, shelling, detail fractures, transverse defects, residual stresses, case study, failure analysis

This paper was prepared for presentation at the ASTM Symposium on Case Studies for Fatigue Education, held in Atlanta, GA on 18 May 1993. There were several prime goals of the symposium. One goal was to stimulate interest in students of fatigue and fracture mechanics through examination of non-trivial, real-world case studies. Another goal was to facilitate student's integration of the elements of engineering that commonly enter into a fatigue design or failure analysis, including mechanics of materials, design of experiments, field data acquisition, physical metallurgy, fractography, material characterization, damage modeling, and life prediction. Still another goal was to dramatize the point that most fatigue design problems do not have one unique solution, in fact the "best" solution is often dictated by financial constraints, time limitations, availability of pertinent material and processing information, liability concerns, and public perception.

Part 1—Background

Shells and Detail Fractures

For those unfamiliar with fatigue cracks in railroad rails, the terminology requires some explanation. A shell crack is a fatigue crack that forms under the running surface of a rail and parallel to that surface. Shells in railroad rails may be surface connected, but often are not, sometimes growing to a considerable length if undetected by nondestructive means. If a shell does develop near the surface of the rail or gets sufficiently long, it may cause spalling of the rail, but these shells, or head checks as they are sometimes called, do not normally cause total rail failure.

For over 40 years, cracks that develop from a shell and propagate approximately perpendicular to the running surface through the head of a rail have been known as detail fractures [8]. More recently, the Sperry Rail Defect Manual [9] has defined a detail fracture from shelling as "a progressive fracture starting from a longitudinal separation close to the running surface of the rail head, then turning downward to form a transverse separation substantially at right angles to the running surface." If a crack forms away from a shell and grows perpendicular to the running surface it is known as a transverse defect. True transverse defects are less common today than detail fractures, because modern rail processing techniques have largely eliminated the blow holes that were common transverse crack starters.

A dramatic example of a detail fracture is shown in Fig. 1. This detail fracture, labeled AT-5, shows the typically observed oval shape that expands with increasing rail traffic across the head of the rail, while remaining contained within the head of the rail until quite large. Since detail fractures can grow through over 50% of the head area without being visible to the naked eye, they can lead to catastrophic rail failures. In fairness, it should be acknowledged that the vast majority of detail fractures are identified through the periodic use of roll-by nondestructive inspection devices. The detail fractures that escape detection are the ones that sometimes cause serious rail failures. (Rail AT-5 did fail during testing at the Transportation Test Center (TTC),² but restraint bars placed loosely on either side of the rail

² The Transportation Test Center is located in Pueblo, CO and is managed by the Association of American Railroads (AAR), which is headquartered in Chicago, IL.

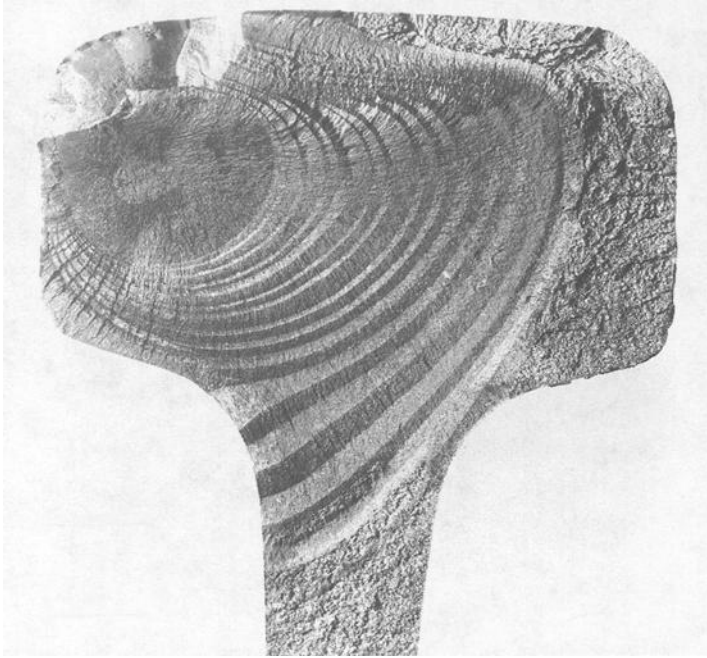


FIG. 1—Detail fracture in rail AT-5.

spanning the section containing the detail fracture prevented derailment of the test train, while allowing the natural evolution of the detail fracture.)

The AT-5 detail fracture (Fig. 1) shows two distinct regions of crack growth. The nearly featureless portion of the fracture developed while the rail was in revenue service. The uneven portion of the flaw developed while the rail was installed in the test track at TTC and was subjected to controlled freight traffic. The growth of the detail fracture was monitored as a function of tonnage carried. Periodic changes in the direction of traffic on the test track contributed to the slight changes in the plane of the detail fracture as it grew, visible in Fig. 1 as alternating light and dark bands emanating from the original detail fracture.

Examples of other detail fractures are shown in Figs. 2 through 5. Although each detail fracture has unique features, there are obvious similarities between them. All of the transverse cracks emanated from a shell crack beneath the gage corner of the rail head, and they all propagated downward and across the head of the rail, largely contained by the gage face and the running surface of the rail. The cracking pattern displayed in Fig. 2 is similar to that shown earlier for AT-5 (Fig. 1). That is because this rail experienced a similar service history to AT-5; it also was removed from revenue (normal) service with a known detail fracture present, and then placed in controlled service testing at TTC in Pueblo, CO. However, this rail did not fail during testing at TTC; it was removed before failure and broken open at a later date for detailed investigation.

Most of the shell cracks display an elongated irregularity in their center, which appears to be their origin. Detailed examinations of these sites have often revealed complex inclusions or stringers. An indication of such a complex inclusion containing aluminum, sulfur, silicon, and manganese is provided in Fig. 6, where an energy dispersive X-ray (EDAX) trace is shown of the shell initiation site in Rail SP-2.

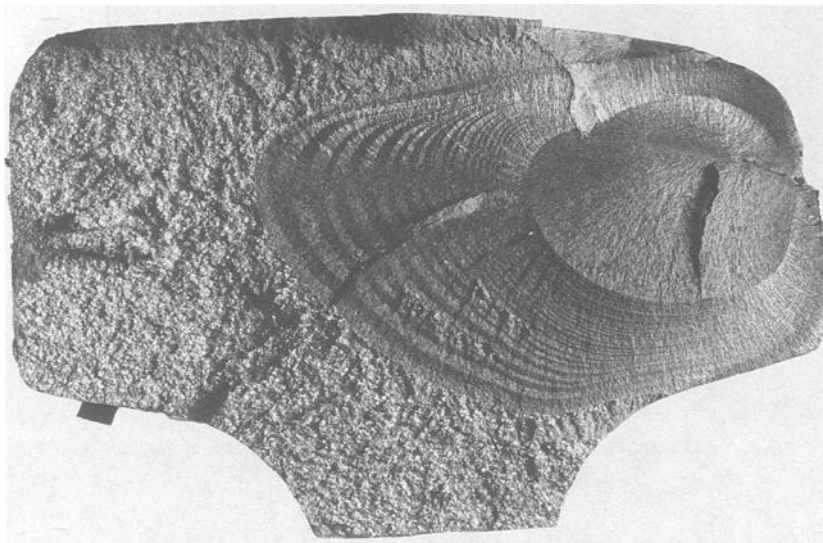


FIG. 2—Detail and shell fracture in rail NW-4.

The shapes of the shell cracks display less consistency than observed on the transverse cracks. Some of the shells are relatively short and essentially circular. Others are 2 to 3 times as long as they are wide (lateral dimension); however, in none of these cases does a shell crack exceed a width of approximately 25 mm, and most are less than 20-mm in width. These trends are fairly typical of other shells observed in defective rails removed from service [3–7]. In some extreme cases shells have been found that are over 0.30-m in length, and some of these very long shells do not have transverse cracks associated with them.

Typical Rail Residual Stress Patterns

Because railroad wheels produce very high Hertzian contact stresses in a rail, the running surface deforms plastically and typically forms a work-hardened, compressive residual stress layer at the running surface. Similarly, periodic impact loads by the wheel flange on the gage face of the rail can produce a compressive residual stress layer at the gage face. Since it was believed that these residual stresses played some role in the formation of shells, detail fractures, and other types of rail defects, the Federal Railroad Administration (FRA) and the Volpe National Transportation Systems Center (VNTSC) supported research to identify them accurately and to determine whether the magnitude of these residual stresses varied with increasing tonnage (a measure of rail traffic) and increasing wheel loads. A detailed, experimental stress analysis technique developed at Battelle and documented by Groom [10] in 1980 was shown to provide reasonably precise and accurate three-dimensional residual stress data for railroad rails. The repeatability of results developed with this intricate rail cutting and finite element analysis (FEA) procedure was found to be within approximately 20 MPa. The accuracy of the technique was found to depend on the severity of the stress gradients, with degradation in accuracy at regions where the gradients are largest, such as at the gage face of a rail.

Fairly consistent patterns of residual stress do develop in railroad rails as a result of repeated wheel loads and subsequent running surface and gage face plastic deformation.

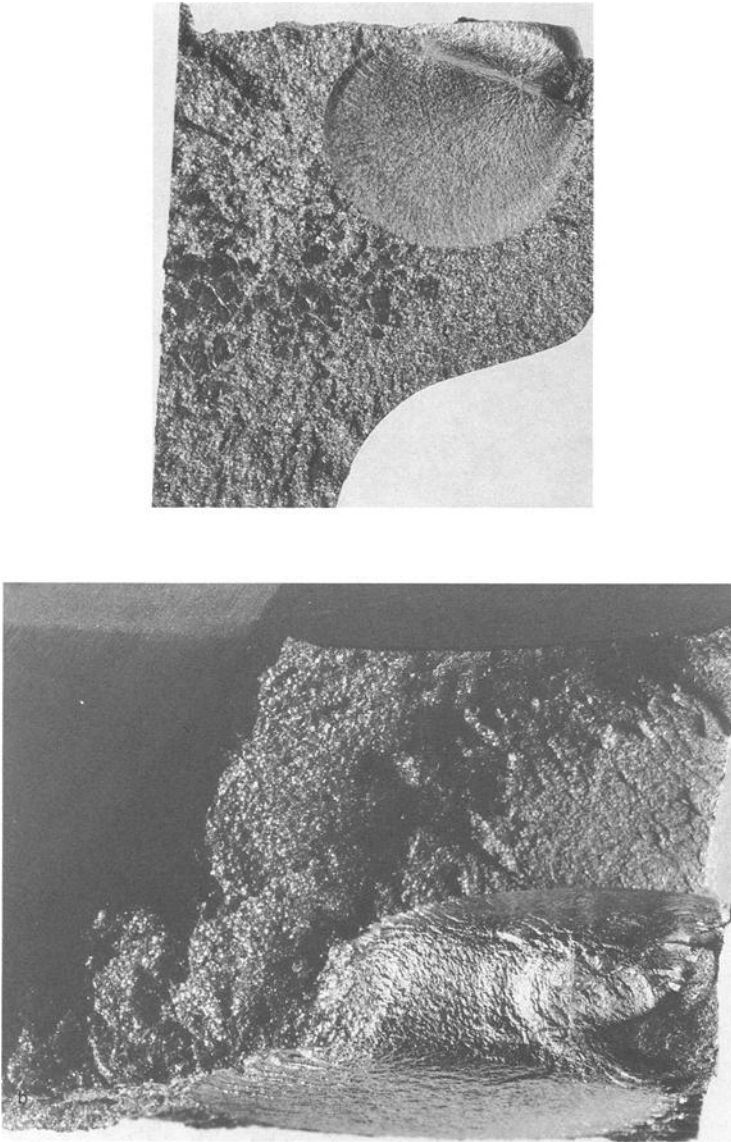


FIG. 3—Detail fracture in rail AT-10. (a) View of transverse crack. (b) View of shell crack.

They also appear to develop and stabilize fairly quickly in the life of a rail. For practical purposes, “shakedown” of the residual stress field does seem to occur [10]. For example, the longitudinal residual stress patterns shown in Fig. 7 are typical for tangent (straight) track. Very large compressive residual stresses are normally seen at the gage corner, and significant compressive residual stresses are usually observed on the gage face and running surface. These compressive residual stresses produce significant tensile residual stresses in the interior of the rail, and they typically display maximum values in the upper center of

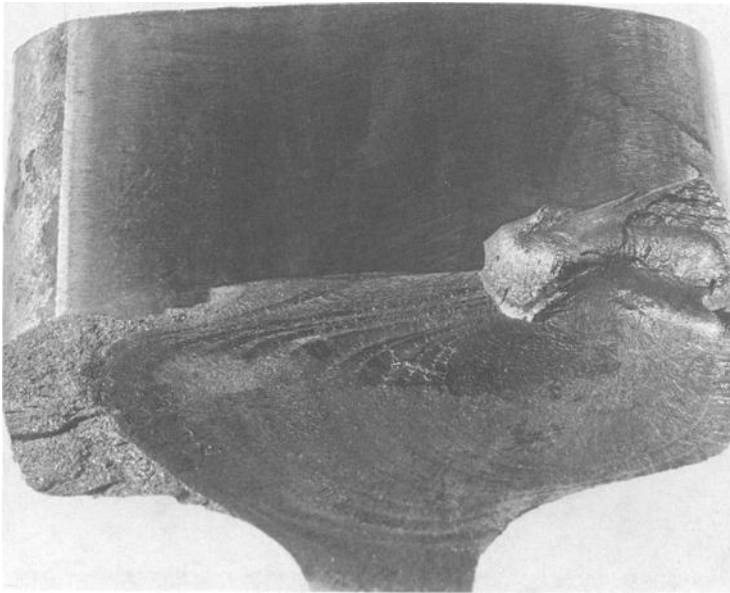


FIG. 4—Detail and shell fracture in rail NW-22.

the rail toward the gage corner. (The small pocket of compressive residual stress near the lower center of the rail head is not usually seen. Residual stresses in this region of the head can effectively be ignored.)

Even more significant in-plane residual stresses have also been observed in all used rails. The pattern of maximum in-plane principal stresses found in a typical rail is shown in Fig. 8. As shown in this figure, the gage face and head are usually in complete compression, while the interior of the rail shows very high maximum principal stresses. The direction of the maximum in-plane principal stresses does vary significantly through the cross-section of the rail head, but there is a tendency for the maximum principal stresses to be oriented on a diagonal downward from the gage corner toward the center of the rail, where the principal stress vectors tend to flatten out.

Wheel/Rail Loading Spectra

Although the average static wheel rail load experienced in revenue freight and passenger service is approximately 65 kN, dynamic wheel/rail loads due to rail joints, rail corrugations, wheel flats, and other wheel/rail interface anomalies, can occasionally exceed 300 kN. As a result, the statistical characterization of wheel/rail loads has been a matter of considerable interest for over 15 years [11]. An illustration of the widely varying loads that are experienced in revenue service is provided in Fig. 9 [12].

The actual severity of a particular type of service can depend more on the magnitude of the occasional high loads than on the average wheel/rail loads. For example, it was found that the cars used for simulated service testing at the Facility for Accelerated Service Testing (FAST) in Pueblo, CO carried average wheel loads about twice those experienced in Amtrak and Conrail service, yet the 1 in 10 000 wheel occurrence (0.01% exceedance) for FAST

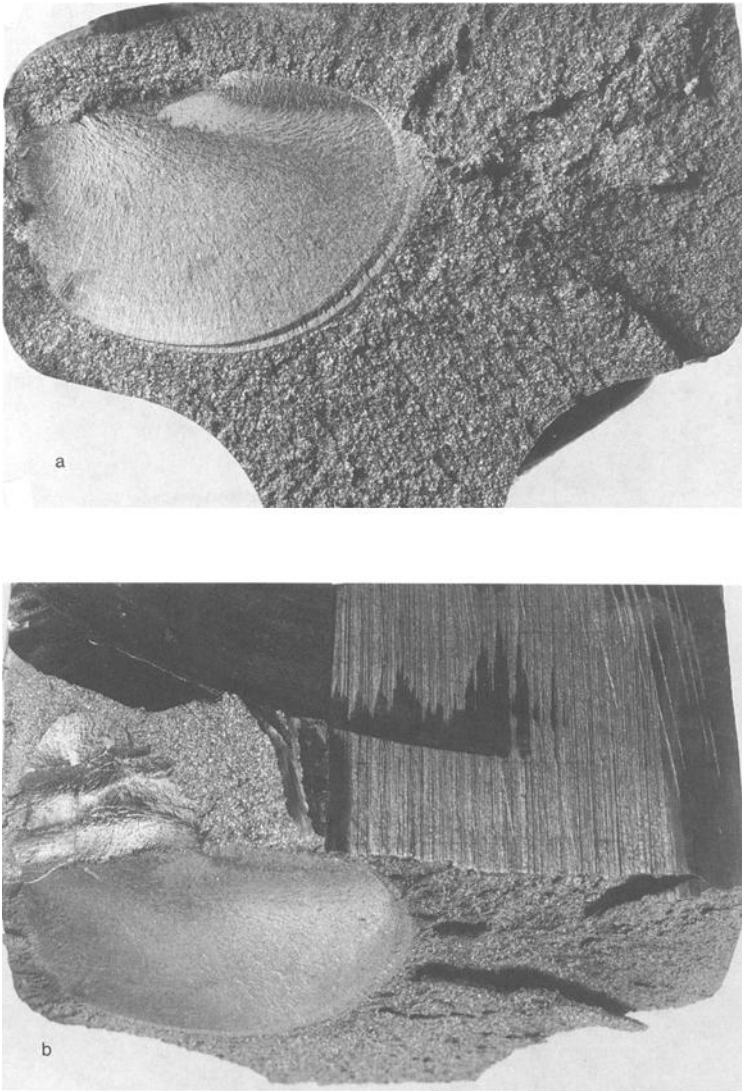


FIG. 5—Detail fracture in rail SP-2. (a) View of transverse crack. (b) View of shell crack.

was only about half that for Amtrak and Conrail (Fig. 9).³ This result is directly attributable to the very high standards of wheel and rail maintenance at FAST, where joint mismatches, wheel flats, and rail corrugations are essentially nonexistent, compared with field service conditions where wheel and rail abnormalities, or both develop and can remain for a period of time before they are addressed.

³ These results may not apply to other rail lines operating at other times. These wheel/rail exceedance curves are offered only as representative data for conditions prevalent in the early 1980s.

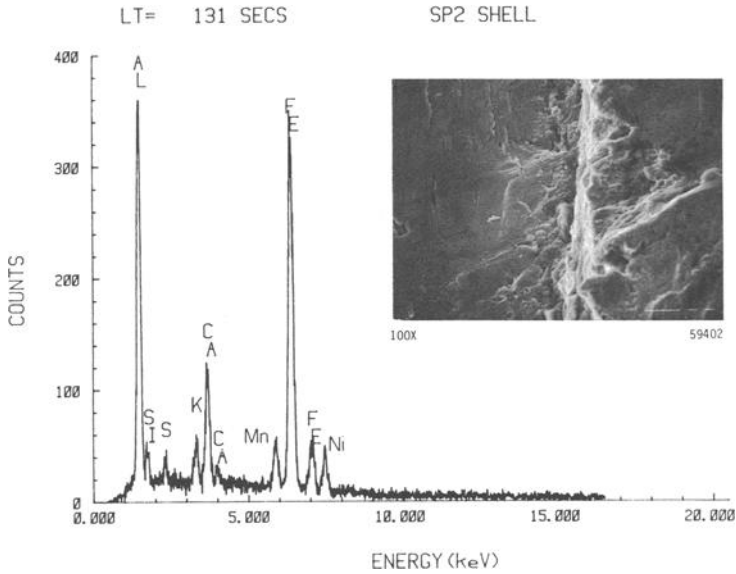


FIG. 6—Energy dispersive X-ray analysis of shell initiation in rail SP-2.

Occasional, very large dynamic wheel/rail loads may accelerate the crack growth rate of a detail fracture, although they are commonly more significant in limiting the maximum flaw size that can be withstood by the rail before failure. The static strength of a rail decreases (on average) with increasing flaw size of a detail fracture. This trend is shown (albeit with considerable variability) in Table 1, from Orringer et al. [13], who developed residual strength data from about 30 used and defective rails. These data were developed from a

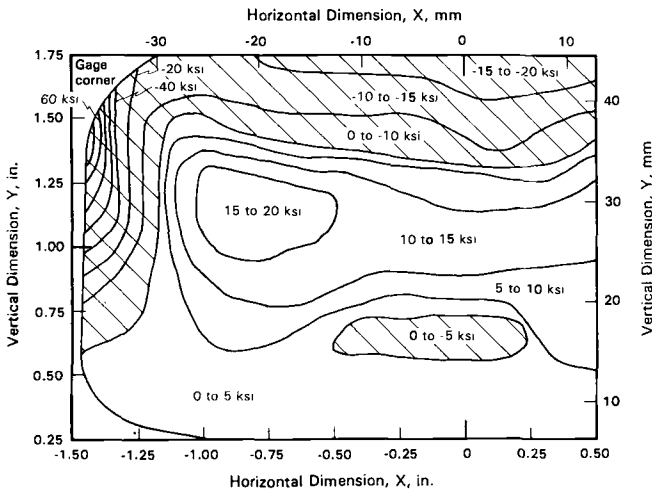


FIG. 7—Longitudinal residual stress pattern in a used railroad rail (1 ksi = 6.895 MPa).

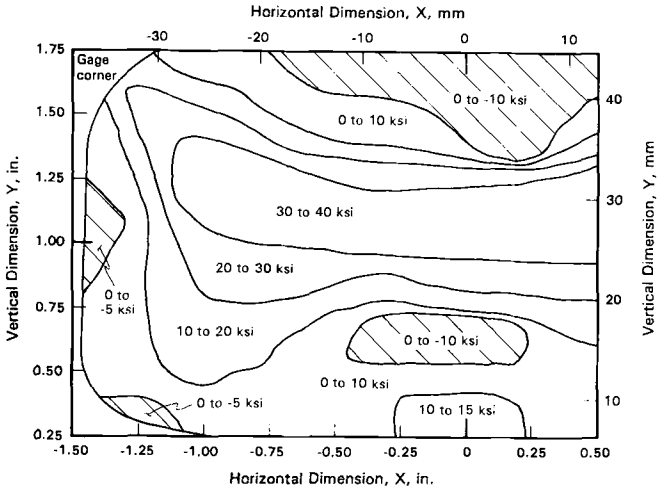


FIG. 8—In-plane, maximum principal residual stress pattern in a used railroad rail (1 ksi = 6.895 MPa).

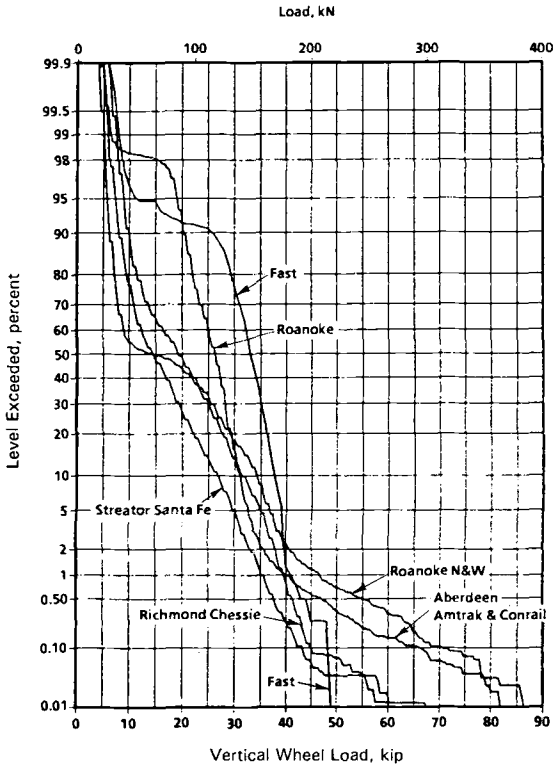


FIG. 9—Statistical characterization of wheel/rail loads on concrete ties.

TABLE 1—Four-point bending static strength results for defective rails.

| Rail ID | Apparent Flaw Size, % of Head Area | Breaking Force, (kN) |
|-------------|---------------------------------------|-------------------------|
| 132 RE RAIL | | |
| NW5 | 3 | 547 |
| NW18 | 10 | 391 |
| NW12 | 18 | 436 |
| NW21 | 18 | 378 |
| NW15 | 20 | 480 |
| NW9 | 22 | 471 |
| NW16 | 22 | 658 |
| NW10 | 25 | 383 |
| NW14 | 25 | 338 |
| NW17 | 25 | 369 |
| NW25 | 26 | 240 |
| NW8 | 28 | 383 |
| NW1 | 34 | 400 |
| NW19 | 35 | 356 |
| NW13 | 36 | 365 |
| NW7 | 37 | 431 |
| NW4 | 46 | 133 |
| NW11 | 54 | 338 |
| NW20 | 58 | 205 |
| NW22 | 89 | 102 |
| 136 RE RAIL | | |
| AT6 | 13 | 356 |
| AT4 | 20 | 347 |
| SP18 | 24 | 365 |
| SP2 | 28 | 325 |
| SP31 | 44 | 285 |
| SP34 | 44 | 258 |
| SP1 | 46 | 231 |
| SP6 | 53 | 311 |
| SP30 | 57 | 133 |
| SP15 | 59 | 316 |
| SP27 | 61 | 231 |
| SP12 | 63 | 231 |
| SP19 | 69 | 236 |
| SP7 | 78 | 276 |
| SP28 | 87 | 187 |

four-point loading test fixture with an outside span of 1.52 m and an interior span between load application points of 0.2 m. Each rail was loaded headdown. The equivalent rail bending moment was found to be approximately $M(N\cdot m) = -1.47P$, where P is the applied load. The detail fracture dimensions for different rails with similar size flaws were sufficiently consistent, so that average flaw shape statistics could be tabulated as a function of flaw size and expressed in terms of percentage of head area, as shown in Table 2. The consistency in the dimensional parameters of each size range of detail fractures is apparent, with typical coefficients of variation in the readings (based on 5 or 6 rails within each size range) of 5 to 10%.

TABLE 2—Average dimensions and location of detail fractures in railroad rail [12].

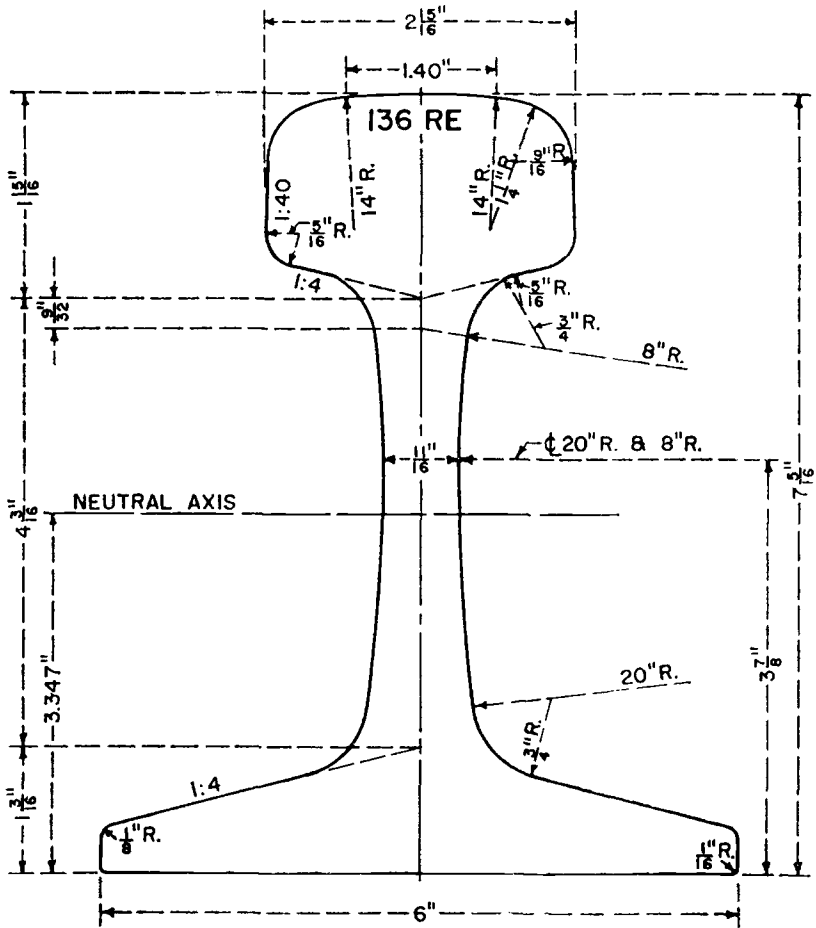
| Average Flaw Size, (% of Head Area) | Average Dimension, mm (Standard Deviation, mm) | | | | |
|-------------------------------------|--|------------------------------|-----------------------|--|--|
| | Upper, Minor Axis of Ellipse | Lower, Minor Axis of Ellipse | Major Axis of Ellipse | Depth of Center of Ellipse Beneath Running Surface | Distance of Center of Ellipse from Gage Face |
| 12.5 | 9.1 (1.0) | 9.7 (1.3) | 13.2 (1.3) | 21.8 (1.8) | 19.8 (1.0) |
| 17.5 | 10.7 (1.5) | 13.0 (0.8) | 15.7 (1.3) | 19.6 (1.8) | 22.4 (0.8) |
| 22.5 | 9.9 (0.8) | 14.7 (1.0) | 17.3 (1.5) | 17.5 (3.0) | 22.4 (0.5) |
| 27.5 | 11.7 (1.0) | 16.3 (0.8) | 19.3 (0.8) | 16.8 (1.5) | 24.1 (0.5) |
| 33.5 | 12.2 (1.0) | 17.8 (2.0) | 21.3 (0.8) | 14.0 (2.0) | 24.9 (1.3) |
| 41.0 | 12.7 (1.5) | 19.8 (1.0) | 23.6 (1.8) | 12.2 (2.5) | 25.7 (1.3) |

Thermal Stresses in Rail

Much of today's rail is continuously welded rail (CWR), made up of sections of rail welded together to form long, continuous sections of track. This is done to avoid the commonly observed adverse effects of rail joints, for example, joint failures and wheel/rail impact loads from height mismatch at a joint. However, these long continuous sections of rail can develop substantial tensile or compressive thermal stresses. These thermal stresses develop as a result of a temperature differential between the so-called rail neutral temperature (at which the longitudinal thermal stress is zero) and the current rail temperature. Initially, the rail neutral temperature is approximately the same as the laying temperature for the rail, but over time the neutral temperature can shift up or down relative to the laying temperature because of shifts in the ballast beneath the ties and other disturbances to the original track condition. Temperatures above the neutral temperature lead to longitudinal compressive stresses in the rail while temperatures below the neutral temperature lead to longitudinal tensile stresses in the rail. This is an especially serious concern in long sections of straight (tangent) track, although curved CWR can also suffer from gage-widening or lateral shift due to thermal stresses.

Typical Wheel-Induced Rail Stresses

The nature and severity of wheel-induced rail stresses vary greatly, depending on a variety of rail and service parameters. The specific case considered here is that of a 133 kN wheel force applied to a 67.6 kg/m rail (Fig. 10) [14]. The load application point was chosen to be approximately 20 mm off-center, toward the gage side, to represent a fairly typical loading point (based on commonly observed head wear patterns). The predicted longitudinal stresses are shown (Fig. 11) for a rail cross-section immediately under the load point. Note that the minimum stress magnitudes are shown, since the head is almost completely in compression. Of course, the greatest compression stresses are predicted near the running surface. The stresses decrease in absolute magnitude farther down in the head of the rail and farther toward the field side of the rail. The maximum in-plane compressive-stress pattern is even more localized around the point of contact (Fig. 12). The direction of maximum in-plane compression stresses is essentially vertical directly under the load point and slanted away from the load point toward the gage face and the center of the rail. (The static and active stresses that are produced within a rail are fully three-dimensional and very complex to model. For purposes of this discussion, only the axial components of stress are considered.)



| | Area Sq In | Percent | Moment of inertia | |
|-------|---------------|---------|-------------------|------------------------------|
| Head | 4.86 | 36.4 | 94.9 | Section modulus, head |
| Web | 3.62 | 27.1 | 28.3 | Section modulus, base |
| Base | 4.87 | 36.5 | 7.11 | Ratio m.i. to area |
| | | | 1.79 | Ratio s.m. head to area |
| | | | 1.22 | Ratio height to base |
| Total | 13.35 | 100.0 | 136.2 | Calculated weight, lb per yd |

Fig. 6—136 RE rail section.

References, Vol. 63, 1962, pp. 498, 768.

(1971)

FIG. 10—Standard cross-sectional dimensions for a 136 RE rail (1 in. = 25.4 mm).

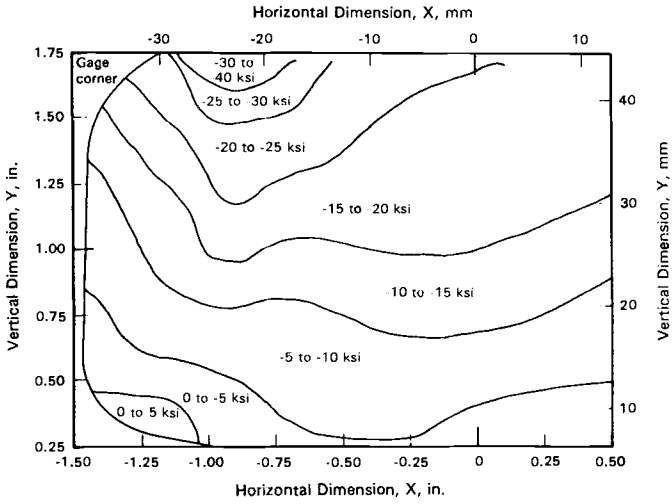


FIG. 11—Predicted longitudinal stress pattern due to a 133 kN off-center wheel load (1 ksi = 6.895 MPa).

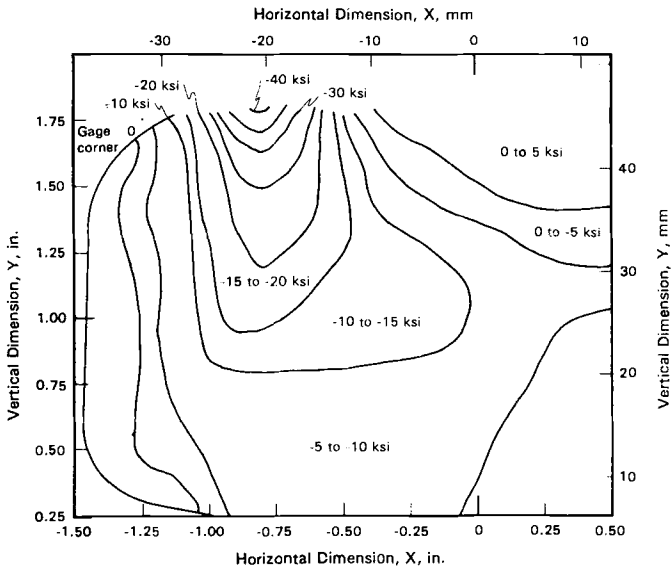


FIG. 12—Predicted in-plane, maximum principal stress pattern due to a 133-kN off-center wheel load (1 ksi = 6.895 MPa).

Rail Crack Growth and Fatigue Properties

In a major study of the fatigue crack propagation properties of standard carbon-steel rail (Standard Specification for Carbon-Steel Rails, ASTM A1-68a) [15] undertaken in the mid-1970s, data were developed for a range of stress ratios and test temperatures, as well as for each orthogonal cracking plane in the rail head [15]. Threshold experiments were also done at three stress ratios ($R = -1.0, 0.0,$ and 0.50) to develop estimates of threshold stress intensity levels, below which crack-growth rates would asymptotically approach zero [16].

With this collection of data it was possible to develop a relatively general crack growth model for average crack growth trends ranging from near threshold through fracture instability for a range of different stress ratios [17]. The equation is stated as follows

$$\frac{da}{dN} = C(1 - R)^2 (K_{max}^2 - K_{th}^2) \frac{K_{max}^n}{K_c - K_{max}} \tag{1}$$

where K_{max} is the maximum crack tip stress intensity at any point in time, and K_c and K_{th} are estimates of the plane stress fracture toughness and threshold stress intensity factor as shown in Fig. 13. If the stress cycle involves a stress ratio less than zero, the value of R in Eq 1 was taken to be zero (that is, the compressive part of the cycle was not considered to influence the crack growth rate). The average data trends compared to the crack growth predictions are shown in Fig. 13 for L/T orientation cracks (longitudinal loading on a transverse crack within the rail head).

The fatigue crack initiation properties of rail steels were also characterized in a later study [18]. These results are presented (Fig. 14) in terms of equivalent strain versus cycles to crack initiation, where the equivalent strain parameter was defined as

$$\epsilon_{eq} = (\Delta\epsilon)^m (\sigma_{max})^{1-m} \tag{2}$$

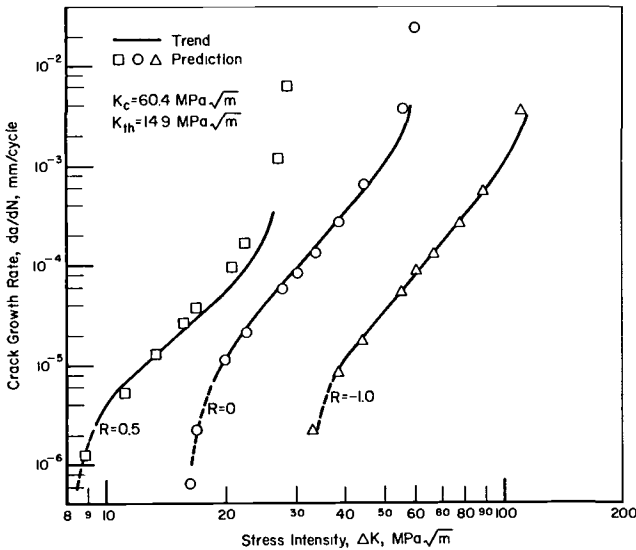


FIG. 13— L/T orientation fatigue-crack growth properties of rail steel, predicted versus actual.

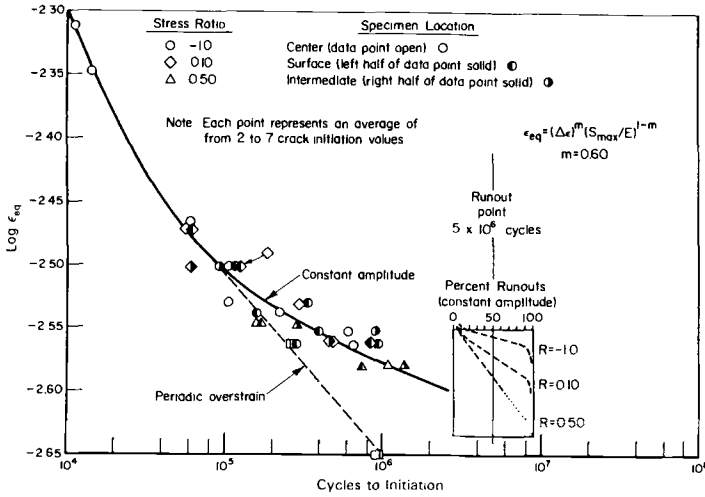


FIG. 14—Crack initiation fatigue properties of rail steel as a function of equivalent strain.

with an optimum m value of approximately 0.6. An approximate relationship between cyclically stable stresses and strains was also developed as follows

$$\Delta\epsilon = \frac{2S_a}{E}, \text{ for } \Delta\epsilon \text{ less than } \Delta\epsilon(1) \tag{3}$$

$$\Delta\epsilon = 2 \left(\frac{S_a}{K_1} \right)^{1/n_1}, \text{ for } \Delta\epsilon > \Delta\epsilon(1), \leq \Delta\epsilon(2) \tag{4}$$

$$\Delta\epsilon = 2 \left(\frac{S_a}{K_2} \right)^{1/n_2}, \Delta\epsilon > \Delta\epsilon(2) \tag{5}$$

where K_1 and K_2 are strength coefficients, n_1 and n_2 are strain hardening exponents, and $\Delta\epsilon(1)$ and $\Delta\epsilon(2)$ are specific values of $\Delta\epsilon$ that denote break points in the tri-log-linear stress-strain curve approximation. The approximate values for the constants in Eqs 3 through 5 are as follows for the tested rail material

- $E = 20 \times 10^4 \text{ MPa,}$
- $K_1 = 2.36 \cdot 10^4 \text{ MPa,}$
- $\Delta\epsilon(1) = 2.7 \cdot 10^3,$
- $n_1 = 0.677,$
- $S_a(1) = 270 \text{ MPa,}$
- $K_2 = 5.55 \times 10^3 \text{ MPa,}$
- $\Delta\epsilon(2) = 4.0 \times 10^{-3},$
- $n_2 = 0.443, \text{ and}$
- $S_a(2) = 354 \text{ MPa.}$

A small number of periodic overstrain, crack initiation fatigue experiments were also

TABLE 3—Periodic overstrain results on new rail material.

| Strain Range, % | | Frequency of Overstrain | Strain Range Components, % | | Stable Stress Range, MPa | Total Cycles to Failure |
|-----------------|--------------|-------------------------|----------------------------|---------|--------------------------|-------------------------|
| Small Cycles | Large Cycles | | Elastic | Plastic | | |
| 0.375 | 0.800 | 10 every 1000 | 0.338 | 0.037 | 643 | 209 240 |
| | | | 0.342 | 0.033 | 629 | 217 600 |
| 0.375 | 0.800 | 10 every 10 000 | 0.345 | 0.030 | 676 | 270 200 |
| | | | 0.346 | 0.029 | 645 | 289 400 |
| 0.300 | 0.800 | 10 every 1000 | 0.289 | 0.011 | 546 | 422 820 |
| | | | 0.296 | 0.004 | 545 | 401 270 |
| 0.300 | 0.800 | 10 every 10 000 | 0.268 | 0.032 | 525 | 900 700 |
| | | | 0.271 | 0.029 | 516 | 930 785 |

performed to evaluate the potential influence of occasional high-stress excursions on the long-life fatigue resistance of rail steel. Those results are presented in Table 3 and shown in Fig. 15. Compared with the expected cycles to crack initiation based on previously generated constant amplitude data, the periodic overstrain tests produced fatigue lives 3 to 5 times shorter than would have been expected if the 0.375% strain range cycles were non-damaging and produced fatigue lives 10 to 50 times shorter than would have been expected if the 0.300% strain range cycles were non-damaging. Significantly, the predictions of fatigue life for simulated service, variable amplitude loading conditions were much more accurately predicted when using the periodic overstrain fatigue curve for the damage summations compared with the constant amplitude fatigue curve [16].

In addition to the information presented here, there are numerous other sources of data on the fatigue and crack growth properties of rail steels, for example, the work of Fowler [19] and Park and Fletcher [20].

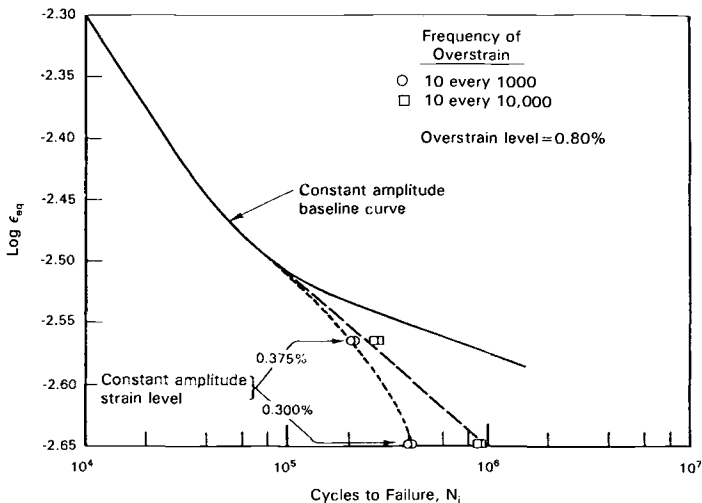


FIG. 15—Effect of periodic overstrains on long-life fatigue properties of rail steel.

Part 2—Student Questions

The following questions are presented to stimulate a careful review of the background information provided in Part 1 and to promote discussion within a class or study group. To heighten the significance of these questions it may be useful to consider the position of railroad maintenance engineers who must make decisions concerning the integrity of the rail lines they inspect and maintain. Or perhaps an even more meaningful, hypothetical situation to consider would be that of an FRA engineer within the Office of Safety or the Office of Research and Development. Your task could be to assess the research that has been done and to evaluate whether important basic questions are understood well enough to propose regulations regarding rail maintenance, inspection, and replacement that will ensure the safe operation of today's rail transportation and freight systems. In addition, if representatives from the Association of American Railroads (AAR) question the merit of these proposed regulations, how will you defend your recommendations? Does additional research need to be performed, and if so, specifically what issues need to be addressed and how can experiments be devised to better understand the unresolved issues?

What Causes Subsurface Shells?

In order to prevent (or at least minimize) subsurface shells it is necessary to develop an understanding of the conditions that lead to subsurface shells in a railroad rail. To what extent do factors such as the magnitude of wheel loads, tensile strength of the material, and the rail/wheel interface condition influence the development of shells? To what extent might track conditions such as the type of ballast and the condition and type of ties be expected to influence the severity and frequency of shell formation?

Why Do Only Certain Shells Become Detail Fractures?

What are the probable key factors that determine when a shell will turn downward and become a detail fracture? And why do some shells grow to substantial lengths while never turning downward to form detail fractures?

Why Do Most Detail Fractures Grow Subsurface?

Detail fractures typically remain contained within the head of the rail until they are quite large. As a result, when left undetected, they occasionally lead to catastrophic failure of a rail. Based on the information presented in Part 1 of this paper and other relevant information that can be found, what factors would most likely contribute to this phenomenon? What conditions must exist before a detail fracture does break through to a free surface?

How Should Detail Fractures Be Modeled?

How could a model be formulated to represent the non-self-similar crack growth of a detail fracture? The model should accommodate the growth of a shell in a plane nearly parallel to the running surface and the subsequent turning of the defect downward onto a plane approximately perpendicular to the original shell. Predicted growth rates should be nearly constant for detail fractures ranging from about 10 to 35% of the head area. Both thermal and residual stresses must be accommodated, in addition to the dynamic, wheel-induced rail stresses.

What Factors Most Influence Rail Head Crack Initiation?

There are numerous variables that can significantly influence the rate of formation of fatigue cracks, which can subsequently lead to shells and detail fractures. What factors would be expected to most strongly influence rail head fatigue crack initiation rates? Some obvious possibilities are:

- (1) rail cleanliness,
- (2) average axle load,
- (3) traffic severity,
- (4) track vertical modulus,
- (5) combined vertical and lateral loads,
- (6) thermal stresses,
- (7) residual stresses,
- (8) head hardness, and
- (9) degree of offset in wheel loading.

The first task in identifying the factors that most influence rail head fatigue crack initiation rates is an assessment of the required background information. What must be known to properly address the influence of one or all of these factors on rail fatigue crack initiation resistance? With available information presented in Part 1 of this paper and elsewhere, which items should be chosen as most important in terms of their influence on rail head fatigue crack initiation lives? What is the justification for these selections? Assuming these selections are reasonable, what measures could be taken to minimize their effect and thereby maximize rail head fatigue crack initiation resistance?

Part 3—Responses to Student Questions

Formation of Subsurface Shells

Subsurface shells are typically associated with complex inclusions (stringers) oriented longitudinally in the rail head at a depth of 6 to 10 mm beneath the running surface. Regardless of the depth beneath the running surface, the shell initiation process is aided by the presence of complex inclusions. In most cases that have been examined [6,7] the inclusions contained aluminum and silicon, and could generally be classified as “oxide-type” inclusions. Aluminum is added for deoxidation, while calcium may arise from interactions with the slag to form non-metallic inclusions. Because nonmetallic (oxide) particles are hard and brittle, the larger inclusions, especially those oriented parallel to the running surface, serve as candidate shell crack initiation sites.

The loading on the rail and its strength are also factors in the likelihood of shell crack formation. The frequency of shell crack formation has been found to be directly related to the magnitude of the stresses generated during rail/wheel interaction. Everything else being equal, increases in the tensile strength and fatigue resistance of the rail steel have been found to decrease the rate of shell cracking [21].

However, the biggest factor in decreasing the frequency of shell crack formation appears to be rail cleanliness (which removes the majority of the likely shell crack initiation sites). An interesting study completed in Japan [22] on over 100 rails with shell defects showed that 70% of the defective rails were rails taken from the top of a semi-killed ingot (which generally contains the largest concentration of inclusions). Other studies in Germany [23] and the former Soviet Union [24] have also shown that shell formation in the heads of rails

can be reduced by decreasing the number and size of nonmetallic inclusions present in the steel.

Microhardness measurements have also been conducted on several rail heads containing shell defects to determine whether there was any relationship between the gradients in the hardness of the rail head surface material [3] and the location of the shell in that same rail. These studies showed that the shells were typically located at the interface between the substantially cold-worked surface layer and the softer material in the bulk of the rail head. This depth within the head of the rail also corresponded approximately with the region that typically contains large in-plane, tensile residual stresses [6].

Transition of Shells into Transverse Defects

The depth of a shell may be the most important factor in determining whether it will turn downward and form a detail fracture. Shells not associated with detail fractures are typically nearer the running surface. The total area and length of a shell are poor indicators of whether a shell will become a detail fracture [6].

Shells that initiate about 10 mm below the running surface tend to be most critical in terms of subsequent formation of detail fractures. It is interesting to note that this depth beneath the running surface corresponds approximately with the depth at which the longitudinal residual stresses become tensile, as shown earlier in Fig. 9. Even though the "live" longitudinal stresses that result from wheel passage at this depth in the rail head are compressive, the tensile residual stresses create a condition from which a tensile stress excursion at the crack tip can result. In other words, when a shell crack branches downward at a depth within the head of the rail where it becomes exposed to significant tensile residual stresses, those tensile residual stresses may "lift" the otherwise compressive stress excursion into tension. The tensile stresses can lead to a significant Mode I stress intensity at the shell crack tip, prompt it to turn, and cause it to progress downward, essentially perpendicular to the rail's running surface. This concept is discussed in some detail in a later section of this paper entitled, *Modelling of Detail Fractures*.

A key assumption in this interpretation of the crack growth process is that Mode I crack growth will tend to predominate in the detail fracture process. This assumption is based on evidence that cracks in rail steel tend to "prefer" Mode I crack growth. Earlier experiments at Battelle designed to force cracks in rail steel to grow in Mode II or III were unsuccessful (Standard Specification for Carbon-Steel Rails, ASTM A1-68a) showing the strong tendency for fatigue cracks to propagate perpendicular to the maximum principal stress direction. This appears to be true even in the early stages of shell crack formation. Evidence suggests that it is only because the Mode I stress intensity along the axis of the rail eventually exceeds the in-plane Mode I stress intensity that the crack turns almost perpendicular to its original direction and transitions from a shell to a transverse defect. Since the longitudinal tensile residual stresses tend to be greatest near the center of the rail head, the detail fracture tends to propagate most rapidly in that direction.

It is certainly possible that the size and orientation of the inclusions also influence whether a shell will turn into a detail fracture. Unfortunately, no evidence to support this argument has been found since extensive mechanical damage is generally apparent on the shell fracture surfaces (caused by the force of the railroad wheels rubbing the two crack surfaces together). Nondestructive techniques are needed for the examination of these defects once a shell crack is detected in a rail. Such techniques could be employed to define the size, shape, and orientation of these defects and to track the growth of a shell crack in service, or in simulated service conditions, such as at the Facility for Accelerated Service Testing (FAST) at TTC.

Growth of Detail Fractures in the Head of a Rail

The physical evidence from retired, defective rails suggests that a detail fracture typically remains contained within the head of a rail until it is quite large because of longitudinal compressive residual stresses that tend to build up along the gage face and the running surface. Until there is a major redistribution of these residual stresses due to propagation of the detail fracture across the head of the rail, there is a minimal Mode I crack driving force along the front of the crack near the gage face and running surface. Since the compressive residual stresses near the running surface tend to be reinforced by continued wheel passages, equilibrium demands that they be offset by an expanding tensile residual stress envelope surrounding the detail fracture. This argument is supported by the common observation that detail fractures tend to grow in a non-self-similar manner across the rail head and downward through it, while there is very little crack growth upward or toward the gage face. Figures 1 and 2 provide examples of this phenomenon.

The angle of the transverse crack, once established, is usually not perfectly vertical, but is tilted from vertical by 0.15 to 0.30 rad. It is believed that this angle is dictated by the direction of traffic, and that drag forces created by the passage of undriven wheels cause a shift in the three-dimensional variable stress field sufficient to tilt the maximum axial principal stress direction from horizontal. The detail fracture pattern in the AT-5 rail (Fig. 1) is a dramatic example of this effect.

Modeling of Detail Fractures

There is no generally accepted approach for modeling the non-self-similar crack growth of a detail fracture. The issue has been examined in considerable detail by various researchers, for example, Orringer et al. [13] and Besuner [25] in the United States, and Mair and Groenhout [26] and Chipperfield [27] in Australia. An alternate approach for modeling the growth of a detail fracture was also developed by the author in Ref 6 and explained in more detail in Refs 28 and 29. A brief summary of the approach is included here.

The combination of residual and wheel-induced stresses apparently provide the major driving force for detail fracture growth. If these stresses are considered together, it is possible to construct a reasonable pattern of the stresses within the rail that are effective in crack initiation and growth. Figure 16 shows the pattern of stress ratios (the ratio of minimum to maximum stress in a wheel-induced stress cycle) that results from the combination of longitudinal residual stresses with predicted wheel-induced stresses. This figure shows that the gage face and running surface withstand stress cycles completely in compression, while the interior of the head experiences stress cycles in tension, and even some cycles with tensile mean stresses. This prediction of cyclic tensile stresses in the longitudinal direction within the head of the rail is significant because it is generally conceded that fatigue cracks are most prone to propagate in a cyclic tensile stress field. Even if a crack does initiate in a largely compressive cyclic stress field [30], it is not likely to propagate. Therefore, it appears unlikely that transverse cracks would initiate near the gage face or running surface and even if they did they would not propagate, at least not perpendicular to the running surface. Transverse cracks would have the greatest tendency for initiation and growth in the interior of the rail where the majority of the stress cycle is in tension, that is, stress ratios above -1.0 . This predicted trend is supported by field data on flawed rails containing transverse defects and detail fractures.

The model that was developed to describe these cracking patterns is based on an embedded elliptical flaw that can change in aspect ratio and tilt. Flaw growth is considered at points

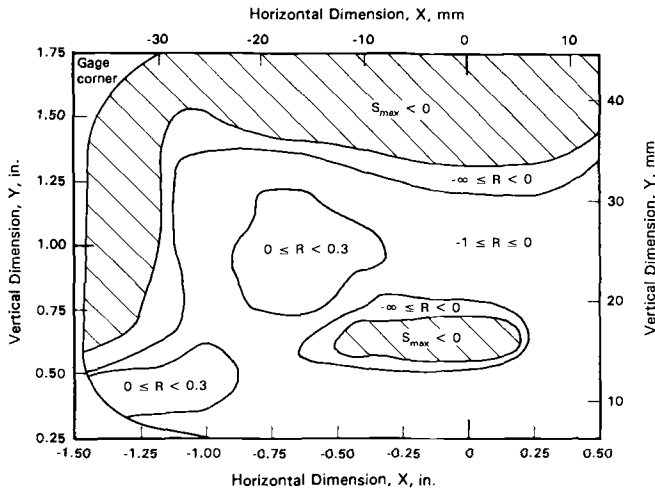


FIG. 16—Estimated pattern of stress ratios resulting from the combination of longitudinal residual stresses and active stresses induced by a 133-kN wheel load.

on the perimeter of an initial small ellipse. The stresses effective in crack growth are assumed to result from combined residual and wheel-induced stresses. The crack growth rate is estimated based on the local Mode I stress intensity factor. After small increments of growth have occurred around the ellipse, a new ellipse is established to approximate the expanded flaw. The process is repeated incrementally and the size and shape of the flaw is monitored as a function of wheel passages.

As mentioned earlier, the stresses effective for crack growth are assumed to arise from the combination of residual and wheel-induced stresses. (Thermal stresses could also be influential; if they are believed to be significant they can be introduced additively throughout the rail cross-section.) The stress field that is believed to drive transverse crack growth is shown schematically in Fig. 17. Three components of longitudinal stress are shown. The first, shown as a broken line, represents the typical distribution of residual stresses ranging from the running surface to the base of the head that develops approximately 20 mm inward from the gage face. The second, shown as a dashed line, represents the wheel-induced stresses, which are entirely compressive from the running surface down through the rail head. The summation of these two longitudinal stress components is represented by the third line, which is dotted. At any given depth, the difference between the first and third stress components represents the predicted stress excursion. Near the running surface this stress excursion is entirely compressive. Further beneath the running surface this stress excursion develops a significant positive component, at least in a used rail that has developed appreciable longitudinal tensile residual stresses. This predicted stress excursion is shown as a continuous sine wave (Fig. 17), which develops 3.14 rad out-of-phase with the applied wheel load.

To begin the crack growth estimation process, a particular point in the rail cross-section was chosen and that point defined the centroid of the hypothetical shell and transverse defects. The assumed shape and tilt of the shell and transverse crack were also specified. The crack growth rates at any point along the periphery of either ellipse was computed based on the local estimate of the crack tip stress intensity. The stress intensity formulation for a completely embedded elliptical flaw was used [31] with no edge or near surface correction

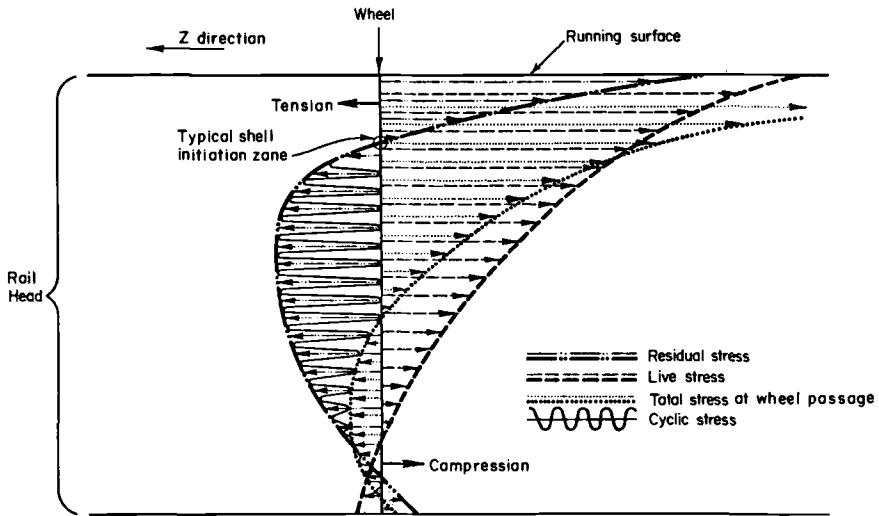


FIG. 17—Predicted longitudinal stresses shown on a vertical plane through the rail head.

factors included. The stress range that was used in each computation of stress intensity was based on the combined residual and active stress excursions (in tension) that were predicted perpendicular to the plane of the crack at 12 sites uniformly spaced around each ellipse.

The residual stress field was assumed to remain constant, even though the cracked area obviously could not sustain any tensile residual stress. This choice was made because it was believed to be conservative, since static equilibrium required that the remaining uncracked area previously in tension had to move to still higher tension if the areas of the head that were experiencing compressive residual stresses remained in compression.

The pattern of evolution of each elliptical flaw was not constrained. The flaws could elongate, translate, or rotate, as long as they remained in the same plane. After incremental extensions of each ellipse, the new ellipse was defined through a regression procedure that best described the now-distorted new crack front.

Using this basic crack growth algorithm, several different cases were run so that comparisons with physically observed cracking patterns could be made. The predicted results for a detail fracture growing in the transverse plane are shown in Fig. 18. It is evident from this figure that the initial transverse defect, which was assumed to be a somewhat elongated ellipse tilted approximately 0.35 rad from vertical, grew predominately downward and inward toward the center of the rail. This pattern was similar to that observed in many actual detail fractures (for example, see Fig. 1).

An example of the shell growth patterns that were obtained is shown in Fig. 19. The initial flaw was assumed to be elliptical. This initial flaw immediately began to elongate along the longitudinal axis of the rail and to grow only moderately in the transverse direction. This pattern of shell growth has been observed in various defective rails.

Another important feature of the shell growth analysis was that the rate of shell growth was found to be highest for shells located approximately 10 mm below the rail surface. This depth corresponds favorably with the location of many nonsurface-connected shells. At depths below 10 mm, the tendency for shell crack growth diminished substantially. This lent further credence to the idea that there is a critical shell depth, below which shells are less

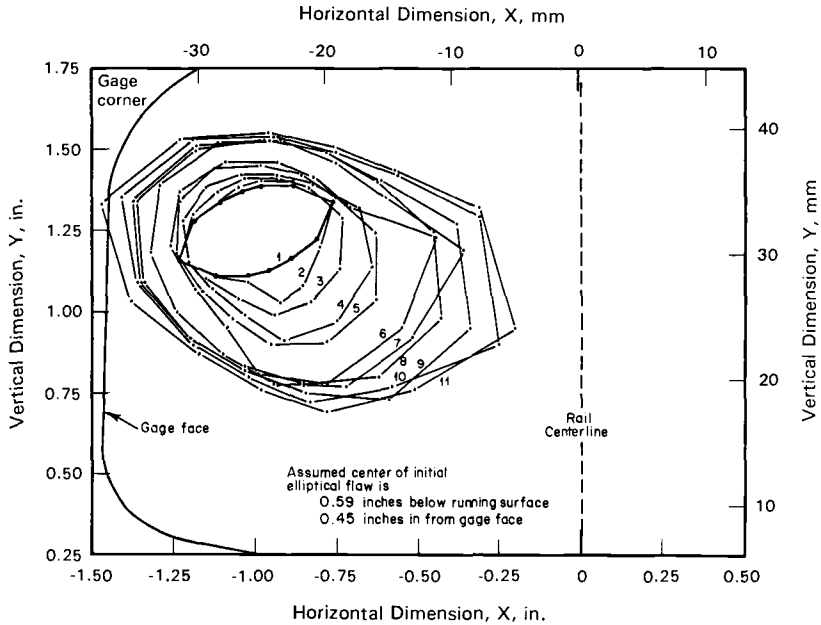


FIG. 18—Predicted crack growth pattern for a transverse defect in a rail head.

likely to continue as shells and are more likely to turn downward and continue in the transverse plane as a detail fracture.

Factors Influencing Rail Head Crack Initiation

Many factors influence the likelihood of fatigue crack initiation in railroad rails. Like many other critical structural elements, fatigue cracks in railroad rails tend to initiate at points of stress concentration, either geometric or microstructural. In the head of a railroad rail, the most likely site for crack initiation is a nonmetallic inclusion. The rate at which cracks will form is directly related to the severity of the loading on the rail and the degree of constraint imposed on the rail by the ties and ballast. Good ballast and ties, which today are often made of concrete, provide higher values of rail vertical modulus, and this tends to reduce rail bending stresses. However, the rail vertical modulus has little effect on the severity of wheel/rail contact stresses, which are primarily dependent on the quality of the wheel/rail interface.

A number of techniques are used to minimize the severity of wheel/rail contact stresses and to minimize their effect. Head grinding or profiling is sometimes used to maintain an optimum wheel/rail contact pattern. Rail lubrication is used regularly on some rail lines [32]. The use of head-hardened and heat-treated rails (to achieve higher overall rail hardness and strength) is becoming more common [33,34].

There have been a variety of studies that have focused on prediction of the effect of operational and material variables on fatigue crack initiation rates in rail steel, for example, Refs 35 and 36. Excerpts from a third study [37] are included here.

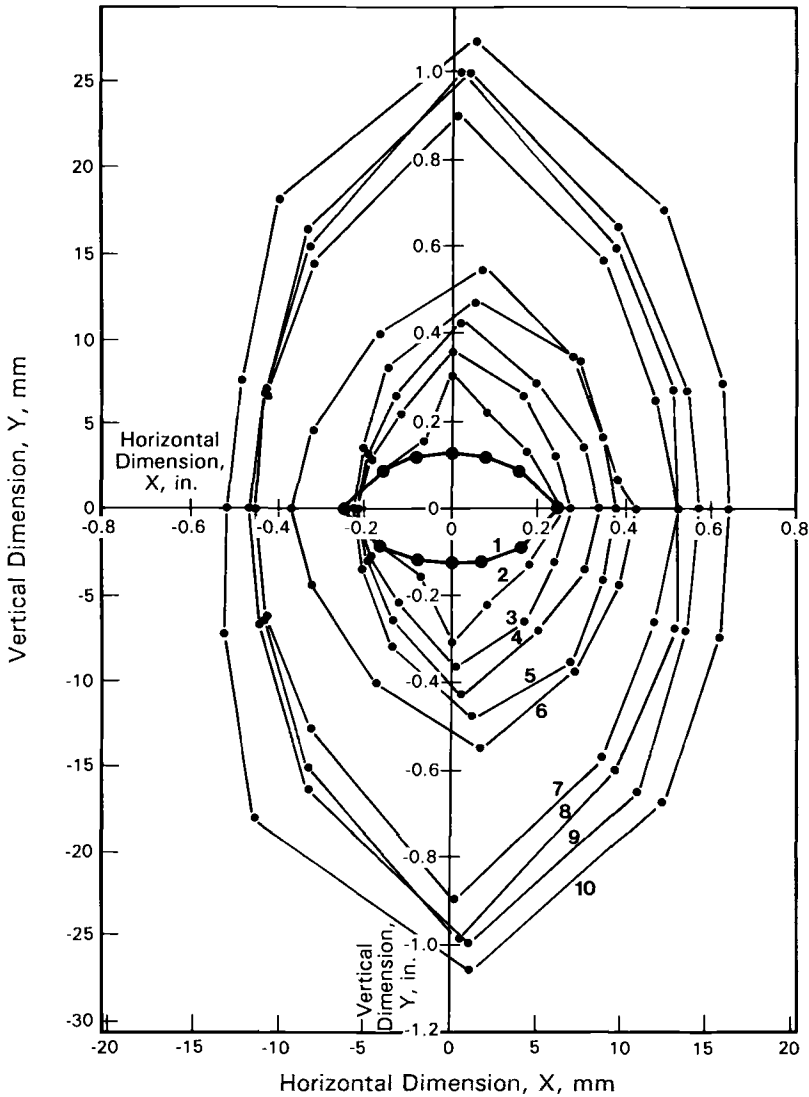


FIG. 19—Predicted crack growth pattern for a shell defect in a rail head.

In this study it was found that variations in rail loads, track support conditions, and the quality and configuration of the rails combine to form a large number of different, potential operating conditions. Variations in some of these conditions greatly affect the stress state and the rate of fatigue damage accumulation while variations in some other operating conditions (within realistic ranges) do not produce significant differences in rail stresses and predicted fatigue lives.

The anticipated influence of these various factors in combination on rail fatigue lives was addressed through a 45-element parametric study. The variety of conditions examined in this parametric study is illustrated in Table 4. (Obviously, only selected combinations of these

TABLE 4—Matrix of conditions chosen for the parametric study of rail fatigue.

| Variable | Units | Levels Examined |
|---------------------------|--|-----------------|
| Rail size | kg/m | 59.2 |
| | | 65.6 |
| | | 67.6 |
| | | 89 |
| Wheel/rail vertical force | kN | 133 |
| | | 222 |
| Wheel/Rail lateral force | kN | 0 |
| | | 44 |
| Wheel/rail loading point | mm from centerline of rail, positive toward gage face | -13.3 |
| | | 0.0 |
| | | 20.1 |
| | | 13.8 |
| Track vertical modulus | MPa | 34.5 |
| | | 55.2 |
| Rail head wear | mm | 0.0 |
| | | 7.6 |

variables were chosen for analysis.) To complete the analysis for each parametric case, a total of 26 locations within the head of the rail were examined. The location of these points coincided with nodal points within the finite element mesh used to generate values of stress and strain.

The most critical locations in the rail head were typically in the upper third of the head toward the gage face. Interestingly, these sites generally corresponded to the location of maximum tensile residual stress. All analyses were based on an eight-level train spectrum developed from a combination of several different train spectra, as shown in Table 5. Periodic overstrain fatigue data trends were used for the cumulative damage analysis.

Using a uniaxial fatigue, equivalent strain model, computed axial rail stresses due to wheel loading were combined with estimated residual stresses to make crack initiation life predictions. Unworn and worn rails were treated as two major categories; type of traffic, lateral load, and vertical modulus were treated as subcases within these categories. The position of the contact patch was found to be a minor factor on predicted lives, except for the worn rail cases, where the contact patch, when shifted from the rail center line toward the gage face, produced significantly higher stresses and shorter fatigue life estimates.

Crack initiation life estimates varied from about 3 to 20 TN of traffic [300 to 2 500 million gross tons (MGT)] for the various cases examined. A 45 kN lateral load typically reduced

TABLE 5—Equivalent train spectrum used for crack initiation fatigue analyses.

| Severity Level, % of Maximum | Cycles per Block | Cumulative Frequency of Occurrence, % | Wheel Load Equivalent |
|---------------------------------|------------------|--|-----------------------|
| 100.9 | 1 | 0.3 | 222 kN, unit train |
| 83.2 | 5 | 2.0 | ... |
| 76.6 | 6 | 4.0 | ... |
| 68.4 | 18 | 10.0 | ... |
| 58.4 | 30 | 20.0 | 133 kN, mixed freight |
| 48.4 | 60 | 40.0 | 133 kN, unit train |
| 35.0 | 60 | 60.0 | ... |
| 23.3 | 120 | 100.0 | ... |

crack initiation life estimates by about a factor of 2, while a low vertical modulus (of about 14 MPa) reduced life estimates by almost a factor of 3 compared with near-optimum vertical modulus conditions (of about 55 MPa). Heavy traffic, involving wheel loads roughly 20% about normal mixed traffic, were predicted to reduce crack initiation lives by roughly 35%. A substantially worn rail, with about 18% of the head area removed, showed substantially higher axial stresses due to wheel loading, and therefore, crack initiation lives were predicted to be about a factor of 2 lower than for unworn rail. (In actual service the wear is normally gradual, which would tend to make the worn rail life estimates somewhat conservative, because the critical damage sites would shift slightly over time.)

Beyond the factors considered in the original parametric analysis, the influence of three other factors on sub-surface crack initiation were also examined: (1) thermal stresses, (2) nonmetallic inclusions, and (3) class of track. A series of hypothetical cases were constructed based on three different load severity curves, as shown in Fig. 20, representing: (1) a nominal location in a well maintained track, (2) a high load location in a well-maintained track, and (3) a high load location in a lower class track. Both 0 and 70 MPa thermal stress conditions were examined. The 70 MPa thermal stress was assumed based on a $-\Delta T$ of about 40°C from the neutral temperature and a coefficient of thermal expansion of 8.6×10^{-6} m/m/C. The influence of potential inclusions at critical sites in the rail cross-section were simply represented by stress concentration factors ranging from 1.0 (no inclusion) to 3.0 (relatively flat, hard inclusion in the rail cross-section).

The analyses that were performed showed that inclusions would be expected to be quite damaging if they happened to lie in a tensile residual stress zone in the rail head. Reductions

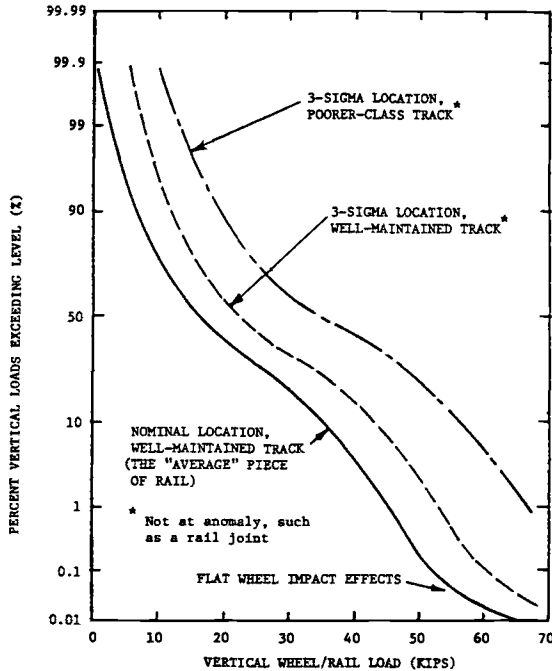


FIG. 20—Example of vertical wheel/rail load spectra due to spatial effects along a track and due to track geometry quality.

in fatigue life of a factor of 10 were predicted for a defective rail with a $K_t = 3$ inclusion compared with a rail without such a defect. If a 70 MPa thermal stress was also superimposed, then the crack initiation fatigue life was reduced by another factor of 3. In comparison with a nominal load location in a well maintained track, fatigue lives were predicted to be 4 times lower at high load locations in a lower class track (with a low vertical modulus of 14 MPa). Depending on the exact combination of deleterious factors, service lives as low as 0.2 TN (20 MGT) were predicted, compared with the "good" rail life prediction of about 20 TN (2500 MGT). It should be noted that these analyses did not include wear as a rail removal criteria; many rails are removed from service because of loss of head area and head grinding or both, before they accumulated about 4 TN (500 MGT) of traffic.

Hypothesis Concerning Detail Fracture Formation

As a result of the various research efforts undertaken over the past decade at Battelle [3-7,28,29] a hypothesis concerning the process of detail fracture formation has been developed. The hypothesis is based on two key elements:

Large cyclic compressive stresses occur in the rail head. These stresses cause fatigue damage and occasional cracks, especially at sites where nonmetallic (oxide) inclusions are present. However, most of these cracks are of little consequence and will normally show erratic growth, if any. A few cracks which develop in the area of large cyclic tensile stresses (immediately under the plastically deformed layer of material) will grow as a result of the cyclic in-plane tensile stresses. Such a crack develops into a shell.

All shell cracks wander and develop small perturbations from their, "straight" path. If a shell wanders upward it enters a region with rapidly decreasing cyclic in-plane tension. Therefore, the perturbation will not persist, and another perturbation will keep the shell crack approximately in its plane. A perturbation downward also causes the crack to enter a region of rapidly decreasing cyclic in-plane tension. However, a perturbation downward also turns the plane of the crack into a direction of high cyclic axial tension (along the axis of the rail). As a result, such a perturbation can persist, turning the crack decisively downward where it encounters increasing cyclic axial tension, and a detail fracture is formed. Depending upon the relative position of the shell in the head of the rail, it may or may not form a detail fracture. The most critical depth will vary from rail-to-rail and depend on the severity of the wheel/rail loading, which, in turn will influence the resultant rail deformations and residual stress fields that develop.

The hypothesis suggests that shells can propagate in tension and Mode I (crack opening) if they happen to initiate in the zone just below the work hardened surface layer of the rail head. (Although this hypothesis does not specifically address crack initiation, evidence cited earlier suggests that most shells do initiate at oxide inclusions or stringers that happen to be located in this region of high multiaxial stress.) Depending on the exact nature of the residual stress field and the alignment of the shell, this horizontal flaw will continue to grow under the influence of substantial longitudinal tensile stress excursions. If stress conditions are right, a downward perturbation in the direction of the shell will cause it to turn gradually into a transverse plane and once again grow in Mode I, but as a detail fracture rather than a shell. The detail fracture will be constrained to develop as an embedded flaw in the early stages of growth because the crack will be impeded at the gage side and surface of the rail head by compressive longitudinal stresses. After the detail flaw grows through a significant portion of the rail head (usually about 35%), and the internal tensile residual stresses are redistrib-

uted, the flaw will break out on the gage side of the rail. At this point the growth rate of the flaw will accelerate significantly and failure of the rail will be imminent.

Conclusions

Detail fractures from shells represent a serious concern to the rail transportation and freight industry in terms of rail reliability and safety since detail fractures typically initiate and grow within the head of a rail and may go unidentified until the strength of the rail is so deteriorated that a sudden failure may occur, which sometimes leads to a train derailment.

Much has been learned regarding the causes of shell defects in railroad rails and effective means for reducing the frequency of their occurrence have been identified, in particular through improvements in the cleanliness of the rail steel to reduce the number and size of nonmetallic inclusions. Plausible concepts have been developed for modeling the transition of shells into detail fractures and for predicting the pattern and rate (at least qualitatively) of crack growth as a function of various material and operating variables.

Increases in tonnage and axle loads on many U.S. railroad lines have placed greater stress on rails and increased the likelihood of many different types of rail defects, including detail fractures. At the same time, profitability of many rail lines has declined, which has forced many railroads to minimize their budgets for rail inspection and replacement. In response to these opposing forces, the railroad industry has responded with comprehensive inspection programs to find and remove defective rails from track. These inspection systems include detailed track records, most of which are computerized [38]. The FRA has also conducted extensive research to develop improved guidelines for rail inspection [39]. According to these new guidelines, it is now possible for railroads to adjust the frequency of rail inspection based on the rate of defect occurrences and their growth characteristics [40]. The next major hurdle will be to extend this knowledge base to the safe use and maintenance of high speed rail lines that will undoubtedly be developed in the United States in the late 1990s and early 21st Century.

Acknowledgments

The research work that forms the basis for this case study was completed by numerous individuals over a period of several decades. Many of those individuals have been cited in the list of references. At Battelle, Mr. Donald Ahlbeck, Mr. Jeffrey Hadden, Dr. James Kennedy, Dr. Frank Dean, and Mr. Robert Prause have been among the most significant contributors. Mr. Ravi Rungta, currently at General Motors, Harrison Radiator Division, was also a key contributor on the rail fractography work. Dr. David Broek, currently a private consultant, was a major contributor in the crack growth prediction work. Mr. Harold Harrison, who is now the President of Salient Systems, Inc., led much of the early work on wheel/rail load measurements.

Within the Department of Transportation, Dr. Oscar Orringer and Mr. James Morris (now deceased) at VNTSC, Mr. Arne Bang at the FRA, and Dr. Roger Steele at the Association of American Railroads have been major contributors and supporters of this research.

References

- [1] National Transportation Safety Board, "Broken Rails: A Major Cause of Train Accidents," Report NTSB RSS 74-1, National Transportation Safety Board, Washington, D.C., 2 Jan. 1974.

- [2] Mack, G. A. and Hopper, A. T., et al., "Statistical Analysis of Burlington Northern and Atchison, Topeka and Santa Fe Rail Failures," Task 5, final report to the Department of Transportation from Battelle Columbus Laboratories, Cambridge, MA, Contract DOT-TSC-1708, 8 June 1982.
- [3] Rungta, R., Rice, R. C., and Buchheit, R. D., "Post-Service Rail Defect Analysis," first interim report to the Transportation Systems Center, Department of Transportation, Cambridge, MA, July 1982.
- [4] Rice, R. C., Rungta, R., and Buchheit, R. D., "Post-Service Rail Defect Analysis," second interim report to the Transportation Systems Center, Department of Transportation, Cambridge, MA, Jan. 1983.
- [5] Rice, R. C., Rungta, R., and Broek, D., "Post-Service Rail Defect Analysis," third interim report to the Transportation Systems Center, Department of Transportation, Cambridge, MA, July 1983.
- [6] Rice, R. C., Rungta, R., and Scott, P. M., "Post-Service Rail Defect Analysis," fourth technical report to the Transportation Systems Center, Department of Transportation, Cambridge, MA, June 1984.
- [7] Rungta, R. and Rice, R. C., "Shelling Behavior in Rails," final report to the Transportation Systems Center, Department of Transportation, Cambridge, MA, Feb. 1987.
- [8] Campbell, J. E., McIntire, H. O., and Manning, G. K., "Summary Report on the Examination of Rails Which Contain Detail Fractures," *Rail*, Appendix 10-b, American Iron & Steel Institute, Birmingham, AL, 1949, pp. 608-620.
- [9] *Rail Defect Manual*, compiled by Sperry Rail Service, Sperry Division of Automation Industries, Inc., Danbury, CT, 1964, 4th printing, 4/68, p. 38.
- [10] Groom, J. J., "Residual Stresses in Railroad Rails," Battelle Columbus Laboratories, Columbus, OH; paper presented at the 1980 Fourth SESA International Congress on Experimental Mechanics, 25-30 May, see also Federal Railroad Administration Report FRA/ORD83/05, May 1983.
- [11] Ahlbeck, D. R., Harrison, H. D., Tuten, J. M., and Johnson, M. R., "Wheel/Rail Load Data—A Statistical Characterization," Interim Report to the U.S. Department of Transportation, Federal Railroad Administration, Jan. 1979.
- [12] Harrison, H. D. and Tuten, J. M., "Correlation of Concrete Tie Track Performance in Revenue Service and at the Facility for Accelerated Service Testing," Report DOT/FRA/ORD-84/02.1, Vol. I, A Detailed Summary, Final Report, Department of Transportation, Washington, D.C., Aug. 1984.
- [13] Orringer, O., Tang, Y. H., Gordon, J. E., Jeong, D. Y., Morris, J. M., and Perlman, A. B., "Crack Propagation Life of Detail Fractures in Rails," Report DOT/FRA/ORD-88-13, final report, U.S. Department of Transportation, Federal Railroad Administration, Washington, D.C., Oct. 1988.
- [14] *Manual for Railway Engineering*, American Railway Engineering Association, Chicago, IL, 1971, pp. 4-1-6.
- [15] Feddersen, C. E., Buchheit, R. D., and Brock, D., "Fatigue Crack Propagation in Rail Steels," Report FRA/ORD-77/14, interim report by Battelle to the U.S. Department of Transportation, Federal Railroad Administration, Washington, D.C., June 1977.
- [16] Broek, D. and Rice, R. C., "Fatigue Crack Growth Properties of Rail Steels," final report, Part I, submitted by Battelle to the U.S. Department of Transportation, Transportation Systems Center, Washington, D.C., July 1977.
- [17] Broek, D., Rice, R. C., and Steele, R. K., "Prediction of Fatigue Crack Growth in Railroad Rails," presentation to the Transportation Research Board, 5 Aug. 1977.
- [18] Rice, R. C. and Broek, D., "Fatigue Crack Initiation Properties of Rail Steels," Report DOT/FRA/ORD-82/05, final report to the U.S. Department of Transportation, Federal Railroad Administration, Washington, D.C., March 1982.
- [19] Fowler, G. J., "Fatigue Crack Initiation and Propagation in Pearlitic Rail Steels," Ph.D. Thesis, University of California, Los Angeles, 1976.
- [20] Park, Y. J. and Fletcher, F. B., "Fatigue and Fracture Toughness of Standard Carbon and High Strength Rail Steels," Paper 82-HH-21, American Society of Mechanical Engineers, New York, 1982, pp. 1-8.
- [21] Marich, S., "Research on Rail Metallurgy," Paper 78-663-8, Bulletin 663, American Railway Engineering Association, Chicago, IL, 1988.
- [22] Ito, A. and Kurihara, "Shelling of Rails Experienced in Japanese Railways," *Permanent Way Society of Japan*, Vol. 8(2), No. 27, 1965, pp. 17-32.
- [23] Heller, W., "The Development and Further Development of the Quality and Service Properties of Modern Rail Steels," *ETR-Eisenbahntechnische Rundschau*, Jan./Feb. 1971, pp. 71-78.
- [24] Zolotarsky, A. F. and Rauzin, Y. R., "Increasing the Strength of Rails and their Reliability in Service on the Railways of USSR," *Rail International*, Dec. 1971, pp. 908-915.

- [25] Besuner, P. M., "Fracture Mechanics Analysis of Rails with Shell-Initiated Transverse Cracks," *Rail Steels—Developments, Processing, and Use, ASTM STP 644*, D. H. Stone and G. G. Knupp, Eds., American Society for Testing and Materials, Philadelphia, 1978, pp. 303–329.
- [26] Mair, R. I. and Groenhout, R., "The Growth of Transverse Fatigue Defects in the Head of Railway Rails," *Rail Research Papers, Vol. 1*, Melbourne Research Laboratories, Melbourne, Australia, 1988, pp. 170–186.
- [27] Chipperfield, C. G., "Modelling Rail Head Fatigue Using Fracture Mechanics," *Rail Research Papers, Vol. 1*, Melbourne Research Laboratories, Melbourne, Australia, 1988, pp. 213–217.
- [28] Rice, R. C. and Rungta, R., "Modeling of Embedded Fatigue Cracks in Railroad Rails," *Fatigue and Fracture of Engineering Materials and Structures*, Vol. 11, No. 3, 1988, pp. 189–203.
- [29] Rungta, R., Rice, R. C., Buchheit, R. D., and Broek, D., "An Investigation of Shell and Detail Cracking in Railroad Rails," *Microstructural Science, Volume 12, Corrosion, Microstructure, and Metallography*, Proceedings of the Sixteenth Annual Technical Meeting of the International Metallographic Society, 1985, pp. 383–406.
- [30] Suresh, S., "Crack Initiation in Cyclic Compression and Its Applications," *Engineering Fracture Mechanics*, Vol. 21, No. 3, 1985, pp. 453–463.
- [31] Tada, H., Paris, P. C., and Irwin, G. R., *The Stress Analysis of Cracks Handbook*, Del Research Corporation, St. Louis, MO, June 1973, p. 26-31.
- [32] Steele, R. K., "The Consequences of Truly Effective Lubrication Upon Rail Performance," ASME Paper 84-WA/RT-17, American Society of Mechanical Engineers, New York, 1984.
- [33] Mutton, P. J. and Epp, C. J., "Factors Influencing Rail and Wheel Wear," *Rail Research Papers, Vol. 1*, Melbourne Research Laboratories, Melbourne, Australia, 1988, pp. 277–282.
- [34] Marich, S., "Development of Improved Rail and Wheel Materials," *Rail Research Papers, Vol. 1*, Melbourne Research Laboratories, Melbourne, Australia, 1988, pp. 147–164.
- [35] Leis, B. N., "Microcrack Initiation and Growth in a Pearlitic Steel—Experiments and Analysis," *Proceedings*, 15th National Fracture Symposium, University of Maryland, July 1982.
- [36] Jeong, D. Y., Orringer, O., Perlman, A. B., and Rice, R. C., "Beam Theory Predictions of Shell Nucleation Life," *Proceedings*, Second International Symposium on Contact Mechanics and Wear of Rail/Wheel Systems, University of Rhode Island, Kingston, RI, 8–11 July 1986.
- [37] Rice, R. C., Ahlbeck, D. R., Kennedy, J. C., Leis, B. N., Meacham, H. C., and Sampath, S. G., "Analysis of Service Stresses in Rails, Report DOT-TSC-1663, final report submitted to the U.S. Department of Transportation, Federal Railroad Administration, Washington, D.C., March 1983.
- [38] Orringer, O. and Bush, M. W., "Applying Modern Fracture Mechanics to Improve the Control of Rail Fatigue Defects in Track," Bulletin 689, American Railway Engineering Association, Chicago, IL, 1983.
- [39] Orringer, O., "Control of Rail Integrity by Self-Adaptive Scheduling of Rail Tests," Report DOT/FRA/ORD-90-05, Volpe National Transportation Systems Center for the U.S. Department of Transportation, Federal Railroad Administration, Washington, D.C., June 1990.
- [40] "Improving Transportation Through Railroad Research: 1988–1991," Report DOT/FRA/ORD-92-14, summary report, U.S. Department of Transportation, Federal Railroad Administration, Office of Research and Development, Washington, D.C., July 1992.

Equating Damped Vibration to Constant Amplitude Fatigue Loading for a Thick-Walled Pressure Vessel

REFERENCE: Stephens, R. I., Adams, T. B., and Carlson, S. L., "Equating Damped Vibration to Constant Amplitude Fatigue Loading for a Thick-Walled Pressure Vessel," *Case Studies for Fatigue Education, ASTM STP 1250*, Ralph I. Stephens, Ed., American Society for Testing and Materials, Philadelphia, 1994, pp. 139–155.

ABSTRACT: A single impulse firing of an A723 steel thick-wall cannon tube has been considered by the U.S. Army to be equivalent in fatigue to a single 0.2 Hz laboratory simulated constant load amplitude test. However, a high frequency (15 kHz) resonant damped vibration has been found to accompany the firing in some situations and hence raise concern about the single loading equivalent simulation fatigue test philosophy. This case describes the analytical and test programs to determine a new fatigue equivalence that incorporates both the normal impulse, the resonant damped vibration, and the constant amplitude simulation tests. Analytical and experimental fatigue lives were based upon strain life (ϵ - N), stress-life (S - N), and linear elastic fracture mechanics LFM ($da/dN - \Delta K$) models. Quasi-equivalence testing was conducted between 0.2 and 30 Hz using both constant amplitude and a damped vibration spectrum with axial smooth specimens and $SE(T)$ specimens. The analytical and experimental results, modified for frequency effects, provide a new fatigue equivalence with significant differences.

KEYWORDS: fatigue (materials), resonant vibration, cumulative damage, life predictions, frequency effects, pressure vessel, case study

The U.S. Army criteria for releasing a new thick-walled cannon tube design for field service require a durability or allowable fatigue life verification. This fatigue life verification requires repeated experimental firings and simulated laboratory pressurizations. The firing pressure-time curve and hence the Lamé hoop stress-time curve for these thick-walled pressure vessels is shown schematically in Fig. 1. The time period for a firing is in milliseconds. The maximum hoop stress value is used in repeated laboratory sinusoidal pressurization tube tests at 0.2 Hz, as shown in Fig. 2. The stress ratio, $R = \sigma_{\min}/\sigma_{\max}$ is zero, as shown. Based upon equivalent fatigue damage or fatigue life, each 0.2 Hz constant amplitude, $R = 0$, simulated pressurization has been shown to correlate essentially 1 to 1 with the actual firing. Thus, for many years, the 1 to 1 equivalence has been an important factor in testing, and hence, setting safe-life firings for thick-walled cannon tube.

It has been found that a resonant variable amplitude vibration at approximately 15 kHz could be superimposed on the cannon tube during firing, resulting in a hoop stress-time history, as shown in Fig. 3. This resultant vibratory stress-time history shows an increasing amplitude phase with zero mean stress, a peak stress, σ_{peak} , followed by a decreasing amplitude phase with a vibratory mean stress, σ_{vm} , similar to the normal Lamé pressurization

¹ Professor and research assistants, respectively, The University of Iowa, Mechanical Engineering Department, Iowa City, IA.

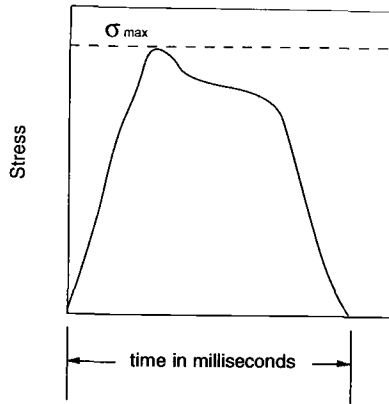


FIG. 1—Schematic of original firing stress history.

stress followed by a drop to zero stress. This new 15 kHz vibratory stress history raises significant concern about the 1 to 1 equivalence stated earlier. The goal of this project is to determine the equivalence of the usual constant amplitude laboratory testing at 0.2 Hz with $R = 0$ to that of the new 15 kHz variable, amplitude vibratory stress history.

Student Questions and Instruction

At this point the class should prepare a list of items that need to be considered in order to determine a new equivalence.

1. What analytical, computational, or experimental aspects and modeling should be undertaken?
2. What literature reviews will be needed to address some of these aspects?
3. What aspects are the most important and what aspects are secondary or of small influence?
4. What additional information will be needed from U.S. Army personnel?

Procedures

Discussions with U.S. Army personnel provided additional information concerning the problem. At first, it was desirable to formulate a complete range of equivalence for many

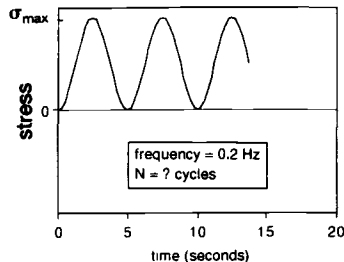


FIG. 2—Low frequency constant amplitude, $R = 0$, stress history.

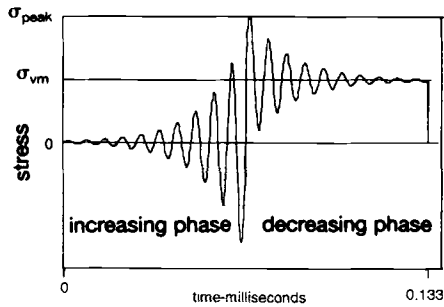


FIG. 3—Schematic representation of the resonant vibratory stress history.

values of σ_{peak} and σ_{vm} . This was soon restricted to more realistic values with $\sigma_{\text{peak}} = 1034$ MPa (150 ksi) and $\sigma_{\text{vm}} = 517$ MPa (75 ksi). This provided an overload ratio, $\sigma_{\text{peak}}/\sigma_{\text{vm}}$, of 2. The number of cycles in each vibratory load history to represent the actual input firing was determined by the Army to be 20, as shown in Fig. 3. With this information available, the key aspects in obtaining the desired equivalence for this ASTM A723, Grade 1, Class 4, Ni-Cr-Mo tempered martensitic alloy pressure vessel steel was then formulated as follows:

1. Possible elimination of the 15 kHz resonant vibration.
2. Equivalent fatigue life prediction models based upon:
 - (a) Local strain approach using low cycle fatigue strain-life ($S-N$) concepts.
 - (b) Nominal stress approach using stress-life ($S-N$) concepts.
 - (c) Fatigue crack growth using linear elastic fracture mechanics (LEFM) concepts.
3. Simulated experimental test program based upon smooth specimens and precracked specimens, or both.
4. Wave form quantification.
5. Cumulative damage models.
6. Mean stress and residual stress effects.
7. Cycle counting methods.
8. Notch or stress concentration effects.
9. Frequency effects for 15 kHz and 0.2 Hz.
10. Environmental effects of corrosion and temperature.
11. Biaxial effects.
12. Material properties needed.
13. Applicable standards.

Elimination of the kHz Resonant Vibration

Many different cannon tube sizes and designs exist in the Army and design changes to alter resonant vibrations are always possible. However, design changes may have restrictions and can take substantial time. U.S. Army personnel preferred to directly attack the problem assuming the resonant condition persisted and thus an equivalence was still sought.

Temperature, Corrosion, Biaxial and Residual Stress, and Notch Considerations

Cannon tubes are expected to be used under all climatic temperature conditions and could involve climatic temperatures from -45° to 50°C . Low climatic temperature fatigue resistance

involving both fatigue crack formation and fatigue crack growth should be equal to or better than that at room temperature for this quality Q&T alloy steel [1]. This generally has also been assumed in previous Army cannon tube equivalence criteria. However, fracture toughness, and hence critical crack size, can be reduced at the lower climatic temperatures. This latter effect has been principally addressed and solved through stringent microstructure, composition, and Charpy V-notch impact requirements. Thus, it was assumed that room temperature modeling and experiments should be conservative relative to low-temperature effects.

The actual elevated temperature of the cannon tube can be expected to exceed that of the highest climatic temperature due to heating effects during firing. In the regions of concern for this resonant vibration loading, temperature should be less than 200°C as shown by previous U.S. Army findings. This temperature is not high enough to form a significant degradation of fatigue resistance for this alloy steel. Thus, it was assumed that room temperature modeling and experiments would be satisfactory for all temperatures involved.

Corrosion from firing and from climatic conditions has been incorporated into the previous successful equivalence criteria by firing each laboratory test cannon tube several times prior to laboratory testing. It was assumed that the 15 kHz resonant vibration would not cause increased corrosion problems, and hence, modeling and experiments excluding additional corrosion considerations should be appropriate.

During firing a large tensile circumferential (hoop) stress and a smaller compressive radial stress exists. For both the analytical and experimental portions of this case study, a uniaxial state of stress was assumed.

Residual stresses and notch (stress concentration) effects significantly alter the fatigue resistance of cannon tubes. These are both taken into consideration with the 1 to 1 equivalence by laboratory testing of actual cannon tube breech sections. By considering the muzzle-end region as the principal 15 kHz resonant vibratory concern, both the residual stress and notch considerations are significantly reduced in importance. Thus, U.S. Army personnel recommended this equivalence study assume residual stresses are small and that the theoretical stress consideration factor, K_t , was equal to one. Other locations that contain significant residual stresses and K_t values could be evaluated at a later date.

Student Questions

1. What information can you find to justify the above assumptions on temperature and corrosion effects?
2. What climatic corrosive and firing corrosive environments actually exist with this cannon tube?
3. Many fatigue life prediction software programs and many laboratory simulation component tests omit temperature and corrosion environments. How are these omissions incorporated into safe durability?
4. What relative changes in fatigue strength or fatigue life can occur in real components under biaxial state of stress and by inducing surface residual stresses or reducing stress concentrations?

Mathematical Representation of the Vibratory Loading Wave Form

An equivalence determination will involve fatigue life calculations and simulated fatigue experiments. Both of these procedures require a quantification of the 15 kHz vibratory wave form of Fig. 3. The needed information is the peak and valley of each cycle or reversal in Fig. 3. This waveform can be thought of as a block loading of 20 sinusoidal cycles lasting

0.133 milliseconds. The stress amplitude of each cycle, however, is variable. For the first ten cycles the waveform is centered around zero and thus can be thought of as fully reversed with the stress amplitude of each cycle increasing exponentially. This first half of the loading is the increasing phase. At the first half of the eleventh cycle, a peak value is reached, σ_{peak} , and then the stress amplitude begins to decrease exponentially. In contrast to the first ten cycles, the last ten cycles (the decreasing phase) are centered about a positive mean stress value, σ_{vm} . After the 20th cycle, the stress amplitude is zero. Then the waveform immediately drops from the positive mean stress to zero stress. From this point, the next repetition of the block loading begins.

Given the exponential characteristics of the waveform, a quantitative representation was produced by employing the mathematical model of the free vibration of a viscously damped, single degree-of-freedom, second-order system expressed by the following ordinary differential equations

$$m\ddot{x}(t) + c\dot{x}(t) + kx(t) = 0 \quad (1)$$

or

$$\ddot{x}(t) + 2\zeta\omega_n\dot{x}(t) + \omega_n^2 x(t) = 0 \quad (2)$$

The solution of these equations for the underdamped case ($0 < \zeta < 1$) can be represented in general form by

$$x(t) = Ae^{-\zeta\omega_n t} \sin \omega_d(t) \quad (3)$$

The frequency of the waveform is known to be 15 kHz or 94 krad/s. This is the same as the damped frequency, ω_d , that has the following relationship to the undamped natural frequency of the system and the viscous damping factor, ζ

$$\omega_d = \omega_n \sqrt{1 - \zeta^2} \quad (4)$$

The viscous damping factor can then be found by its relationship with the logarithmic decrement, δ , given as

$$\zeta = \frac{\delta}{\sqrt{(2\pi)^2 + \delta^2}} \quad (5)$$

The logarithmic decrement is a quantity determined by the rate of decay of the vibration

$$\delta = \frac{1}{n-1} \ln \left(\frac{x_1}{x_n} \right) \quad (6)$$

If the amplitudes of two peaks are known, for example x_1 and x_n , the logarithmic decrement can be calculated. This in turn yields the viscous damping factor and finally the undamped natural frequency can be calculated. The last variable of Eq 3 to be found is the amplitude coefficient, A . The amplitude, $x(t)$, at the first peak, x_1 , is known. This will occur at the first quarter cycle or $t = 0.01667$ milliseconds. Now A can be solved for by substituting the known values into Eq 3.

To apply this model to the quantitative formulation of the block vibratory loading of interest, both the increasing and decreasing phases had to be calculated separately and superimposed at the peak stress of 1 034 MPa. The increasing phase of the waveform was simply assumed to be a mirror image of the second-order system just formulated. The initial peak amplitude, x_1 , of this vibration is known to be 1034 MPa and then essentially damps out to zero after ten and a half cycles. Note that because of the overlap at the peak stress, an additional half-cycle had to be added to the increasing phase. Next a value had to be chosen for "zero" since the theoretical waveform amplitude continues to oscillate at very small amplitudes. "Essentially zero" was chosen realistically to be one percent of the initial peak amplitude, or $x_{11} = 10.3$ MPa. With these values and the frequency, the waveform was generated and then reversed to yield the increasing phase of the waveform shown in Fig. 3.

Next, the decreasing phase had to be generated and combined with the increasing phase. The decreasing phase of the waveform decays exponentially from the peak value, but there is a positive mean stress, σ_{vm} , imposed on these cycles. In order to make this portion of the waveform consistent with the assumptions for both exponential decay and the value of zero, a separate logarithmic decrement had to be calculated that depended on the mean stress. Note that because of these assumptions, imposing a mean stress on the decreasing phase also changes the stress amplitude of these cycles. Finally, the increasing and decreasing phases were combined at the peak stress of 1 034 MPa to form the complete waveform. The damping characteristics of the completed waveform are given in Table 1 for both the increasing and decreasing amplitude phases. From these values, the needed magnitudes of all peaks and valleys were obtained.

Equivalence Fatigue Life Prediction Model Selection

Both the local strain model using low cycle fatigue strain-life (ϵ - N) concepts and the nominal stress model using stress-life (S - N) concepts were chosen to evaluate the fatigue life equivalence. These models assume the fatigue life of a component is that to form a crack of several millimeters in size and is based upon the usual crack size of fracture that occurs in reference small specimen constant amplitude tests. An LEFM model was also used to determine reasonable fatigue crack growth life equivalence. These models are clarified in Refs 2-5.

The general ϵ - N model used is

$$\frac{\Delta\epsilon}{2} = \frac{\Delta\epsilon_e}{2} + \frac{\Delta\epsilon_p}{2} = \frac{\sigma_f'}{E} (2N)^b + \epsilon_f'(2N)^c \quad (7)$$

along with the constitutive equation

TABLE 1—*Damping characteristics for the variable amplitude block history, $\sigma_{\text{peak}} = 1\,034$ MPa, $\sigma_{\text{vm}} = 517$ MPa.*

| Characteristic | Increasing Amplitude | Decreasing Amplitude |
|----------------|----------------------|----------------------|
| n | 11 | 10 |
| X_1/X_n | 100 | 67.7 |
| δ | 0.461 | 0.467 |
| ζ | 0.0731 | 0.0741 |
| w_n rad/s | 94 500 | 94 510 |
| A | 1 160 | 1 161 |

$$\frac{\Delta\epsilon}{2} = \frac{\sigma_a}{E} + \left(\frac{\sigma_a}{K'}\right)^{1/n'} \quad (8)$$

The general S - N model is

$$\frac{\Delta\sigma}{2} = \sigma_a = \sigma_f'(2N_f)^b \quad (9)$$

which is the elastic component of Eq 7. Both the Morrow mean stress model (Eq 10), and the Smith, Watson, and Topper mean stress model (Eq 11), were used in the local strain based approaches

$$\frac{\Delta\epsilon}{2} = \frac{(\sigma_f' - \sigma_m)(2N)^b}{E} + \epsilon_f'(2N)^c \quad (10)$$

$$\sigma_{\max} E \frac{\Delta\epsilon}{2} = (\sigma_f')^2 (2N)^b + \sigma_f' \epsilon_f' E (2N)^{b+c} \quad (11)$$

and

$$\sigma_{\max} = \sigma_m + \sigma_a \quad (12)$$

The modified Goodman mean stress model (Eq 13), was used for the nominal stress approach

$$\frac{\sigma_a}{S_f} + \frac{\sigma_m}{S_u} = 1 \quad (13)$$

where S_f is the fatigue strength at a specific fatigue life. Additional symbols are defined in Table 2. Actual tensile, cyclic stress-strain, and low cycle fatigue A723 material properties,

TABLE 2—*Monotonic, cyclic, and low cycle fatigue properties of ASTM A723 steel [6].*

| | |
|--|--------|
| Young's modulus, E , GPa | 200 |
| 0.2% offset yield strength, S_{ys} , MPa | 1 170 |
| Ultimate tensile strength, S_u , MPa | 1 262 |
| % elongation | 13 |
| % reduction in area | 50 |
| Strain hardening coefficient, K , MPa | 1 483 |
| Strain hardening exponent, n | 0.037 |
| Rockwell hardness, HR_c | 40 |
| Cyclic strength coefficient, K' , MPa | 1 581 |
| Cyclic strength exponent, n' | 0.071 |
| 0.2% offset cyclic yield strength, S'_{ys} , MPa | 1 014 |
| Fatigue strength coefficient, σ_f' , MPa | 2 123 |
| Fatigue strength exponent, b | -0.110 |
| Fatigue ductility coefficient, ϵ_f' | 0.489 |
| Fatigue ductility exponent, c | -0.783 |
| Young's modulus at half-life, E' , GPa | 193 |

obtained by Koh and Stephens [6], and used in the ϵ - N and S - N models are also given in Table 2.

Fatigue crack growth models used were the Paris model (Eq 14) and the Foreman model (Eq 15)

$$\frac{da}{dN} = C(\Delta K)^n \quad (14)$$

$$\frac{da}{dN} = \frac{C(\Delta K)^n}{(1 - R)K_c - \Delta K} \quad (15)$$

Partial constant amplitude fatigue crack growth data for A723 steel were available from the Army; however, a wider range of da/dN was desirable and additional fatigue crack growth testing was performed to obtain the needed fatigue crack growth parameters.

The above three models must incorporate cycle counting procedures. The rainflow counting model is by far the most common procedure because it brings into effect closed hysteresis loops and mean stress. Rainflow counting was used to cycle count the vibratory load history of Fig. 3 and to provide both stress amplitude and mean stress.

The above three models must also incorporate a cumulative damage procedure. For the ϵ - N and S - N approaches, the Palmgren-Miner linear damage rule has been the most common rule for the past several decades. It was decided, however, to evaluate other cumulative damage models to determine if better models could be used in the equivalence calculations. In order to review this topic comprehensively, three computer data bases were employed as a means of locating references: COMPENDEX PLUS, which corresponds to the Engineering Index, the National Technical Information Service (NTIS), and Applied Science and Technology. From these references and subsequent additional references, existing cumulative damage models were evaluated as to their applicability to this problem. Numerous papers and overviews of these methods were found in the literature search. References 7 through 11 include significant overviews of the different cumulative damage models. Many models of differing complexity were found in the literature review. Non-linear damage and interaction effects are very difficult to overcome. The more complex models often require empirical parameters that require extensive testing. It was decided, as has been done by most others, that the simplicity and oftentimes reasonable accuracy makes the Palmgren-Miner linear damage rule very attractive. It will be used in the ϵ - N and S - N fatigue life equivalence calculations.

Frequency Effects

The previously mentioned three computer data bases were again used to obtain references evaluating frequency fatigue effects in metals. Temperature, corrosion, and strain rate sensitive stress-strain constitutive relations were shown to be important parameters affecting frequency fatigue effects. Excluding the temperature and corrosion effects, frequency metal fatigue effects between 0 and 200 Hz were usually small. Generally within this frequency range the fatigue resistance based upon ϵ - N , S - N , and da/dN - ΔK could increase slightly with increased frequency. This small influence was important in deciding later what test frequency to choose for representing the constant amplitude 0.2 Hz simulated pressurizing.

Most recent kHz fatigue testing has been run at about 20 kHz since this frequency is above the available range of the human ear. Four recent comprehensive publications on high

frequency fatigue were evaluated [12–15] along with other papers. Pneumatic, piezoelectric, and magnetostrictive test systems have been used to test at frequencies in the kHz range. Smooth, notched, and crack growth specimens have been tested. Various cooling media such as air, water, water modified with corrosion inhibitors, and oil have been used to cool specimens because of self-heating caused by internal friction during high frequency testing.

Figure 4 shows representative $S-N$ curves for three carbon steels and one CrMo steel tested at lower frequency (27 to 70 Hz) and at 20 kHz [16]. For all four steels, the $S-N$ curve shifts upward and to the right for the high frequency loading indicating increased fatigue resistance at the kHz frequency range. Figure 5 shows representative $da/dN-\Delta K$ curves for several steels tested at 70 Hz and at 22 kHz [17]. The band of results indicate significant increase in fatigue crack growth resistance for the kHz frequency range.

The above $S-N$ and $da/dN-\Delta K$ frequency results are representative of much of the data. However, quantitative values of increased fatigue resistance at kHz frequencies range from almost zero to values higher than depicted in Figs. 4 and 5. This depends upon test specimens, corrosion, heating, and microstructure. Less increase in fatigue resistance was noted by Kuzmenko [15] for steels with substantial Ni content. Puskar [18] has recommended several quantitative correction factors for $S-N$ and $da/dN-\Delta K$ curves for steels. These along with suggestions by Kuzmenko [15] form the following shifts in kHz fatigue resistance relative to 0 to 25 Hz for this A723 steel that will be used in forthcoming fatigue life calculations.

S-N Curve

1. Shift the fatigue limit from 10^7 cycles to 10^8 cycles.
2. Increase the fatigue limit by a factor of 1.1.
3. Retain the same slope for $<10^8$ cycles.

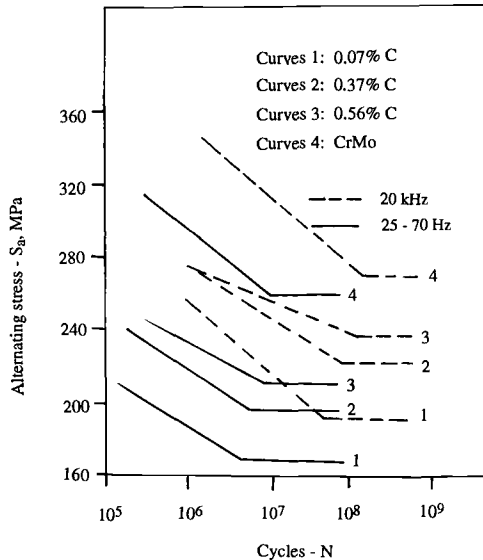


FIG. 4—Frequency effect on S-N curves for four steels tested at 25 to 70 Hz and 20 kHz [16].

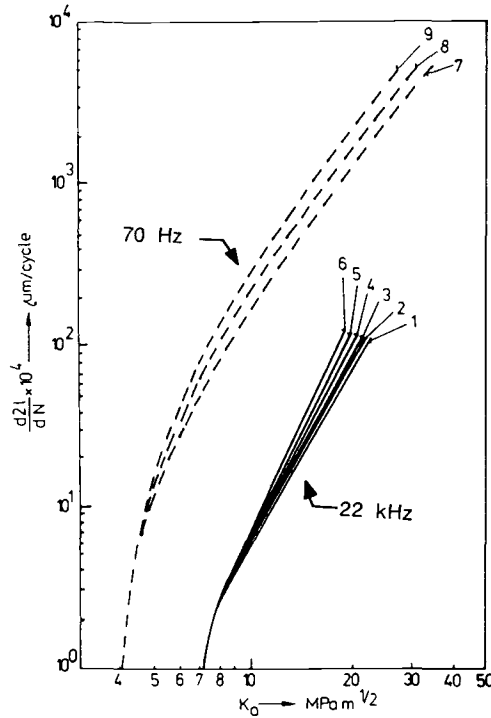


FIG. 5—Frequency effect on $da/dN-\Delta K$ for several steels tested at 70 Hz and 22 kHz [17].

The above shifts will result in a factor of twelve increase in life for a given alternating stress level and a 31% increase in alternating stress for a given life.

$\epsilon-N$

1. Shift the elastic curve the same as the given preceding $S-N$ curve.
2. Shift the plastic curve up 10%.
3. Retain the same elastic and plastic slopes.

These shifts will change the value of σ'_f to 2788 MPa and ϵ'_f to 0.538 for 15 kHz. This results in an increase in fatigue life between a factor of 2 at higher strain amplitudes and a factor of 12 at lower strain amplitudes. These shifts also correspond to a 12% increase in alternating strain for short lives and up to a 31% increase in alternating strain at the longer lives.

$da/dN-\Delta K$

1. Increase ΔK_{th} by a factor of 1.1
2. Decrease the region II Paris coefficient C by a factor of 5.
3. Retain the same Paris exponent n .

These shifts will have the effect of increasing the fatigue crack growth life by over a factor of 5, depending on the closeness to ΔK_{th} .

Additional information concerning the formulation of the above decisions can be found in Ref 19.

Student Questions

1. At this point, the class should prepare constructive criticism of the fatigue life calculation models and the kHz frequency correction factor decision.
2. What testing/specimens/standards should be considered to aid in obtaining the proper loading equivalence?

ϵ - N and S - N Fatigue Life Equivalence Calculations and Experiments

Calculations

Fatigue life calculations for the constant amplitude 0.2 Hz loading of Fig. 2 with the Lamé hoop stress σ_{max} (σ_{vm}) = 517 MPa were obtained based on the S - N approach (Eq 9) with the Goodman mean stress model (Eq 13) and the ϵ - N approach using the Morrow model (Eq 10), and the SWT model (Eq 11), along with A723 material properties, given in Table 2. These calculations indicated greater than 10^7 cycles would exist for the S - N model and the Morrow model. The SWT model gave 4.4×10^6 cycles. These values are shown in Table 3 for eventual comparisons with experimental values.

The number of blocks to failure with the resonant vibratory stress history of Fig. 3 for damping characteristics given in Table 1 and the Lamé hoop stresses σ_{peak} = 1034 MPa and σ_{vm} = 517 MPa were calculated using the Lifest[®] software program (SoMat Corporation, Champaign, IL 1988). This program incorporates rainflow counting, linear cumulative damage, and both S - N and ϵ - N approaches using Goodman, Morrow, or SWT mean stress models. Calculations were made with and without frequency correction factors and the number of calculated blocks are given in Table 4.

The equivalent number of calculated constant amplitude, $R = 0$ cycles were obtained by dividing values of Table 3 by values of Table 4 for each model. Equivalent cycles with and without frequency correction factors are given in Table 5. These equivalent calculated values are very high, ranging from $>2 \times 10^3$ to $>2 \times 10^4$ cycles.

Experiments

The objective of the test program was to determine an experimental equivalence to compare with the calculated equivalence. The tests involved smooth un-notched axial 6-mm

TABLE 3—Constant amplitude ($R = 0$) life calculations based on S - N and ϵ - N analysis plus experimental results.

| Calculated Lives-Cycles | | | Experimental Lives-Cycles |
|-------------------------|---------------------------|------------------------|---------------------------|
| S - N , Goodman | ϵ - N , Morrow | ϵ - N , SWT | |
| $>10^7$ | $>10^7$ | 4.4×10^6 | $>10^7$ |

TABLE 4—Variable amplitude life calculations based upon S-N and ϵ -N analysis plus experimental results.

| | Lives-Blocks | | | Average Experimental |
|---------------------------------|--------------|-----------------------|--------------------|-------------------------|
| | S-N, Goodman | ϵ -N, Morrow | ϵ -N, SWT | |
| Without frequency effects | 407 | 458 | 390 | 4076 |
| With 15 kHz frequency effect | 4840 | 1240 | 1700 | 14 000 |

diameter cylindrical specimens machined from stress-relieved thick-walled A723 pressure vessels. The longitudinal axis was in the direction of the pressure vessel hoop stress. After machining, specimens were polished with 600 grit emery paper. Specimens satisfied Practice for Strain-Controlled Fatigue Testing (ASTM E 606). All tests were conducted in load control with $R = 0$ using an 89 kN closed loop electrohydraulic test system with hydraulic grips. No high frequency (kHz) testing was done because of experimental limitations. Thus, kHz frequency correction factors previously described were also incorporated into the experimental equivalence.

Twelve constant amplitude $R = 0$ tests depicted in Fig. 2 were performed with σ_{\max} ranging from 517 to 1 034 MPa. Tests were run between 0.2 and 25 Hz with no noticeable frequency effect. The test results are plotted as an S-N diagram in Fig. 6. The key stress level for equivalence calculations was $\sigma_{\max} (\sigma_{vm}) = 517$ MPa where a run-out at 10^7 occurred.

Two variable amplitude tests with $\sigma_{\text{peak}} = 1\,034$ MPa and $\sigma_{vm} = 517$ MPa as depicted in the block history of Fig. 3 were run at 20 Hz. A brief rest period at zero load was added between each variable amplitude block. The number of blocks to fracture for these duplicate tests were 2 685 and 5 466, with an average of 4 076. Since no kHz frequency testing was possible, the 20 Hz variable amplitude blocks were adjusted by an empirical correction factor based upon averaging the Morrow and SWT ϵ -N frequency results in Table 4, that is, $(1\,240 + 1\,700) \div (458 + 390) = 3.36$. This was used to form a pseudo-experimental average block kHz life of $(3.36) \cdot (4\,076) \approx 14\,000$.

Both constant and variable amplitude experimental lives or blocks have been included in Tables 3 and 4 for better comparison to calculated values. The experimental equivalence has been included in Table 5 again for better comparison to calculated equivalencies. It is seen in Table 5 that the experimental equivalence values are significantly less than the calculated values.

TABLE 5—Equivalent number of constant amplitude ($R = 0$) cycles with and without frequency effect.

| | S-N, Goodman | ϵ -N, Morrow | ϵ -N, SWT | Average Experimental |
|---------------------------------|---------------------------|-----------------------|--------------------|-------------------------|
| | Without frequency effects | >24 600 | >21 800 | >11 300 |
| With 15 kHz frequency effect | >2 100 | >8 100 | 2 600 | >700 |

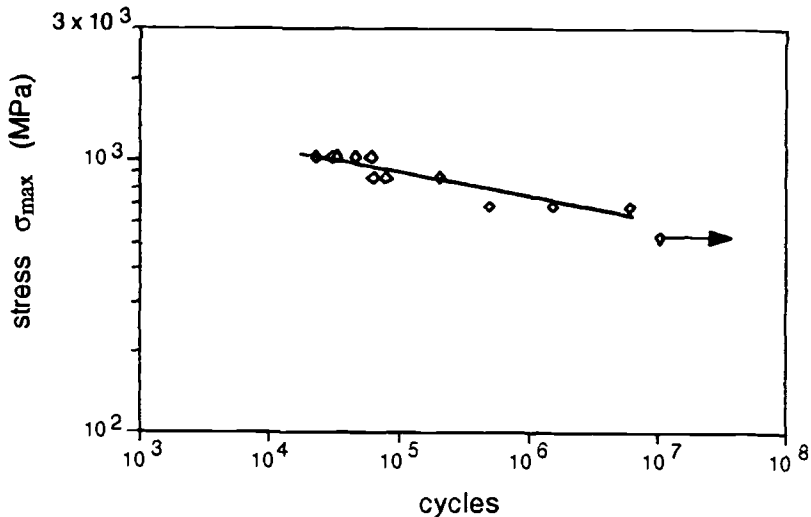


FIG. 6—S-N diagram for constant amplitude, $R = 0$, smooth axial specimens, A723 steel.

Student Questions

1. What test replication improvements are needed?
2. Why do calculated and experimental equivalence differ? Is this a significant difference?
3. Final frequency corrected equivalence ranged from >700 to >8100 cycles. Why such large equivalence when the previous loading was considered 1 to 1?

LEFM Fatigue Crack Growth Life Equivalence

Experimental

Fatigue crack growth experimental equivalence was obtained by simulating the thick-walled pressure vessel with an $SE(T)$ specimen having a thickness, t , of 5 mm and a width, W , of 25.4 mm. Specimens were machined from stress-relieved thick-walled A723 pressure vessels. The longitudinal axis was in the direction of the pressure vessel hoop stress. The initial crack size and nominal test stress σ_{max} , (σ_{vm}), was chosen to have an initial stress intensity factor, K , of $27.5 \text{ MPa}\sqrt{\text{m}}$. This value was chosen to be consistent with initial values of K for crack sizes and hoop stresses found in many similar thick-walled cannon tubes [20]. Thus, the initial stress intensity factors for σ_{peak} and σ_{vm} from Fig. 3 were 55 and $27.5 \text{ MPa}\sqrt{\text{m}}$, respectively. An initial crack length of 5.5 mm was chosen for both variable and constant amplitude tests. Specimens were machined with three grip holes at each end to allow for a monoball gripping fixture that would allow for both tension and compression loads.

Regions I and II $R \approx 0$ fatigue crack growth data were obtained using load shedding and constant amplitude loading, respectively, as per Standard Test Method for Measurement of Fatigue Crack Growth Rates (ASTM E 647). Test frequency varied from 5 to 30 Hz, depending upon da/dN . Cracks were monitored with a traveling telescope using stroboscopic lighting. The fatigue crack growth data were reduced using a secant method to $da/dN-\Delta K$

and the results are shown in Fig. 7. Very little scatter is seen. The region II Paris equation obtained by log-log linear regression was

$$\frac{da}{dN} = C(\Delta K)^n = 4.93 \times 10^{-11} (\Delta K)^{2.36} \tag{16}$$

This value was modified to

$$\frac{da}{dN} = \frac{C}{5} (\Delta K)^n = 9.86 \times 10^{-12} (\Delta K)^{2.36} \tag{17}$$

in order to incorporate kHz frequency effect described earlier. The threshold stress intensity factor, ΔK_{th} , was obtained at 10^{-10} m/cycle as per ASTM E 647 to be 4.3 MPa \sqrt{m} . This value was increased by 10% to 4.7 MPa \sqrt{m} for kHz frequency effect. The stress intensity at fracture, K_{fc} , was taken as 163 MPa \sqrt{m} , as seen in Fig. 7. The above fatigue crack growth properties were used later for both constant and variable amplitude fatigue crack growth life calculations.

Three *SE(T)* specimens were tested using the Fig. 3 variable amplitude loading with the previously described initial crack length of 5.5 mm and K_{peak} initial and K_{vm} initial equal to 55 and 27.5 MPa \sqrt{m} , respectively. The frequency was 20 Hz and the loading history was repeated until fracture. The crack length versus applied blocks data are shown in Fig. 8 where it is seen that very little scatter existed in these triplicated tests. Crack lengths at fracture were between 11 and 12 mm and the blocks to failure were 1 681, 1 754, and 1 767, which yields an average blocks to fracture of 1 734. This number obtained at 20 Hz will be adjusted to a pseudo kHz number of blocks to be used in equivalence determination.

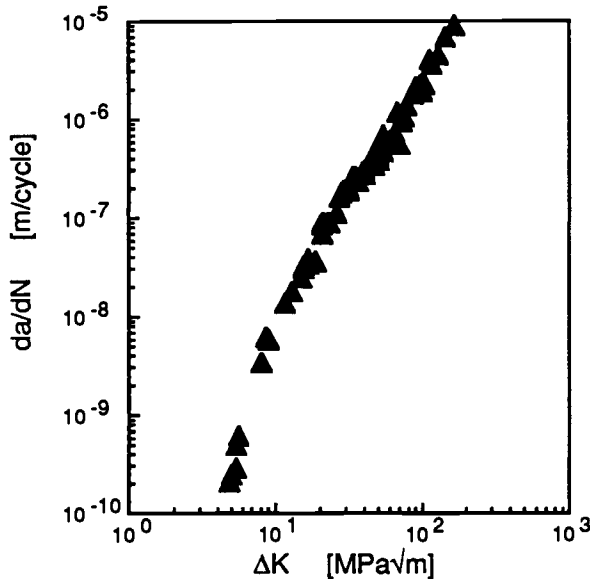


FIG. 7—Fatigue crack growth rate behavior for ASTM A723 steel, R = 0.05.

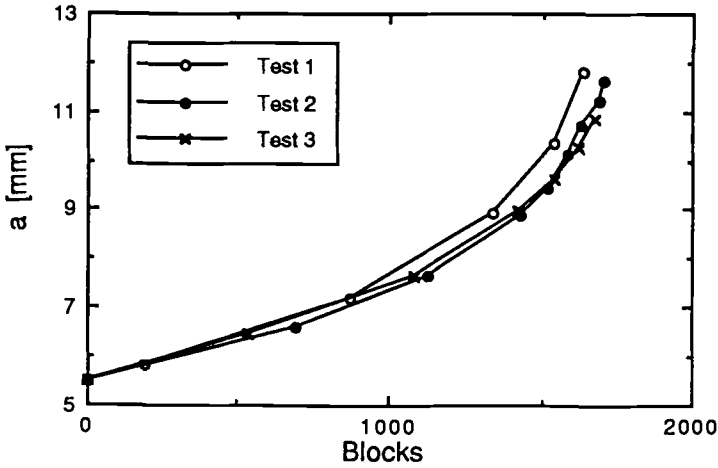


FIG. 8—Crack length, a , versus applied variable amplitude blocks.

Calculations

Fatigue crack growth lives were calculated for both constant and variable amplitude tests in order to obtain the needed simulated crack growth life equivalence. The commercial Lifest® and the NASA-developed FLAGRO® (NASA, Johnson Space Center, Houston, TX, 1989) software programs were used for both constant and variable amplitude calculations. Neither program incorporates interaction effects on fatigue crack growth life, but simply sums incremental crack extension cycle by cycle using numerical integration. The Lifest® program uses the Paris (Eqs 14 and 16) and the FLAGRO® program uses a modification of the Foreman (Eq 15). Both programs incorporate ΔK_{th} and K_{fc} . Lifest requires rainflow counting while FLAGRO uses successive peaks and valleys. In each case the calculations were made for the $SE(T)$ specimen with $a_i = 5.5$ mm, and initial stress intensity factors of 27.5 and 55 MPa, respectively, for σ_{vm} and σ_{peak} . The numerical integration was carried out until fracture at $K_{fc} = 163 \text{ MPa}\sqrt{\text{m}}$.

The variable amplitude calculations were obtained with and without kHz frequency corrections. The number of calculated variable amplitude blocks for both Lifest and FLAGRO are given in Table 6 along with the average experimental results. The pseudo high-frequency experimental results were obtained by using the ratio of the calculated blocks with and

TABLE 6—Variable amplitude fatigue crack growth block calculations plus experimental results for simulated $SE(T)$ specimen.

| | Lives-Blocks | | |
|---------------------------|--------------|--------|----------------------|
| | LifEst | FLAGRO | Average Experimental |
| Without frequency effects | 1 550 | 1 189 | 1 734 |
| With frequency effects | 7 770 | 5 435 | 8 360 |

TABLE 7—Constant amplitude ($R = 0$) fatigue crack growth life calculations for simulated $SE(T)$ specimen.

| LifEst Cycles | FLAGRO Cycles |
|---------------|---------------|
| 18 700 | 17 728 |

without frequency effects as: $(7\,770 + 5\,435) \div (1\,550 + 1\,189) = 4.82$. This ratio was multiplied by the experimental average blocks, 1 734, to obtain the pseudo experimental value of 8 360 blocks in Table 6. Calculations and experimental lives were very similar, being less than a factor of 2. The Lifest block calculations were slightly larger than the FLAGRO values.

Calculated constant amplitude, $R = 0$, fatigue crack growth cycles to failure are given in Table 7. Again, the Lifest value was slightly larger than the FLAGRO value. The fatigue crack growth equivalence was determined by the ratio of the constant amplitude cycles to failure to the variable amplitude blocks to failure. Equivalence with and without kHz frequency effects are given in Table 8. Here it is seen that very little difference in calculated or average experimental equivalence occurred. The fatigue crack growth equivalence for the frequency corrected $SE(T)$ model was between 2.3 and 3.3. These equivalence values are significantly less than those obtained using the $\epsilon-N$ or $S-N$ models.

Student Questions

1. Does it seem reasonable that two fatigue crack growth software programs should give different results? Is the percentage difference significant?
2. Comment on the use of the $SE(T)$ specimen as used in the experimental and calculated equivalence as regards to a thick-walled pressure vessel. What better simulation model(s) do you propose and why?
3. Why does the equivalence using $\epsilon-N$ and $S-N$ approaches differ so much from that of the LEFM approach?
4. What final equivalence is most reasonable for this problem?
5. Is additional evaluation needed to form reasonable equivalence? What do you recommend?

Discussion of Equivalence Results

The equivalence values using $S-N$ or $\epsilon-N$ models and experiments were bounded by >700 and $>8\,100$ or an order of magnitude difference. The equivalence values for LEFM based fatigue crack growth models and experiments were between 2.3 and 2.4, or a negligible

TABLE 8—Equivalent number of constant amplitude ($R = 0$) fatigue crack growth cycles with and without frequency effect.

| | LifEst | FLAGRO | Average Experimental |
|---------------------------|--------|--------|----------------------|
| Without frequency effects | 12.1 | 14.9 | 11 |
| With frequency effects | 2.4 | 3.3 | 2.3 |

difference. A major concern, however, was how to resolve/explain the two to three orders of magnitude difference between the $S-N$ or $\epsilon-N$ results and the LEFM results. The answer is best obtained by realizing that the $S-N$ or $\epsilon-N$ results were based upon no stress concentrations, that is, $K_t = 1$, at the muzzle location of the resonant frequency. Normally, fatigue failures in these thick-walled pressure vessels occur in the rifling where significant stress concentrations exist. Thus, these equivalence values can be altered by incorporating a stress concentration factor, K_t , or fatigue strength reduction factor, K_f . This will drastically reduce the $S-N$ or $\epsilon-N$ equivalence values. The addition of a stress concentration will have only a small influence on the LEFM fatigue crack growth equivalence.

References

- [1] Stephens, R. I., Ed., *Fatigue at Low Temperatures*, ASTM STP 857, American Society for Testing and Materials, Philadelphia, 1985.
- [2] Fuchs, H. O. and Stephens, R. I., *Metal Fatigue in Engineering*, Wiley Interscience, New York, 1980.
- [3] Rice, R. C., Ed., *Fatigue Design Handbook*, 2nd Edition SAE Publication AE-10, Society of Automotive Engineers, Warrendale, PA, 1988.
- [4] Bannantine, J. A., Comer, J. J., and Handrock, J. L., *Fundamentals of Metal Fatigue Analysis*, Prentice Hall, Englewood Cliffs, NJ, 1990.
- [5] Dowling, N. E., *Mechanical Behavior of Materials*, Prentice Hall, Englewood Cliffs, NJ, 1993.
- [6] Koh, S. K. and Stephens, R. I., "Fatigue Life Predication of an Autofrettaged Thick-Walled Pressure Vessel with an External Groove," *Journal of Pressure Vessel Technology*, Vol. 13, Aug. 1991, pp. 368-374.
- [7] Fackler, W. C., *Equivalence Techniques for Vibration Testing*, Naval Research Laboratory, Washington, DC, 1972.
- [8] Collins, J. A., *Failure of Materials in Mechanical Design-Analysis Predication Prevention*, John Wiley and Sons, New York, 1981.
- [9] Osgood, C. C., *Fatigue Design*, John Wiley and Sons, New York, 1982.
- [10] Kutt, T. V. and Bieniek, M. P., "Cumulative Damage and Fatigue Life Prediction," *AIAA Journal*, Vol. 26, No. 2, 1988, pp. 213-219.
- [11] Buch, A., *Fatigue Strength Calculations*, Trans. Tech. Publications, Aedermannsdorf, Switzerland, 1988.
- [12] Wells, J. M., Buck, O., Roth, L. D., and Tien, J. K., Eds., *Ultrasonic Fatigue*, The Metallurgical Society of the American Institute of Mining, Metallurgical and Petroleum Engineers (AIME), Warrendale, PA, 1982.
- [13] Willertz, L. E., "Ultrasonic Fatigue," *International Metal Review*, Vol. 25, No. 2, 1980, pp. 65-78.
- [14] Puskar, A., *The Use of High Intensity Ultrasonics*, Elsevier, New York, 1982.
- [15] Kuzmenko, V. A., "Fatigue of Structural Materials at High-frequency Cyclic Loading," *Advances in Fracture Research (Fracture '84)*, *Proceedings of the 6th International Conference on Fracture*, ICFG, S. R. Valluri, D. M. R. Taplan, P. Rama Rao, and J. K. Knott, Eds., Pergamon Press, 1984, Vol. 3, pp. 1791-1798.
- [16] Puskar, A. and Golovin, S. A., *Fatigue in Materials: Cumulative Damage Processes*, Elsevier, New York, 1985.
- [17] Puskar, A., "Fatigue Properties of Steels at Low and High Loading Frequencies," *Ultrasonic Fatigue*, Wells, J. M., Ed., The Metallurgical Society of the American Institute of Mining, Metallurgical and Petroleum Engineers (AIME), Warrendale, PA, 1982, pp. 223-227.
- [18] Puskar, A., "Fatigue Process Modifications at High Frequency Loading," *Basic Mechanisms in Fatigue of Metals*, Elsevier, New York, 1988, pp. 331-338.
- [19] Adams, T. B., "Cumulative Fatigue Damage of a Repeated High Frequency Vibratory Loading," M.S. Thesis, The University of Iowa, Iowa City, IA, May 1991.
- [20] Underwood, J. H., "Fracture Damage and Failure of Cannon Components by Service Loading," Technical Report ARLCB-TR-83004, Feb. 1983.

Development of a Numerical Model for Predicting Fatigue Lives of Tubular Threaded Connections

REFERENCE: Liebster, T. D. and Glinka, G., “Development of a Numerical Model for Predicting Fatigue Lives of Tubular Threaded Connections,” *Case Studies for Fatigue Education*, ASTM STP 1250, Ralph I. Stephens, Ed., American Society for Testing and Materials, Philadelphia, 1994, pp. 156–173.

ABSTRACT: Tubular threaded connections are used in the off-shore oil industry for applications such as tension leg platforms and drill string components. The design of these components requires full-scale fatigue testing to ensure their reliability. This is an extremely expensive undertaking (actual connectors may be as large as 1.2 m in diameter). Therefore, an analytical method is needed to provide preliminary estimates of how various parameters will affect the fatigue lives of the connections. This model must have the ability to estimate fatigue life under variable amplitude cyclic loading conditions. The key to such a model is relating the applied variable amplitude loading history to the local elasto-plastic stress-strain response at the roots of the threads. The load dependent nature of the stress concentration factor in pre-loaded threaded connections requires the use of a numerical solution to determine the local stresses. The development of this model is described starting with a discussion of the type of loading and fatigue failure that must be modeled, the assumptions that are made in developing the model, and the synthesis of the numerical solution and its application to predicting the fatigue life of a real connector geometry. The fatigue crack initiation life is calculated using the strain-life approach. The model is then used to demonstrate the effects on fatigue life that result from changing various aspects of the connector design, such as geometry and load configuration.

KEYWORDS: threads, fatigue, stress concentration factor, load distribution, finite element analysis (FEA)

Threaded connections refer to all screw-nut systems, studs in a block, or threaded pipe joints. The characteristic parameters of threads, such as diameter, pitch, and thread form, are standardized for most applications. However, threaded joints become complicated structures that pose difficult design and analysis problems when they are large in size and subject to major cyclic stresses. Applications of this nature include pressure vessel end closures, threaded joints for off-shore tension leg platforms (TLPs), drill strings, and other large diameter connections used in the oil industry.

Understanding how large tubular threaded connections will perform in terms of fatigue can only be quantified by conducting fatigue experiments on actual components. The test connections must be subjected to load histories that are comparable to the actual service loads. For very large connections, this type of testing is extremely expensive and time consuming. Therefore, it is desirable to have analytical means to establish the expected impact

¹ Graduate student and professor, respectively, University of Waterloo, Department of Mechanical Engineering, Waterloo, Ontario, Canada, N2L 3G1.

that parameters such as connector geometry, loading, number of engaged thread pitches, and so forth would have on the fatigue life.

An analytical model would be useful for deciding what aspects should be explored in full-scale fatigue tests. The information from such an analysis would also provide useful information pertaining to the design of the experimental program.

Many studies of threads have addressed the role of specific thread geometries on the magnitude of the stress concentrations [1–4], information that is important for a fatigue analysis. However, most of the information pertaining to whole threaded assemblies are of an empirical nature, determined under static loading conditions, rather than a systematic analytical or numerical analysis. For fatigue analysis of threads, it is necessary to find the answers to such questions as:

1. When the threaded assembly is subject to cyclic traction, how are the reactions between the different threads distributed?
2. Where are the regions with the maximum local stress amplitudes?
3. What are the stress concentrations?

Direct calculation of stresses by numerical modeling of a threaded assembly does not in itself pose any special technical problems; however, it is extremely cumbersome and expensive for large assemblies, even for monotonic loading. In the case of cyclic, variable amplitude loading that induces local nonlinearities, such calculations are practically not feasible. These difficulties are magnified for multiple repetitions of calculations, such as is the case with parametric studies.

Statement of the Problem

This case study examines the development of a fatigue life prediction model that was required by a large petroleum company for the design of large tubular threaded connections in off-shore structures. The problem was to develop an analytical model that could be used for screening connector designs and establishing which should be built for evaluation by full-scale testing. The model needed to be efficient, yet encompass enough of the parameters associated with fatigue so that the calculated results were reasonable within the scope of existing fatigue life prediction methods. The relative effects of various geometric and load parameters on fatigue crack initiation could then be evaluated to determine which aspects of the design should be modified to gain the greatest benefit in terms of improved fatigue life.

A model that serves the purpose stated above should:

- predict the loads on the threads, since ultimately it is the loads that cause the stresses;
- predict the stresses at the location where the fatigue failure is expected to occur; and
- have the ability to handle a variety of geometries, materials, and loading histories.

General Approach to the Problem

The solution to this problem must consider the general characteristics of threaded assemblies. The threads, which may be geometrically and mechanically complex, are a small component of a mechanical system that connects two large diameter pipes. Each thread pitch is reproduced in the assembly many times. Therefore, the solution uses only a small, detailed portion of the assembly (that is, a few thread pitches) to characterize the load and stress parameters that are affected only by the thread geometry. The local model is multiplied, as

necessary, to solve the large-scale problem of the full assembly, where the physical parameters of the complete assembly are taken from a numerical solution of the local model.

In general, the calculation process determines the macro properties of the threaded assembly from local data obtained independently of the loading on the complete assembly. The macro model is easily solved for different loads, making it possible to return to the local level at any critical point in the threaded assembly, where the resulting stresses and strains in the thread root can be obtained.

Background Information

In developing any engineering simulation of a mechanical component, it is necessary to ask questions whose answers will provide the best understanding of how the component behaves in actual service. This ensures that the model will be as realistic as possible. The following questions must be answered to produce a model that encompasses the appropriate parameters for the fatigue life calculation of a large diameter, tubular threaded connection, used in a TLP application.

What is the General Geometry and Configuration of TLP Tether Connections?

The typical configuration of a tether connection for a TLP is illustrated in Fig. 1. These threaded connections consist of an externally threaded pipe, called the pin, and an internally threaded pipe, called the box. For both components, the free end of the threaded length is called the toe, and the end of the threads closest to the pipe is called the heel. The external diameter of the box may be as large as 1.2 m. In many cases, the threads are tapered, as shown in Fig. 1, to facilitate ease of assembly. To prevent seawater from entering the pipe and the threads during service, the end of the box is tightened against the shoulder on the pin. This initial tightening is called preloading, or pretorquing.

What is the Loading on Tether Connections?

There are three sources of load that result in stresses at the roots of the threads: the externally applied load that the connection was designed to carry, the internally generated load that results from preloading the connection, and thermal loading that is caused by differences in temperature throughout the connection. For this analysis, thermal loads will not be considered. Preloading the connection results in an initial static loading condition that must be accounted for in the fatigue analysis.

In this case, the preload is applied at the end of the box, against the shoulder on the pin (Fig. 1). The connection is assembled, and the two components are screwed together until the box end is tightened against the preload shoulder, the same idea as “finger tightening”

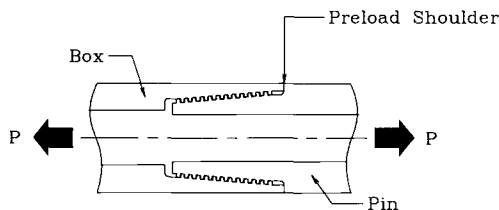


FIG. 1—Typical tether connection for a tension leg platform application.

a bolt and nut assembly. Then, the two halves of the connection are further tightened by a specified torque. The resulting interference at the preload shoulder causes the box of the connection to be nominally placed in compression, and the pin to go into tension. The preload, as defined in this paper, is the magnitude of the resulting force at the preload shoulder.

The loading on the legs of a TLP is axial. An example of a TLP dynamic load history that has been normalized with respect to the maximum load is shown in Fig. 2. Since TLP's are semi-submerged structures that are held in place by the tethers, the upwards buoyant force causes a load history that cycles about a mean tensile load. The load fluctuations are caused by environmental loading, such as wind and waves. The nature of the load history depends considerably on the geographic location of the drilling platform. For example, platforms that are located in the North Sea experience more severe loading spectra than those located in the Gulf of Mexico. Load histories for this type of fatigue analysis must be obtained either by direct measurement or by careful simulation.

What is the Main Mechanism and Location for Fatigue Failure of Tubular Threaded Connections?

As is the case for most types of threaded connections, tubular connections usually fail due to cracks that form in the roots of the threads. This location is most susceptible to fatigue failure because of the stress concentrations associated with the notch-like geometry of the thread roots.

As a result of the non-uniform load distribution along the engaged length of threads, the magnitude of the peak stress varies from thread pitch to thread pitch. Fatigue failures generally occur in the root of the thread with the highest cyclic stresses. This thread, termed the critical thread, is usually the one that carries the highest static load.

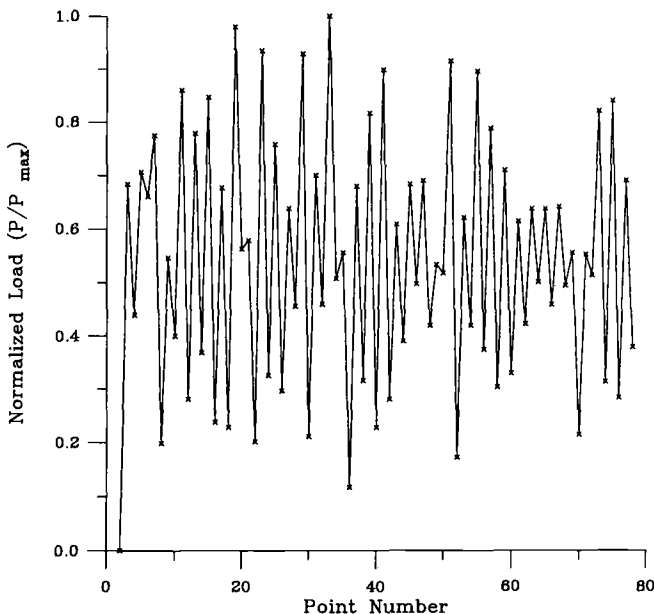


FIG. 2—Example of a normalized load history for a tension leg platform.

What Type of Fatigue Analysis is Appropriate?

Since the fatigue analysis for this problem involves notches, variable amplitude loading, and prestressed components, the strain-life method has been chosen for this case. This method accounts for any notch root plasticity as well as any variations of the local mean or residual stresses. The strain-life method requires the notch root strain history, which may be obtained from the local elastic stress history by using either Neuber's rule [5], or the equivalent strain energy density (ESED) method [6].

Summary of Requirements

Based on the above information, the model must fulfill the following requirements:

1. it must predict the distribution of load in a threaded connection for different levels of external load and different amounts of initial preload, and
2. it must be able to predict the elastic stresses in the thread roots that result from those loads.

By meeting the above two requirements, standard strain-life analysis methods for notches can be used to estimate the fatigue life of the connection. Of course, this leads to some basic assumptions and limitations to the analysis as well. The load on the threaded components must always remain nominally elastic; plasticity in the notch root must be very localized. It is assumed that small amounts of localized plasticity will not significantly affect the elastic behavior of the connection.

Development of the Model

There are four steps needed to simulate the behavior of the threaded connection: deriving the elastic stress concentration factor based on the thread loads, deriving the thread load distribution in the connection, determining the local elasto-plastic strain response in the thread roots, and then calculating the fatigue initiation life using the Manson-Coffin strain-life curve for the material.

The fatigue analysis model for this case is developed for a tubular threaded connection. The geometry of the connection is the same as that studied with photoelastic experiments by Broadbent and Fessler [7,8], providing a means of comparing the calculated load distribution and stress analysis results to actual experimental values. This aids in establishing that the model correctly predicts the behavior of the connection.

Parametric Study of a Tubular Threaded Connection

The threaded tubular connection to be considered for fatigue testing is shown in Fig. 3. It is required to establish the expected effects that the following design changes would have on fatigue life:

1. increasing the level of preload from zero, and
2. increasing the length (number of engaged threads) of the connection while maintaining a constant preload.

The connection is to be fabricated from 4340 steel; the mechanical properties are given in Table 1.

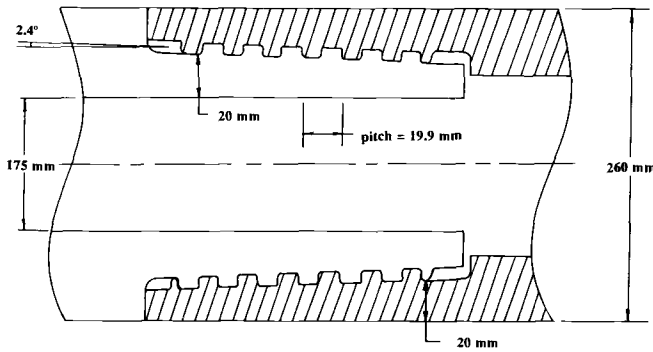


FIG. 3—Tubular threaded connection analyzed in this case study.

Deriving the Stress Concentration Factor

Stress concentration factor, K_t , is defined for a component as the ratio of the local peak stress to the nominal stress. For tubular threaded connections, it is common for the peak stress to be taken at the root of the thread, and the nominal stress to be the average stress in the pipe wall. However, this definition of stress concentration factor is not rigorous enough since it does not consider any internal loading due to preload.

A complete definition of the stress concentration factor must account for all of the loads acting on the structure. Consider the case of a tubular threaded connection that is not loaded externally, but subject to a shoulder preload due to pretorquing. The nominal stress in the pipe section due to external load is equal to zero while clearly there are non-zero stresses in the material within the connector. This load configuration results in an infinite value for K_t , which does not provide a useful representation of the stresses in the thread root.

The first step in developing the stress concentration factor is to clearly define the loads at each thread root. This can be characterized by introducing the load ratio, m , which is the ratio of the load in the cross-section at the thread root to the load on the thread

$$m_i = \frac{P_{nom,i}}{P_i} \quad (1)$$

where

TABLE 1—Mechanical properties of 4340 steel.

| | |
|--|-------------|
| Elastic modulus, E | 208.9 GPa |
| Cyclic strength coefficient, K' | 1760.9 MPa |
| Cyclic strain hardening exponent, n' | 0.146 |
| Fatigue strength coefficient, σ_f' | 1713.3 MPa |
| Fatigue strength exponent, b | -0.095 |
| Fatigue ductility coefficient, ϵ_f' | 0.83 |
| Fatigue ductility exponent, c | -0.65 |
| Transition fatigue life, $2N_t$ | 4100 cycles |
| Yield strength, σ_{ys} | 1103.2 MPa |
| Tensile strength, S_u | 1172.1 MPa |
| True fracture strength, σ_f | 1634.0 MPa |
| True fracture ductility, ϵ_f | 0.83 |

- m_i = the load ratio at thread i ,
- $P_{nom,i}$ = the load on the cross section at the root of thread i , and
- P_i = the load acting on thread i .

These are the two modes of loading that contribute to the total stress in the root of the thread. One component of the total stress is caused by the tensile load acting on the notched body, $P_{nom,i}$, and the other results from the local bending load, P_i , on the thread. Consider these two load cases, as illustrated in Fig. 4. A segment of the threaded connection, shown in Fig. 4a, has a membrane load, P_m , applied across its section. The resulting maximum principal stress component at any given axial position, x , along the surface of the thread root is $\sigma_m(x)$. Therefore, a corresponding normalized stress distribution, $K_m(x)$, may be defined as

$$K_m(x) = \frac{\sigma_m(x)}{S_m} \tag{2}$$

where

- $K_m(x)$ = the normalized membrane stress distribution on the surface of the thread root,
- $\sigma_m(x)$ = the maximum principal stress component in the thread root due to the membrane load, and
- S_m = the nominal stress in the thread root section due to the applied membrane load.

The nominal stress in the root section, S_m , is the average stress on the cross-sectional area, A ,

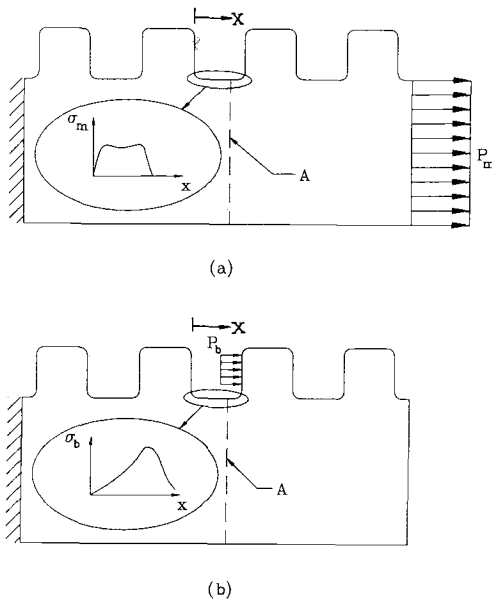


FIG. 4—Schematic diagram of the two loading modes; (a) membrane load, and (b) thread bending load.

$$S_m = \frac{P_m}{A} \quad (3)$$

Similarly, Fig. 4*b* shows the same segment of threads with one thread load, P_b , applied. For this case, the principal stress distribution, $\sigma_b(x)$, may be expressed as a normalized stress distribution, $K_b(x)$, by using the nominal section stress caused by the thread load

$$K_b(x) = \frac{\sigma_b(x)}{S_b} \quad (4)$$

where

$K_b(x)$ = normalized stress distribution as a function of position, x , that results from the applied bending load;

$\sigma_b(x)$ = the distribution of the maximum principal stress component; and

S_b = the nominal stress in the thread root section due to the applied thread load.

In this case, the average stress in the thread root section, S_b , is caused by the load acting on the thread and is defined by

$$S_b = \frac{P_b}{A} \quad (5)$$

The concept of the *bending* stress distribution, used in Eq 4, is a notional one because the load acting on the one thread pitch does create both bending and membrane stresses. For a threaded component that is nominally loaded in tension, it is always the case that $m \geq 1$. By the definition of the load ratio, Fig. 4*b* shows the case for $m = 1$.

For an elastic stress analysis, the principle of superposition may be used to determine the total stress in the thread root. The distribution of total stress in the thread root, $\sigma(x)$, may be expressed as the sum of the membrane and bending stress distributions

$$\sigma(x) = \sigma_m(x) + \sigma_b(x) \quad (6)$$

Each stress distribution term in Eq 6 can be expressed by the nominal stress and the normalized principal stress distributions given by Eqs 2 and 4 such that

$$SK_t(x) = S_b K_b(x) + S_m K_m(x) \quad (7)$$

Substituting for the nominal stresses with the applied loads gives

$$\frac{(P_m + P_b)K_t(x)}{A} = \frac{P_b K_b(x)}{A} + \frac{P_m K_m(x)}{A} \quad (8)$$

that can be simplified by multiplying both sides by the cross sectional area, A , and dividing by $P_m + P_b$

$$K_t(x) = \frac{1}{P_m + P_b} [P_b K_b(x) + P_m K_m(x)] \quad (9)$$

Finally, the load ratio m for this superposition of the load cases in Figs. 4a and b, is given by

$$m = \frac{P_m + P_b}{P_b} \quad (10)$$

Substituting P_b in terms of P_m and m into Eq 9 gives the relationship between K_t and m

$$K_t(x) = \frac{1}{m} [K_b(x) - K_m(x)] + K_m(x) \quad (11)$$

In Eq 11, $K_b(x)$ and $K_m(x)$ are independent of the applied load, and depend only on the thread geometry. However, the total normalized stress distribution, $K_t(x)$, depends on the current distribution of load in the connection.

The stress distributions in Eq 11 can be obtained from a small local model of four thread pitches and two different load cases, shown in Fig. 5. An axisymmetric finite element model is used to represent the threaded connection. This means that the thread helix is modeled by a series of rings on the cylindrical body. This simplification is a generally accepted assumption for thread analysis that is suitable when the diameter of the threads is large compared to the pitch and the helix angle. The first load case, shown in Fig. 5a, is a tensile membrane load applied evenly across the face of the model. The stress distribution along the surface of the thread root, normalized with respect to the average stress in the section for this load

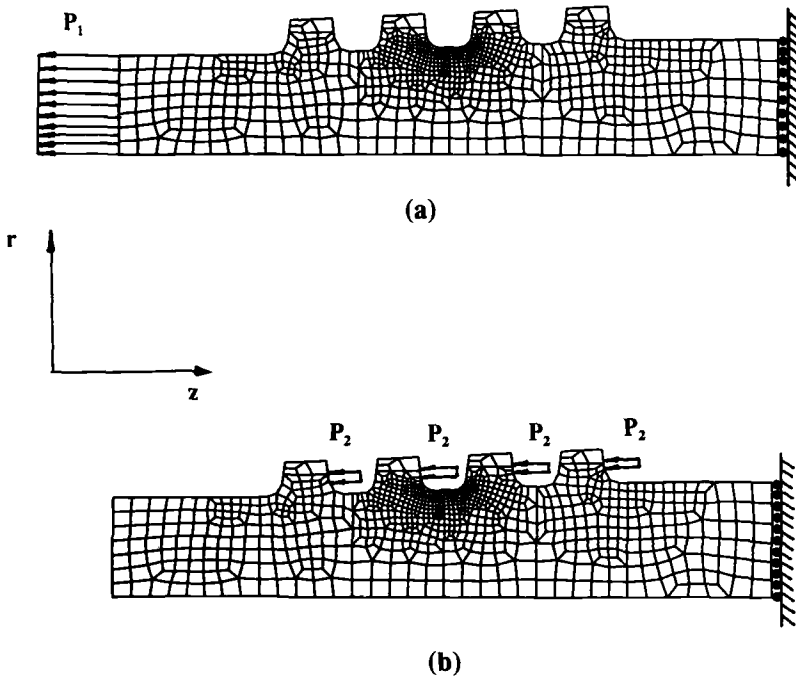


FIG. 5—Axisymmetric finite element models of four pitches from the pin of the connector; (a) membrane load condition, and (b) thread bending load condition.

case, gives the $K_m(x)$ curve for this thread root geometry. The second load case, shown in Fig. 5b, is loading applied to the face of each thread in the model. The magnitude of the axial component of each load is the same for all of the threads. Note that this load case does *not* represent the bending load case used for Eq 4. It provides the normalized total stress distribution, $K_t(x)$, for the specific case of $m = 2$, which will be referred to as $K_2(x)$. Even though $K_b(x)$ cannot be determined directly from either of these two load cases, they provide enough information to solve for $K_t(x)$ by using Eq 11. Thus, the general expression for $K_t(x)$, derived from the numerical solution, can be expressed as

$$K_t(x) = \frac{1}{m} [2K_2(x) + (m - 2)K_m(x)] \tag{12}$$

The stress concentration factor, K_t , is the maximum value of the $K_t(x)$ distribution for a given value of the load ratio, m . The normalized stress curves obtained from each load case are shown in Fig. 6, and Fig. 7 presents K_t as a function of the load ratio, m .

Broadbent and Fessler [8] presented normalized peak stresses from their photoelastic analysis of the connector. In Fig. 8, these are compared to the peak stresses that were predicted with the stress concentration factor relationship (Eq 12), and normalized by using the same method as Broadbent and Fessler. The load ratio values were calculated from the predicted thread load distribution, which is derived in the next section. It is important to understand that the ends of the thread helix in the photoelastic model are constructed with a thread *run-out*. Run-out is a decrease in the thread width to zero (like a wedge) over one half of a pitch. The effect of this is a greatly reduced thread stiffness that causes the thread loads and stresses to increase at the ends of the engaged length. In practice, unlike the threads modeled by Broadbent and Fessler, the run-out is removed so that only fully formed threads carry any load.

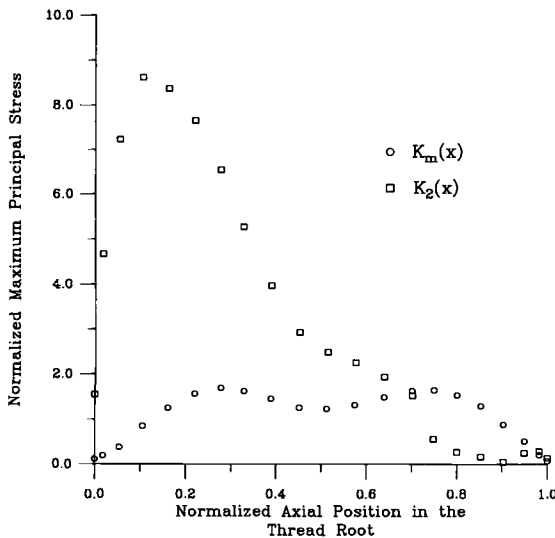


FIG. 6—Normalized thread root surface stresses obtained from the finite element solution.

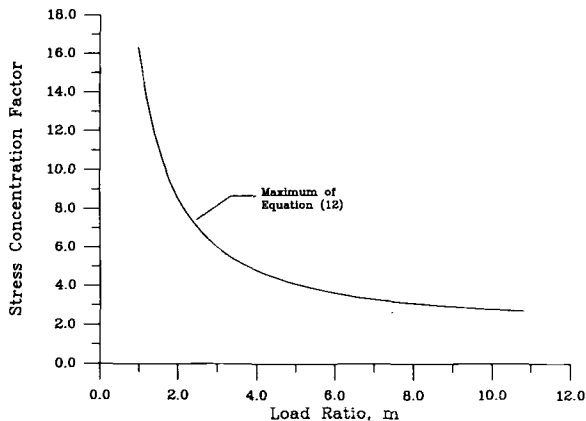


FIG. 7—Stress concentration factor as a function of the load ratio.

Load Distribution Analysis

It has been shown that the local elastic stress concentration for the thread roots can be calculated once the load ratio, m , is known. Therefore, the second part of the model must allow the load distribution to be calculated so that the individual thread loads can be found. There have been many analytical solutions to this problem; however, the method proposed

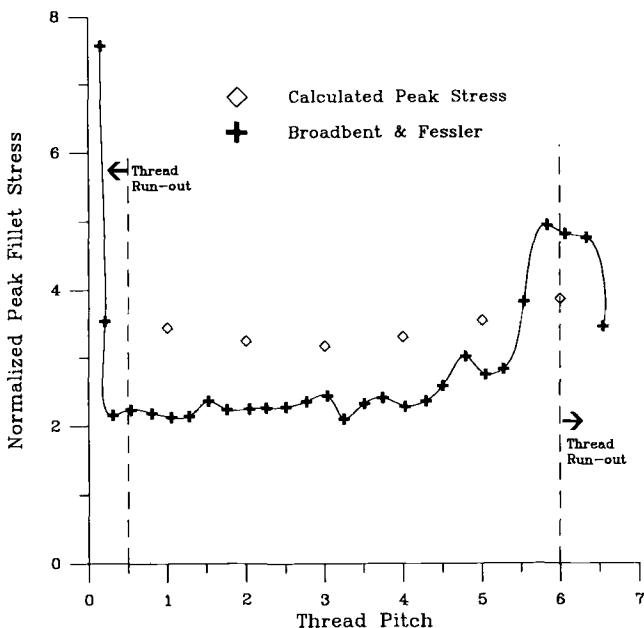


FIG. 8—Normalized thread root stresses calculated from Eq 12 compared to the photo-elastic results of Broadbent and Fessler from Ref 8.

by several researchers in the past [9-11] is best suited for computer fatigue calculations. This method uses a linear spring network analogue to represent the deformation of the threaded connection. The basic concept of the analogue model is to separate the different components of deformation in the threaded connection into those that can be represented by using simple analytical techniques. The component deformations are then mathematically reassembled so that the total deformed configuration may be determined by satisfying force equilibrium.

The elastic deformations are modeled by linear spring elements. Figure 9 shows spring elements superimposed onto a schematic of a connection with three engaged thread pitches so that the physical meaning of each element may be illustrated. The two modes of deformation considered are the axial deformations of the cylindrical core sections in the box and pin, and the lumped shear and bending deformation of each thread pitch on an elastic support. For bending and shear, one spring element is used to represent the total deformation of two mating threads. All of the elements in the model are assumed to be rigidly connected so that only one-dimensional axial deformation is considered.

The stiffness values for the springs in the network are obtained by using analytical and numerical methods. The axial stiffness values are calculated analytically with the following equation

$$k_A = \frac{AE}{p} \tag{13}$$

where

- k_A = the axial stiffness,
- A = the cross sectional area at the root of the thread,
- E = Young's modulus, and
- p = the thread pitch.

The bending stiffness values are obtained from the same finite element model that was used to determine the stress concentration factor for the thread roots. For the load case where all of the threads in the small model are loaded, the displacements of nodes on the pitch line of the threads are used in conjunction with the axial stiffness values calculated using Eq 13 to solve for the values of k_B . This is illustrated in Fig. 10. For example, the value of k_{B3} is easily found from the nodal displacement u_3 , and the known forces and axial stiffness values by

$$u_3 = \frac{F}{k_{B3}} + \frac{2F}{k_{A3}} + \frac{3F}{k_{A2}} + \frac{4F}{k_{A1}} \tag{14}$$

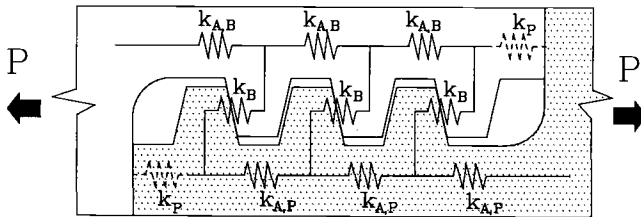


FIG. 9—Schematic of a connector with three engaged thread pitches and the corresponding spring element model.

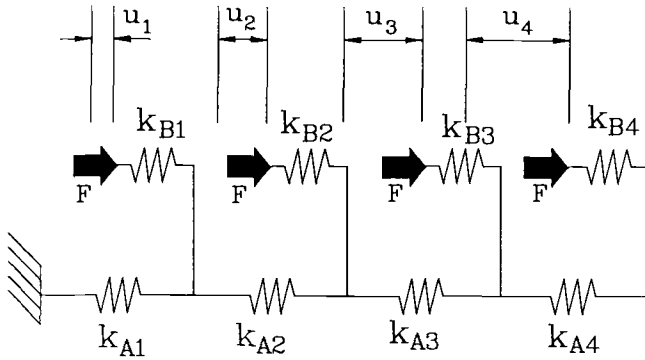


FIG. 10—Spring network used for calculating thread bending stiffness from the finite element results.

The load distribution in the connection is obtained by solving a matrix solution for static equilibrium of the spring network for the entire connection, with the appropriate load and displacement conditions. For the connection analyzed experimentally by Broadbent and Fessler [7], the load distribution is given in Fig. 11. It is compared to the load distribution calculated by using the spring network analogue. The calculated results are presented for a connection with six engaged thread pitches. The photoelastic results of Broadbent and Fessler were for a connection having between six and seven engaged threads including the thread run-out. (See the discussion on run-out in the previous section.) Their results were obtained by sectioning the 3D model at 90-degree intervals and summing the shear stresses across the base of the thread to obtain the average load at that point. Therefore, there are up to

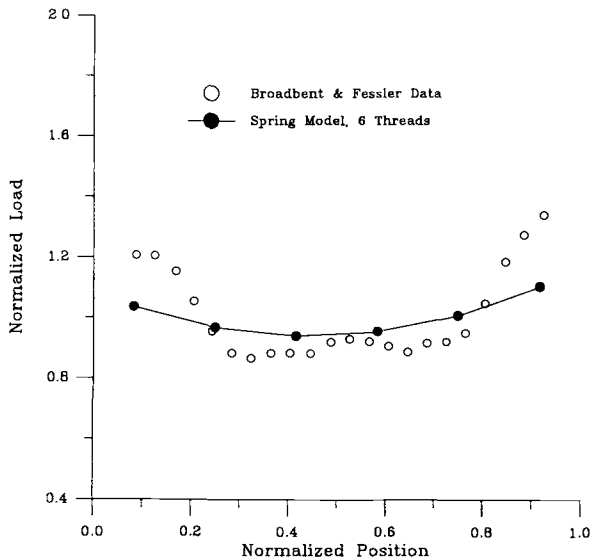


FIG. 11—Analogue model solutions for the load distribution in a connector with six engaged thread pitches compared to the photo-elastic results of Broadbent and Fessler from Ref 7.

four data points per thread pitch around the thread helix. The spring element model can only represent entirely engaged, fully formed thread pitches; the calculated loads represent the average load over one thread pitch. Results for a connector with only a preload applied to it are presented in Fig. 12.

Fatigue Life Calculations for the Parametric Study

For every case in the parametric study, the local elastic stress history was calculated for each peak of the loading history, shown in Fig. 2. A maximum load 6783.5 kN was used for all of the fatigue calculations. This load represents a nominal stress in the heel of the pin that is approximately 50% of the yield stress of the material. Note that in all cases, the maximum applied load exceeds the magnitude of the preload. For tubular threaded connections, the load at the preload shoulder may be lower than the maximum applied load. This is different from the design requirements of bolted joints for which the effect of the preload is diminished by exceeding the initial clamping load; this occurs in direct proportion to the applied load. In tubular threaded connections, as external load is applied the load at the preload shoulder decreases at a rate that is lower than that of the increasing applied load. The effect of preload in tubular connections is diminished by reducing the load at the preload shoulder to zero.

In tubular threaded connections, the magnitude of the applied load that is necessary to cause the preload shoulder load to go to zero is termed the *critical load*; this load may be many times greater than the initial preload applied to the connection. For this example, the critical load is approximately eight times the magnitude of the preload.

The local elasto-plastic strain history was determined by the application of Neuber's rule [5] and the hysteresis loop was obtained by doubling the cyclic stress-strain curve. The state of stress on the surface of the thread roots is biaxial, with stress components in the axial and hoop directions.

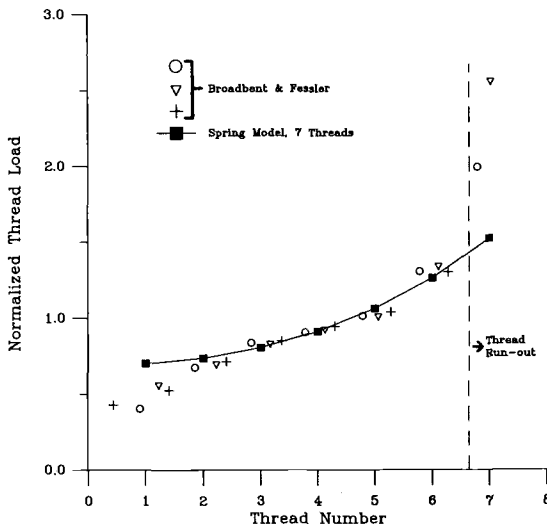


FIG. 12—Analogue model solution of the load distribution for preload only compared to the photoelastic results of Broadbent and Fessler from Ref 7.

Therefore, a plane stress assumption is not appropriate for this analysis. Plane strain assumptions are better for this application since they more closely approximate the actual stress state in the thread roots. Although the strain in the hoop direction is not equal to zero, it is small compared to the strains in the axial direction.

Plane strain was assumed for this analysis and applied with Neuber's rule and the plane-strain modification to the stress-strain curve suggested by Dowling et al. [12]. Neuber's rule is usually presented with the term $K_t \Delta S$ for the change in elastic stress. It is important to note that in preloaded tubular threaded connections, K_t varies nonlinearly with applied load. Therefore, Neuber's rule must be used in the following form

$$\frac{(\Delta\sigma)^2}{E} = \sigma\epsilon \quad (15)$$

where $\Delta\sigma$ is the total change of the local elastic peak stress for one load reversal.

The local elasto-plastic strain history was used to determine the fatigue damage from the strain-life curve (the parameters are given in Table 1) with Morrow's correction for mean stress [13]

$$\frac{\Delta\epsilon}{2} = \frac{\sigma'_f - \sigma_m}{E} (N_f)^b + \epsilon'_f (N_f)^c \quad (16)$$

where σ_m is the mean stress.

Rainflow counted cycles were used with a linear damage cumulation rule (Miner's rule) to estimate the expected fatigue lives.

Results

The effect of preload on the fatigue life of the connector is illustrated in Fig. 13. Absolute values of predicted life are purposely left out to emphasize that this model is intended to estimate the *relative* effect of parameters on fatigue as an aid to designing actual fatigue tests. Only after actual testing is conducted, could the calculated fatigue life predictions be quoted as absolute values.

Figure 13 shows that increasing the preload protects the threads on the pin by decreasing the amplitude of the cyclic stresses in the root of the thread (Fig. 14). This is effective up to a certain level at which the increasing mean stress predominates the fatigue damage and the total life starts to drop off again.

Figure 15 illustrates the effect of increasing the number of threads in the connection. It can be seen that adding more threads results in higher fatigue lives, but with diminishing returns. Increasing the number of threads reduces the overall load carried by each thread pitch. However, the amount of load reduction also decreases until adding more threads does not yield any significant benefit.

Summary and Conclusions

The key aspects of the solution technique may be summarized as follows:

1. An axisymmetric finite element model of a small segment of the threaded connection is solved for two different load cases: tensile membrane loading and direct thread

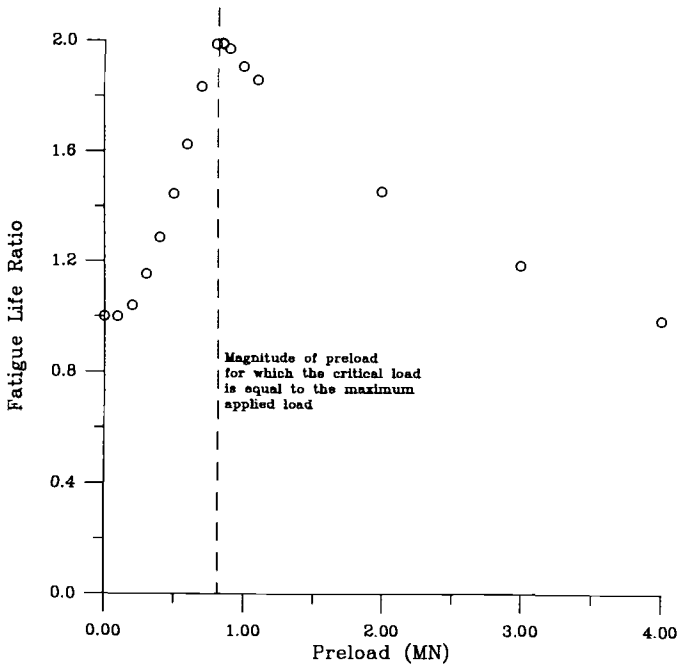


FIG. 13—Ratio of the calculated fatigue life at the root of the critical thread to the calculated fatigue life for a connector with no preload. This ratio is plotted as a function of the preload level.

- loading. The results are used to obtain the stress concentration factor relationship and the bending stiffness of the threads.
2. The axial and bending stiffness values are used in a spring network model of the entire connection to determine the thread load distribution as a function of the applied load and the preload.
 3. For each peak in the applied load history, the load ratio at the thread of interest is calculated and used to find the stress concentration factor. The local elastic stress history is derived from the load history.
 4. Notch strain analysis such as Neuber's rule or the ESED method are used to generate the local elasto-plastic strain history at the thread root.
 5. An appropriate cycle counting and damage hypothesis are applied with the strain-life curve to calculate the fatigue life of the threaded connection.

This efficient method for estimating the fatigue life of tubular threaded connections provides a convenient means for estimating the impact of design parameter changes on the overall fatigue performance of the connection. Understanding the behavior of the connections is essential in designing meaningful fatigue tests for full-scale connections. The results of the model are subject to the same caveats and limitations of the strain-life analysis that is used. Use of the model for estimating the actual service life of a large threaded connection is not valid without actual experimental tests to verify the results from the model.

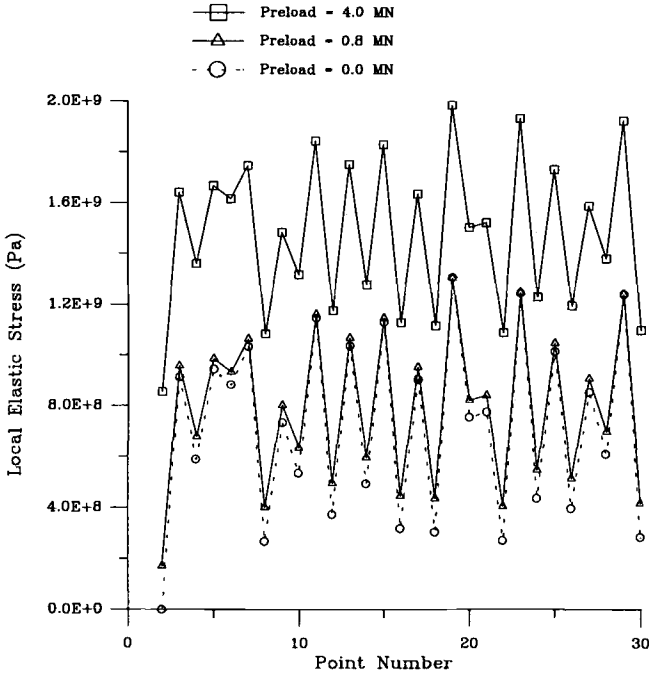


FIG. 14—Local elastic stress history at the root of the critical thread for three different levels of preload (only the first 30 points are plotted for clarity).

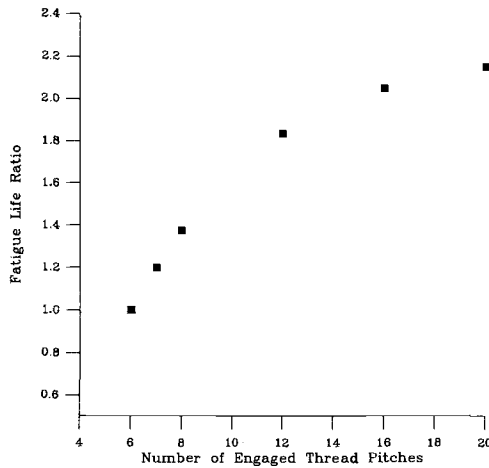


FIG. 15—Ratio of the calculated fatigue life at the root of the critical thread to the calculated fatigue life for a connection with six engaged thread pitches. The ratio is plotted as a function of the thread length (in number of pitches). The preload is 1.0 MN in all cases.

Student Questions

1. There are many different ways that this model can be made more or less conservative. List the aspects of the model that make it conservative. Suggest ways to make the model less conservative, (and, therefore, "more accurate").
2. Could this model be used to model other types of threaded connections, such as nut/bolt connections, or the end closures to pressure vessels? Which assumptions used in the development of this model would need to be re-examined if the model were to be applied to other situations?
3. Give possible reasons why even with a pin protecting preload that leaves the threads at the heel of the box completely unprotected and subject to the full amplitude of the applied loading history, that connections still fail predominantly at the first thread pitch in the pin.
4. While the model indicates that the optimum preload would provide a critical load equal to the maximum applied load, explain why this is not possible in practice. What would be a suitable preload for this connection, assuming that the calculated fatigue life were verified in testing?
5. If at first, cracks were to form and start growing in a thread root that was in the middle or towards the toe of the pin, explain why the connection would be likely to fail at the root of the first thread in the pin anyway?

References

- [1] Kenny, B. and Patterson, E. A., "Load and Stress Distribution in Screw Thread," *Experimental Mechanics*, Vol. 25, No. 3, 1985, pp. 205–213.
- [2] Seika, M., Sasaki, S., and Hosono, K., "Measurement of Stress Concentrations in Threaded Connections," *Bulletin of the JSME*, Vol. 17, No. 111, 1974, pp. 1151–1156.
- [3] Brown, A. F. C. and Hickson, V. M., "A Photo-elastic Study of Stresses in Screw Threads," *Proceedings of the Institution of Mechanical Engineers*, Institution of Mechanical Engineers, London, 1952, pp. 605–612.
- [4] Hetenyi, M., "The Distribution of Stress in Threaded Connections," *Experimental Stress Analysis*, Vol. 1, No. 1, 1943, pp. 147–156.
- [5] Neuber, H., "Theory of Stress Concentration for Shear Strained Prismatical Bodies with Arbitrary Non-Linear Stress Strain Law," *Journal of Applied Mechanics*, Dec. 1961, pp. 544–550.
- [6] Glinka, G., "Energy Density Approach to Calculation of Inelastic Stress-Strain Near Notches and Cracks," *Engineering Fracture Mechanics*, Vol. 22, No. 3, 1985, pp. 485–508.
- [7] Broadbent, T. P. and Fessler, H., "Distribution of Thread Load in Screwed Tubular Connections," *Fatigue of Offshore Structures*, W. D. Dover and G. Glinka, Eds., Engineering Materials Advisory Service (EMAS), Cradley Heath, England, 1988.
- [8] Broadbent, T. P. and Fessler, H., "Stress Analysis of Screwed Tubular Joints," *Fatigue and Crack Growth in Offshore Structures, Proceedings of the Institute of Mechanical Engineers*, Institute of Mechanical Engineers, London, 1988, pp. 171–186.
- [9] Bluhm, J. L. and Flanagan, J. H., "A Procedure for the Elastic Stress Analysis of Threaded Connections Including the Use of an Electrical Analogue," *Experimental Stress Analysis*, Vol. XV, 1957, p. 85.
- [10] Miller, D. L., Marshek, K. M., and Naji, M. R., "Determination of Load Distribution in a Threaded Connection," *Mechanism and Machine Theory*, Vol. 18, No. 6, 1983, pp. 421–430.
- [11] Newport, A., Topp, D. A., and Glinka, G., "The Analysis of Elastic Stress Distribution in Threaded Tether Connections," *Journal of Strain Analysis*, Vol. 22, No. 4, 1987, pp. 229–235.
- [12] Dowling, N. E., Brose, W. R., and Wilson, W. K., "Notched Member Fatigue Life Predictions by the Local Strain Approach," *Fatigue Under Complex Loading: Analyses and Experiments*, Society of Automotive Engineers (SAE), Warrendale, PA, 1977, pp. 55–84.
- [13] Morrow, J., "Cyclic Plastic Strain Energy and Fatigue of Metals," *Internal Friction, Damping and Cyclic Plasticity, ASTM STP 378*, American Society for Testing and Materials, Philadelphia, 1965, p. 45.

Herbert J. Sutherland,¹ Paul S. Veers,¹ and Thomas D. Ashwill¹

Fatigue Life Prediction for Wind Turbines: A Case Study on Loading Spectra and Parameter Sensitivity

REFERENCE: Sutherland, H. J., Veers, P. S., and Ashwill, T. D., “Fatigue Life Prediction for Wind Turbines: A Case Study on Loading Spectra and Parameter Sensitivity,” *Case Studies for Fatigue Education, ASTM STP 1250*, Ralph I. Stephens, Ed., American Society for Testing and Materials, Philadelphia, 1994, pp. 174–207.

ABSTRACT: Wind turbines are fatigue-critical machines used to produce electrical energy from the wind. These rotating machines are subjected to combinations of wind, gravity, and gyroscopic loadings that are highly irregular in nature. Historical examples of fatigue problems in both research and commercial wind-turbine development are presented. Some example data on wind-turbine environments, loadings, and material properties are also shown. Before a description of how the authors have chosen to attack the cumulative damage assessment, questions are presented for the reader's reflection. The solution technique used by the authors to define the loading spectrum for wind turbines is then presented. Special emphasis is placed on the development of a loading spectrum for use in the fatigue analysis. Less attention is paid to methods of cumulative damage assessment; Miner's rule and constant amplitude *S-n* data are used. A case study then applies the procedures to an actual wind-turbine blade joint. The wind turbine is the 34-m diameter vertical axis wind turbine (VAWT) erected by Sandia National Laboratories near Bushland, TX. The case study examines parameter sensitivities for realistic uncertainties in inputs defining the turbine environment, stress response, and material properties. The fatigue lifetimes are calculated using a fatigue analysis program, called LIFE2, which was developed at Sandia. The LIFE2 code, described in some detail in the Appendix, is a PC-based, menu-driven package that leads the user through the steps required to characterize the loading and material properties, then uses Miner's rule or a linear-crack propagation rule to numerically calculate the time to failure. Only *S-n* based cumulative damage applications are illustrated here.

The LIFE2 code is available to educational institutions for use as a case study in describing complicated loading histories and for use by students in examining, hands on, parameter sensitivity of fatigue life analysis

KEYWORDS: fatigue, wind turbines, loading spectrum, damage assessment, Miner's rule, uncertainty, variability

History

Most large, modern windmills (currently called wind turbines) are used to produce electrical power for utility applications. The largest concentration of this class of turbines in the world (about two-thirds of the world's capacity) is contained in three California sites. California has over 16 000 turbines with a total rated capacity of between 1500 and 1600 MW, generating approximately 1% of California's total electrical usage. In 1992, they generated

¹ Distinguished member of technical staff, senior member of technical staff, and senior member of technical staff, respectively, Wind Energy Technology Department, Sandia National Laboratories, Albuquerque, NM 87185-0708.

2.8 billion kWh of electricity, which is sufficient to supply the residential electricity needs of a city the size of San Francisco, CA or Washington, D.C. for one year. In that year alone, they averted emission of more than 2.8 billion lbs of carbon dioxide, a major greenhouse gas, and 17 million lbs of other pollutants that would otherwise be produced by fossil-fuels [1,2]. While additional developments are continuing throughout the United States, additions to European wind installations are projected to surpass U.S. capacity before the turn of the century, when Europe will have two-thirds of the world's wind power [3].

Wind turbines may be divided into two generic groups based on their axis of rotation: horizontal axis wind turbine (HAWT) blades rotate about a horizontal axis and vertical axis wind turbine (VAWT) blades rotate about a vertical axis. A typical HAWT, the Northern Power Systems 100-kW turbine, is shown in Fig. 1 [4]. An example of a VAWT is shown in Fig. 2. This turbine, the Sandia/DOE 34-m Test Bed, is a 500-kW research turbine, located near Bushland, TX, and built as part of the U.S. Department of Energy (DOE) wind energy research program [5]. Other turbines have more or fewer blades (some have only one) and HAWTs may have either an up-wind or down-wind blade orientation. The VAWT Test Bed is used in an example presented here; however, the discussions and analysis techniques presented in this paper are applicable to wind turbines of either configuration.

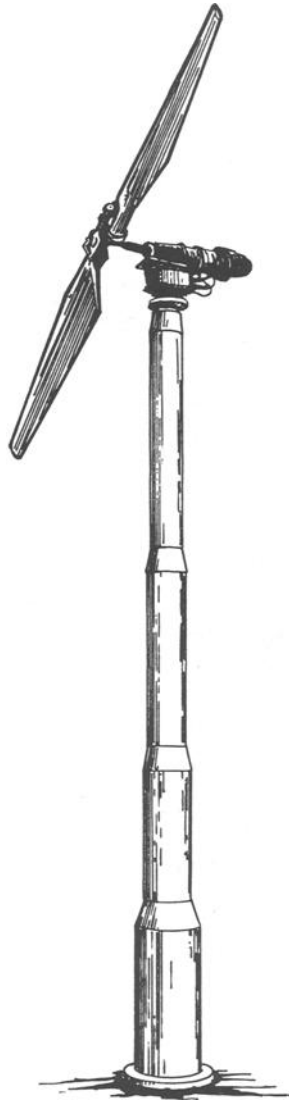
Fatigue Problems with Wind Turbines

The first truly modern wind turbine, the Smith-Putnam megawatt scale HAWT, was built in New England during World War II under wartime motivation to save oil. The machine experienced continual problems with blade fatigue and was never able to achieve its promised productivity. When wind energy again gained prominence in the early 70's (following the Arab oil embargo), there was a tendency to view implementation of the technology as basically a problem in aerodynamics. The first research machine installed at Sandia National Laboratories was operated on the roof of a three-story building in the center of a populated area. No structural measurements were collected during initial performance testing. Only later, when a strain gage was monitored, was it discovered that the blades were loaded nearly to their yield strength on every rotation. The testing resumed with reinforced blades in a more remote site.

A large HAWT research machine of mid 70's vintage, the NASA 100 kW Mod-0, also experienced fatigue problems. Maintenance workers first saw evidence of hydraulic fluid leaking from blade cracks during a visual inspection from the ground. A fairly complicated joint, between a steel spar and the aluminum stressed skin of the blade, had numerous cracks. Crack patching efforts only extended the life marginally, providing time to obtain performance data. Subsequent analyses revealed that the loads on the turbine due to wind shear (the variation in wind with height) and tower shadow (wind blockage by the tower) had been grossly underestimated².

Even nominally simple components with simple designs and loadings can experience fatigue problems. The multi-megawatt (2.5 MW) Mod-2 turbines located near Goodnoe Hills, WA had a simple, hollow, circular main shaft (the shaft that connects the blades to the gear box). The predominant load on the shaft was due to the weight of the rotor, that is, simple gravity loading on a rotating shaft. Access ports into the center of the shaft were thoroughly analyzed before installation. Unfortunately, unknown to the designers and analysts, installation crews drilled tiny holes near the access ports for a set of mounting brackets. A crack started in one of these holes, propagated to the larger ports, and was almost half way around

² Spera, David, private correspondence, 1993.

FIG. 1—*The NPS HAWT.*

the shaft before a maintenance technician, working on the parked rotor for completely unrelated reasons, noticed the huge crack.²

Problems were also experienced in the commercial sector during this period. One entrepreneurial start-up company of the early 80's was sponsored by investors who were seeking to harvest tax credits. These credits required that the turbines be installed before the end of the calendar year. The company's sole engineer was trying desperately to get some operating data (performance, stress levels, and so forth) off the prototype machine on a windy New Mexico mesa while supervising the production and installation of a group of machines near Palm Springs, CA. Equipment malfunctions and telemetry problems on the prototype made

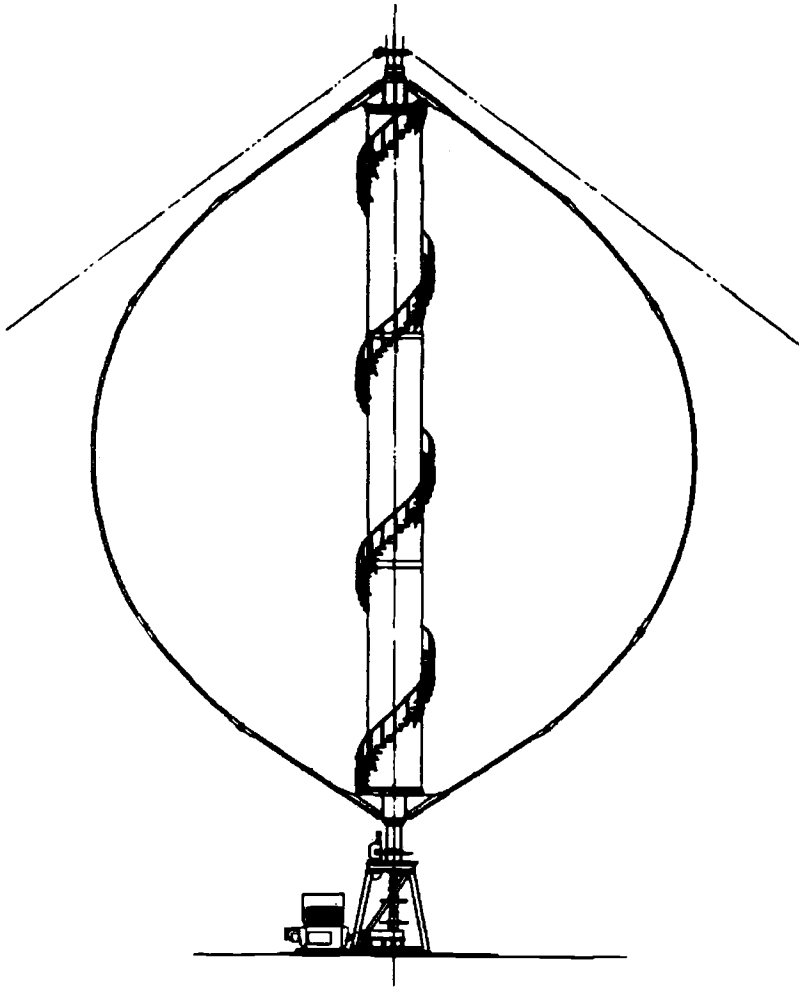


FIG. 2—The Sandia 34-m VAWT Test Bed.

time series data hard to get, but data in the form of hardware kept appearing on the ground. Every time the prototype was operated, broken bolts were strewn about the turbine. Subsequent operational and modal test results indicated that the rotor had not one, but two natural frequencies of vibration coincident with the rotational speed of the turbine. Either one of these resonant conditions would have been sufficient to shake the turbine apart in a few hours of operation.³

Virtually all of the turbines built in California in the early 80's have experienced fatigue problems in "energetic" sites (sites with an average wind speed of 7 m/s or more). Blades

³ The production machines had to be erected before the end of the year for tax purposes. Although retrofit with stiffening struts to eliminate the resonances, they were plagued with problems and never became productive machines. The company soon went bankrupt. After standing idle for a decade, the machines were removed.

have been repaired or replaced on most of the turbines. Inspection and maintenance programs have progressed tremendously as the operators gain the wisdom of thousands of hours of operating experience on thousands of turbines. Turbines installed more recently have demonstrated tremendous improvements in availability. In addition, research programs at the national laboratories are measuring material fatigue properties, defining turbine loadings, and creating fatigue lifetime estimation tools for use in the design of the new generation of machines currently on the drawing board at a handful of U.S. companies.

Why so Many Fatigue Problems?

A wind turbine residing in a farmer's pasture on a midwestern plain or in a mountain pass near a hot California desert is subject to the whims of Mother Nature. It must rotate when the wind is blowing anywhere from 5 to 25 m/s (12 to 60 mph), enduring many cycles of vibration. The machine must also be able to stop in any wind condition and survive bone-rattling gusts (in a parked condition) greater than 55 m/s (120 mph).

At rotation rates from 30 to 60 rpm, it does not take long to accumulate large numbers of oscillations. The blades of a 30-year life turbine typically must withstand at least 10^9 cycles, quite large for any rotating piece of equipment. The stress concentrations at "hot spots" are often not known, and the fatigue properties of typical turbine materials are not well characterized.

Wind turbines were installed in large numbers in California in the early 1980's. The driver for this installation frenzy was the tax advantage to the investor of an installed machine, regardless of the eventual revenue stream.⁴ Some particularly poorly engineered machines were blown down by the first major storms through the mountain passes where the wind farms are located. But most machines had no trouble with the severely stormy environments; they just tended to break under the continual cyclic loading of operation.

Even the most successful of the early turbine designers had overlooked a significant component of the loads. The designers assumed the loads could be approximated using a spatially uniform incoming wind, with variations in the average proceeding very slowly. However, unlike aircraft, which fly in normally uniform flows high above the ground, wind turbines always operate in the earth's turbulent boundary layer. Thus, the incoming wind fluctuates significantly in both time and space. Turbulence was originally thought to produce dynamic loads at sufficiently low frequencies to be neglected. But because the blades produce relatively large lift forces as they move through the wind, the turbulence-induced loads are magnified and shifted to higher frequencies (just as the speed of a car driving over a rough road affects the frequency of the loads). The broad-band nature of turbulence also excites the natural frequencies of the turbine more than had been expected.

Economics

As illustrated in the examples cited above, wind turbines are subjected to at least a billion fatigue cycles during the course of a service lifetime. In comparison, transport aircraft are typically designed for between one and ten million stress cycles. The turbine must therefore endure the lifetime stress cycles of an aircraft every three months of its service lifetime. The ability of turbine designers to address a difficult design problem with "high tech" solutions is greatly restricted by economics. Wind turbines are designed to produce electrical power

⁴ The wind industry is currently opposed to any tax incentives based on *installation*, but instead favors *production* based measures to rectify inequities in relative treatment of competing electricity sources.

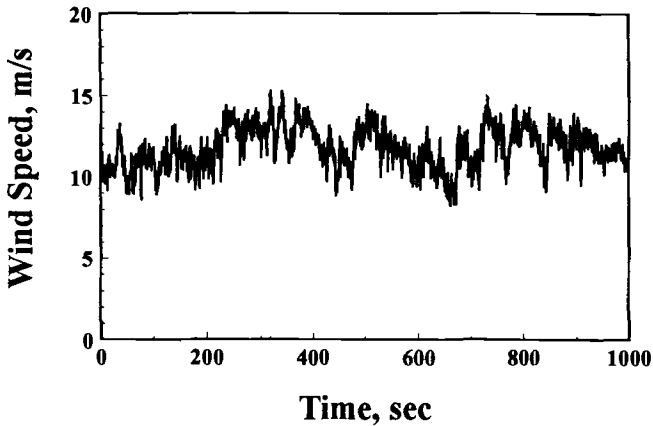


FIG. 3—Typical wind speed time series data.

for the grid and therefore compete economically with conventional sources of electrical power generation. As an example, the use of aerospace class materials to reduce weight and to enhance the reliability and structural properties of turbine blades is almost impossible because of the cost. The wind industry typically builds blades using fiberglass composites from boat building technology or aluminum alloys typically reserved for architectural trim.

The Problem

Overview

After the previous brief perspective on the difficulties and constraints of the wind business, we now turn our attention to the problem of predicting fatigue lives for wind turbine components. First, raw data from operating wind turbines are presented to provide an example of typical environments, loadings, and material properties for wind turbines. The reader is then asked to stop and reflect on questions about how to approach the cumulative damage assessment under such circumstances. The solution technique developed by the authors is then presented with special emphasis on development of the fatigue loading spectrum. A computer code called LIFE2 [6-11], capable of calculating fatigue lifetimes for wind turbine components, is described in some detail in Appendix A. The last major section of this paper uses the LIFE2 code to conduct a case study on the variability of fatigue life predictions due to realistic uncertainties in the input parameters required by this analysis technique.⁵

Raw Data Examples

The wind itself, of course, is random. An example of a wind time series from the Texas Panhandle is shown in Fig. 3. This data record lasts approximately 15 min (1000 s), during which time the wind speed varies between 8 and 15 m/s. The so-called turbulence intensity, a measure of the amount of fluctuation in wind speed, is computed by dividing the standard deviation by the mean. The average wind speed in Fig. 3 is 11.4 m/s, and the turbulence

⁵ The LIFE2 code is available by request from the authors.

intensity is 11.7%. Most current wind farms in the United States are located in mountain passes where the winds are much more turbulent, with intensities between 15 and 30%.

Turbine blades are the most fatigue-sensitive component of the turbine because of the magnitude and number of stress cycles they experience. Research turbines, prototypes, and even some production turbines are strain-gaged to measure the response of the blades in various conditions [12]. Figure 4 shows the response of the 34-m Test Bed blades in both the flatwise bending (about the chord line of the airfoil) and lead-lag bending (about an axis

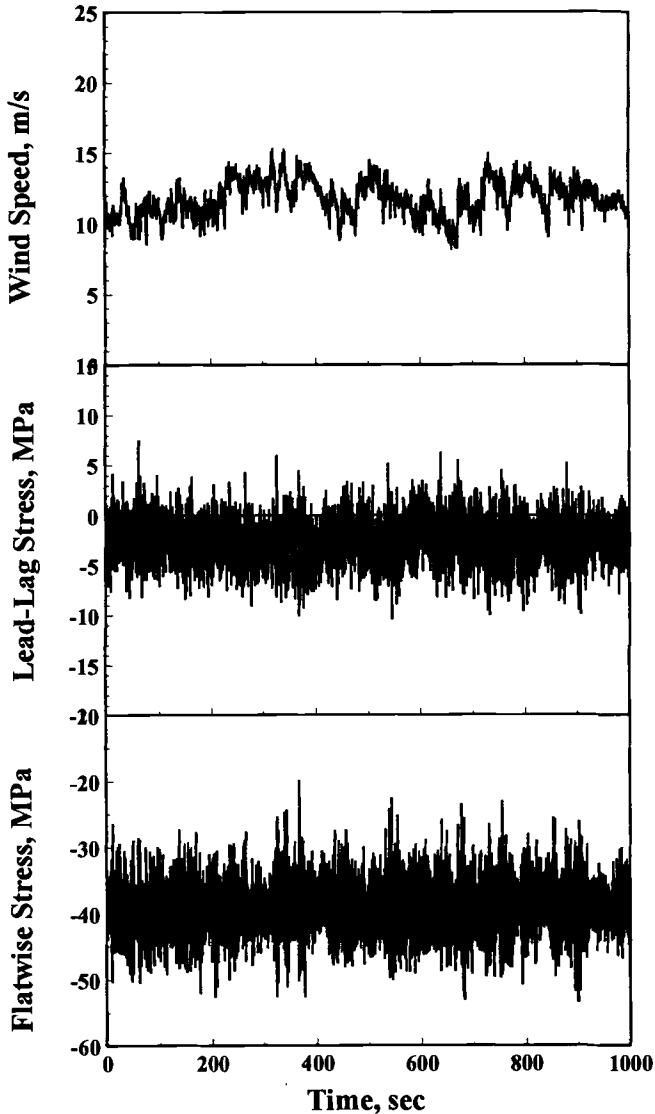
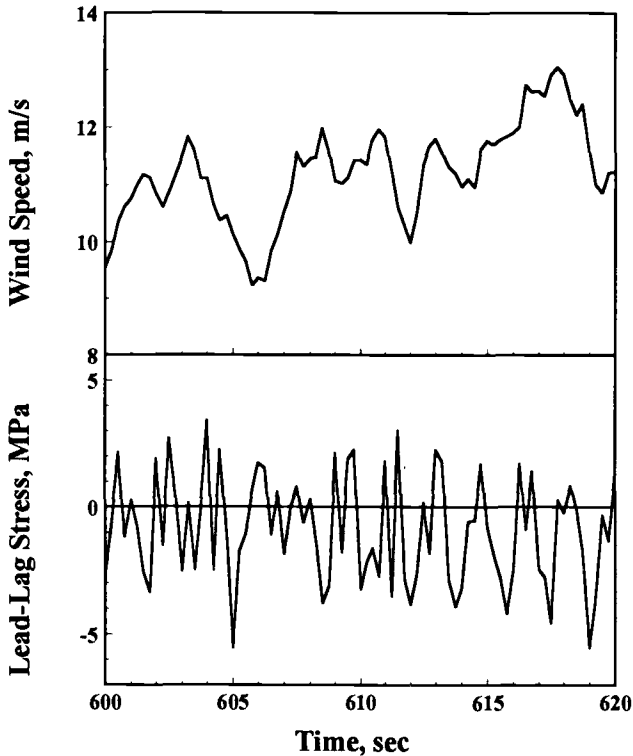


FIG. 4—Test Bed blades stresses, flatwise and lead-lag in 11 m/s winds.



perpendicular to the chord).⁶ It is apparent that the character of the blade response is different from that of the wind input. (The wind speed is measured about two rotor diameters upwind of the turbine.) Twenty-second segments of Fig. 4 are expanded in Figs. 5 and 6, showing the flatwise and lead-lag responses, respectively, in more detail. Even for such a short time segment, the wind speed fluctuates considerably, between 9.5 to 13.5 m/s. This is not atypical. The turbine blades respond in a more narrow-band fashion than the wind in both the lead-lag and flatwise directions, and the stress amplitudes do not consistently correlate with the wind peaks.

Examples of turbine response while operating in winds around 19 m/s are shown in Fig. 7. The stress levels while the rotor is operating at relatively low winds of 6 m/s are shown in Fig. 8. The stress levels while the rotor is parked (not rotating) in 14 m/s winds are shown in Fig. 9.

Fatigue properties can be difficult to find for those materials not already used in aerospace or ground vehicle applications (as is typical for most wind turbine blades). The so-called

⁶ The 34-m Test Bed has been equipped with a large array of sensors to monitor all aspects of the machine's performance. Current instrumentation includes 72 strain signals from the rotor, 25 environmental signals, 22 turbine performance signals, and 29 electrical performance signals. An overview of the instrumentation is provided in Ref 5.

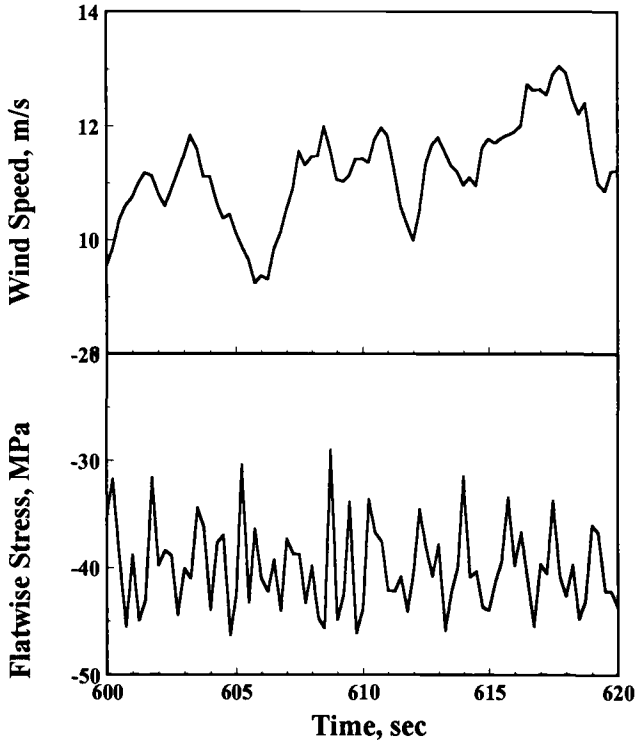


FIG. 6—Twenty second time series of flatwise stresses.

endurance limit (stress amplitude with zero mean at 10^7 cycles to failure) is the most likely property to be found in handbooks. An S - n curve would provide the next level of detail, if it can be found. In many cases, coupon testing will be required to characterize the specific material used for the blades. Figure 10 shows the raw data that resulted from coupon tests of (1) an extruded aluminum alloy (6063) [13] and (2) a unidirectional fiberglass composite [14], two typical materials used in wind-turbine blades. The aluminum data are shown in tabular form in Appendix B.

Questions

Before proceeding, it may be useful to think through one's own method of attacking the problem of calculating fatigue life under the conditions laid out above. The reader is therefore asked to pause here, before becoming biased by the solution technique laid out in subsequent sections, and reflect on the following questions.

- How would you formulate the cumulative damage problem for wind-turbine blades? How do you categorize events? How do you assign damage to events? What parameters are required? Which ones do you think are most important?
- How can one categorize wind speed with its large variability into something that can be used in a fatigue analysis? How can turbulence intensity be included?

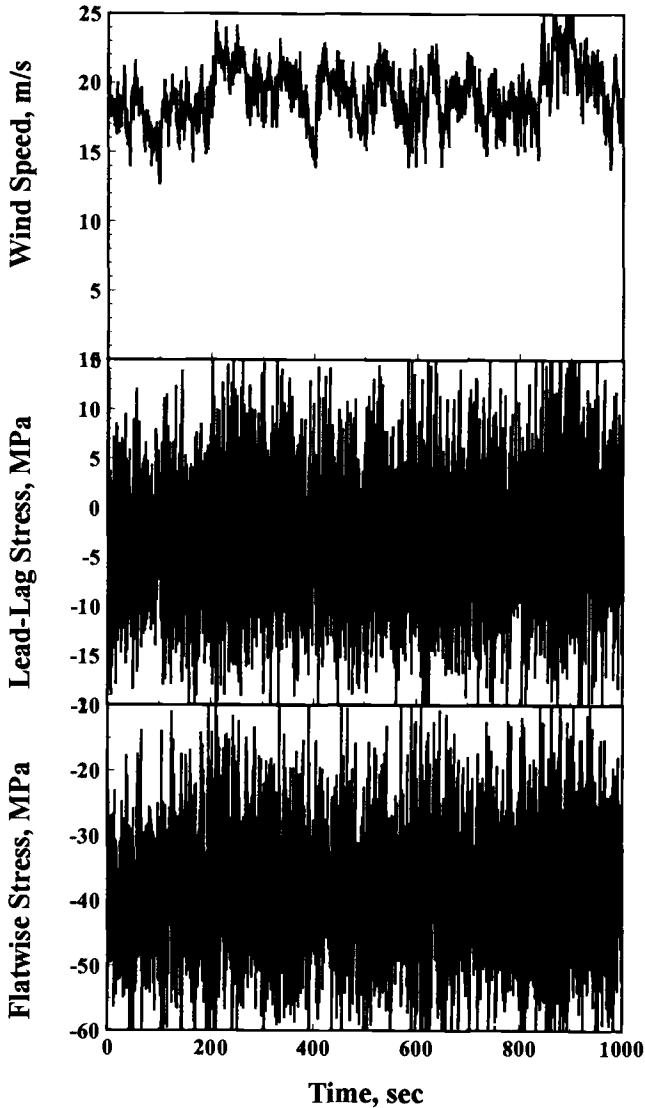


FIG. 7—Flatwise and lead-lag stresses in 19 m/s winds.

- How would you find the highest stressed location(s) on a wind turbine blade?
- How do you characterize irregular loadings like those shown in Figs. 4 to 9? Do they need to be considered in the analysis?
- How important is the actual sequence of the peaks and valleys in the loading?
- Why is the character of the blade response so much different from the wind input?
- How can time histories of turbine response be used in the fatigue analysis procedure?
- What operating data on the wind turbine would you collect and how would you reduce (analyze) the data?

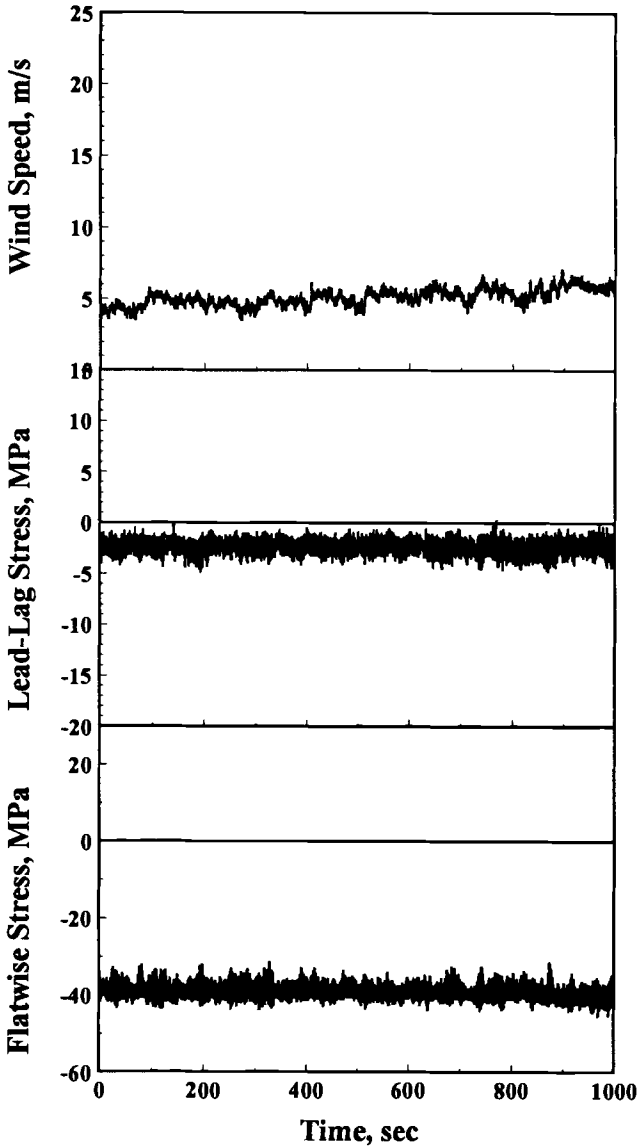


FIG. 8—Flatwise and wind-log stresses in 6 m/s winds.

- Could the published S - n curve of a similar but different alloy (or composite lay-up) along with a published endurance limit be used to create an S - n curve for the 6063 aluminum (or fiberglass blade)? If so, how?
- How could one fit a curve or set of curves to such a wide spread of S - n data, shown in Fig. 10 and Appendix B? How would you combine mean and amplitude information in an analytical model? How would you expect curve fitting or modeling differences to affect the predicted fatigue life of a component?
- What sensitivity do you expect in fatigue life predictions? (that is, what is the difference

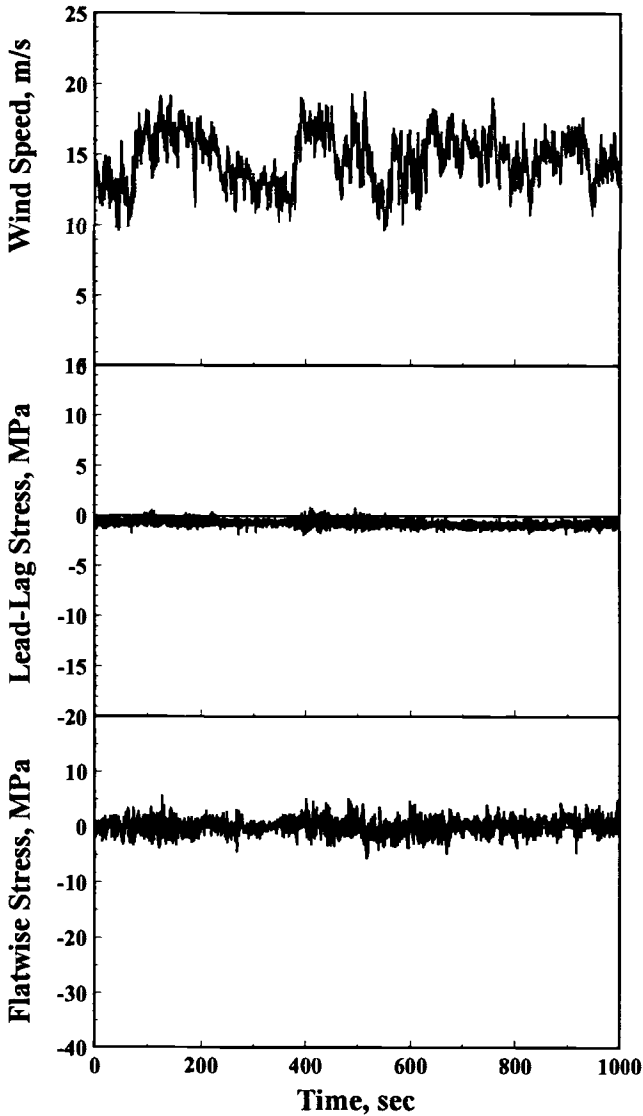


FIG. 9—Parked blade stresses, both flatwise and lead-lag, in 14 m/s winds.

in predictions due to 5 to 10% changes in input parameters?)

The reader is left with many questions. Information is provided below to illustrate how we answered some, but not all, of the questions that are posed here.

Solution Technique

Approach

Due to the complexity of constantly varying stresses excited by constantly varying wind speeds, a general, analytical solution to the prediction of fatigue lifetime for a wind turbine

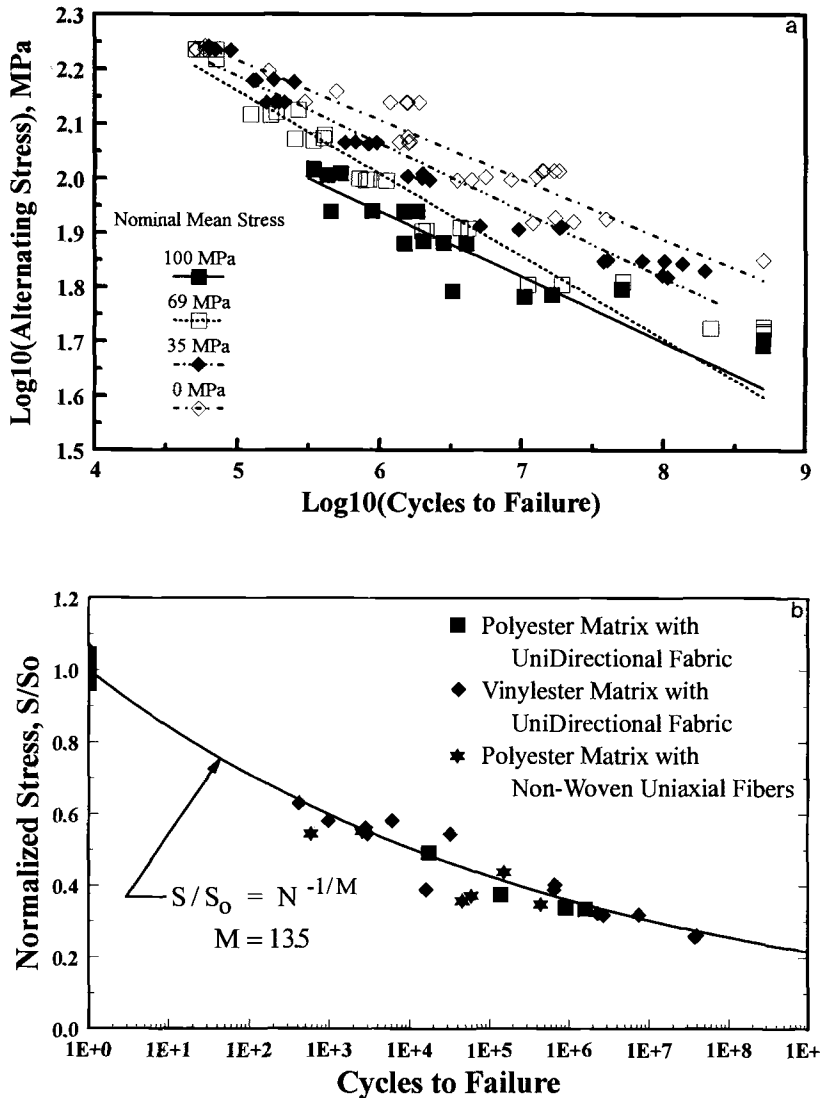


FIG. 10—Fatigue test results. (a) 6063 aluminum. (b) unidirectional fiberglass composite.

does not appear to be tractable unless significant assumptions are introduced. The loading spectrum problem is broken up into a series of smaller, tractable problem sets that are based upon the operational state of the turbine. The approach can be summarized by starting with the detailed stress spectrum definitions and integrating over successively broader segments of the machine's operational states. First, the stresses at each nominal wind speed are defined by a histogram (or probability density function) of stress cycles. The annual damage at a particular wind speed is determined by integrating over the stress cycle distribution, weighting by the amount of time spent at that wind speed, and using Miner's rule to sum damage based on constant amplitude S - n data. The total damage during operation is calculated by

integrating over all wind speeds. Finally, damage during other transient events, such as start-up or buffeting while parked, are added to estimate the total damage over an average year, that is, the annual damage rate. Lifetime is the reciprocal of the average damage rate. This approach has the distinct advantage of allowing the analyst to repeat the calculation for different wind sites, which is of interest since a turbine will rarely be designed for a single site.

The calculations are done with the aid of the previously mentioned LIFE2 code (see Appendix A). It leads the user through the problem set-up in four steps. First, the wind speed distribution for the turbine site is described by an average annual distribution. The second input describes the material fatigue properties required by the damage rule being used to predict the service lifetime of the component. The third input is a joint distribution of mean stress and stress amplitude (stress states) for all of the various operational states of the turbine. These "cycle count matrices" can be defined for each operational state using time series data, obtained from simulated or measured time series, using a rainflow counting algorithm, [15] or from analytical/numerical models. The fourth input describes the operational parameters for the turbine and the stress concentrations factor(s) for the turbine component. (Wind speed distribution, operating stress-state distribution, and material data are described in more detail below.) Finally, the damage caused by cycles at each "stress state" can be summed, first over the distribution of operational stress states at each wind speed, and then over all wind speeds and other turbine states. The LIFE2 code actually contains two fatigue analysis approaches; the first applies Miner's rule to S - n data and the second is a linear crack propagation model [9,16].

Assumptions

In the case of wind turbines, any design that has a chance of success must be able to endure a large number of cycles. Therefore, the material response must be nominally elastic. Either fatigue life or crack growth analysis can, and has been, used to estimate wind turbine fatigue lifetimes. We will restrict the discussion here to an S - n analysis using Miner's rule [16]. While this approach has many flaws, wind turbine applications create fewer problems than most with Miner's rule because of the high-cycle, limited-plasticity nature of the loading, keeping load sequence effects relatively small. (Reference 19 has a discussion of the relative errors to be expected in applying simple damage rules in wind turbine applications.) Therefore, loading statistics that preserve the average numbers of cycle amplitudes are sufficient for our purposes. Keep in mind that this approach is a rough approximation in the wind turbine case and may be less suited to other applications. However, the case study results that follow suggest that errors in the fatigue modeling may be swamped by the effects of uncertainty in the input parameters.

The internal stresses in the turbine blades are assumed to be described by beam bending with local stress concentrations at bolt holes and other nonuniformities. All the measurements from the operating turbine are collected as beam-bending loads and converted to nominal, maximum-fiber stresses using Mc/I . Local stresses are estimated by applying stress concentration factors to the nominal stress.

The Wind Regime

Typically, a wind turbine is designed for a generic site such as California mountain passes, the Great Plains of the United States, the North Sea coast of Europe, and so forth. In the initial design phase, the annual wind speed distribution for these sites is modeled using a Weibull or a Rayleigh probability density function [17]. The Weibull distribution is defined

by the average wind speed and a “shape factor.” The Rayleigh distribution is a special case of the Weibull with a shape factor of two. As the design, testing, and installation of a turbine continue, the generic descriptions can be replaced with site-specific data, usually in the form of a histogram of the annual wind speed distribution.⁷ The percentage of time spent in any range of wind speeds is defined by the integral of the distribution over the range (or the sum over the normalized histogram cells).

Constitutive Properties

A stress-based fatigue life approach using Miner’s rule to accumulate damage from each stress cycle requires that the number of cycles to failure be described as a function of cycle mean and amplitude. For many materials this function, typically called an S - n diagram, may be posed using Goodman or Gerber models [16]. In both of these models, the mean stress component, S_m , and the alternating stress component, S_a , of the cycle are mapped into an effective stress state, S_{eff} that corresponds to the S - n diagram at zero mean stress (Appendix B).

Typically, the S - n behavior can be found in material handbooks or via a literature survey. However, for wind turbines there are two significant difficulties. The first is that the preponderance of available data is for aerospace materials. These data are of little value here because the high cost of these materials has restricted their use in wind turbines. The second is that many fatigue critical designs do not need to resist 10^9 cycles. Thus, the available S - n data bases typically contain little or no very high-cycle data. For these reasons, material fatigue properties have been derived from extensive coupon test programs sponsored by the DOE wind energy program through the national laboratories. The raw data on extruded 6063 aluminum are tabulated in Appendix B. These data are used, in conjunction with a Goodman mean stress formulation, to evaluate blade joint lives in this 34-m Test Bed case study.

Operating Stresses

The wind driving a wind turbine is constantly fluctuating, even in the steadiest of sites. Even for the brief periods when a measured wind speed is seen to be relatively constant, stresses on a wind turbine rotor can be seen to be fluctuating “randomly.” Similar responses are found in many applications, including ground vehicles, aircraft, off-shore structures, and bridges.

Rainflow counting [15] is typically used to find closed hysteresis loops in the material response, which are defined to be the cycles. Cycle means and amplitudes are collected into histogram bins and displayed as either frequency of occurrence or exceedance diagrams. The first is equivalent to a probability density function and the second is like an inverse cumulative distribution function from probability theory. Frequency-of-occurrence examples of joint distributions of cycle means and amplitudes for the HAWT in Fig. 1 are shown in Fig. 11.

Malcolm [18] has used VAWT examples to illustrate how the shape of the stress-range distribution, when normalized by the root mean square (RMS) of the stress time series, can be independent of wind speed. Once the distribution type has been established, only the

⁷ The annual wind speed distribution is also one of the prime variables that determine the annual power production of a wind turbine. This wind speed distribution enables investors to project the “return-on-investment” from power sales over the turbine’s lifetime. Thus, site wind speed statistics are not only a major factor in determining the service lifetime, they are *the determining factor for the economics* of turbine placement.

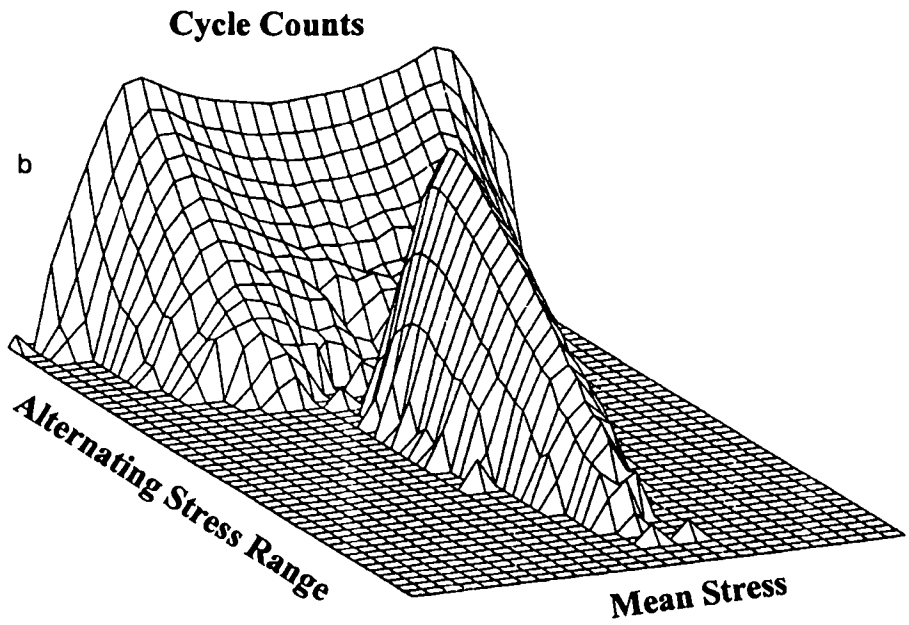
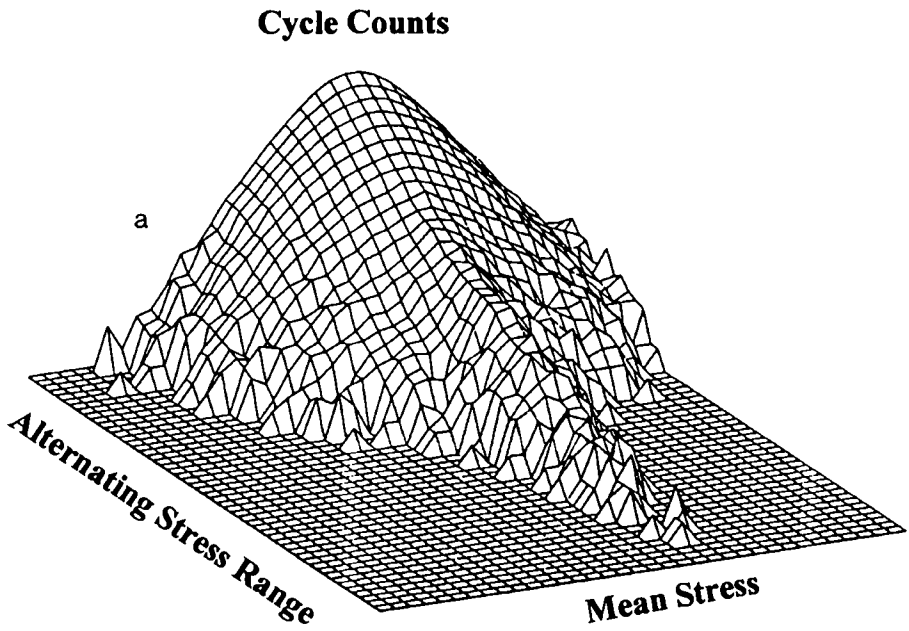


FIG. 11—Joint histogram of blade stress means and amplitudes for the NPS HAWT: (a) root flap bending stress. (b) root edgewise bending stress.

functional relationship between the RMS and the wind speed needs to be defined. (Defining the high amplitude “tail” of the distribution can be quite difficult and is a topic of current research interest.) In addition, the magnitude of the mean stress fluctuations (during operation) is generally small when compared to the material strength and can therefore be neglected. However, the shift in mean stress between operating and parked states may produce significant damage in the turbine blades, like the G-A-G cycle in aircraft. The histogram in Fig. 12 is typical of the distribution of rainflow counted ranges when the mean stress variations are ignored.

Veers [19,20] has shown that most VAWT operating stresses may be modeled as a narrow-band Gaussian process. The resulting Rayleigh distribution of stress amplitudes and ranges (Fig. 12) is a one-parameter distribution described by the RMS of the time series. To use this model for the operational stresses, only the RMS stress, mean stress, and cycle rate must be defined as functions of wind speed. This model works best for flatwise VAWT response where the stresses are largely a random vibration response to turbulence. But the model is often poor in lead-lag response because of a substantial sinusoidal gravity load (in HAWTs) and cyclic torque (in VAWTs).

Case Study

Introduction

This case study is presented to illustrate the variation in fatigue analysis results for an actual machine using analytical, measured, and reference-book estimates of the quantities

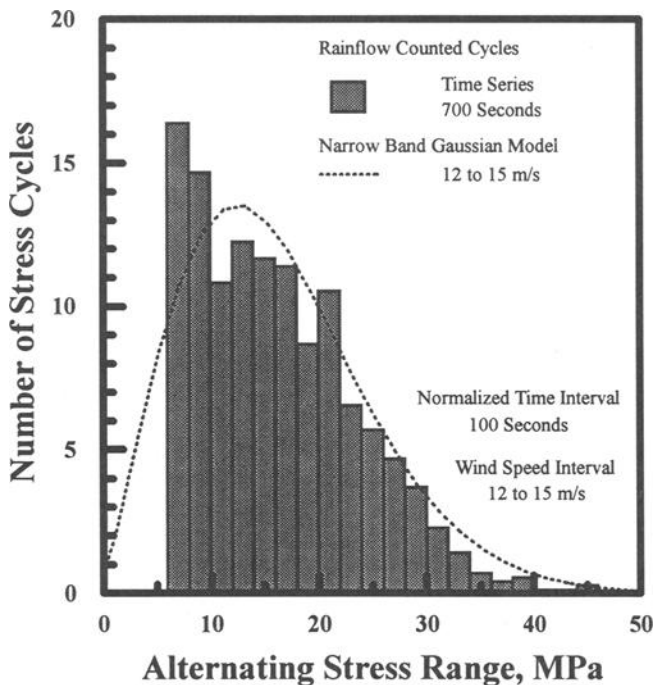


FIG. 12—Histogram of rainflow counted stress amplitudes for the Test Bed.

governing the fatigue analysis. The wind turbine under consideration is the Test Bed shown in Fig. 2. This fatigue analysis was originally conducted by Ashwill et al. [21]. As discussed above, some of the analysis presented here depends on the design characteristics of this particular turbine; however, the discussions and analysis techniques are applicable to all wind turbines. For this case study, we only consider the stresses imposed on the turbine during operation, that is, the operational stresses.

This example follows the sequence established above and implemented in the LIFE2 code (Appendix A). We describe the Test Bed, the four input parameter sets, and finally, we calculate the predicted service lifetime for the turbine blade. The latter calculations are presented as a parametric study for variations in the input quantities. The LIFE2 code was used for all fatigue life calculations.

Sandia/DOE 34-m VAWT Test Bed

The Test Bed (Fig. 2) is a 34-m diameter VAWT erected by Sandia National Laboratories near Bushland, TX (just west of Amarillo) for research purposes. The turbine and site have been equipped with a large array of sensors that permit the characterization of the turbine under field conditions [5,22,23]. The extensive experimental data base allows us to illustrate the fatigue analysis of a wind turbine component and to examine the sensitivity of lifetime predictions to various estimates of the input data.

Structural dynamic analysis confirmed by test measurements [12] indicated the highest stressed region of the turbine was at the upper blade-to-tower joint (called the upper root). (Figure 13a shows the mirror-image lower root.) This example examines the stresses imposed on the blade at this joint. The blade coming into the joint has an airfoil shape with a 48-in. cord (Fig. 13b), and a bolted "clam shell" joint connecting it to the central column. The stresses in both the flatwise bending direction (about the cord of the airfoil) and the lead-lag bending direction (about an axis perpendicular to the chord) are critical in fatigue.

The Wind Regime

For the Test Bed example, we examine the differences created by using three different annual wind speed distributions. The first distribution is a generic description of the wind speeds in the Texas panhandle region of the U.S. Great Plains, which could be obtained from a wind energy atlas [24]. A Rayleigh distribution with an average wind speed of 6.3 m/s (14 mph) is typical of the area. The second distribution, focusing more directly on the specific site, is a histogram of 17 years of data at the Amarillo Airport⁸ and has an average of approximately 6.6 m/s (15 mph). The third distribution, obtained over 6 years (1983 to 1988) at the Bushland site,⁸ has a 5.8 m/s (13 mph) average. All three distributions are shown in Fig. 14.

There are three major differences in these wind speed distributions that affect the service lifetime predictions. The first is that the Rayleigh distribution has a long tail extending out to very high winds, whereas the Bushland and Amarillo distributions contain little occurrence of winds above 20 m/s. The second is that the Amarillo distribution has a hump in moderate winds that is not seen in the Bushland data. The third difference is reflected in the average wind speeds that range from 6.6 to 5.8 m/s. For turbine operation between 6 and 20 m/s, the Amarillo site is the most energetic and the Bushland site is the most benign.

⁸ Clark, N., USDA Agricultural Research Center, Bushland, TX, private correspondence, 1989.

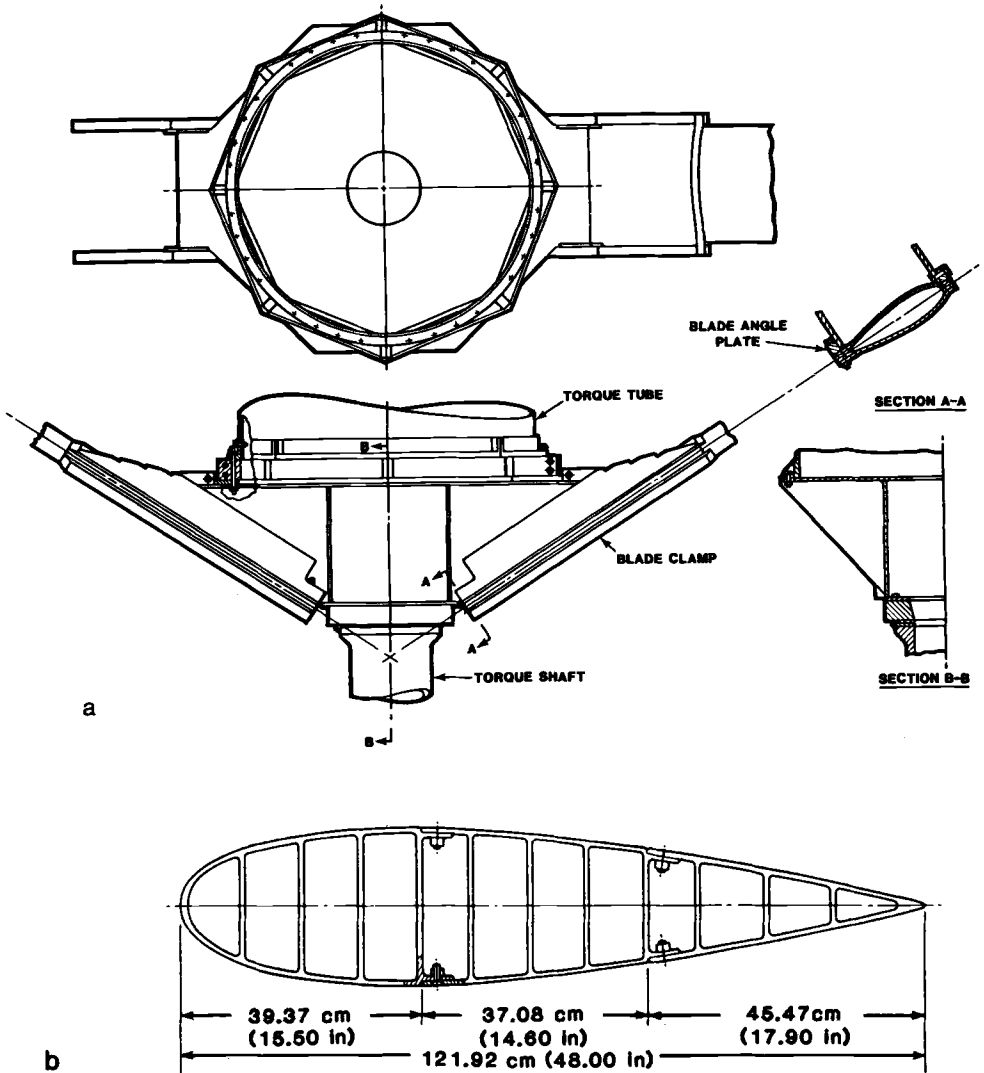


FIG. 13—The upper root of the 34-m Test Bed. (a) blade-to-tower joint. (b) airfoil cross section near the tower.

Constitutive Properties

The Test Bed blades were extruded from 6063 aluminum alloy. Initially, only limited fatigue data for this material were available in the literature. S - n properties had to be extrapolated from this limited data set and knowledge of the properties of other aluminum alloys [25]. The resulting zero mean stress S - n curve is shown in Fig. 15. This curve was expanded to include mean stresses using Goodman's rule with an ultimate stress of 241 MPa (35 ksi). These data (Fig. 15) are described here as the "reference data."

Because the reference data were suspect, a series of S - n material tests was conducted on the extruded aluminum blade material [13]. The test data at various mean and alternating

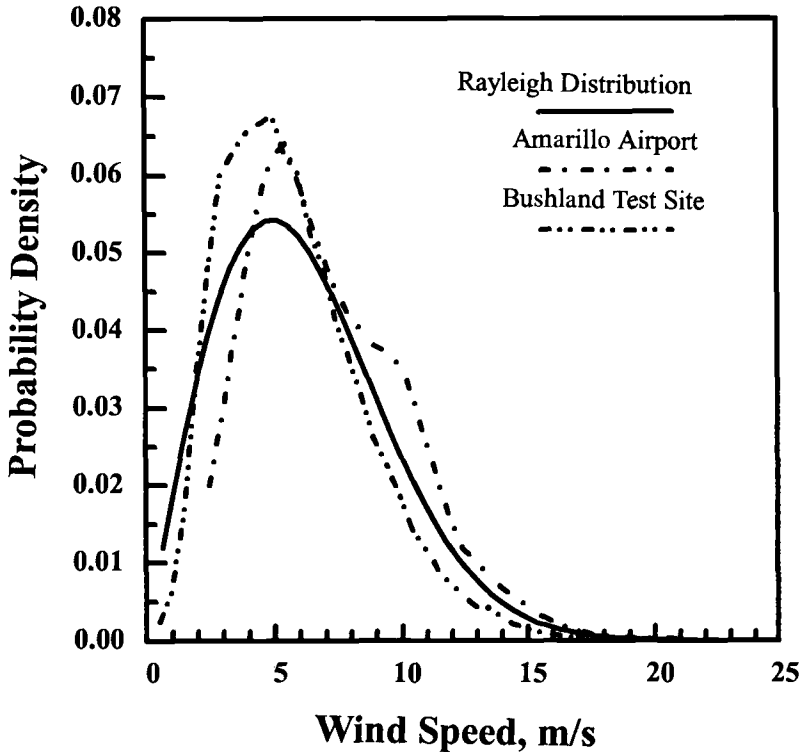


FIG. 14—Typical wind speed distributions.

stress levels shown in Fig. 10a have been converted to “effective” stress levels using a Goodman rule, based on the measured ultimate stress of 244 MPa (35.4 ksi) [8].

Three formulations of the S - n behavior were derived from the above data set. The first is the mean or “least squares curve” (LSC) fit to the data, which approximates a 50% survival level. The second, based on a Weibull fit to the variations about the LSC, is an estimate of the 95% survival level. A third eliminates the change in slope at about 10 million cycles in the LSC fit and linearly extends the curve out to the high cycle region [26]. (This is equivalent to the extrapolation of low-cycle S - n data to high cycles.) These formulations (Fig. 15) will be called the LSC, the 95%, and the high cycle extrapolation fits, respectively.

Stress States

For this example, we examine only the operational stresses on the turbine, neglecting cycles accumulated while parked in high winds and the start-stop cycles. The narrowband Gaussian model for stress response is used here.⁹ The stress states have been measured and

⁹ The rainflow counting technique may be used to create histograms of stress states for this turbine since a large amount of time series data is available. However, the narrow band Gaussian model was chosen for this case study for its simplicity and because it yields better insight into the dependence of the operational stress levels on wind speed.

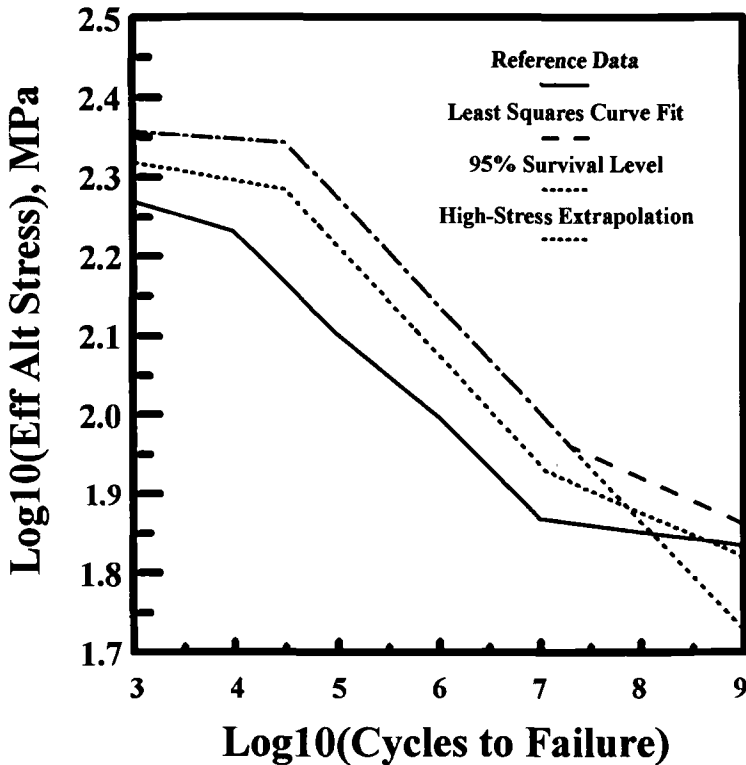


FIG. 15—Constitutive properties for the 6063 aluminum.

compared to analytical predictions with good results [12,22]. As mentioned above, the highest stressed region of the blade is where the 48-in. chord blade section attaches to the tower.

Predicted and Measured RMS Stresses—The stress states at many locations along the blades were predicted before the turbine was built using a beam finite-element model adapted at Sandia to perform frequency-response analysis for VAWT structures [27]. The analysis gives the magnitudes of stress responses at several driving frequencies. The RMS for the sum of the sinusoids at all the driving frequencies is used as an estimate of the RMS of the random response. The stress states for the upper root were measured using strain gages¹⁰ located 36 in. from the blade root [28]. Based on a finite element analysis of this region, the measured stresses had to be multiplied by factors of 1.08 for lead-lag and 1.23 for flatwise to adjust them to the maximum nominal (section) stress in the root joint [12,21 and 22]. The RMS is calculated from the time histories of the local stresses after removal of the mean. The measured and predicted flatwise RMS stresses, for fixed speed operation at 28, 34, and

¹⁰ Strain gages are used in pairs on the blades as bending load sensors. The gages are wired in Wheatstone bridges to add bending and cancel axial and torsional loadings. Known bending moments were applied to the blades before the turbine was assembled to calibrate the moment measuring sensors. Nominal stress levels at the maximum fiber are then estimated by the beam bending formula Mc/I are the standard blade-bending output from the instrumentation system.

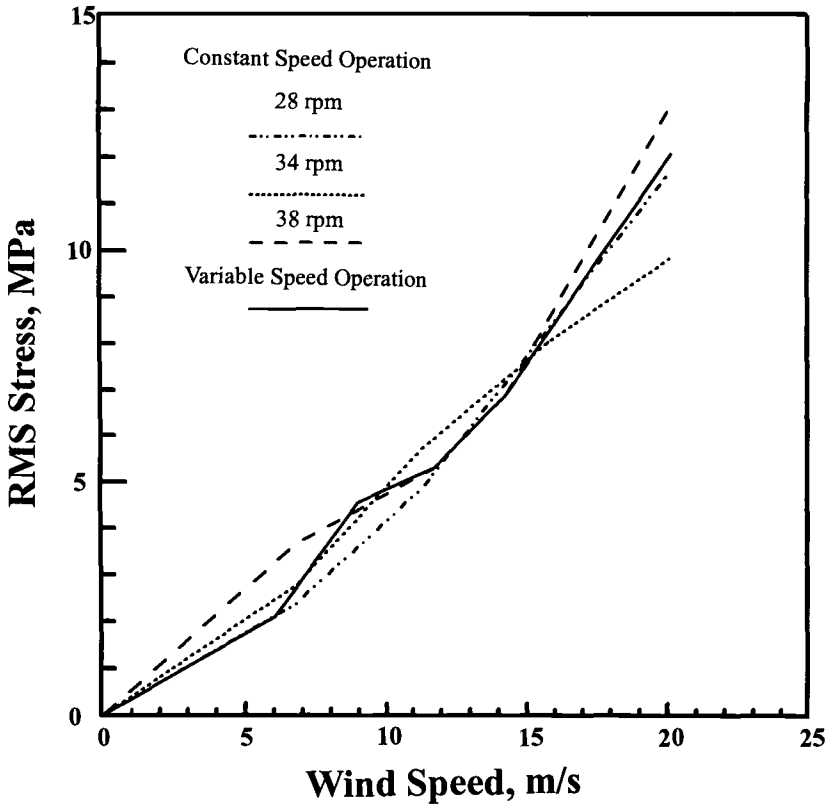


FIG. 16—Measured flatwise RMS stresses at the upper root.

38 rpm, are shown in Figs. 16 and 17, respectively. Comparison of the measured and predicted RMS stresses for variable speed operation is shown in Fig. 18. The lead-lag stresses are not shown here, but are reproduced in Ref 22.

Stress Concentration Factor—A stress concentration factor (SCF) was applied to the maximum nominal bending stress to account for stress risers in the bolted root joint. The exact SCF for the upper root joint is unknown, but is expected to be three or more. Early fatigue analyses suggested that these stress levels were sufficient for the application (that is, a one of a kind research machine with frequent inspections) so no detailed stress analysis or component testing was done.

Cycle Rate—The rate at which stress cycles are accumulated is a necessary parameter for determining service lifetime when using the narrow-band Gaussian model [20]. For these predictions, the estimated rate for the predicted RMS stresses was approximated at three times the rotational rate of the turbine for the lead-lag stress cycles and two times for flatwise stress cycles.¹¹ For the measurements, this rate was determined using the average “mean-crossing” rate [29]. The differences were small, except at 28 rpm, where the measured flatwise cycle rate was approximately 50% higher than the estimated rate.

¹¹ These cycle rates are selected based on the interaction of the frequency content of the aerodynamic loading and the structural dynamics of the turbine rotor.

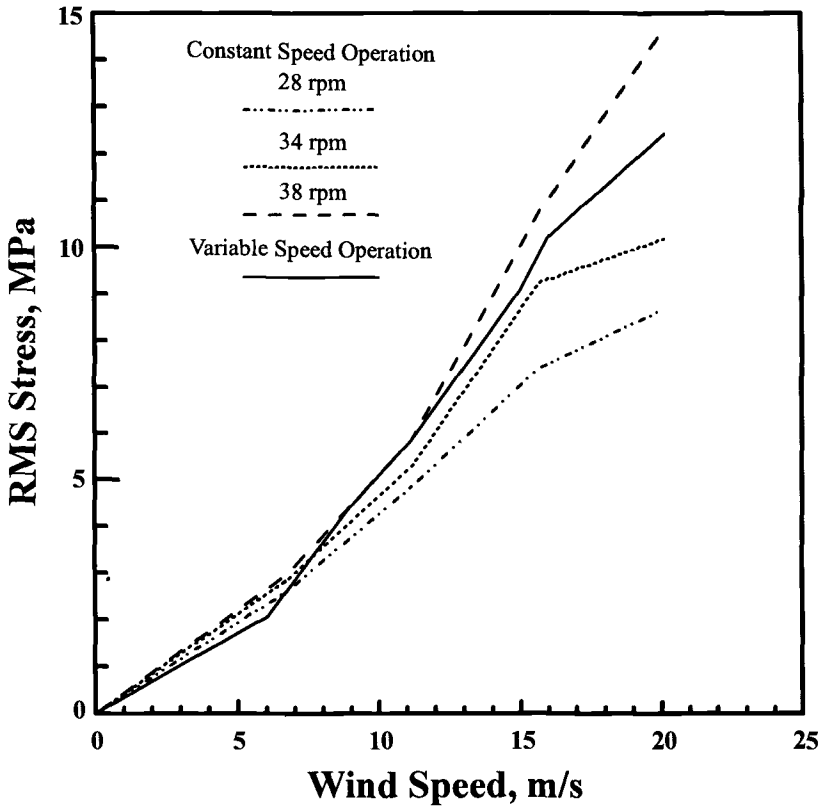


FIG. 17—Predicted flatwise RMS stresses at the upper root.

Operational States

This variable-speed turbine has been operated at fixed speeds throughout its operating range of 18 to 38 rpm and in a continuously variable-speed mode. Variable speed is used to track the highest aerodynamic efficiency, increasing rotor speed with wind speed until the maximum design speed is reached. The turbine operates at maximum design speed until increasing wind would overpower the generator. The turbine speed is then reduced to limit power. The mapping between turbine speed and wind speed is shown in Fig. 19 [30].

Baseline Life Estimates

To establish a reference frame for this parametric sensitivity study, two baseline sets of parameters are used to calculate reference service lifetimes for the upper root joint. The first baseline case represents the limited data available early in the design process. The wind speed distribution is taken to be Rayleigh distributed with a 6.3 m/s mean. The stress states are assumed to follow the narrow-band Gaussian model with analytically predicted RMS versus wind speed behavior. The reference S - n curve is used to define the material fatigue properties. The second baseline uses measured quantities from turbine operating experience. The wind speed distribution is for the Bushland site. The RMS stress levels are as measured

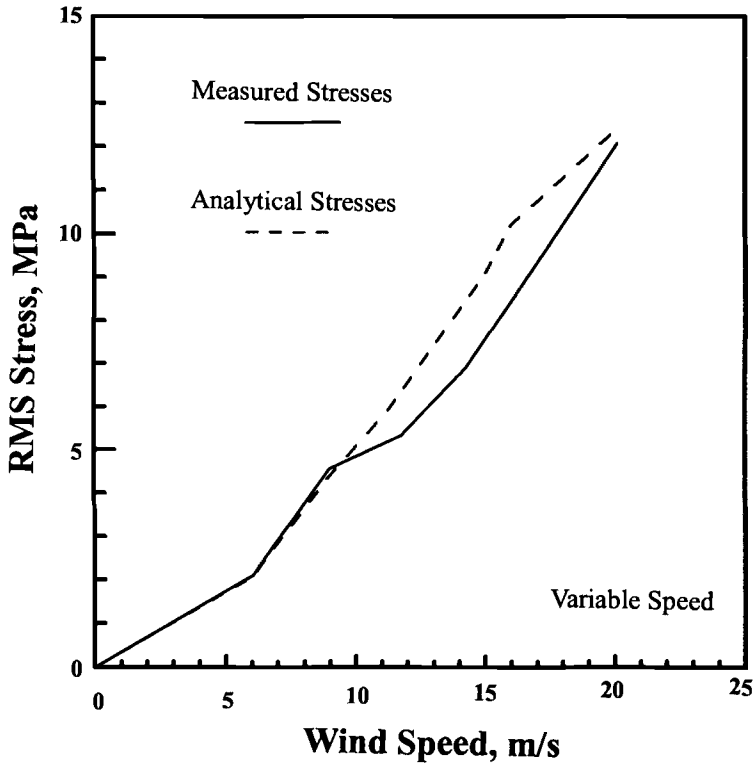


FIG. 18—Comparison of the measured and predicted RMS flatwise stresses with variable speed operation.

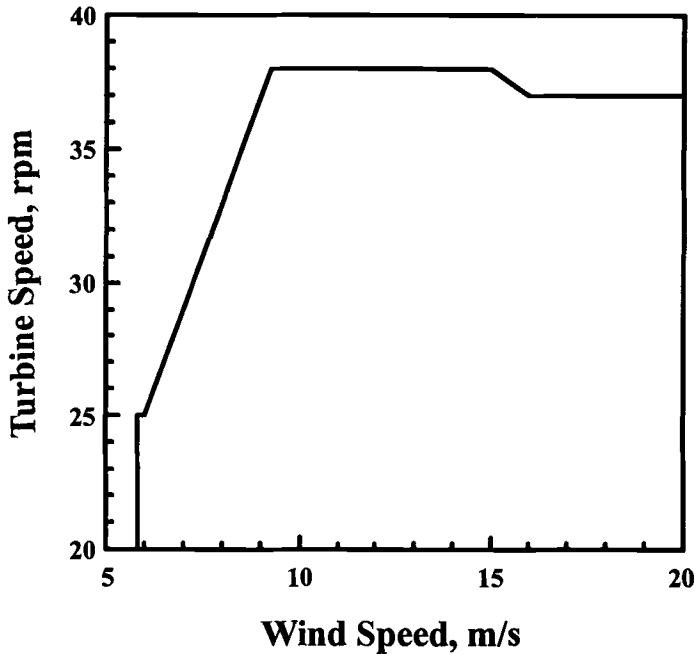


FIG. 19—Mapping between turbine speed and wind speed for variable speed operation.

TABLE 1—Key for the tables.

Wnd—Annual Wind Speed Distribution

- R—Rayleigh distribution with 14 mph average
- A—distribution for the Amarillo airport, 17 years of data
- B—distribution at the Bushland test site

Fat—*S-n* Fatigue Data for Extruded 6063 Aluminum

- Ref—reference data
- LSC—least square-curve-fit to experimental data
- 95%—curve fit of experimental-data at 95% survival level
- Hgh—extrapolation of the high-stress experimental data

OPS—Operation Stress States

- Ana—analytical predictions for the stress states
- Mea—measured stress states
- Flat—flatwise stresses
- L-L—lead-lag stresses

and adjusted to the maximum nominal root stress. The *S-n* data are the LSC fit to the coupon tests. Three fixed operating speeds, 28, 34, and 38 rpm are used, as well as a variable speed case. The SCF is taken to be 3.0 and cycle rates are estimated for both cases. A key to the abbreviations used in the case study is given in Table 1. The lifetimes, in years, calculated using the LIFE2 code, are shown in Table 2.

Parameter Sensitivity

Wind Regime Variation

Table 3 lists the estimated fatigue lives, as in Table 2, but applying each of the three candidate wind speed distributions to each baseline case. Notice that the Amarillo and Bushland wind distributions produce lead-lag predictions that vary by a factor of 10.

S-n Data

The four different *S-n* estimates from Fig. 15 are applied to the baseline cases in Table 4. Although different treatments of the test data result in differences up to a factor of 2, the reference data is more conservative by factors of 3 to 6.

Stress States

Table 5 lists results for the difference between analytical estimates of the RMS stress and measured RMS stresses. Although the fit between analysis and measurement shown in Fig.

TABLE 2—Reference service lifetimes (in years) for the case study.

| Wnd | Fat | OPS | Flatwise Stress States | | | | Lead-Lag Stress States | | | |
|-----|-----|-----|------------------------|--------|--------|------|------------------------|-----------|--------|-------|
| | | | 28 rpm | 34 rpm | 38 rpm | Var | 28 rpm | 34 rpm | 38 rpm | Var |
| R | REF | Ana | 1360 | 33.1 | 2.21 | 11.9 | 61.1 | 205 000 | 0.91 | 19.40 |
| B | LSC | Mea | 966 | 504 | 286 | 391 | 296 000 | 9 470 000 | 73.9 | 494 |

TABLE 3—*Effect of the wind regime on lifetime (in years).*

| Wnd | Fat | OPS | Lifetime | |
|-----|-----|-----|----------|------|
| | | | Flat | L-L |
| R | Ref | Ana | 11.9 | 19.4 |
| A | Ref | Ana | 7.86 | 10.1 |
| B | Ref | Ana | 29.4 | 109 |
| R | LSC | Mea | 150 | 125 |
| A | LSC | Mea | 100 | 71.0 |
| B | LSC | Mea | 391 | 494 |

18 is as good as any analyst could expect, the fatigue life predictions vary by about a factor of 3.

Stress Concentration Factor (SCF)

Finally, the SCF is varied only slightly from 3.0 to 3.5 to illustrate its impact of fatigue lifetime; results are shown in Table 6. Notice that the change in lifetimes ranges from a low of a factor of 4 to a high of a factor of 20. This sensitivity is the highest found in the case study and is, interestingly, on the parameter about which the least is known about the joint. It should be noted that for the shortest lifetimes predicted in the study, some of the assumptions that rely on the high-cycle, nominally elastic nature of the material response may be violated.

Questions

As we noted in the beginning of this paper, many questions about the determination of service lifetimes for wind turbine components have not been answered. In addition to those questions raised previously, the reader should consider these additional questions.

- With the variability in lifetime estimates shown in the case study, how would you present your fatigue life predictions to the corporate executives who need to decide whether to fund an initial production run of these turbines? What additional work do you recommend to reduce the financial risk?

TABLE 4—*Effect of the constitutive formulation on lifetime (in years).*

| Wnd | Fat | OPS | Lifetime | |
|-----|-----|-----|----------|------|
| | | | Flat | L-L |
| R | Ref | Ana | 11.9 | 19.4 |
| R | LSC | Ana | 59.7 | 149 |
| R | 95% | Ana | 35.7 | 70.3 |
| R | Hgh | Ana | 52.8 | 135 |
| B | Ref | Mea | 104 | 83.7 |
| B | LSC | Mea | 391 | 494 |
| B | 95% | Mea | 243 | 249 |
| B | Hgh | Mea | 307 | 430 |

TABLE 5—*Effect of the operational stresses on lifetime (in years).*

| Wnd | Fat | OPS | Lifetime | |
|-----|-----|-----|----------|------|
| | | | Flat | L-L |
| R | Ref | Ana | 11.9 | 19.4 |
| R | Ref | Mea | 33.5 | 15.7 |
| B | LSC | Ana | 121 | 602 |
| B | LSC | Mea | 391 | 494 |

- Critique the analysis procedure presented here. What assumptions have the potential to produce the greatest error in life prediction? How would you improve the procedure? What steps would you take first? Second?
- Could you come up with a closed form solution for the (approximate) time to failure? What assumptions do you consider appropriate? How much error would they produce? Is it acceptable? Is it conservative?
- Would you expect different lifetimes for identical machines in different locations? Why or why not? If so, by how much?

Observations on the Utility of the Results

As observed in the case study presented here, fatigue life estimates for wind turbines can (and typically do) have a large amount of uncertainty associated with them. Miner's rule may be off by a factor of 2 or more, high or low, in the prediction of service lifetimes. As illustrated by this case study, measured wind speed distributions from relatively close sites can change life estimates by a factor of 4 up to a factor of 8. And, a change of 15 percent in the root stress can translate into more than an order of magnitude change in the life estimate. With such uncertainty in the estimation, one must wonder whether the performance of a fatigue analysis is even justified in the design phase of a wind turbine.

The goal of fatigue-critical engineering is to design components that can endure their loading environment for the design lifetime and to be economically competitive. (As discussed above, economics is one of the main drivers in a viable design for wind turbines.) With the uncertainties cited here, fatigue analyses find their greatest utility in providing order-of-magnitude life estimates for turbine components and relative life estimates for competing design options; that is, they identify design deficiencies and permit trade-off analyses of

TABLE 6—*Effect of the stress concentration factor on lifetime (in years).*

| Wnd | Fat | OPS | SCF | Lifetime | |
|-----|-----|-----|-----|----------|------|
| | | | | Flat | L-L |
| R | Ref | Ana | 3.0 | 11.9 | 19.4 |
| R | Ref | Ana | 3.5 | 1.53 | 0.52 |
| B | LSC | Mea | 3.0 | 391 | 494 |
| B | LSC | Mea | 3.5 | 108 | 37.6 |

various design options. Thus, even with all of its problems, the estimated service lifetime is important to the design process.

As noted by Veers et al. [31], maybe the designer should be asking the question: "What is the probability that the turbine design will meet its designed service lifetime?" rather than asking "What is the service lifetime of this turbine?" The former question requires the designer to evaluate the uncertainties and inherent randomness of the input variables used in the fatigue analysis. For this case study, a median lifetime of hundreds of years still yields a probability for premature failure of over 2% for a 20-year lifetime [31]. Thus, the designer must "over-design" the turbine to account for the lack of knowledge of the load spectrum and material properties for this analysis. Only with an improved state of knowledge from turbine testing, turbine operating experience, and improved material characterizations will the designer be able to refine the turbine design and increase its reliability.

Conclusions

Wind turbines are subjected to a severe and unrelenting environment driving the materials to their limits of fatigue endurance. The loadings are random in nature and continuously fluctuating in both cyclic amplitude and global intensity. Formulating the problem requires breaking it down into manageable pieces while making simplifying assumptions to permit tractable solutions. The procedure developed at Sandia National Laboratories is presented here as a case study. It is neither perfect nor exhaustive, but serves to illustrate how sense can be made out of complete randomness. The LIFE2 fatigue and fracture analysis code used for the calculations in the case study is explained in an Appendix A and is available from the authors, complete with user's manuals and supporting documentation. The case study illustrates the tremendous variability in life predictions that can occur with relatively modest changes in turbine placement, stress analysis results, or assumptions on uncertain inputs. With the LIFE2 code [6-11], additional studies or specific problem assignments can be formulated to lead students through the process of cumulative damage summation and to demonstrate the range of life estimates that will result from parameter variations.

Acknowledgments

This work is supported by the U.S. Department of Energy at Sandia National Laboratories under contract DE-AC04-94AL85000.

APPENDIX A

The LIFE2 Code

The LIFE2 code [6-11] is a fatigue/fracture mechanics code that is specialized to the analysis of wind turbine components. It is a PC-based, menu-driven FORTRAN code that is written in a top-down modular format. The package leads the user through the input definitions required to predict the service lifetime of a turbine component. In the current formulation, the service lifetime of turbine components may be predicted using either Miner's rule with constant amplitude $S-n$ data or a linear-elastic crack propagation rule [8]. The code is described in Refs 6 to 9, and a complete set of user's manuals are provided in Refs 7, 8, 10, and 11. The code does have the ability to plot input and output variables.

The LIFE2 code requires four sets of input for the prediction of the service lifetime for a turbine component: (1) the annual wind speed distribution at the site under investigation, (2)

an S - n diagram (fatigue data) or crack growth rate data (linear crack propagation) for the material comprising the component under investigation, (3) the stress cycles of the total stress states on the component as a function of the operating state of the turbine and the average wind speed, and (4) the operating parameters and stress concentration factor(s) for the component.

Numerical Formulation

The LIFE2 code is based on the assumption that the total set of fatigue cycles on the turbine is the sum of a set of cycle distributions (histograms) characterized by wind speed and operating conditions (that is, parked or rotating). The analysis proceeds by integrating the fatigue cycles imposed on the turbine using a damage accumulation model.

To illustrate this formulation, we use Miner's rule to describe the accumulation of damage in a component during normal operation of the turbine. Miner's rule states that the damage accumulated from n stress cycles at stress state S is determined by the following relation

$$D = \frac{n(S)}{N(S)} \quad (\text{A-1})$$

where N is the number of stress cycles at stress state S required to fail the material. The damage is then integrated (summed) over all stress states to determine the total damage accumulated in the component. The component fails when the damage D sums to one. Typically, the stress cycles at stress state S are written as a function of the cycles' mean and alternating stress components. Thus, the integration of the damage relation over all stress states may be written as

$$D|_V = \int_0^\infty \int_{-\infty}^\infty \frac{n(S_m, S_a)}{N(S_m, S_a)} dS_m dS_a \quad (\text{A-2})$$

For the wind turbine, we assume that each stress cycle may be written as function of the input wind speed; thus, Eq A-2 is the damage at a given wind speed, V . When integrated over the distribution of wind speeds imposed upon the turbine, the total damage becomes

$$D = \int_{V_{ci}}^{V_{co}} D|_V p_V(V) dV = \int_{V_{ci}}^{V_{co}} p_V \int_0^\infty \int_{-\infty}^\infty \frac{n(S_m, S_a, V)}{N(S_m, S_a)} dS_m dS_a dV \quad (\text{A-3})$$

where V_{ci} and V_{co} are the cut-in and cut-out wind speeds; that is, the wind speed at which the turbine is turned on and the wind speed above which the turbine is no longer operated. The wind speed distribution is typically described using the probability density function p_V for the annual wind speed distribution. Thus, for a time of Δt , the damage accumulated by the operating wind turbine equals

$$D(\Delta t) = \int_{V_{ci}}^{V_{co}} p_V \int_0^\infty \int_{-\infty}^\infty \frac{n(S_m, S_a, V, \Delta T)}{N(S_m, S_a)} dS_m dS_a dV \quad (\text{A-4})$$

and the predicted service lifetime for the turbine component, T_f in years, is given by

$$T_f = \frac{1}{D(\Delta t)} \text{ for } \Delta t = 1 \text{ year} \quad (\text{A-5})$$

The LIFE2 code computes these relations numerically. Similar descriptions are developed for other aspects of turbine operation and wind conditions (for example, the stress cycles produced by starting and stopping the turbine and by high winds "buffeting" a stopped

turbine) and for other damage criteria (linear crack propagation). A complete description of the algorithms used in the code are given in Ref 8.

Input Variables

As mentioned above, the LIFE2 code requires four sets of input information to determine service lifetimes. They are (1) the annual wind speed distribution, (2) the constitutive equation for the damage law being used, (3) the cyclic stresses as a function of wind speed and operating conditions of the turbine, and (4) the parameters describing the operation of the turbine. Each of these inputs is described in detail in the case study presented above. Each input may be described using tabular data or specialized input functions.

Stress States

The most difficult data set to obtain for input into the LIFE2 code is the cycle count function $n(S_m, S_a)$ (Eqs 1 through 5). For the LIFE2 code, this function takes the form of a series of cycle count matrices. Each matrix is used to describe a single aspect of turbine operation.

The first class of the cycle count matrices used by the LIFE2 code is for the "operational stresses," namely, the stresses that occur during operation of the turbine under normal wind conditions. These cycle counts for this operation state are divided into a series of cycle count matrices; each defines the stress cycles as a function of wind speed. The cycle count matrices must be defined for sufficient wind speed to cover the entire operating range of the turbine.

The second and third classes of matrices describe special events and loads that occur when the turbine is not operating. The second class contains cycle count matrices for start-stop cycles, emergency stops, loss-of-grid stops, and so forth. The third class contains matrices for high-wind events; that is, the stress cycles induced by "buffeting" of the turbine by high winds when it is parked.

Data Input

All three classes of cycle count matrices may be entered into the LIFE2 code using several input techniques. For all of the cases, if the cycle counts are known from other analyses or measurements, they may be entered directly into the code. Time series data from either measurements or simulations from time-domain structural analysis codes¹² may be used also. For this case, the stress histories are entered via a data file. The LIFE2 code uses a rainflow counting algorithm [15] to process the data into the appropriate cycle count matrices [9-11]. Frequency domain input data for the operational stresses may be used by the LIFE2 code as well [32,33]. The spectral stress response of the structure is entered via a data file. The LIFE2 code uses an inverse fast fourier transform (FFT) to transform the frequency domain data into the time domain. The rainflow counting algorithm, cited above, is then used to cycle count the data.

Narrow Band Gaussian Model

This model uses a Rayleigh distribution defined by the root-mean-square (RMS) of the stress time series to define cycle amplitudes. To use this model in the LIFE2 code for the

¹² As discussed in the opening remarks, the analysis of wind turbines using structural analysis codes is a tedious and difficult problem. The input loads to the codes must be determined first using aerodynamics codes that include the effects of turbulence in the incoming wind. From these loads the structural dynamics codes must determine the stresses in the structure. For VAWT structures, successful simulations have been conducted in the frequency domain for "quasi-steady" input conditions [21]. Transient events [34] and the analysis of HAWT structures [35] require time domain solutions.

operational stresses, the RMS parameter must be defined as a function of wind speed. The code accepts this function in tabular form. To complete the modeling of the cycle counts, the mean stress and the cycle rate are assumed to be a constant for all cycles in the distribution.

Computational Modules

The code is written in a top-down modular format with an “executive module” that controls the overall operation of the code and the five main computational modules. The first four define the input parameters and data sets, and the fifth module performs the damage calculation. Auxiliary modules permit data to be plotted and stored for future reference. Data may be plotted on a video display or sent to a printer. All common graphics drivers are supported. A menu system is used to facilitate movement about the code and to input data into the code.

Platform

The LIFE2 code is a PC-compatible FORTRAN code. Both the source code and an executable file are available. The code adapts, via input variables, to various video and printer configurations. The code requires 640 kbytes of memory, and a hard disk is recommended. Currently, the LIFE2 executable files occupy approximately 0.5 Mbyte. The source files occupy almost 1 Mbyte. Files to describe a typical problem occupy several Mbytes.

APPENDIX B

Material Data for 6063 Aluminum

The fatigue analysis of turbine structures using Miner’s rule requires a detailed knowledge of the fatigue properties of the material under analysis. For 6063-T5 aluminum, the material used in the blades of the 34-m Test Bed VAWT, an appropriate data base was not available in the literature. The necessary data base was obtained by Van Den Avyle and Sutherland [13] and Mohamadian and Graham¹³ using standard ASTM techniques.

The 6063-T5 aluminum had a measured yield stress of 205 MPa and a measured ultimate stress of 244 MPa. The S - n data base, required for Miner’s rule damage law, was obtained using approximately 100 bend specimens cycled at five alternating stress amplitudes and at four mean stress levels. A summary of the raw data from these experiments is listed in Table B-1, which follows. This table contains two data sets: the first set was obtained by Van Den Avyle and Sutherland and the second was obtained by Mohamadian and Graham. The former data are noted by the numbered specimens and the latter are noted by specimens labeled with the letter “S” for Southern University. The final 8 data entries in this table list data from specimens that did not fail during the experiments. These “run-out” fatigue tests were terminated at 5×10^8 (500 000 000) stress cycles.

For our analysis of these data, we chose to fit the data with a Goodman Fit using the ultimate strength of the material S_u . This rule states that the fatigue life at alternating stress S_a and mean stress S_m is equal to the fatigue life at an equivalent zero-mean-stress alternating stress state of S_{eff} through the relation

$$S_a = S_{eff} \left(1 - \frac{S_m}{S_u} \right) \quad (\text{B-1})$$

¹³ Mohamadian, H. P. and Graham, I. J., Southern University, Baton Rouge, LA, private correspondence.

TABLE B-1 —S-n data for 6063-75 aluminum.

| ID | Mean Stress (MPa) | Cyclic Amplitude (MPa) | Cycles to Failure |
|----|-------------------|------------------------|-------------------|
| 74 | 0.00 | 82.92 | 11,994,100 |
| 80 | -0.34 | 83.47 | 22,963,800 |
| 75 | 0.00 | 84.36 | 39,155,300 |
| 73 | 0.00 | 84.92 | 17,149,200 |
| 25 | -0.34 | 99.36 | 3,492,700 |
| 23 | 0.00 | 99.44 | 4,420,900 |
| 24 | -1.03 | 99.63 | 8,375,200 |
| 85 | 0.00 | 100.70 | 5,550,000 |
| 26 | 0.34 | 101.13 | 12,679,800 |
| S | 0.00 | 103.42 | 13,890,000 |
| S | 0.00 | 103.42 | 14,182,000 |
| S | 0.00 | 103.42 | 16,832,000 |
| S | 0.00 | 103.42 | 18,256,000 |
| 8 | 0.34 | 116.15 | 1,594,700 |
| 10 | 0.00 | 116.58 | 1,378,200 |
| 9 | -0.34 | 116.93 | 1,612,000 |
| 6 | 0.70 | 119.18 | 1,571,000 |
| S | 0.00 | 137.90 | 1,183,000 |
| S | 0.00 | 137.90 | 1,532,000 |
| S | 0.00 | 137.90 | 1,565,000 |
| S | 0.00 | 137.90 | 1,884,000 |
| 2 | -0.34 | 138.24 | 297,900 |
| 3 | -5.00 | 144.69 | 498,500 |
| 5 | 2.43 | 157.43 | 165,100 |
| S | 0.00 | 172.37 | 50,800 |
| S | 0.00 | 172.37 | 51,600 |
| S | 0.00 | 172.37 | 59,500 |
| 4 | 0.00 | 174.91 | 59,700 |
| 90 | 42.01 | 65.91 | 105,443,900 |
| 89 | 42.69 | 66.40 | 97,376,300 |
| 88 | 44.66 | 67.67 | 193,322,400 |
| 87 | 42.69 | 69.80 | 134,251,700 |
| 82 | 33.36 | 70.44 | 37,282,900 |
| 84 | 33.61 | 70.58 | 69,989,100 |
| 81 | 33.61 | 70.58 | 100,409,400 |
| 83 | 33.95 | 70.92 | 39,839,300 |
| 66 | 33.61 | 80.67 | 9,529,400 |
| 68 | 34.76 | 81.32 | 18,437,900 |
| 65 | 34.06 | 81.74 | 19,026,200 |
| 67 | 34.47 | 81.77 | 5,081,000 |
| 27 | 34.25 | 99.31 | 2,222,400 |
| 28 | 34.32 | 100.17 | 1,965,500 |
| 29 | 34.80 | 100.92 | 1,555,200 |
| 30 | 34.50 | 102.10 | 1,983,500 |
| 15 | 34.06 | 115.80 | 844,500 |
| 17 | 34.93 | 116.42 | 960,500 |
| 18 | 33.61 | 116.58 | 576,500 |
| 16 | 34.13 | 116.87 | 682,200 |
| S | 34.47 | 137.90 | 159,200 |
| S | 34.47 | 137.90 | 183,300 |
| S | 34.47 | 137.90 | 194,500 |
| S | 34.47 | 137.90 | 213,000 |
| 13 | 34.40 | 150.21 | 249,100 |
| 11 | 33.74 | 151.48 | 128,800 |
| 12 | 34.72 | 151.62 | 134,700 |
| 14 | 34.63 | 151.91 | 179,200 |
| 20 | 32.74 | 171.90 | 89,600 |
| 19 | 34.88 | 172.36 | 70,400 |
| 21 | 34.32 | 172.95 | 64,300 |
| 22 | 35.05 | 174.58 | 63,300 |
| 91 | 71.97 | 53.05 | 211,987,300 |
| 71 | 67.15 | 63.78 | 18,978,500 |
| 72 | 67.24 | 63.87 | 10,999,300 |
| 69 | 68.69 | 64.62 | 51,097,000 |
| 45 | 69.80 | 80.04 | 1,983,000 |
| 47 | 69.22 | 80.30 | 2,114,600 |
| 48 | 69.79 | 80.95 | 4,201,100 |
| 46 | 70.17 | 81.39 | 3,689,900 |
| 44 | 68.55 | 99.25 | 1,110,000 |
| 42 | 69.11 | 99.36 | 803,000 |
| 41 | 68.67 | 99.57 | 844,000 |
| 43 | 69.11 | 100.05 | 722,800 |
| 31 | 68.35 | 117.37 | 343,400 |
| 35 | 69.44 | 118.29 | 252,200 |
| 36 | 69.79 | 118.64 | 405,300 |
| 34 | 70.74 | 120.26 | 412,800 |
| 38 | 68.33 | 130.82 | 170,600 |
| 37 | 69.04 | 131.18 | 124,100 |
| 40 | 69.06 | 132.23 | 187,500 |
| 39 | 70.26 | 133.50 | 267,600 |
| S | 68.95 | 165.47 | 71,000 |
| S | 68.95 | 172.37 | 51,300 |
| S | 68.95 | 172.37 | 61,800 |
| S | 68.95 | 172.37 | 70,900 |
| 64 | 100.97 | 80.58 | 10,335,100 |
| 53 | 102.80 | 61.13 | 16,116,300 |
| 80 | 102.53 | 62.07 | 3,194,800 |
| 52 | 102.39 | 62.67 | 49,925,900 |
| 59 | 103.70 | 76.05 | 4,060,100 |
| 62 | 103.63 | 76.08 | 1,487,100 |
| 61 | 104.59 | 76.29 | 2,806,500 |
| 63 | 105.80 | 76.84 | 2,015,200 |
| 55 | 102.87 | 87.09 | 1,476,500 |
| 58 | 103.70 | 87.11 | 1,824,500 |
| 56 | 103.77 | 87.12 | 454,700 |
| 57 | 101.77 | 87.33 | 887,900 |
| 54 | 101.57 | 101.57 | 429,500 |
| 51 | 102.46 | 102.46 | 532,200 |
| 49 | 103.84 | 103.84 | 343,400 |
| 50 | 104.25 | 104.25 | 340,300 |
| 86 | 0.34 | 70.81 | 500,000,000 |
| 93 | 66.82 | 53.32 | 500,000,000 |
| 94 | 66.83 | 51.90 | 500,000,000 |
| 92 | 68.50 | 52.30 | 500,000,000 |
| 96 | 88.78 | 49.31 | 500,000,000 |
| 97 | 89.87 | 49.91 | 500,000,000 |
| 98 | 89.88 | 49.93 | 500,000,000 |
| 95 | 94.46 | 50.58 | 500,000,000 |

When these data are mapped into the equivalent stress state, there are two distinct regions to the curve. We chose to fit each segment with a straight line on a log-log plot of the form:

$$\log_{10}(S_{eff}) = a + b \log_{10}(n) \quad (\text{B-2})$$

References

- [1] Phillips, J. A., "Wind Power's Coming of Age," *The Electricity Journal*, Vol. 5, No. 3 April 1992, pp. 22–32.
- [2] *Annual Energy Outlook, 1993 with Projections to 2010*, DOE/EIA-0383(93), Energy Information Administration, Jan. 1993.
- [3] "A Growth Market in Wind Power," *EPRI Journal*, Vol. 17, No. 8, Dec. 1992, pp. 4–15.
- [4] Coleman, C. and McNiff, B., *Final Report: Dynamic Response Testing of the Northwind 100 Wind Turbine*, Subcontractor Report, SERI/CP-217-3315, American Wind Energy Association (AWEA), Solar Energy Research Institute, Golden CO, Dec. 1989.
- [5] Ashwill, T. D., Berg, D. E., Gallo, L. R., Grover, R. D., Klimas, P. C., Ralph, M. E., Rumsey, M. A., Stephenson, W. A., and Sutherland, H. J., "The Sandia 34-Meter VAWT Test Bed," in *Proceedings of WindPower '87*, SERI/CP-217-3315, American Wind Energy Association (AWEA), Washington, D.C., 1987, pp. 298–308.
- [6] Sutherland, H. J. and Schluter, L. L., "The LIFE2 Computer Code, Numerical Formulation and Input Parameters," in *Proceedings of WindPower '89*, SERI/TP-257-3628, American Wind Energy Association, Washington, D.C., 1989, pp. 37–42.
- [7] Schluter, L. L. and Sutherland, H. J., *Reference Manual for the LIFE2 Computer Code*, SAND89-1396, Sandia National Laboratories, Albuquerque, NM, Sept. 1989.
- [8] Sutherland, H. J., *Analytical Framework for the LIFE2 Computer Code*, SAND89-1397, Sandia National Laboratories, Albuquerque, NM, Sept. 1989.
- [9] Schluter, L. L. and Sutherland, H. J., "Rainflow Counting Algorithm for the LIFE2 Fatigue Analysis Code," in *Ninth ASME Wind Energy Symposium*, SED-Vol 9, D. E. Berg, Ed., American Society of Mechanical Engineers (ASME), New York, 1990, pp. 121–123.
- [10] Schluter, L. L. and Sutherland, H. J., *User's Guide for LIFE2's Rainflow Counting Algorithm*, SAND90-2259, Sandia National Laboratories, Albuquerque, NM, Jan. 1991.
- [11] Schluter, L. L., *Programmer's Guide for LIFE2's Rainflow Counting Algorithm*, SAND90-2260, Sandia National Laboratories, Albuquerque, NM, Jan. 1991.
- [12] Ashwill, T. D., "Initial Structural Response Measurements for the Sandia 34-Meter VAWT Test Bed," in *Eighth ASME Wind Energy Symposium*, SED-Vol. 7, D. E. Berg and P. C. Klimas, Eds., American Society of Mechanical Engineers (ASME), New York, 1989, pp. 285–292.
- [13] Van Den Avyle, J. A. and Sutherland, H. J., "Fatigue Characterization of a VAWT Blade Material," in *Eighth ASME Wind Energy Symposium*, SED-Vol. 7, D. E. Berg and P. C. Klimas, Eds., American Society of Mechanical Engineers (ASME), New York, 1989, pp. 125–129.
- [14] Mandell, J. F., Reed, R. M., Samborsky, D. D., and Qiong, P., "Fatigue Performance of Wind Turbine Blade Composite Materials," SED-Vol. 14, in *Wind Energy—1993*, S. Hock, Ed., ASME, New York, 1993, pp. 191–198.
- [15] Downing, S. D. and Socie, D. F., "Simple Rainflow Counting Algorithms," *International Journal of Fatigue*, Vol. 4, No. 1, 1982, pp. 31–40.
- [16] Osgood, C. C., *Fatigue Design*, 2nd Edition, Pergamon, Oxford, 1982.
- [17] Barchet, W. R., "Wind Energy Data Base," in *Proceedings of the Fifth Biennial Wind Energy Conference and Workshop II*, SERI/CP-635-1340, Solar Energy Research Institute, Golden, CO, 1981.
- [18] Malcolm, D. J., "Prediction of Peak Fatigue Stresses in a Darrieus Rotor Wind Turbine under Turbulent Winds," in *Ninth ASME Wind Energy Symposium*, SED-Vol 9, ASME, 1990, pp. 125–136.
- [19] Veers, P. S., "Simplified Fatigue Damage and Crack Growth Calculations for Wind Turbines," in *Eighth ASME Wind Energy Symposium*, SED-Vol. 7, D. E. Berg and P. C. Klimas, Eds., ASME, New York, 1989, pp. 133–140.
- [20] Veers, P. S., *A General Method for Fatigue Analysis of Vertical Axis Wind Turbine Blades*, SAND89-2543, Sandia National Laboratories, Albuquerque, NM, 1983.
- [21] Ashwill, T. D., Sutherland, H. J., and Veers, P. S., "Fatigue Analysis of the Sandia 34-Meter Vertical Axis Wind Turbine," in *Ninth ASME Wind Energy Symposium*, SED-Vol. 9, ASME, New York, 1990, pp. 145–151.

- [22] Ashwill, T. D. and Veers, P. S., "Structural Response Measurements and Predictions for the Sandia 34-Meter Test Bed," in *Ninth ASME Wind Energy Symposium*, SED-Vol. 9, ASME, New York, 1990, pp. 137-144.
- [23] *Selected Papers on Wind Energy Technology, January 1989-January 1990*, P. S. Veers, Ed., SAND90-1615, Sandia National Laboratories, Albuquerque, NM, 1990.
- [24] Elliott, D. L., Holladay, C. G., Barchet, W. R., Foote, H. P., and Sandusky, W. F., "Wind Energy Resource Atlas of the United States," DOE/CH10093-4, DE86004442, Pacific Northwest Laboratory, March 1987.
- [25] Sutherland, H. J., Ashwill, T. D., and Slack, N., "The LIFE Computer Code: Fatigue Life Prediction for Vertical Axis Wind Turbine Components," SAND87-0792, Sandia National Laboratories, Albuquerque, NM, 1987.
- [26] Mitchell, M. R., "Fundamentals of Modern Fatigue Analysis," in *Fatigue and Microstructure*, American Society for Metals, Metals Park, OH, 1979, pp. 385-437.
- [27] Lobitz, D. W. and Sullivan, W. N., *Comparison of Finite Element Predictions and Experimental Data for the Forced Response of the DOE 100 kW Vertical Axis Wind Turbine*, SAND82-2534, Sandia National Laboratories, Albuquerque, NM, 1984.
- [28] Sutherland, H. J. and Stephenson, W. A., *Rotor Instrumentation Circuits for the Sandia 34-Meter Vertical Axis Wind Turbine*, SAND88-1144, Sandia National Laboratories, Albuquerque, NM, 1988.
- [29] Crandall, S. H. and Mark, W. D., *Random Vibration in Mechanical Systems*, Academic Press, New York, NY, 1963.
- [30] Ralph, M. E., "Control of the Variable Speed Generator on the Sandia 34-Metre Vertical Axis Wind Turbine," in *Proceedings of WindPower '89*, SERI/TP-257-3628, Solar Energy Research Institute, Golden, CO, Sept. 1989, pp. 99-104.
- [31] Veers, P. S., Sutherland, H. J., and Ashwill, T. D., "Fatigue Life Variability and Reliability Analysis of a Wind Turbine Blade," *Probabilistic Mechanics and Structural and Geotechnical Reliability*, Y. K. Lin, Ed., ASCE, American Society of Civil Engineers, New York, July 1992, pp. 424-427.
- [32] Sutherland, H. J. and Osgood, R. M., "Frequency-Domain Synthesis of the Fatigue Load Spectrum for the NPS 100-kW Wind Turbine," in *Proceedings of WindPower '92*, American Wind Energy Association, (AWEA), Washington, DC, Oct. 1992, pp. 321-328.
- [33] Sutherland, H. J., "Effect of the Flap and Edgewise Bending Moment Phase Relationships on the Fatigue Loads of a Typical HAWT," in *Wind Energy—1993*, SED-Vol. 14, S. Hock, Ed., ASME, New York, 1993, pp. 181-187.
- [34] Dohrmann, C. R. and Veers, P. S., "Time Domain Structural Response Calculations for Vertical Axis Wind Turbines," in *Eighth ASME Wind Energy Symposium*, SED-Vol 7, D. E. Berg and P. C. Klimas, Eds., ASME, New York, 1989, pp. 107-114.
- [35] Wright, A. D., Buhl, M. L., and Thresher, R. W., *FLAP Code Development and Validation*, SERI/TR-217-3125, Solar Energy Research Institute, Golden, CO, 1988.

Fatigue Cases Involving the Use of Wood and a Wood Composite

REFERENCE: Kyanka, G. H., “Fatigue Cases Involving the Use of Wood and a Wood Composite,” *Case Studies for Fatigue Education, ASTM STP 1250*, Ralph I. Stephens, Ed., American Society for Testing and Materials, Philadelphia, 1994, pp. 208–219.

ABSTRACT: Many wood and wood-composite structural elements are exposed to fatigue loading situations in service. Because wood is composed of a complex cellulosic fiber-based structure at the microscopic level, fatigue cracking phenomena are not commonly observed. Fatigue-related failures can look just like static failures. Fatigue cracking does occur under certain types of loading, however, and some examples are presented.

The special properties of wood are briefly examined to show why fatigue fracture/cumulative damage is so difficult to interpret in wood and wood products. Some historical insights are covered. The development of special tests to gather fatigue data for wood is discussed to further point out the unique concerns of designers working with the material.

Two case studies involving parallel to the grain fatigue fractures are presented. The case of a failed shotgun stock represents a regular repeated load situation on a component that was redesigned. Broken necks in bowling pins are due to a more complex dynamic loading regime, but exhibit similar cracking patterns in a laminated composite product.

KEYWORDS: wood, cellular structure, orthotropic properties, cellulose, grain direction

Wood is, by volume, the most widely used construction material in the world in solid and converted forms. Most engineering students, however, are taught very little about the structural performance of wood in service. Very little information on properties such as fatigue performance is found in common texts and references for engineering materials. Even successful designers such as Dr. Fokker, the famed aircraft engineer of World War I, expressed the idea that wood is, in fact, immune to fatigue [1]. The truth is that wood, like other materials, can sustain structural damage due to repetitive loading, and can ultimately fail in fatigue due to such loads [2]. The mode of fracture is often misunderstood, since fatigue fractures in wood and wood composites can look just like static load induced fractures. To explain how this can be true, it is necessary to look at some unique structural characteristics at the microscopic level and above.

The structure of wood at the visible level is orthotropic, the three principal axes being the longitudinal, radial, and tangential. Common usage is that these are along the grain or across the grain of wood. The grain (Fig. 1) is defined by rows of cells of varying sizes and orientation (Fig. 2) that are arranged in repetitive patterns. Each cell is made up of layers of microfibrils of cellulose bound in a matrix of lignin, a complex polymeric adhesive material. Since all of the components are polymers, they exhibit a combination of elastic and viscoelastic behavior. The assemblage is quite complicated, as seen in Fig. 3.

The presence of a large number of holes, density gradients, and variable cell sizes creates

¹ Professor, SUNY College of Environmental Science and Forestry, Faculty of Wood Products Engineering, Syracuse, NY 13210-2786.

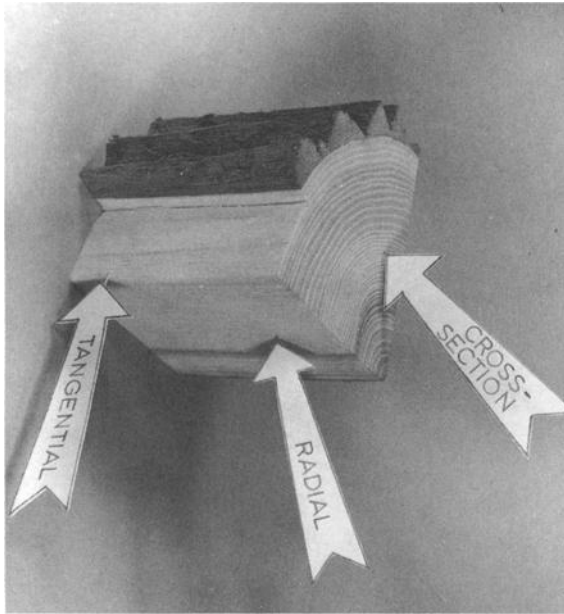


FIG. 1—Fiber direction and principal planes in wood.

a system of crack absorbing and deflecting mechanisms such that most crack fronts only move a small distance before stopping or changing form. In crystalline metals, the front assembles itself and progresses as loading continues. In wood, much local damage may occur before anything visible appears. Wood can provide for six different crack propagation patterns in fatigue, leading to a Mode I fracture (Fig. 4). Therefore, it is necessary to evaluate each direction for its significance in a fatigue situation.

The LR and LT cracks are those associated with longitudinal, or along the grain, loads. These are the ones that are easiest to arrest and that are normal to the strongest direction in wood. The broken tennis racquet in Fig. 5 shows how hard it is to create failures in these planes. After 1.6 million serves, it shows a large number of cracks with no complete separation. This type of fracture would occur if it was caused by a static bending load normal to the racquet face. There is no identifiable point or points of origin for the cracks.

The TR and RT modes of fracture in wood are easier to create due to the cellular structure of wood, but are not of great concern since wood is rarely loaded to any large stress levels in these directions. One major exception to this occurs when large torsional loads are put on long poles, such as those used to carry electrical service lines. Such twisting can produce stresses that progressively break down the wood along concentric “shells” from the center to the outside diameter. This can lead to failures in high winds due to loss of bending strength in the pole. A few such cases have been documented, but this mode of fracture is not common [3].

The easiest direction for a propagating crack to move is one along the RL or TL directions, or somewhere between them. These are the crack planes used to easily split firewood. The wood fibers are parallel to the crack and the large cell openings can serve to channel the crack along. There are fewer arrest sites in these directions, and the properties of wood strength perpendicular to its grain direction are its weakest. Most wood design manuals refer

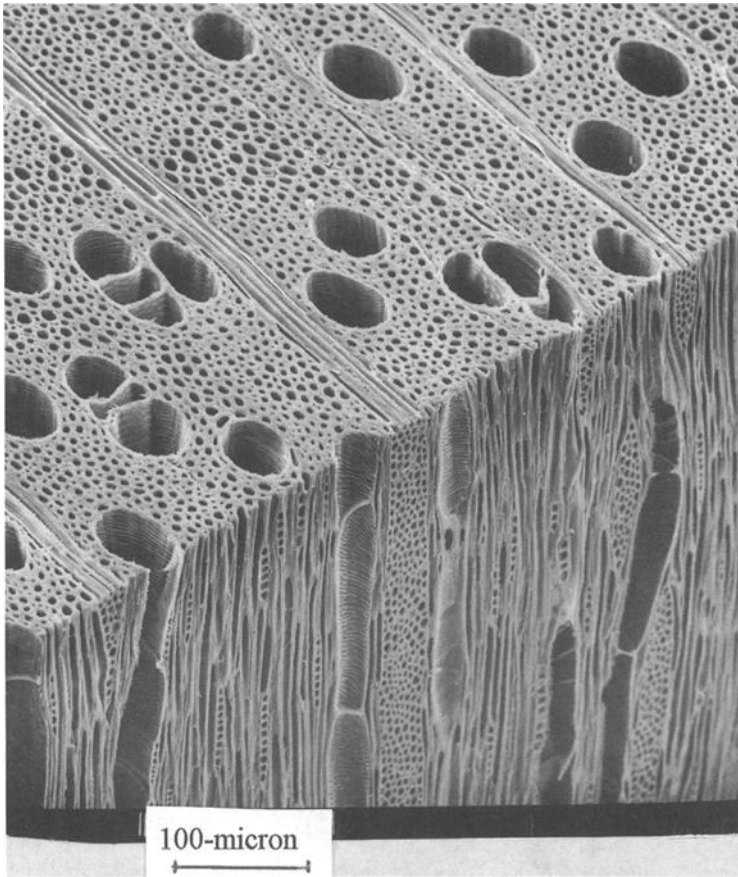


FIG. 2—Cross section of wood showing fibers and arrangement (maple magnified approximately 250 \times).

to wood in tension perpendicular to grain as a condition to be avoided in designing. Sometimes the stresses cannot be avoided, and this is where our case studies are taken from.

It is interesting to note that fatigue data for wood has been largely generated by tests made specifically for wood. One such test is cantilever bending of a beam by an electric motor and eccentric drive arm. The test does not result in fracture of the beam, but rather is called a failure when the damage in the wood reaches a point such that the elastic curve of the bent beam changes due to cell wall damage [4]. This is in keeping with the earlier discussion of how hard it is to cause LR or LT cracks to propagate.

Case Studies

Case 1

As part of manufacturer's product verification tests for new shotgun models, most manufacturers require a number of bench test firings. The guns are held in a vise and mechanically triggered. After the number of required firings the model is then checked for wear and

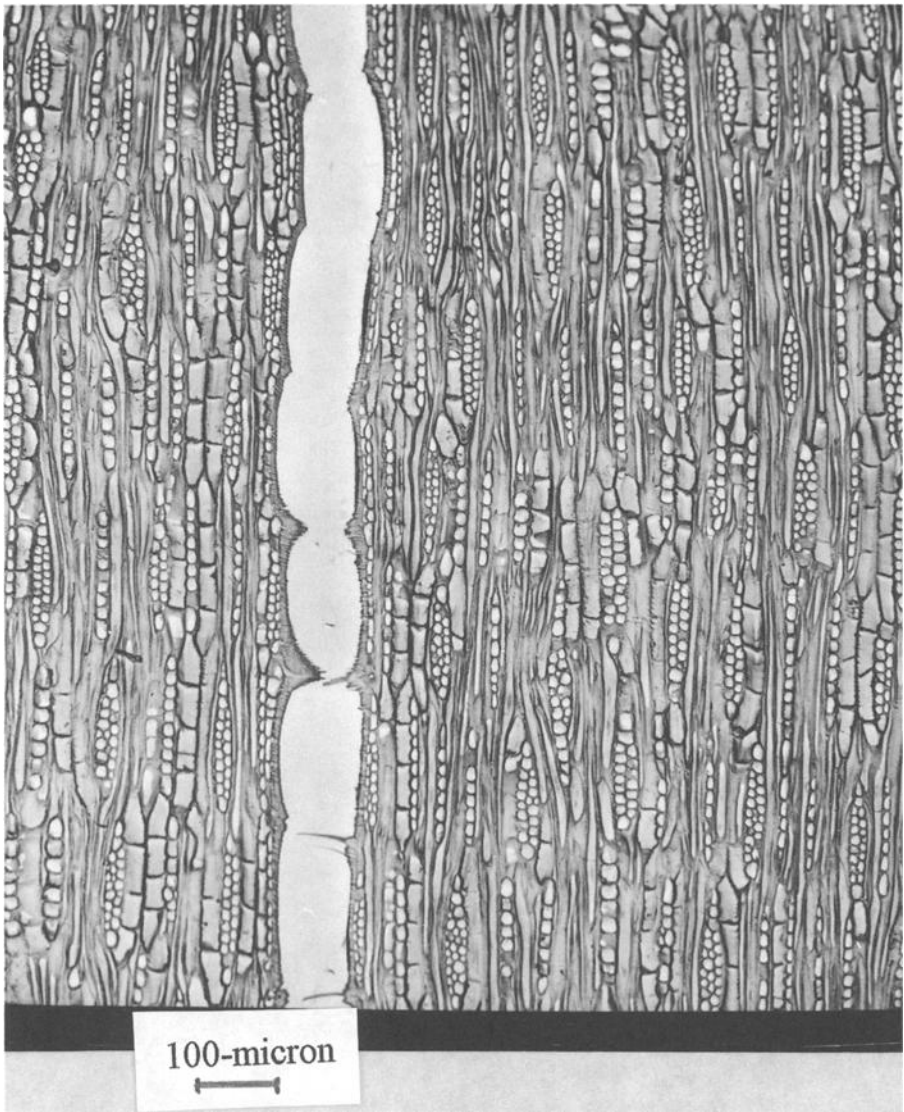


FIG. 3—Radial view of persimmon wood (approximately 200 \times).

so forth. The fatigue incident occurred when a gun snapped off the front (fore) stock during test and flipped upward upon a firing. The lower half of the stock was still in the vise. Subsequent testing of similar guns was halted and the used models were checked closely to see if there were similar problems. Several stocks were noted to have cracks running along the grain (TL or RL), starting at the front edge of the wood (Figs. 6 and 7).

The model being tested was a semiautomatic 12-gage shotgun. The cartridges used were ejected and replaced through the use of the gas pressure from the previous round. These gases were routed through a cylinder that ran under the barrel. This cylinder entered the forestock where the cracks were noted.

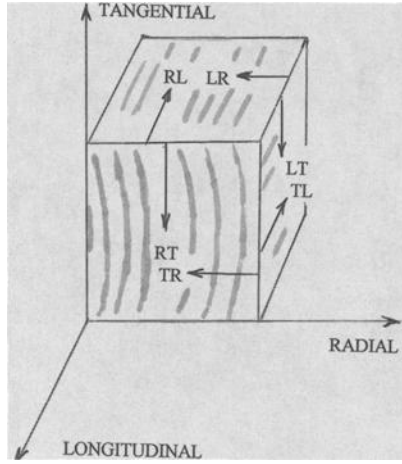


FIG. 4—Planes of crack propagation in wood.

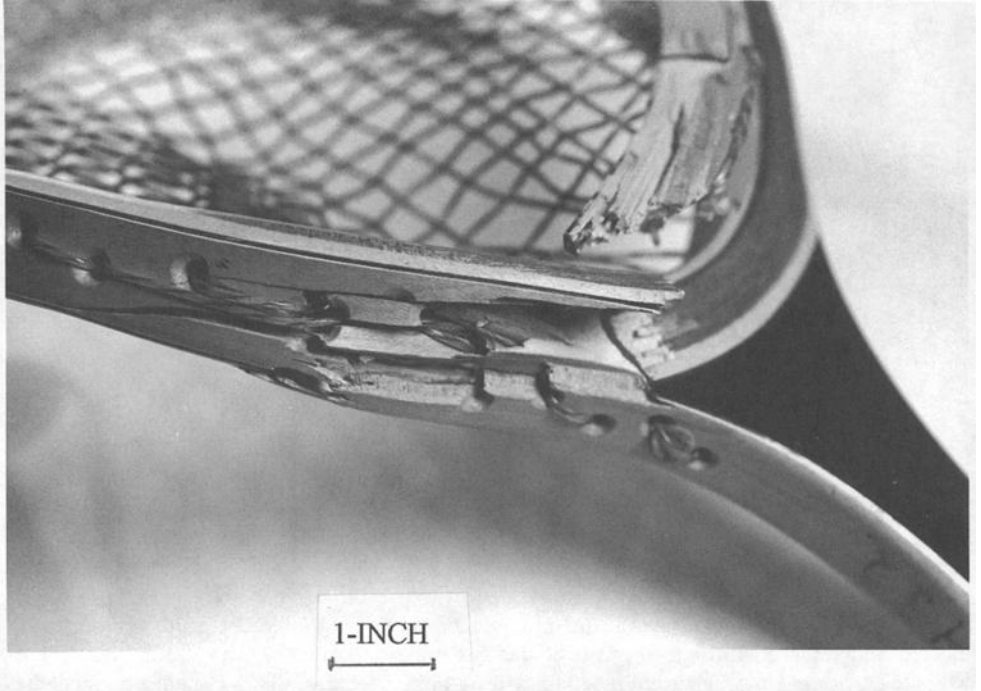


FIG. 5—Wood tennis racquet broken in fatigue tester after 1.6 million serves.

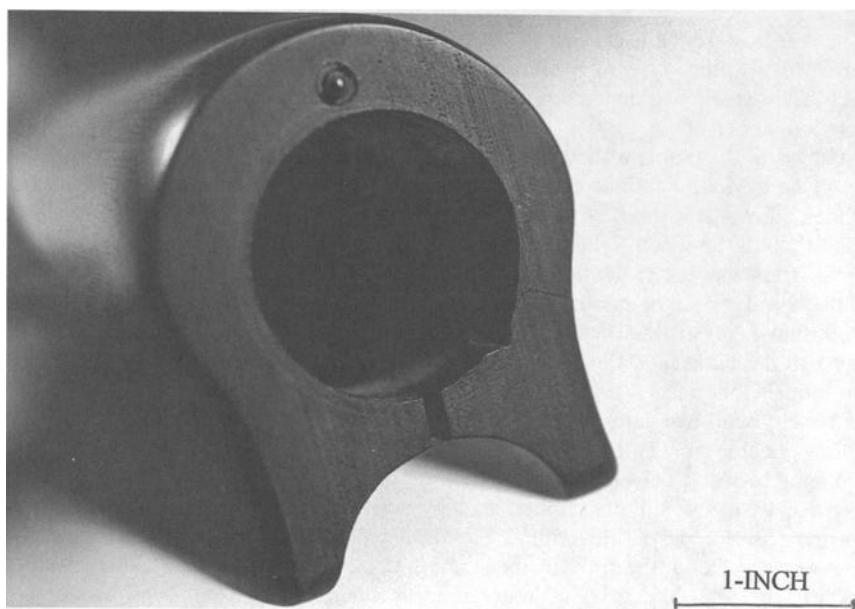


FIG. 6—Walnut gun stock showing fatigue crack.

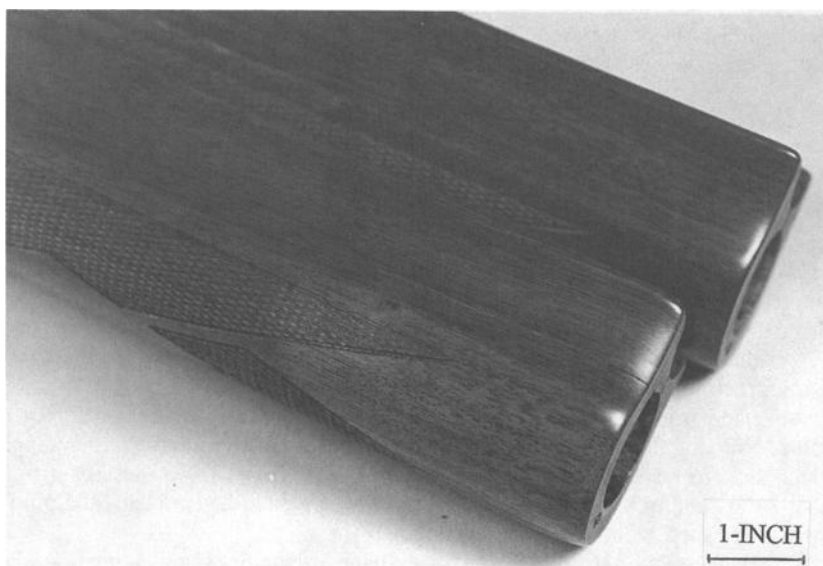


FIG. 7—View of fatigue crack in Fig. 6 showing propagation into stock.

The rear (toward the user) end of the forestock was not tightly attached to the gas cylinder. There was no other type of force applied to the stock other than the pressure and recoil effects. The stock was made from Black Walnut (*Juglans nigra*) supplied from midwest plantation stock.

Analysis of the problem showed the gas charge produced swelling of the cylinder sufficient to produce a Mode I fatigue crack that could move into the wood. The tight fit around the cylinder allowed the cracked wood to return after each shot and a brass retaining screw helped to hold the wood tightly enough to allow each subsequent surge of pressure to create normal stresses at the crack tip and move the crack along.

Since similar designs had been used on other models without problems, it was apparent that further analysis was needed. The wood used was sapwood. Heartwood is the wood nearest to the bark and is also acceptable for use. Sapwood had traditionally been used in prior models, but needed to be colored (it is white in the tree) and is usually low in specific gravity. Physical evaluation of the wood typically supplied for this product showed that it had low specific gravity compared to the average for walnut. All wood strength properties are related to wood density to a power n ranging from 1.1 to 2.0 [5]. This combination of lower-density wood, slightly thinner cross sections in the stock for the new design, and tight fit at the gas cylinder led to failure. The design was re-evaluated and made acceptable by using a soft gasket at the front of the stock to dampen pressure surges, increasing the stock thickness by 20%, and using a larger reinforcement screw. There was no attempt to get higher-density wood since current wood supplies from midwest plantations were all found to be from smaller, faster-grown trees that produce lower-density wood. This type of problem can be expected to become more common unless designers compensate for decreasing density in their wood products.

Case 2

Bowling pins take a severe beating in service and may fracture before their desired service life. Pins are given a life expectancy in "lines." A line is a complete ten-frame game by a bowler. Two thousand lines is desired for a pin. At that time, the finish will be cracked and the wood crushed at contact areas, but, if possible, still in one piece. During 2000 lines, a pin may undergo between 100 000 and 200 000 impacts against the floor, walls, and other pins.

A pin is shaped so that the mass of the head and the base resonate through the neck to give the familiar and pleasant sounds produced when the pins are struck by a ball. The frequency is in the mid-2000 Hz range. A propagating crack in the neck region can alter the resonance and cause the pin to sound "dead," or make a clanking noise when struck. In the extreme, the head can break off. Figures 8 and 9 show a pin that exhibits small cracks in the body, moving up the neck area. A complete neck fracture is shown in Fig. 9.

An increase in premature pin breakage occurred and was investigated to determine why rates of breakage and returns increased with no basic design change. The review involved a thorough evaluation of the raw material, hard maple (*Acer saccharum*), and the sequence of fabrication processes used to produce the pin.

Pins are made from laminated boards to expose the impact surfaces to forces that are distributed to a combination of radial and tangential faces, thereby lowering the opportunity for a deep split to develop. The laminating process uses over 20 pieces for a pin and is important for its ability to control pin weight by using drilled layers inside the pin (Fig. 8). The boards are glued with a urea-formaldehyde resin.

The failures were found to be heavily concentrated at glue lines, indicating a weaker-than-normal bond. Investigation of the manufacturing process showed that the only change was

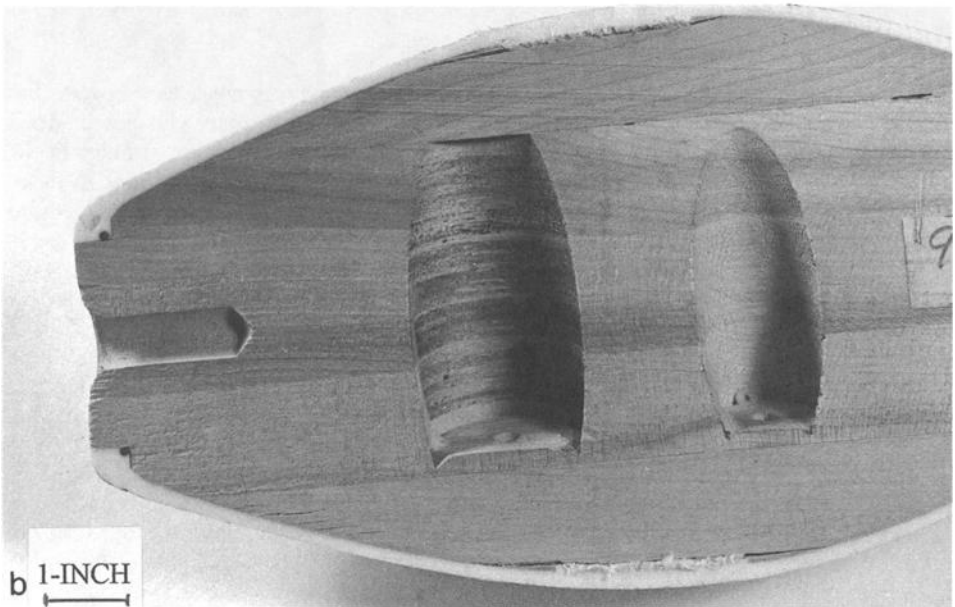
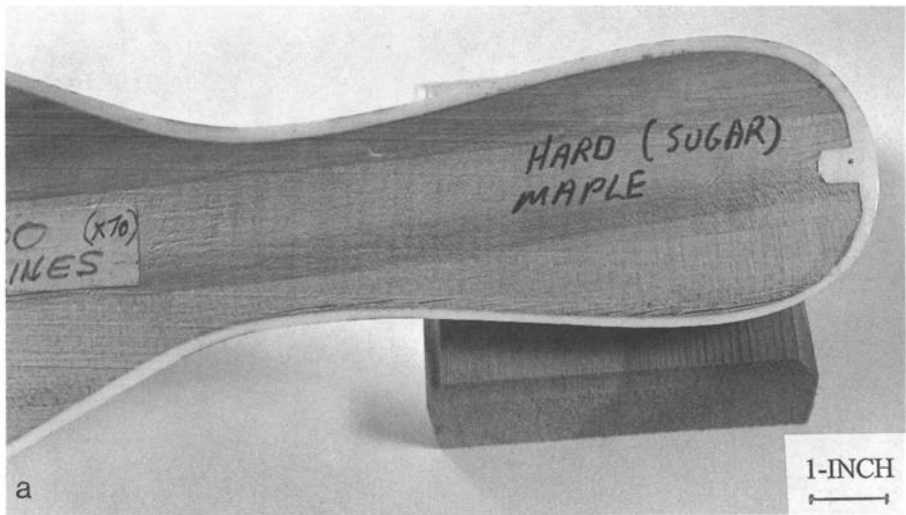


FIG. 8—Bowling pin cross-section showing small cracks along grain.

a new surface planer that machined the faces of the used boards. The new planer used a large abrasive belt rather than rotating knife blades. A look at the planed surfaces showed heavy fiber damage and loose debris on surfaces. The problem was that adhesive was being used to coat a very large and loose surface. The adhesive bond formed was degraded and the pin was weakened at the glue lines. Figure 10 shows a machine-sanded surface. (Compare Fig. 10 to Fig. 2, which was prepared by knife cutting the surfaces).

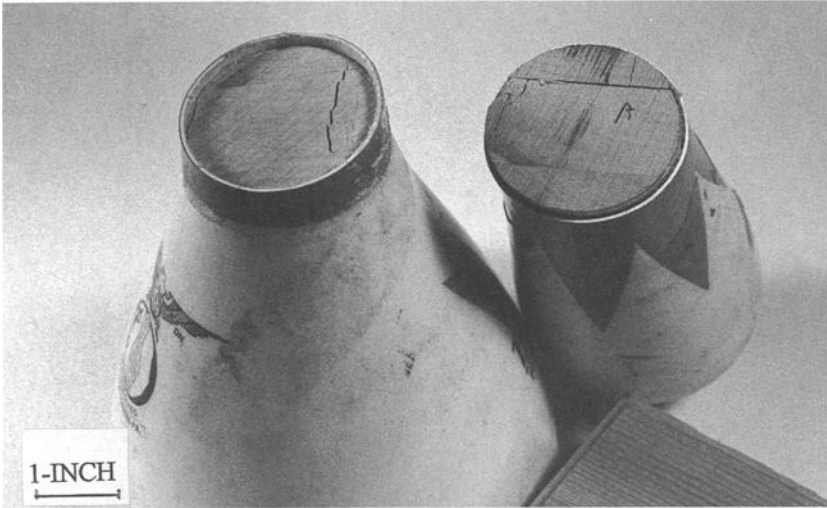


FIG. 9—Fractured bowling pin head showing cracks through wood and on glue line.

Some General Comments on Wood Fatigue

In loading conditions where tension perpendicular to the grain is not a factor, wood has extremely good resistance to fatigue failure [6]. In bending, the primary changes in wood structure after many reverse load cycles is the occurrence of compression wrinkles in the cell walls. This microbuckling can accumulate and resemble stacked dislocations in metal crystals. These buckled zones lose their compressive strength and transfer their loads to adjacent fibers. Even when cumulative damage is large, wood components, such as beams, only weaken by becoming effectively reduced in the cross-sectional area, where the damaged fibers are located. The result is a more flexible beam with a reduced static load capacity, without a propagating crack leading to fracture. A simple experiment to demonstrate this is to run a long-term flexure test under constant amplitude and monitor the power input to the test apparatus. As damage occurs, the power to flex the beam drops off. After long test periods, a microscope can be used to look at the highest stressed wood (the compression zone is best) to observe fiber damage, such as cell-wall buckling and collapse.

A good experiment for students is to observe the development of damage in a cantilever beam specimen undergoing flexural cycling. The experimental set-up used here is one where the beam is loaded by a rotating cam on an electric motor in contact with a roller follower on the cantilever end. A deflection proportional to 80% of the static modulus of rupture is the starting point. After the specimen undergoes 10 000 cycle load sequences, a thin section is removed from the face of the beam at the base attachment. As the beam is cycled, the student can observe these thin sections in a light microscope and note the progress of a wrinkled zone from the compression face into the beam cross section. A sketch of the system is shown in Fig. 11.

Observing macroscopic fatigue failures in wood is very difficult since they are obvious only under very specific load situations, such as tension perpendicular to grain and large torsional loads, which are unusual in wood product design. Composites made of wood, such as strandboard, paper, or plywood are less likely to show fatigue since their highly irregular microstructures are more able to diffuse cracks [6].



FIG. 10—Sanded (abrasive planed) surface of Maple before laminating into bowling pin (compare to Fig. 2, also maple).

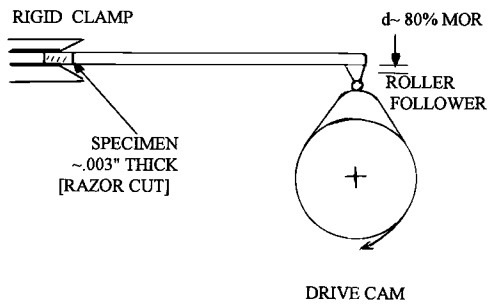


FIG. 11—Cantilever beam tester for laboratory demonstration.

Composites of wood base include paper, which is made of individual wood fibers, wafer or flake board products, and laminated or veneered products. Observing and verifying fatigue failures in these materials is even more difficult than in solid wood, because the fiber axis system is random. Fatigue has been noted in the manufacture and use of paper products under high tensile stress [5]. Engineers designing with wood chip or fiber composites would be prudent to develop appropriate tests to evaluate their designs under simulated use conditions.

Although the early engineers who said that fatigue is not found in wood structural components were wrong, it is easy to see how they were perhaps fooled by the forgiving nature of wood in use. Finding well documented and verifiable fatigue failures is unusual in wood, but possible. It is most likely to occur in products where the loading is in directions that stress the weaker planes. Stresses perpendicular to the grain are a special concern and the main reason why design handbooks for wood caution against any applications leading to such conditions.

Conclusions

It might appear from the preceding information that there is little need to study wood fatigue since it is relatively rare. In fact, the situation is changing rapidly in the use of wood and a few recent developments indicate that fatigue in wood may become a more serious concern.

The design of wood structures has traditionally been based on very conservative design stresses that are assigned by applying large strength-reducing ratios to the measured strength of clear wood. The resultant low stresses have kept wood members well below load levels where fatigue damage has any effect. In the past two years, a new test program using actual breaking loads within specific grades of lumber has resulted in a revision of design stresses. Some allowable stresses are now higher within a grade [7].

There is considerable effort being made to use wood in the design of small to medium highway bridges in order to upgrade the highway infrastructure. The designs used will use wood structural elements at higher stresses than previous designs. Engineers are concerned about fatigue for these applications [8].

Another factor that maintains fatigue as a concern is the gradual reduction in specific gravity of all common-wood species [9]. The walnut used in the earlier gun stock example is not an isolated situation. More wood is plantation grown, heavily fertilized, and intensely managed to produce larger volumes of timber, with resulting lower density. All wood strength properties are directly related to density, by a variable power relationship [5]. There are data [10] that shows that the average density of commercial lumber has been decreasing for at least the past 50 years. The design values published for timber have been decreasing over this same period of time. Therefore, the threshold where fatigue is a concern is being lowered [10].

When the increase in now used design stresses is combined with a raw material of decreasing strength qualities, it is clear that fatigue will be an issue that should be considered and watched during design. It may very well continue to be a secondary concern in most wood designs, but certainly not one to be routinely neglected.

References

- [1] Barlow, T. M., "The Weight of Aircraft," *Aircraft Engineering*, Vol. 1, 1929, p. 29.
- [2] Lewis, W. C., "Design Considerations for Fatigue in Timber Structures," *Journal of Structural Division*, May 1960, pp. 15-23.

- [3] "Duration of Load and Fatigue in Wood Structures," *Proceedings*, Paper 1361, ST-5, Vol. 83, Subcommittee on Timber Structures, American Society of Chemical Engineers (ASCE), Sept. 1957, pp. 1-12.
- [4] Lewis, W. C., "Fatigue of Wood and Glued Joints Used in Laminated Construction," *Proceedings of the Forest Products Resource Society*, Vol. 5, Forest Products Resource Society, 1951, pp. 221-229.
- [5] Bodig, J. and Jayne, B. A., *Mechanics of Wood and Wood Composites*, Van Nostrand-Reinhold, New York, 1982, pp. 307-312.
- [6] Kyanka, G. H., "Fatigue Properties of Wood and Wood Composites," *International Journal of Fracture*, Vol. 16, No. 6, Dec. 1980, pp. 609-616.
- [7] *National Design Specification for Wood Construction*, National Forest Products Association, Washington, DC, 1991.
- [8] Ritter, M. A., *Timber Bridges*, Publication EM 7700-8, U.S. Department of Agriculture, Washington, DC, 1990.
- [9] Green, D. W. and Kretschman, D. E., "Stress Class Systems," USDA Forest Products Laboratory Research Paper, FPL-RP-500, 1990.
- [10] Ethington, R. L., Galligan, W. L., Montrey, H. M., and Freas, A. D., "Evolution of Allowable Stresses in Shear for Lumber," General Technical Report FPL 23, U.S. Department of Agriculture, Madison, WI, 1979.

ISBN 0-8031-1997-6